Analysis of the Suction Chamber of External Gear Pumps and their Influence on Cavitation and Volumetric Efficiency

A thesis submitted to the Universitat Politècnica de Catalunya
for the degree of Doctor of Philosophy in the
Escola Tècnica Superior d'Enginyeries Industrial i Aeronàutica de Terrassa

David del Campo Sud

March, 2012

Universitat Politècnica de Catalunya (UPC)
Laboratorio de Sistemas Oleohidráulicos y Neumáticos (LABSON)

Analysis of the Suction Chamber of External Gear Pumps and their Influence on Cavitation and Volumetric Efficiency

Author
David del Campo Sud
Aeronautical Engineer

Director
Esteban Codina Macià
Doctor Mechanical Engineer

Codirector
Roberto Castilla López
Doctor Physicist

The only people for me are the mad ones, the ones who are mad to live, mad to talk, mad to be saved, desirous of everything at the same time, the ones that never yawn or say a commonplace thing, but burn, burn, burn like fabulous yellow roman candles exploding like spiders across the stars and in the middle you see the blue centerlight pop and everybody goes "Awww!"

Jack Kerouac, On The Road.

A la memoria de mi abuelo, Ramón.

Agradecimientos

En primer lugar quiero dar mi más sincero agradecimiento a mis directores de tesis, Dr. Esteve Codina Macià y Dr. Roberto Castilla López, por confiar en mi para llevar a cabo esta investigación y por la notable dedicación, esfuerzo y apoyo brindado a lo largo de todo el trabajo.

También quiero agradecer muy especialmente al anterior director de la Escola Tècnica Superior d'Enginyeries Industrial i Aeronàutica de Terrassa (ETSEIAT), Dr. Jaume Gibert Pedrosa, y a su actual directora, Dra. Eulalia Griful Ponsati por todo el apoyo que de ellos he recibido en estos años, y por depositar en mi su total confianza, tanto en el ámbito de la investigación como en el de la docencia, poniendo a mi servicio todos los recursos humanos y económicos que han sido posibles.

Al departamento de Mecánica de Fluidos de la ETSEIAT, por sus buenos consejos, su apoyo, y por cederme tanto sus instalaciones experimentales como sus recursos informáticos. En especial quiero agradecer su ayuda a los profesores Pedro Javier Gámez, Gustavo Rausch, Munir Khamashta, la secretaria María Contijoch, y los técnicos de laboratorio, Justo Zoyo y Jaume Bonastre.

Al coordinador del Área de Ingeniería Aeronáutica de la ETSEIAT, Dr. Miguel Mudarra López. A mis compañeros de área y muy buenos amigos Vanessa del Campo y Miquel Sureda, siempre dispuestos a ayudarme en todo, y con quienes he compartido tantos buenos momentos, dentro y fuera del despacho, sin los cuales hubiera sido mucho menos llevadero este trabajo. Y por supuesto al resto de compañeros: Oriol Lizandra, Roberto Flores, Elena Fantino, Gisela Detrell, Francesc Xavier, Josep Farre y a todos los profesores asociados. Me considero un afortunado al poder trabajar con personas como ellos cada día.

Al profesor Antón Vernet, de la Escola Tècnica Superior d'Enginyeria Química de la Universidad Rovira i Virgili, y a su doctoranda, Nihal Erturk, con quienes he realizado conjuntamente los ensayos en el laboratorio, por compartir conmigo sus conocimientos y experiencia en la técnica del PIV. Al profesor Gerber van def Graaf, por su ayuda con el código GPIV, con el que he realizado el procesado de las imágenes de PIV.

A mis tutores en las estancias realizadas en Universidades y centros de investigación extranjeros: El director del Departamento de Mecánica del Politécnico di Torino (Turín, Italia), Dr. Guido Belforte; el director del instituto de investigación IMAMOTER (Ferrara, Italia), Roberto Paoluzzi; y el investigador del IMAMOTER, Massimo Martinelli. Ellos han hecho que mis estancias en Turín y Ferrara hayan sido, además de provechosas para la consecución de esta investigación, muy agradables.

También quiero agradecer su apoyo a otros profesores y personal de administración y servicios de la ETSEIAT que hacen que trabajar en esta escuela sea un privilegio: Bea, Iria, Gloria, Mireia, Nuria, Inés, María, Pep, Dani, Merche, Mari Carme, Pilar, Marina, Alicia, Mari Carme, Teresa, Emi...

En lo personal, he de agradecer el apoyo de tantos buenos amigos, que citarlos a todos haría esta sección excesivamente larga. Aún así, no puedo dejar de nombrar a Jaime, Daniela, María "alegría" Björnberg, Yulia Barkova, Yulia Bulyigina, Luce, Andrei y Marina, Marta y Antonio, Paloma y Maribel, Guillermo y Natalia, María Soledad, Conchi, Beti, Carolina, Trini, Belén, Margarita y Mario, Jose, Pura, Angélica y Cano, Diego y Sara, Mark, Sonja, Katia, Nacho, Inés, Elena, Eva, Juan, Nora, Bea... además de los ya mencionados en otros párrafos.

Por último, quiero agradecer muy especialmente a mi madre, María Ángeles, y a mi abuela, Pepita, el inmenso esfuerzo que siempre han puesto en mi eduacación y el amor con que lo han hecho. Sin ello este trabajo no sería una realidad. A Alan Raeburn, mi padrastro, por todo lo que siempre aprendo de él y muy especialmente por la revisión del inglés. Por último, a una princesa india, de los quillasinga, llamada María Isabel por ser lo mejor que me ha pasado en estos años de tesis, por su amor incondicional, su casi infinita paciencia, su alegría, y por mucho más.

Thanks & Acknowledgements

First of all I want to truly thank my thesis conductors, Dr. Esteve Codina Macià and Dr. Roberto Castilla López, for having relied on me to carry out this research. I thank them too for their continuous and remarkable dedication, effort and support while doing this work. Special thanks to the former Director of the Escola Tècnica Superior d'Enginyeries Industrial i Aeronàutica of Terrassa (ETSEIAT), Dr. Jaume Gibert Pedrosa, and its current Director, Dr. Eulalia Griful Ponsati for their support during these years and for having fully relied on me in both the research and lecturing fields. Also for having made available human and financial resources.

Grateful thanks go to:

The ETSEIAT Fluid Mechanics Department, for their advice and support and for having let me use both their laboratories and computing resources. I want to particularly thank the lecturers Pedro Javier Gámez, Gustavo Rausch and Munir Khamashta, the secretary María Contijoch, and the lab technicians Justo Zoyo and Jaume Bonastre.

To the coordinator of the ETSEIAT Aeronautical Engineering Area, Dr. Miguel Mudarra López. To my area colleagues and very good friends Vanessa del Campo and Miquel Sureda, always ready to help me in everything. We have shared many good times in and out of the office. Without them this work would have seem harder. I also thank my other colleagues: Oriol Lizandra, Roberto Flores, Elena Fantino, Gisela Detrell, Francesc Xavier, Josep Farre and all the lecturers and associates. I consider myself lucky for working with them everyday.

To the lecturer Antón Vernet, from the Escola Tècnica Superior d'Enginyeria Química of the Rovira i Virgili University, and to his PhD student, Nihal Erturk, with whom I have done the lab trials, for having shared with me their knowledge and experience in the PIV technique. To the lecturer Gerber van def Graaf, for his help with the code GPIV, with whom I have done the processing of the PIV images.

To my tutors during my time at the Universities and Research Centres of different countries: Director of the Department of Mechanics of the Politécnico di Torino (Turin, Italy), Dr. Guido Belforte; Director of the Research Institue IMAMOTER (Ferrara, Italy), Roberto Paoluzzi; and the Researcher of the IMAMOTER, Massimo Martinelli. They made my stays in Turin and Ferrara apart from worthy for the complexion of this research, very grateful.

To the other lecturers, administration and services staff of the ETSEIAT: Bea, Iria, Gloria, Mireia, Nuria, Inés, María, Pep, Dani, Merche, Mari Carme, Pilar, Marina, Alicia, Mari Carme, Teresa, Emi... for their support. Working with them at this college has been a privilege.

On the personal side, I must thank so many friends for their support that to name all of them

would make this section too long. Even though, I have to name Jaime, Daniela, María “alegría” Björnberg, Yulia Barkova, Yulia Bulyigina, Luce, Andrei y Marina, Marta and Antonio, Paloma and Maribel, Guillermo and Natalia, María Soledad, Conchi, Beti, Carolina, Trini, Beughlén, Margarita and Mario, Jose, Pura, Angélica and Cano, Diego and Sara, Mark, Sonja, Katia, Nacho, Inés, Elena, Eva, Juan, Nora, Bea... apart from the ones already named above.

Finally I want to give very special thanks to my mother, María Ángeles, and my grandmother, Pepita, for the huge effort they always put into my education and their love for me. Without them this work would have never existed. To Alan Raeburn, my stepfather, for all I always learn from him and especially for checking the English of this thesis. Finally, to an Indian princess from the quillasinga, named María Isabel for being the best thing that happened to me during these years of the thesis, for her unconditional love, her almost never ending patience, her joyfulness, and for many more things.

Abstract

Hydraulic machines are faced with increasingly severe performance requirements. The need to design smaller and more powerful machines rotating at higher speeds in order to provide increasing efficiencies, has to face a major limitation: cavitation.

A two-dimensional numerical approach, by means of Computational Fluid Dynamics (CFD), has been developed for studying the effect of cavitation in the volumetric efficiency of external gear pumps. Several cavitation models and grid deformation algorithms have been studied, and a method for simulating the contact between solid boundaries has been developed. The velocity field in the inlet chamber has also been experimentally measured by means of Time-Resolved Particle Image Velocimetry (TRPIV) and results have been compared to the numerical ones in order to validate the accuracy of the model.

Our two-dimensional model is not able to predict the real volumetric efficiency of the pump, since several simplifications are involved in it. Nevertheless, this model shows to be valid to understand the complex flow patterns that take place inside the pump and to study the influence of cavitation on volumetric efficiency. The influence of the rotational speed of the pump has been analyzed, as well as the effect of the geometry of the inlet chamber, the working pressure, the inlet pressure loss factor, and the flow leakage through the radial clearances of the pump between gears and casing.

Contents

List of Figures

List of Tables

Nomenclature

Roman Symbols

$\dot{m}$	Mass flow rate.
$\vec{a}$	Acceleration.
$\vec{F}_D$	Drag force.
$\vec{n}$	Normal vector.
$\vec{r}$	Vector from the center of edge i to the center of the neighboring cell.
$\vec{v}$	Flow velocity.
$\vec{v}_g$	Velocity of the deforming grid.
A	Area.
a_p, a_{nb}, b	Coefficients of the discretized equations.
A_r	Flow area across the recess.
A_w	Width of the blending function.
B	Bulk modulus.
b	Depth of the gears.
c	Wave propagation velocity.
C_μ	$k-\varepsilon$ turbulence model constant.
C_d	Discharge coefficient.
C_p	Pressure coefficient.
C_s	Scattering cross section.
C_v	Volumetric capacity.
$C_{1\varepsilon}, C_{2\varepsilon}, C_{3\varepsilon}$	$k-\varepsilon$ turbulence model constants.
$C_l^*, A_\mu, A_\varepsilon$	Enhanced wall treatment model constants.
D	Distance between two contact points.

d	Distance from the contact point position.
d_a	Radius of the high-viscosity area surrounding the contact point position.
D_g	Distance between centers of gears.
D_h	Hydraulic diameter.
D_p	Particle diameter.
D_t	Throat length of the venturi nozzle.
d_{CP}	Distance between gears at the contact point position.
f	Cloud shedding frequency.
F_{vap}, F_{cond}	Cavitation model constants.
g	Acceleration of gravity.
G_b, Y_M	$k-\varepsilon$ turbulence model constants.
G_k	Generation of turbulent kinetic energy due to velocity gradients.
h_t	Tip clearance height.
I	Turbulent intensity.
I_0	Laser intensity incident on the particle.
I_g, I'_g	Grey intensity values from first and second image respectively.
j	Imaginary unit.
k	Cavitation number. Turbulent kinetic energy.
$k_1, k_2, k_3, k_4, k_5, k_6$	Experimental coefficients.
K_e	Pump coefficient.
k_L	Loss coefficient.
L	Lenght of the rigid pipe. Length of the line of action.
l	Integral turbulent length scale.
L_c	Average cavity length.
l_μ, l_ε	Modified turbulent length scales.
m	Mass. Modulus of the gear.
m_B	Mass of a bubble.
M_i	Mass flow imbalance.

n_b	Number of bubbles per unit volume.
n_t	Number of teeth adjacent to the casing, on one gear.
P	Perimeter.
p	Pressure.
P_s	Total scattered power.
p_x	Pressure amplitude at a point x along a pipeline.
Q	Volumetric flow rate.
q	Normalized diameter.
Q_S	Flow pulsation source.
Q_{th}	Theoretical mean flow rate.
R	Bubble radius.
r	Pitch radius.
R^{ϕ}	Scaled residual for variable ϕ.
r_a	Addendum radius.
r_b	Base circle radius.
R_c	Cross-correlation function.
R_S	Source reflection coefficient.
R_T	Termination reflection coefficient.
R_{lv}	Net mass transfer rate from liquid to vapor.
r_{nuc}	Nucleation site volume fraction.
Re	Reynolds number.
S	Surface. Modulus of the mean stress rate tensor.
S_c	Cell surface.
S_e	Surface of a equilateral triangle with the same circumradius of the cell.
S_k, S_ε	$k-\varepsilon$ turbulence model source terms.
S_{ij}	Mean stress rate tensor.
Sk	Equivolume skewness of a cell.
St	Stokes number.
T	Temperature.

t	Time.
T_g	Time period of the flow pulsation.
T_r	Residence time of a fluid particle inside the orifice.
T_s	Torque applied to the shaft.
u	Instantaneous length of action. Velocity.
U, v	Velocity.
U_t	Teeth tips velocity.
V	Volume.
V_b	Bubble volume.
V_m	Volume displaced in one revolution.
V_T	Total volume.
w_p	Vertical velocity of the particle.
x	Spatial coordinate.
y	Wall normal distance.
z	Number of teeth in each gear.
Z_L	Impedance of the rigid pipe.
Z_S	Source impedance.
Z_T	Impedance of the system's load valve.

Greek Symbols

α	Air volume fraction.
α_v	Bunsen coefficient.
β	Termination reflection coefficient. Relaxation factor.
χ	Evolution rate.
δ	Flow rate irregularity index.
δ_{ij}	Kronecker delta.
η	Total efficiency.
η_m	Mechanical efficiency.
η_v	Volumetric efficiency.
κ_v	Volumetric ratio.

λ	Wave length of the incident light.
λ_ε	Blending function.
μ	Dynamic viscosity.
$\mu_{t,enh}$	Modified turbulent viscosity for near-wall treatment.
$\mu_{t,w}$	Turbulent viscosity in the near-wall region.
μ_{tm}	Modified turbulent viscosity for the cavitation model.
μ_t	Turbulent viscosity.
ν	Kinematic viscosity.
ω	Rotational speed of the gears.
ϕ	Generic variable.
Ψ	Pressure angle.
ρ	Density.
σ	Surface tension.
$\sigma_k, \sigma_\varepsilon$	$k-\varepsilon$ turbulence model source terms.
τ_ϕ	Difussion coefficient for the variable ϕ.
τ_{ij}	Reynolds stress tensor.
τ_k	Kolmogorov time scale.
τ_p	Particle response time.
θ	Angular displacement of the gear.
θ_g	Angular period of the flow pulsation.
θ_{op}	Angular region of the gear in contact with the suction chamber.
ε	Contact ratio. Dissipation rate of the turbulence energy per unit mass.
ξ	Wave attenuation coefficient.

Subscripts

0	Equilibrium / atmospheric conditions.
∞	Upstream / far field conditions.
air	Air.
av	Refers to a phase-averaged magnitude.
B	Conditions inside the bubble.

c	Choking cavitation conditions. Refers to a grid cell.
cav	Due to cavitation.
$comp$	Due to compressibility.
$corr$	Corrected value.
D_h	Hydraulic diameter.
eff	Effective.
f	Refers to a grid face. Refers to the fluid.
G	Gas.
i	Node / edge / grid point index. Incipient cavitation conditions.
in	Refers to the inlet conditions.
it	Refers to the inter-teeth volume.
j	Refers to phase j. Refers to component j.
L, l	Liquid phase.
lag	Refers to the velocity lag.
$leak$	Due to leakages.
m	Mixture.
max	Maximum.
med	Median.
min	Minimum.
mod	Modified value.
nb	Refers to the neighboring cells.
$nocav$	Not simulating cavitation.
oil	Oil.
out	Refers to the outlet conditions.
p	Refers to cell p. Refers to the particle.
pd	Due to pressure drop.
rec	Across the recess.
ref	Reference value.
$s90, s180$	90° and 180° scattering directions.

sq	Refers to the squeeze volume.
tip	Across the tip of a tooth.
$tooth$	Across one tooth.
v	Vapor phase.
vd	Due to viscous drag.
x	Refers to the x direction.
y	Based on the wall-normal distance.

Superscripts

$*$	Minimum C_p conditions. Reference value.
n	Refers to time step n.
n, m	Refers to the n^{th} / m^{th} time step.
n_i	Number of vertices connected to vertex i.

Abbreviations

CFD	Computational Fluid Dynamics.
IA	Interrogation area.
NPSH	Net Positive Suction Head.
PIV	Particle Image Velocimetry.
rev	Revolution.
rpm	Revolutions per minute.
TRPIV	Time-Resolved Particle Image Velocimetry.

Mathematical Symbols

$'$	Variable referred to its time-average.
Δ	Refers to a jump in the value of a property.
$\dot{}$	Time derivative.
$\langle\rangle$	Time average in a gearing cycle.
∂	Refers to the boundary.

Chapter 1

Objectives and scope

1.1 Preamble

Cavitation is a complex multiphase phenomenon that takes place when, in some point of a fluid volume, pressure drops below a certain value related to the vapor pressure. This leads to a process of gas bubble inception, growth and collapse, and therefore the fluid becomes multiphasic. Associated to this process, undesirable effects such as material damage, noise and vibration usually occur. Cavitation is a generally unwanted effect that should be taken into account in the design of hydraulic machinery, and represents a major limitation to their performance.

External gear pumps are one of the most common types of pumps for hydraulic fluid power applications, and are not exempt from the problems related to cavitation. The problems associated with material damage, noise and vibration, have been studied experimentally by various authors. Beyond these problems, the presence of cavitation also affects the suction capability of gear pumps. Our aim in this work is to study how cavitation influences the volumetric capacity of external gear pumps. The problem will be approached from both the numerical and the experimental fields.

The fluid-dynamic process that takes place in an external gear pump is a complex, turbulent, three-dimensional, phenomenon. Furthermore, when cavitation conditions are reached, it becomes even more complex. Nowadays, the use of advanced algorithms and high-speed computers allow us to tackle the problem from the field of Computational Fluid Dynamics (CFD). Nevertheless, many difficulties arise when trying to fully characterize the unsteady velocity field, and the numerical methods to be used should be carefully selected and validated.

From the experimental point of view, the technique of Time-Resolved Particle Image Velocimetry (TRPIV), has become very popular in the last decade, thanks to the fast development of digital high-speed photography. It is the most extended velocimetry technique when a instantaneous velocity field is to be measured. This technique is based in the mathematical processing of high-speed photographies taken to the fluid flow, which should contain tiny tracing particles and should be illuminated by a thin laser sheet. One of the requirements of this method is that particles should be homogeneously distributed within the flow. This makes the technique difficult to be applied in multiphasic flows. Therefore this technique will only be applied in experiments at low operating speeds, where no cavitation appears, in order to validate the numerical methods selected.

The pump has been modeled as two-dimensional, since three-dimensional simulations including cavitation effects would be too expensive from the computational point of view. This fact prevents us from being able to predict the three-dimensional characteristics of the flow, which are related to the inlet and outlet circular pipes and to the effect of the compensation plates that enclose the gears. The implications of these limitations will be carefully studied, and it will be seen that, despite the volumetric efficiency obtained cannot be compared to the real values. The model is appropriate for studying the influence of cavitation in the pump performance, by comparing simulations in which cavitation effects are simulated against identical ones in which these effects are not simulated.

As cavitation is a phenomenon associated with low pressures, it generally originates at the teeth meshing region and propagates upstream through the inlet chamber. The influence of the geometry of this inlet chamber in how cavitation develops and affects the volumetric efficiency will also be investigated. Our study will be based on a reference pump. Starting from it, four alternative models, in which the geometry of the inlet chamber is modified, will be studied.

Some of the work that has been done for selecting and developing the numerical models that are presented in chapter 4, represent major contributions in the fields of numerical simulation in external gear pumps and cavitation modeling with oil.

1.2 Objectives of the current work

The principal aim of this project is **to advance the understanding of the influence of cavitation on the volumetric displacement performance of external gear pumps**.

This has been achieved through the use of Computational Fluid Dynamics (CFD). The selection, development and experimental validation of the appropriate numerical methods for the simulation of cavitating flows in external gear pumps is necessary. The main contributions done in these areas are:

- **Study of mesh deformation algorithms** in order to keep an acceptable mesh quality in all the simulated gearing cycles.
- A **method to simulate contact between gear's tips and casing** by changing the dynamic viscosity of the fluid.
- A **study of cavitation modeling algorithms** by performing simulations in a venturi nozzle and in a circular orifice, then comparing the results against numerical and experimental data obtained by other authors. This has been necessary since most of the existing studies of cavitation models use water as working fluid, while the cavitating properties of hydraulic oil are radically different from those of water.
- **Experimental analysis of the velocity field in the inlet chamber** of an external gear pump by means of Time-Resolved Particle Image Velocimetry (TRPIV).

The influence of the following parameters will be studied:

- The rotational speed of the pump.

- The geometry of the inlet chamber.
- The working pressure.
- The inlet conditions.
- The effect of the clearance between gear's tips and casing.

1.3 Organization

This thesis is divided into seven chapters, three appendices, and a bibliography section.

This chapter serves as an introduction and reviews the subjects related to the thesis.

Chapter 2 presents an introduction to the phenomenon of cavitation and aeration including some definitions, a classification of its different types, a description of its phases, from bubble inception to collapse, and a mathematical model for the bubble radius evolution. Also the main effects of cavitation on hydraulic machinery (material damage, noise, vibration...) are described. Finally, special attention is paid to the effect of aeration on hydraulic oil.

Chapter 3 contains the theory related to the characteristics of hydraulically balanced external gear pumps. The ideal suction capacity is deduced and the volumetric efficiency is defined. The different sources that contribute to reduce the real flow rate are presented and analyzed, along with the mechanisms that are generally used in order to minimize them. Mathematical models for predicting flow and pressure fluctuations are also analyzed. Finally, a simple model is used to study the dependence of volumetric efficiency against working pressure and rotational speed in non-balanced pumps.

Chapter 4 describes the numerical models employed in the numerical simulations that we have run, including a description of the discretization employed, turbulence and multiphase flow modeling, and mesh deformation algorithms. Special attention is paid to the modeling of cavitation with hydraulic oil. For selecting a cavitation model and tuning its constants, simulations with a venturi nozzle and an orifice are presented and compared to experimental data. A study of mesh resolution and quality is presented. Also, a technique that has been developed to simulate the contact between moving parts without affecting the mesh quality will be described. Finally, after presenting the boundary conditions to be employed, the limitations of our numerical model are discussed, analyzing up to which point each simplification affects to how the volumetric capacity of the real pump can be predicted with our model, and justifying its suitability within the scope of the thesis.

Chapter 5 presents an introduction to the experimental technique of Time Resolved Particle Image Velocimetry (TRPIV), from the experimental set-up to its mathematical background. After paying attention to the state of the art of PIV within the field of oleo-hydraulics, the equipment, set-up and experimental procedure employed in our tests is presented, along with the procedure followed for later image processing. Finally, the results are analyzed and compared to those of the numerical simulations, validating our numerical model.

In chapter 6 the results of the numerical simulations are presented and discussed, and final conclusions are given.

Conclusions and suggestions about how this research can be continued are presented in chapter 7.

In appendix A the mechanical properties of involute gear pumps are presented.

In appendix B the numerical results of each numerical simulation performed are tabulated.

Appendix C shows the Used-Defined functions that we have implemented in the numerical code in order to properly set up the simulations.

Finally, a bibliography section is given.

Chapter 2

Cavitation

2.1 Introduction

Cavitation is normally defined as the formation of bubbles filled with vapor/gas or their mixture and subsequent activities, such as growth, collapse and rebound, in liquids. Cavitation is almost always an unwanted phenomenon in hydraulic machinery (although it has some favorable effects in other fields) and constitutes a main obstacle to the development of high-performance machines.

Although the problem of cavitation in hydraulic machines is an old one, dating back at least to the time of Galileo, it has not yet been completely solved. Hydraulic machines are faced with increasingly severe performance requirements, and the need to provide cheaper designs involving smaller and more powerful machines rotating at higher speeds continues to heighten the danger of cavitation.

Despite improved experimental techniques have been developed for detecting and measuring cavitation, and advanced numerical algorithms have been created for modeling it, the complexity of the physics involved in this phenomenon still makes it difficult to accurately predict and characterize complex cavitating flow fields, as the ones associated to hydraulic machinery.

Beyond the material damage, noise, and vibrations, cavitation has also a direct effect on the performance of hydraulic machinery. In this thesis we will investigate, by means of numerical simulations, the development of cavitation in the inlet chamber of external gear pumps, in order to understand how does it influence their volumetric efficiency. Prior to doing this, the main aspects of the cavitation process and its consequences should be well understood. These general aspects will be discussed in this chapter, paying especial attention to the particular characteristics of hydraulic oil from the point of view of cavitation.

In this chapter, cavitation will be defined, a classification of its different types will be made, and the three stages of its evolution will be described. The adverse effects of cavitation and the methods to detect it will also be presented. As our interest is centered in cavitation phenomena in hydraulic oil, its particular characteristics in relation with gas solubility and aeration will be finally presented.

2.2 Definition of cavitation

Cavitation is a complex two phase flow phenomenon involving the inception, growth and collapse of gas, or vapor and gas filled bubbles.

The term cavitation was first cited by R. E. Froude, S. W. Barnaby and Sir Charles Parson in connection with propeller performance breakdown of early steamships. In 1895 Parson made the first water tunnel in order to study cavitation. After 20 years of experiments he made the connection between cavitation and erosion of marine propellers.

In some aspects, cavitation is similar to boiling, except that the latter is generally considered to occur as a result of an increase of temperature rather than a decrease of pressure. This difference in the direction of the state change in the phase diagram is more significant than might, at first sight, be imagined. It is virtually impossible to cause any rapid uniform change in temperature throughout a finite volume of liquid. Rather, temperature change most often occurs by heat transfer through a solid boundary. Hence, the details of the boiling process generally embrace the detailed interaction of vapor bubbles with a solid surface, and the thermal boundary layer on that surface. On the other hand, a rapid, uniform change in pressure in a liquid is commonplace and, therefore, the details of the cavitation process may differ considerably from those that occur in boiling.

In order to achieve a better understanding of the phenomenon let us consider other definitions that should be taken into consideration.

Description of the fundamental cavitation process given by Knapp et al. [52]:

> When a mass of liquid is heated under constant pressure, or when its pressure is reduced at constant temperature by static or dynamic means, a state is reached ultimately at which vapor or gas –and vapor– filled bubbles, or cavities, become visible and grow. The bubbles growth may be at a nominal rate if it is by diffusion of dissolved gases into the cavity or merely by expansion of the gas content with temperature rise or pressure reduction. The bubble growth will be explosive if it is primarily the result of vaporization into the cavity. This condition is known as boiling if caused by temperature rise, and cavitation if caused by pressure reduction at essentially constant temperature. Bubble growth by diffusion is termed *degassing* although it is also called *gaseous cavitation* (in contrast to *vaporous cavitation*) when induced by pressure reduction.

As we can see, even though the start of boiling and cavitation processes are the same, cavitation is a completely different phenomenon. During boiling, vapor bubbles grow continuously. By contrast, in the cavitation process, when the growing bubble is subjected to a pressure increase, its growth will be stopped and reversed. Hence the bubble will collapse implosively. Bubble inception, bubble growth and bubble collapse are the complete sequence of the cavitation phenomenon. A more accurate definition of the growing process was given by Pearce and Lichtarowic [83]:

> At a pressure corresponding to the saturation pressure of the gas dissolved in the liquid, the original microscopic bubbles will begin to grow by diffusion of the gas out of solution. Since the dissolved gas is usually air, this process can be called aeration. A further reduction in pressure, to slightly below vapor pressure, results in the growth of vapor bubbles, and this is cavitation.

We see that different authors have used different names for the same phenomena. *Degassing*, *gaseous cavitation* or *aeration* are used for the process that involves the diffusion of air into the bubble, while *vaporous cavitation* or simply *cavitation* are used for the process that involves the growth of the bubble by evaporation of the fluid.

Holl [5] introduced the concept of *pseudo-cavitation* for the growth of the bubble due to changes in the surrounding pressure with no change in the bubble mass:

> In order to illustrate the differences between these various phenomena, let us assume that a bubble is initially in equilibrium at a pressure P_1 and suddenly the pressure is reduced to P_2. Vaporous cavitation occurs if the bubble is observed to grow explosively without bound and is caused by the rapid conversion of liquid to vapor. This form of cavitation can occur only if $P_2 < P_v$. Pseudo-cavitation (apparently the words gaseous cavitation are sometimes used to mean pseudo-cavitation), occurs if the bubble is observed to grow to a larger equilibrium radius at pressure P_2. Thus, in pseudo-cavitation, the essentially constant mass of gas in the bubble is merely responding to the change in liquid pressure outside of the bubble, and P_2 can be less than, equal to, or greater than P_v depending on conditions. Gaseous cavitation will occur at pressure P_2 if the bubble grows due to the transport of gas across the interface and this can only happen if the liquid is over-saturated. Furthermore, like pseudo cavitation, gaseous cavitation can occur above or below vapor pressure.
>
> Thus vaporous cavitation is caused by the rapid increase in mass of vapor inside the bubble, pseudo cavitation by a change in pressure with negligible change of mass in the bubble, and gaseous cavitation by the increase in mass of the gas in the bubble. Vaporous cavitation is a very rapid process whereas gaseous cavitation is relatively slow unless appreciable convective effects occur.

2.3 Types of cavitation

There are a number of ways of classifying cavitation. A classification attending to the flow regime (gaseous, pseudo or vaporous cavitation) has just been presented. Knapp et al. [52] proposed a classification attending to the conditions in which cavitation take place as well as to the principal physical characteristics. This classification distinguish between the following types of cavitation:

1. Traveling Cavitation

   In this case, individual transient cavities or bubbles form in the liquid and move with it as they expand, shrink, and collapse. These cavities move continuously with the local velocity of the flowing liquid. The traveling cavities first become visible in the liquid very close to the boundary surface at the minimum pressure zone. They grow in size during their transit through the low-pressure region and start to collapse shortly after they are swept into the region in which the pressure exceeds the vapor pressure. Collapse to an invisible size is often followed by a series of re-openings and re-collapses which suggest pressure pulsations.

2. Attached Cavitation

Refers to the situation, after inception, in which the liquid flow detaches from the rigid boundary of an immersed body or a flow passage to form a pocket or cavity attached to the boundary. Fixed cavities sometimes have the appearance of a highly turbulent boiling surface, or, in other cases, the surface between the liquid and the large cavity may be so smooth as to be transparent. The liquid adjacent to the large cavity surface has been observed to contain a multitude of small traveling transient cavities. These traveling cavities grow rapidly to nearly their maximum size at the upper end of the main cavity and remain fairly constant until they reach the downstream end of the cavity and disappear. Termination may be by the main liquid stream returning to the solid surface downstream of a leading edge or *breakaway* line, or the cavity may extend well beyond the body before the main liquid stream closes together enveloping the pocket, which is known as *supercavitation*.

3. Vortex Cavitation

   Flow regions with concentrated vorticity can develop cavitation in their central cores due to the low pressures generated. If the tips of these vapor filled vortices are in contact with a solid surface they become potentially erosive since the final collapse of the whole cavity takes place on them. A typical example of this type of cavitation can develop if Von Kármán vortex-shedding occurs at the trailing edge of a hydrofoil and pressure is low enough. As a result, lift fluctuations, synchronized with the shedding frequency, appear. Vortex cavitation can also occur in the flow channels of hydraulic machines when they operate at part load. In the case of a coupling phenomena with a natural frequency this can lead to fatigue damage. This type of cavitation is often referred to as tip cavitation.

4. Vibratory Cavitation

   The forces that cause the cavities to form and collapse are due to a continuous series of high amplitude, high frequency pressure pulsations in the liquid.

2.4 Cavitation process

According to the literature, the two main stages of cavitation are incipient and developed cavitation. The term *incipient cavitation* is used to describe cavitation that is just barely detectable. In this stage bubbles are small and the zone where cavitation occurs is limited. With changes in flow conditions towards promoting an increase of vaporization rate and, hence, growth of the bubbles, the term developed cavitation is used. Apart from this, Holl [4] introduced the term *desinent cavitation* to name the moment in which cavitation disappears. This happens at the desinent pressure.

As we have mentioned, cavitation is a process that implies the inception, growth and collapse of cavities in a liquid. Lets consider each stage of the cavitation process.

2.4.1 Inception

Inception is the term given to the moment in which cavitation begins, either because the liquid starts to evaporate or because dissolved air comes out of the solution.

Although experiments show inception to occur near the vapor pressure, there are deviations of various degrees that are not reconcilable with the vapor pressure concept. There is, of course, an extensive body of literature on this subject, and we shall not attempt a comprehensive review. The reader is referred to reviews by Knapp, Daily and Hammit [52], Acosta and Parkin [2], Arakeri [3] and Brennen [9] for more detail.

Vapor pressure is defined as the equilibrium pressure, at a specified temperature, of the liquid vapor which is in contact with an existing free surface. If a cavity is to be created in a homogeneous liquid, the liquid must be ruptured and the stress required to do this is not measured by the vapor pressure but is the tensile strength of the liquid at that temperature (Knapp et al., [52]).

As pure liquids can sustain very high stresses, it is reasonably concluded that something causes weak spots to exist in the liquid or in its contact with its container. In nearly all practical cases, liquids are not pure but containing gas. Hence it is concluded that undissolved gas is the basic impurity that reduces the tensile strength of liquid from its high theoretical value to the low effective values encountered in cavitation measurements. Because of this contamination, substantial differences in the inception cavitation number (and, indeed, the form of cavitation) have been observed in experiments in different water tunnels, and even in a single facility with differently processed water (Lindgren and Johnson [56], Johnson [41]). The role of dissolved-undissolved gas was demonstrated by Harvey et al. [31].

For example, a micro-bubble of radius, R_0, containing only vapor, is in equilibrium when the liquid pressure takes the value

$$p = p_v - \frac{2\sigma}{R_0} \tag{2.1}$$

where σ is the surface tension. It follows that such a micro-bubble would result in a critical tension of $2\sigma/R_0$, and the liquid pressure would have to fall below $p_v - 2\sigma/R_0$ before the micro-bubble would grow to a visible size. For example, a $10\,\mu$m bubble in water at 20^{o}C leads to a tension of $0.14\,$bar.

In hydraulic oil, there is 10% of dissolved air under normal conditions. Because of these contaminants the stress required to rupture the oil is not measured by the liquid's tensile stress, but by its vapor pressure, for rapid rupture, or by its gas saturation pressure, for slow rupture (Lamb [54]).

For the purposes of the present discussion we shall consider a steady, single-phase flow of a Newtonian liquid of constant density, ρ_L, velocity field, $u_i\,(x_i)$, and pressure, $p\,(x_i)$. In all such flows it is convenient to define a reference velocity, U_∞, and reference pressure, p_∞. In external flows around solid bodies, U_∞ and p_∞ are conventionally the velocity and pressure of the uniform, upstream flow. The equations of motion are such that changing the reference pressure results in the same uniform change to the pressure throughout the flow field. Thus the pressure coefficient

$$C_p\,(x_i) = \frac{p\,(x_i) - p_\infty}{\frac{1}{2}\rho U_\infty^2} \tag{2.2}$$

is independent of p_∞ for a given geometry of the macroscopic flow boundaries. Furthermore, there will be some location, x_i^*, within the flow where C_p is a minimum, and that value of $C_p\,(x_i^*)$ will be denoted for convenience by C_{pmin}.

Viscous effects within the flow are characterized by the Reynolds number, $Re = \rho_L U_\infty l/\mu_L =$

$U_\infty l/\nu_L$. For a given geometry, C_{pmin} is a function only of Re in steady flows. In the idealized case of an inviscid, frictionless liquid, Bernoulli's equation applies and C_{pmin} becomes dependent only on the geometry of the flow boundaries and not on any other parameters. For purposes of the present discussion, we shall suppose that for the flow geometry under consideration, the value of C_{pmin} for the single-phase flow is known either from experimental measurement or theoretical calculation.

It is conventional to characterize how close the pressure in the liquid flow is to the vapor pressure (and therefore the potential for cavitation) by means of the cavitation number, k, defined by

$$k = \frac{p_\infty - p_v\left(T_\infty\right)}{\frac{1}{2}\rho_L U_\infty^2} \tag{2.3}$$

where $p_v\left(T_\infty\right)$ is the saturated vapor pressure of the liquid at the reference temperature T_∞. In a particular flow, as k is reduced, cavitation will first be observed to occur at some particular value of k called the incipient cavitation number and denoted by k_i . Further reduction in k below k_i would cause an increase in the number and size of the vapor bubbles.

In the hypothetical case of a liquid that cannot withstand any tension and in which vapor bubbles appear instantaneously when p reaches p_v, the incipient cavitation number would be ascertained from observations or measurements of the single-phase flow, as it would be clear that $k_i = -C_{pmin}$.

Unfortunately, many factors can cause the actual values of k_i to depart radically from $-C_{pmin}$ and much research has been conducted to explore these departures because of the importance of determining k_i accurately. Among the most important factors are:

- The ability of the liquid to sustain a tension so that bubbles do not grow to observable size until the pressure falls a finite amount below the vapor pressure. The magnitude of this tension is a function of the contamination of the liquid and, in particular, the size and properties of the microscopic bubbles (cavitation nuclei) that grow to produce the observable vapor bubbles (see, for example, Billet [6]).

- The fact the cavitation nuclei require a finite residence time in which to grow up to an observable size.

- The fact that measurements or calculations usually yield a minimum coefficient of pressure that is a time-averaged value. On the other hand many of the flows with which one must deal in practice are turbulent and, therefore, nuclei in the middle of turbulent eddies may experience pressures below the vapor pressure even when the mean pressure is greater than the vapor pressure.

The above discussion identifies the parameters that must be controlled or at least measured in systematic experiments on cavitation inception:

- The cavitation number, k.

- The Reynolds number, Re.

- The liquid temperature, T_∞.

- The liquid quality, including the number and nature of the free stream nuclei, the amount of dissolved gas, and the free stream turbulence.
- The quality of the solid bounding surfaces, including the roughness (since this may affect the hydrodynamics) and the porosity or pit population.

Since this is a tall order, and many of the effects such as the interaction of turbulence and cavitation inception have only recently been identified, it is not surprising that the individual effects are not readily isolated from many of the experiments performed in the past. Nevertheless, some discussion of these experiments is important for practical reasons.

2.4.2 Bubble growth

Bubble growth is governed either by the action of surface tension, inertia, viscosity, heat or mass transfer, or by some combination of these effects. Persson [68] investigated the importance of these parameters on the bubble growth. The size of a bubble is controlled by the internal and external forces acting on it. The growing of a bubble is normally caused by a reduction in the liquid pressure. Attending to bubble growth, Holl [5] distinguished between three types:

- Gaseous cavitation: When the pressure surrounding the bubble reaches the saturation pressure, the bubble grows by transport of gas across the interface. This is a relatively slow process unless appreciable convective effects occur.
- Pseudo cavitation: When the bubble grows by change of pressure without change in the mass of the bubble.
- Vaporous cavitation: When the pressure surrounding the bubble reaches the vapor pressure, the bubble grows by the rapid evaporation of liquid across the interface. This is a very rapid process.

The behavior of a single bubble in an infinite domain of liquid, which is at rest and with uniform temperature far from the bubble will be examined first. This spherically symmetric situation provides a simple case that is amenable to analysis and reveals a number of important phenomena.

Consider a spherical bubble of radius, $R(t)$, in an infinite domain of liquid whose temperature and pressure far from the bubble are T_∞ and $p_\infty(t)$ respectively, as shown in figure 2.1. The temperature, T_∞, is assumed to be a simple constant since temperature gradients were eliminated a priori and uniform heating of the liquid due to internal heat sources or radiation will not be considered. On the other hand, the pressure, $p_\infty(t)$, is assumed to be a known input which regulates the growth or collapse of the bubble.

Though compressibility of the liquid can be important in the context of bubble collapse, it will, for the present, be assumed that the liquid density, ρ_L, is a constant. Furthermore, the dynamic viscosity, μ_L, is assumed constant and uniform. It will also be assumed that the contents of the bubble are homogeneous and that the temperature, $T_B(t)$ and pressure, $p_B(t)$, within the bubble are always uniform.

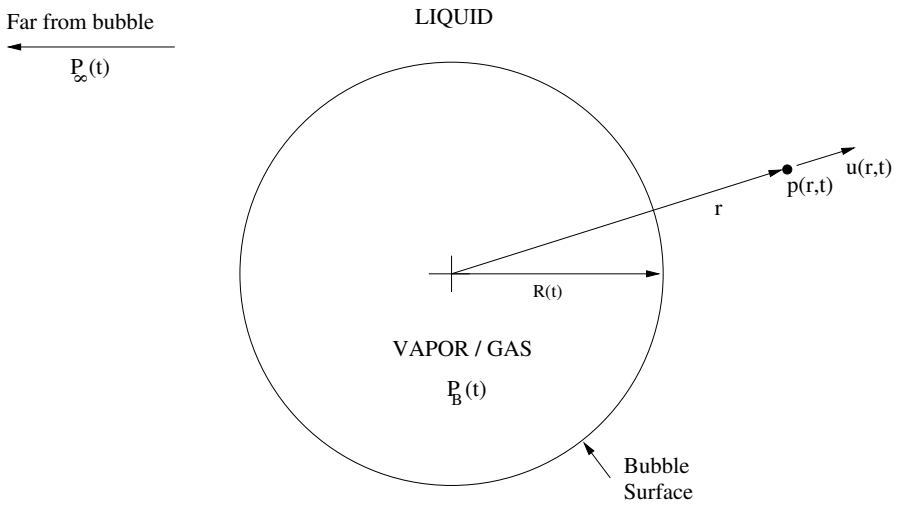

Figure 2.1: Schematic representation of a spherical bubble in an infinite liquid medium.

In this case, and in the absence of mass transport across the boundary (evaporation or condensation), bubble growth is governed by the generalized Rayleigh-Plesset equation for bubble dynamics:

$$\frac{p_B(t) - p_\infty(t)}{\rho_L} = R\frac{\mathrm{d}^2R}{\mathrm{d}t^2} + \frac{3}{2}\left(\frac{\mathrm{d}R}{\mathrm{d}t}\right)^2 + \frac{4\nu_L}{R}\frac{\mathrm{d}R}{\mathrm{d}t} + \frac{2\sigma}{\rho_L R} \tag{2.4}$$

Given $p_\infty(t)$ this represents an equation that can be solved to find $R(t)$ provided $p_B(t)$ is known. In the absence of the surface tension and viscous terms, it was first derived and used by Rayleigh [71] in 1917. Plesset [69] first applied the equation to the problem of traveling cavitation bubbles, in 1948.

2.4.3 Collapse

If the pressure of the liquid surrounding the bubble is increased, the bubble will start to collapse. As it does so, more and more energy is concentrated into progressively less space. This is a very complicated process, and despite the extensive research done, it is not yet completely understood. If collapse is quick enough, very high pressures will be generated which can damage both hydraulic components and the hydraulic fluid.

In 1917, Lord Rayleigh [71] calculated the pressure developed in a liquid during the collapse of a spherical cavity. He assumed that a cavity was instantaneously introduced into a pressurized inviscid and incompressible fluid, and by considering the interchange of potential and kinetic energy, he was able to predict the life history of the cavity. This theory predicted infinite pressures at the point of collapse. Later studies that have included real fluids have predicted high pressures which will radiate shock waves.

Knapp and Hollander [53] used a high speed camera to photograph the collapse of a cavity and measured collapse velocities of 250 m/s. As a result it is clear that large pressures will develop at the instant of the collapse. Indeed, bubble collapse pressures greater than 1 GPa have been reported.

Knapp [51] and Hammitt [37] showed that the Rayleigh model (spherical collapse) is unlikely to occur in practice. A collapsing cavity is unstable and any slight disturbance will cause rapid distortion.

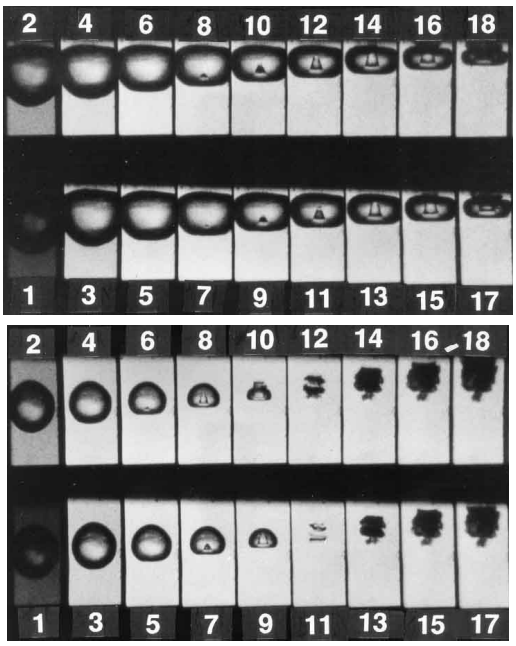

Figure 2.2: Series of photographs showing the development of the micro-jet in a bubble collapsing very close to a solid wall (up) and with a larger separation from the wall (down). The interval between the numbered frames is 2 μs and the frame width is 1.4 mm. From Tomita and Shima [85].

In a subsequent paper Hammitt showed that a cavity moving into a region of higher pressure tends to distort into a toroidal shape, while at the same time ejecting a high velocity micro-jet, at the instant of collapse. This process can be divided into the following stages:

- An initial spherical bubble.
- The bubble collapses asymmetrically with the upper surface of the bubble moving towards the solid surface.
- As collapse continues, the bubble becomes toroidal with the upper fluid penetrating the center of the bubble.
- A micro-jet is formed at the center of the toroid.

Figure 2.2 illustrates these stages in a series of photographs taken by Tomita and Shima [85] in two different cases. It can be seen that when the bubble is not too close to the wall, two toroidal vortex bubbles, instead of one, can be formed.

Although both the liquid micro-jet impact, for non-symmetrical collapse, and shock waves from so-called *rebounding* bubbles appear in the process of bubble collapse, it has been shown (Fujikawa et al. [24] and Kimoto et al. [50]) that only the shock waves cause damage.

Research has also shown that when a bubble collapses near a solid boundary (vane or shroud), the direction of the micro jet will, almost always, be towards that boundary. In other words, the entire energy of collapse is directed at a microscopic area of the impeller's surface and metal erosion occurs.

Furthermore, it has been shown [97] that a cavity cloud has higher collapse pressure or strength than that of a single bubble due to the interactions of the bubbles.

This combination of highly concentrated energy and focused direction makes a collapsing bubble so destructive. Even if the bubbles collapse well above the surface of the impeller and erosion is avoided, the shock waves can still cause severe vibration which can lead to other forms of damage.

The potential intensity of such mechanisms can explain damage for even the hardest and strongest materials as a result of cavitation.

2.5 Effects of cavitation

Although cavitation may be aggravated by poor design, it may occur in even the best designed equipment when the latter is operated under unfavorable conditions. Unfortunately, within the field of applied hydrodynamics, the effects of cavitation are undesirable (with very few exceptions). In the field of hydraulic machinery it has been found that cavitation is susceptible to happen in all types of turbines (from low specific speed Francis to high specific speed Kaplan), in centrifugal and axial flow pumps and in positive displacement pumps. Cavitation may also occur in devices which do not involve the input or output of mechanical energy such as valves or fittings that involve a change in the velocity of the liquid passing through them, as fluid meters, venturi meters, orifices or nozzles.

2.5.1 Material damage

Perhaps the most ubiquitous problem caused by cavitation is the material damage that cavitation bubbles can cause when they collapse in the vicinity of a solid surface. Consequently, this aspect of cavitation has been intensively studied for many years. The problem is complex because it involves the details of a complicated unsteady flow combined with the reaction of the particular material of which the solid surface is made. The pitting caused by the collapse of cavities produces great wear on components and can dramatically shorten a pump's lifetime.

As we have seen in the previous section, cavitation bubble collapse is a violent process that generates highly localized, large amplitude disturbances and shocks in the fluid at the point of collapse. When this collapse occurs close to a solid surface, these intense disturbances generate highly localized and transient surface stresses. Repetition of this loading due a multitude of bubble collapses can cause local surface fatigue failure, and the detachment of pieces of material. This is the generally accepted explanation for cavitation damage. It is consistent with the appearance of cavitation damage in most circumstances. Unlike the erosion due to solid particles in the flow, for which the surface appears to be smoothly worn with scratches due to larger particles, cavitation damage has the crystalline and jagged appearance of fatigue failure. An example of cavitation damage on the compensation plate on an external gear pump is shown in figure 2.3.

After a surface is initially affected by cavitation, it tends to erode at an accelerating pace. The cavitation pits increase the turbulence of the fluid flow and create crevasses that act as nucleation sites for additional cavitation bubbles. The pits also increase the component's surface area and leave behind residual stresses. This makes the surface more prone to stress corrosion (Stachowiak and Batchelor[79]).

Figure 2.3: Cavitation damage on the compensation plate on an external gear pump.

2.5.2 Hydrodynamic effects

The various hydrodynamic effects of cavitation have their source in the interruption of the continuity of the liquid phase as cavities appear. As the cavity volume displaces liquid, the flow pattern is modified and the dynamic interaction between the liquid and its boundaries is altered. Usually the effect of cavitation is to limit or lessen the force that can be applied to the liquid by the surface. The overall resistance to flow and reduced turning effect combine to lower the performance of the equipment involved. Decrease in power output and head are indications of cavitation causing a decrease in guidance and hence effective momentum transfer between liquid and rotor. The decrease in efficiency is a measure of the increased losses. Hydrodynamic effects in positive displacement pumps will be extensively discussed in the following chapters.

2.5.3 Vibration

Cavitation is an inherently unsteady process and may involve large fluctuating forces. The amplitudes of vibration do not usually exceed alert values unless resonance is involved. The spectra produced usually has a very wide frequency range and low amplitude. Cavitation-induced vibration may lead to other forms of pump damage.

2.5.4 Noise

Noise is a consequence of the momentary large pressures that are generated when the contents of the bubble are highly compressed. In consequence, it is mainly caused by the shock-wave mechanism that appears in the bubble collapse process. The crackling noise that accompanies cavitation is one of the most evident characteristics of this phenomenon. The onset of cavitation is often detected first by this noise rather than by visual observation of the bubbles. Moreover, it is often the primary means of detecting cavitation in devices such as pumps and valves. Indeed, several empirical methods have been suggested that estimate the rate of material damage by measuring the noise generated (for example, Lush and Angell [58]). Most of the analytical approaches to cavitation noise build on knowledge of the dynamics of collapse of a single bubble. Fourier analysis of the radiated acoustic pressure due to a single bubble were first visualized by Rayleigh [71] and implemented by Mellen [61] and Fitzpatrick and Strasberg [22].

2.5.5 Sonoluminescence

Sonoluminescence can occur when a sound wave of sufficient intensity induces a gaseous cavity within a liquid to collapse quickly, producing the emission of light. The mechanism of the phenomenon of sonoluminescence remains unsettled. Theories include: hotspot, bremsstrahlung radiation, collision-induced radiation and corona discharges, among others.

2.5.6 Beneficial effects

Despite cavitation is generally an unwanted phenomenon, it can also be employed in our favor in some cases. Some of the main applications of the cavitation effects are:

- Cavitation noise boomer is used as a sound source to study the ocean bottom conditions.
- Cavitation provides a choking phenomenon that can be used as a flow control mechanism (in an orifice or venturi).
- Controlled cavitation can be used to enhance chemical reactions or propagate certain unexpected reactions because free radicals are generated in the process due to disassociation of vapors trapped in the cavitating bubbles. For instance, cavitated corn slurry show higher yields in ethanol production compared to uncavitated corn slurry in dry milling facilities.
- In industry, cavitation is often used to homogenize, or mix and break down, suspended particles in a colloidal liquid compound such as paint mixtures or milk. Many industrial mixing machines are based upon this design principle.
- In industrial cleaning applications, cavitation has sufficient power to overcome the particle-to-substrate adhesion forces, loosening contaminants.
- Cavitating water purification devices have also been designed, in which the extreme conditions of cavitation can break down pollutants and organic molecules.
- Cavitation plays an important role for the destruction of kidney stones in shock wave lithotripsy.
- Nitrogen cavitation is a method used in research to lyse cell membranes while leaving organelles intact.
- Cavitation plays a key role in non-thermal noninvasive fractionation of tissue for treatment of a variety of diseases.

2.5.7 Cavitation in nature

Pistol shrimp, the noisiest animal in the shallow ocean, provokes cavitation to stun their prey with the noise generated. It is also the first known instance of an animal producing light by sonoluminescence effect. It achieves this by quickly snapping a specialized claw (Lohse at al. [57]). It has subsequently been discovered that another group of crustaceans, the mantis shrimp, contains species whose club-like forelimbs can strike so quickly and with such force as to induce sonoluminescent cavitation bubbles upon impact.

Cavitation also occurs in the xylem of vascular plants when the tension of water within the xylem becomes so great that dissolved air within the water expands to fill either the vessel elements or tracheids.

For powerful swimming animals like dolphins and tuna, cavitation may be detrimental, because it limits their maximum swimming speed (Brahic [8]). Even if they have the power to swim faster, dolphins may have to restrict their speed because collapsing cavitation bubbles on their tail are too painful. Cavitation also slows tuna because the cavitation bubbles create an air film around their fins that limits their speed.

Finally, in the last half-decade, coastal erosion in the form of inertial cavitation has been generally accepted (Panizza [67]).

2.6 Cavitation detection methods

2.6.1 Direct Observation

The direct method offers the only possibility for detailed study of the hydrodynamic phenomenon either at inception or for advanced stages of cavity development. Nowadays, the development of high-speed CCD cameras and optical techniques such as Particle Image Velocimetry (PIV), has increased the popularity of these methods. Nevertheless, in many cases (which often include those of hydraulic machinery), the region in which cavitation takes place cannot be visually accessed, therefore indirect detection methods are needed.

2.6.2 Indirect Observation

Indirect methods are based on the measurement of variables affected by cavitation and on the previous understanding of the cavity dynamics and its relation with the measured variables. Some of these methods are:

- Determining the effect of cavitation on the performance of a piece of equipment. This method gives no information about the character of the hydrodynamic phenomenon.
- Measuring the effect on the distribution of pressure over the boundary at which cavitation occurs: It gives information about the location of the cavitating zone and about force and moment transmission between the liquid and the boundaries.
- Analyzing the noise emitted by cavitation. It provides a very sensitive way of detecting amounts of cavitation that may be too small to detect by direct observation.
- Analyzing the structural vibrations caused by cavitation.
- Allowing cavitation to scatter laser-beam light into a photocell. This is a very sensitive way to indicate the presence of extremely small cavities.

2.7 Gas solubility

Air can appear in the fluid in dissolved form, as the fluid absorbs the gas till the saturation state. The volume of gas dissolved in the liquid in the saturation state at a given pressure, p, is given by Henry's Law:

$$V_G = V_L \alpha_V \frac{p}{p_0} \tag{2.5}$$

being V_G the dissolved gas volume, V_L the liquid volume, p_0 the atmospheric pressure, and α_V the Bunsen coefficient, which represents the volume of gas to volume of fluid ratio at atmospheric conditions. This coefficient is very little dependent upon temperature and viscosity.

When a local pressure lower than the one at which the gas dissolving occurred appears, the gas will be coming out of the solution until a new saturation state, corresponding to the new pressure, is reached. As explained in the previous sections, this phenomena is called pseudo-cavitation. Furthermore, at the saturation pressure of the dissolved air, the original microscopic bubbles will begin to grow by diffusion of the air out of solution, resulting in aeration. Therefore, it is very important to know the Bunsen coefficient of the working fluid.

The Bunsen coefficient for the mineral oil used in this work has a value of 0.09, which means a very high solubility of air if compared to water (0.02). When pseudo-cavitation occurs, the air release is much faster than the dissolving speed and, in the case of oils, becomes very intensive at an absolute pressure of 0.6 bar.

The change of size of a bubble due to oil pressure and temperature has been studied by Katakura et al. [45], Cha [14], Mori et al. [63] and Tsai et al. [86]. These studies show that the rates of solution are much more complicated. They depend on several parameters, such as the degree of super or under saturation, agitation, fluid type and fluid properties, for which it is difficult to get quantitative information. Therefore, Henry's Law is valid under laboratory conditions, but in real cases, many factors contribute to modify the predicted volume of dissolved air.

The evolution rate, χ, is defined as the variation of the volume of gas (V_G) with respect to the volume of liquid (V_l) as a function of time:

$$\chi = \frac{\mathrm{d}}{\mathrm{d}t}\left(\frac{V_G}{V_L}\right) \tag{2.6}$$

Schweitzer et al. [76] studied the evolution rate and they concluded that it is proportional to the super-saturation degree (and the solution rate to the under-saturation degree) and represents an exponential function of time.

2.8 The effect of aeration on hydraulic oil

Entrained air in hydraulic circuits is assumed to appear in the form of small bubbles. It can enter the system from the reservoir, where the free surface of oil is agitated, and small pockets of air my be trapped in the fluid and carried into the pump suction line. Another source of air is from fittings, where some air may be allowed to enter into the system. This is common in old systems, in which fittings have become loose due to structural vibration.

There are two main effects of the entrained air affecting cavitation: one important effect is on the physical properties of the fluid, which can change drastically. The other relates to the cavitation inception as bubbles act as nuclei where cavitation can start.

The effective bulk modulus is affected by the bubbles formed by the entrained air in the following way:

$$\frac{1}{B_{eff}} = \frac{1}{B_{oil}} + \frac{\alpha}{B_{air}} \tag{2.7}$$

being B_{eff} the effective bulk modulus, B_{oil} and B_{air} the bulk modulus of oil and air respectively, and α the air volume fraction.

With a typical value of $B_{oil} = 1.6\,10^9$Pa and $B_{air} = 10^5$Pa, it is clear than even very small fractions of air reduce drastically the effective bulk modulus. Equation 2.7 can be rewritten as a function of pressure:

$$B_{eff} = \frac{B_{oil} p^2}{p^2 + B_{oil}\alpha p_0} \tag{2.8}$$

The fluid density is affected in an analogous way:

$$\rho = (1 - \alpha)\,\rho_{oil} + \alpha\rho_{air} \tag{2.9}$$

The effective viscosity of the fluid is also affected by the dissolved air, as shown by the empirical relation (Hayward [32]),

$$\mu_{eff} = \mu\,(1 + 1.5\alpha) \tag{2.10}$$

The viscosity of the oil, μ, is usually supplied by the fluid manufacturers and is generally a function of temperature.

This increase of viscosity may be beneficial as it increases the damping in pressure transients, although the subsequent increase in friction provides more heating, reducing the life of oil.

Nevertheless, our main interest in this entrained volume is that it provides nuclei in which gaseous cavitation can take place. When system pressure drops, vapor escapes to the small air bubbles (Sato and Kakutani [72]). Holl and Treaster [33] suggested that surface, rather than free stream nuclei may be more influential because of the high surface tension of spherical bubbles.

In order to reduce the number of entrained bubbles, a fine gauze may be placed across the reservoir outlet, to trap the bubbled therefore preventing them to be transported into the system. A very large reservoir would also reduce the number of air bubbles, because oil that enters from the return line would have more time when air could rise to the surface before it re-enters the system.

The rate at which air is released from the solution depends on many factors. There is a need for a free surface for the air to escape to. This can appear in the form of the surface in the reservoir (Schweitzer et al. [76]) or the perimeter of an air bubble entrained in the fluid (Wiggert et al. [93]). This second type of surface provide cavitation nuclei, and contribute to greatly reduce the tensile strength of the fluid, as they can grow at pressures far below the tensile strength of the liquid. The temperature of the fluid and its degree of agitation also affect the air release rate.

2.9 Conclusions

In this chapter, the main types of cavitation have been presented and the physical process related to this phenomenon has been described. In order to include cavitation effects in the numerical simulations of external gear pumps that will be presented in later chapters, mathematical models for multiphase flow and cavitation phase transfer mechanisms should be studied. In chapter 4 these models will be presented, and it will be seen that the fact of using hydraulic oil as working fluid requires us to carefully tune the model constants. For this reason, the influence of aeration in hydraulic oil, its high gas solubility compared to that of water, and the implications related to this fact, have also been presented in this chapter.

Chapter 3

Working principles and volumetric efficiency of external gear pumps

3.1 Introduction

Hydraulic pumps are the power-supplying components within hydraulic systems. Their mission is to transform the mechanical energy supplied into hydraulic energy. Most of the pumps used in fluid power systems are of the positive displacement type. A positive displacement pump has an expanding cavity on the suction side and a collapsing cavity on the discharge side. Liquid flows into the pump as the cavity on the suction side expands and the liquid flows out of the discharge as the cavity collapses. Among the positive displacement pumps, fixed displacement gear pumps are often used in circuit applications where customers are sensitive to the initial purchase cost of the system and where the overall operating efficiency does not need to be extremely high. Also, gear pumps can be operated at high speeds and can be used in applications where the operating pressures are low or moderate (below 250 bar). Gear pumps use a very simple mechanism to generate flow, and therefore have a minimum number of parts associated with the design. The simplicity of the gear pump design translates into higher reliability as compared to other positive displacement pumps that use a more complex design.

The fundamental working principle of an external gear pump is the volumetric displacement of a volume. In figure 3.1 a scheme of the working principle of an external gear pump is presented. The increase and reduction of the volume is made by means of two gearwheels that mesh, steeling towards the suction chamber, in the center of the pump. The gear that rotates by means of the power applied externally through the drive shaft is called “driving gear”, while the other one, which is dragged by meshing with the driving gear, is called “driven gear”. The energy transformation process takes place in three phases:

- Suction: In the suction side, a volume opens and is consequently filled by fluid. The filling takes place due to the pressure in the inlet pipe (generally atmospheric pressure, or higher in gravity-filled pumps), which predominates over the vacuum at the opening volume. Gravity-filled pumps present a better behavior against cavitation, as pressures at the suction side are higher.

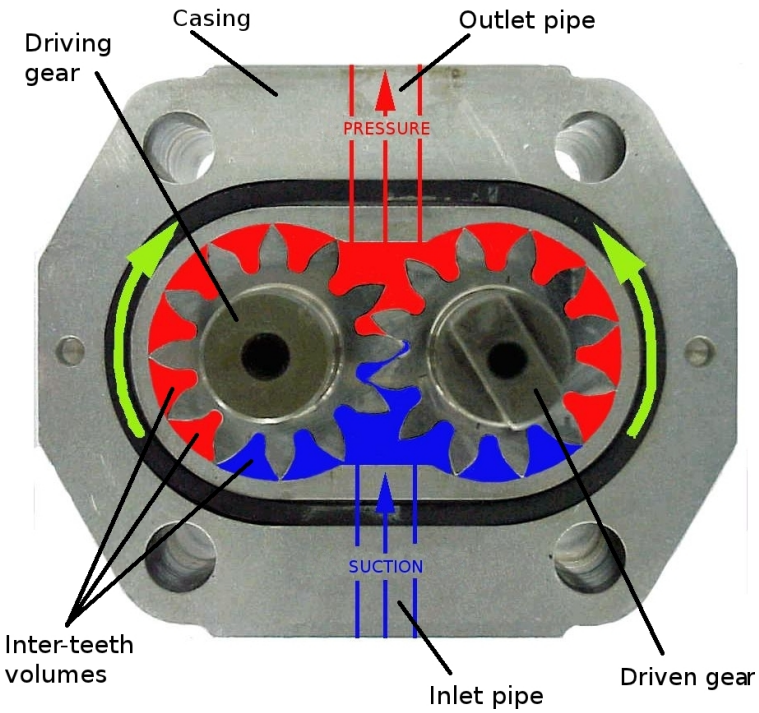

Figure 3.1: Working principle of an external gear pump. Oil is carried from the suction port to the pressure port between the gears and the casing.

- Displacement: The fluid trapped in the inter-teeth volumes is transported between the gears and the casing, to the pressure side.
- Impulsion: At the pressure side, the volume containing the liquid is reduced, impulsing it through the outlet pipe. Nevertheless, the pump is unable to create pressure itself, but only when a hydraulic impedance (valve, cylinder, motor...) is present in the compression circuit.

The teeth profile to be employed is the involute-type one, as it is the most commonly used nowadays, due to its interesting properties. In appendix A a physical description of the main elements and mechanical properties of involute gears is presented.

In this chapter, the main contributions to the understanding and development of external gear pumps will be summarized. The morphology and working principles of hydraulically balanced external gear pumps will be described. The concept of volumetric efficiency will be defined and the main loss mechanisms that contribute to diminish it in hydraulically balanced pumps will be explained. Some mathematical models that have been developed to predict flow and pressure pulsations in external gear pumps will also be mentioned.

For performing the numerical simulations that will be presented in the following chapters, it will be required to make some drastic simplifications regarding the complex flow leakage mechanisms that take place in real pumps. All these assumptions will be carefully analyzed and justified in chapter 4, which refers to the numerical simulations that have been performed. After these simplifications, the simulated pump will be fully two-dimensional, with no axial leakage, unity contact ratio, and constant tooth head clearance. In the last section of this chapter, a simplified model, which will help us to understand the influence of the main geometrical and operational parameters on the volumetric efficiency of this simplified model, will be presented.

3.2 State of the art

In the last decades, a big effort has been made, in the theoretical, numerical and experimental fields, to better understand the performance of external gear pumps. In this section, the main contributions done in the theoretical and experimental fields in relation with our thesis are mentioned. The main contributions in the numerical simulation of external gear pumps will be cited in chapter 4.

Huang et al. [36] derived an exact closed solution for the kinematic flowrate characteristics of external gear pumps, including the effect of the relief grooves. Design and performance of gear pumps with a non-involute tooth profile has been studied by Nagamura et al. [65]. Borghi et al. [7] have developed a mathematical model to predict volumetric efficiency in pumps with hydraulically balanced bearing blocks that takes into account different internal leakage sources as well as compressibility effects, does not account for cavitation. Manring et al. [60] have calculated the theoretical mass flow of external gear pumps with different number of teeth in each gear, not taking into account internal leakages, neither cavitation effects. Myllykylä [64] has developed a semi-empirical method for predicting the real suction capability (defined as the point where cavitation starts) of large external gear pumps. Khalaf [49] studied the performance of external gear pumps under marginal suction condition.

From the point of view of the pressure pulsation, the following works should be mentioned: Freitas [23] has studied the generation and transmission of pressure fluctuations in the pump suction lines. Eaton et al. [18] have developed an analytical model, through an equivalent hydraulic circuit, in order to predict the pressure fluctuations within the trapped volumes between the gears. This model takes into account cavitation through the use of a simple barotropic model (the minimum void pressure is fixed at the appropriate vapor pressure), as well as fluid compressibility. Then, the model is validated against experimental results. Edge and Johnston [19] suggested a method to measure the pressure ripple generated by systems and components and to predict the flow ripple from the pressure ripple.

Among the main World's research centers within the field of external gear pumps, we should mention the ones shown in table 3.1.

3.3 Morphology and working principle of hydraulically balanced external gear pumps

The reference pump to be studied in this thesis is an hydraulically balanced Roquet PLA model. In order to study, in further sections, the factors that influence its volumetric efficiency, the function of each component should be understood. Figure 3.2 shows a transversal cut of the pump along with the name of the main elements. Figure 3.3 shows a picture of the whole pump, and figure 3.4 shows pictures of each of its components.

In this kind of machines, two compensation plates are pressing against the gears, and two bearing bushes are positioned between the compensation plates and the casing. The gears are supported by the sliding bearings. The compensation plates have the function of maintaining reduced leakages through the clearances that exist between the bushes and the gears. This is obtained by feeding

Country	City	Center	University
United Kingdom	Bath	Center for Power Transmission and Motion Control	University of Bath
Finland	Tampere	Department of Intelligent Hydraulics and Automation (IHA)	Tampere University of Technology
Poland	Warsaw	Institute of Machines Design and Operation	Wroclaw University of Technology
Spain	Terrassa	Oil-hydraulic and Pneumatic Systems Laboratory (LABSON)	Polytechnic University of Catalonia
Germany	Aachen	Institute for Fluid Power Drives and Controls	Aachen University
Italy	Torino	Fluid Power Research Laboratory	Politecnico di Torino
	Modena	Fluid Power Research Group	University of Modena and Reggio Emilia
Japan	Yokohama	Fluid Power Research Department of Mechanical Engineering	Faculty of Engineering Kanagawa University
United States	West Lafayette	Maha Fluid Power Research Center	Purdue University

Table 3.1: Excellence research centers in the field of external gear pumps.

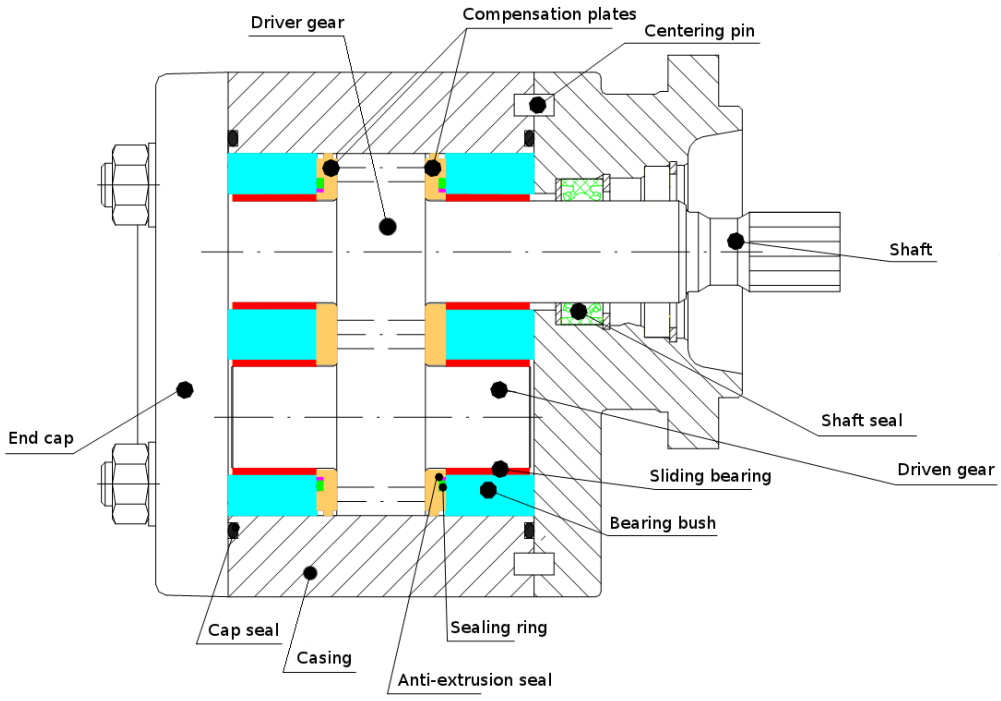

Figure 3.2: Transversal cut of a hydraulically balanced external gear pump.

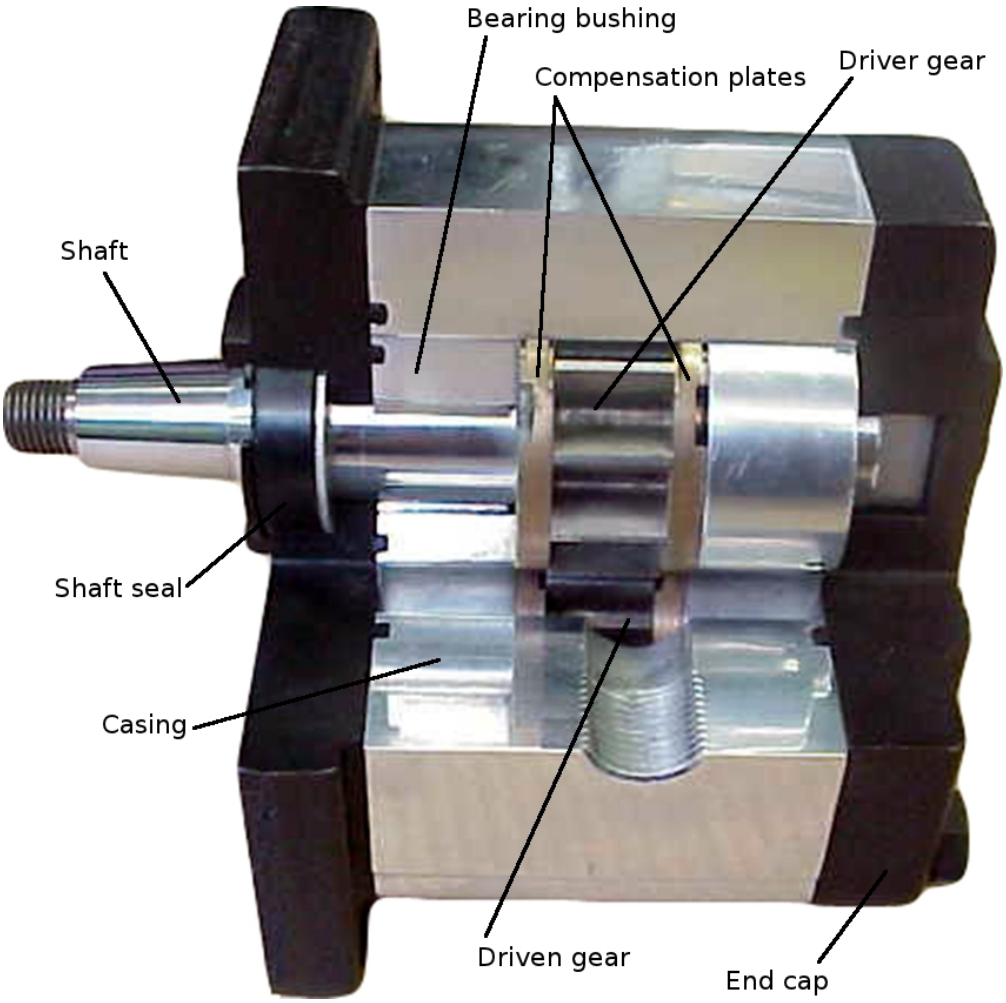

Figure 3.3: Photograph of the pump that will be analyzed in this thesis.

Figure 3.4: Components of the pump that will be analyzed in this thesis.

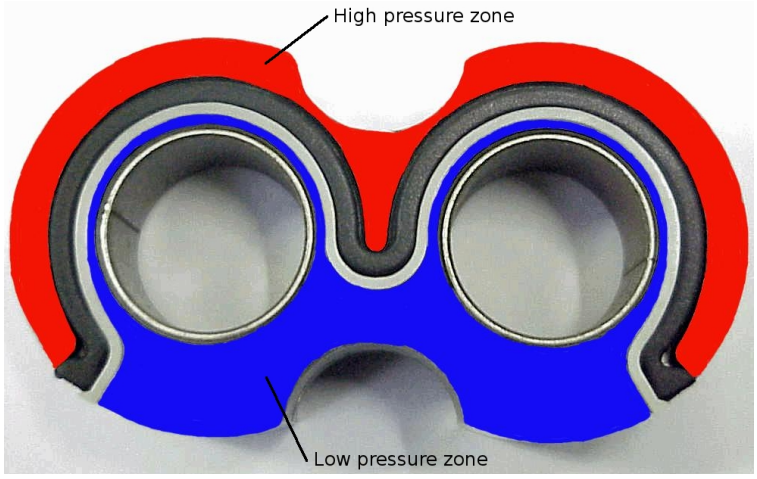

Figure 3.5: Balancing surface of the compensation plate (rear side).

delivery pressure on the rear side of the compensation plates, which acts on a well defined area, delimited by a sealing ring. The combination of this hydrostatic load and of the seal per-load assures low leakage in all the delivery pressure conditions. The internal surface of the compensation plates present circumferential grooves, whose task is to force the involved inter-teeth volumes pressure to be equal to the high pressure value. The high pressure area at the rear side of the compensation plates is marked in red color in figure 3.5. Some models of hydraulically balanced pumps don't use compensation plates, but delivery pressure is directly fed on the rear side of the bearing bushes, which act in a similar way.

3.4 Pump efficiency and suction capability

Due to the intermittent meshing of the gears, the pumping action causes pulsating flow even though the pump is driven at constant speed. The theoretical flow ripple of a gear pump with involute profile depends on the contact ratio, ε, which is defined as the number of angular pitches through which a tooth surface rotates from the beginning to the end of contact. In a simple way, it can be defined as a measure of the average number of teeth in contact during the period in which a tooth comes and goes out of contact with the mating gear. In real pumps this number is higher than unity, which indicates that before a teeth pair separate, the contact between the next pair has started.

The theoretical flow rate of gear pumps with involute profile has been studied, among others, by Molly [62]. In the case of identical gears, the instantaneous flow rate delivered by one tooth pair is:

$$Q_i = b\omega \left[r_a^2 - r^2 - u^2\right] \tag{3.1}$$

being b the depth of the gears, ω their rotational speed, r_a the addendum radius, r the pitch radius, and u the instantaneous length of action (distance from the pitch point to the contact point).

The angular period of the flow pulsation is $T_g = 360/z$ degrees, being z the number of teeth in each gear. For unity contact ratio ($\varepsilon = 1$), no decompression slots are needed, as no liquid gets trapped between two contact points at any instant. In this case, the gearing period takes place as the contact

point covers the line of action between its intersections with the addendum circles of the gears, from $u = -L/2$ to $u = L/2$. In real pumps, where $\varepsilon > 1$, a new contact between teeth appears before the previous pair has separated. This effect causes a new cycle to start earlier than in the case of $\varepsilon = 1$, thus reducing the amplitude of the flow pulsation. Each contact point still covers the same distance, L, of the line of action, but this distance represents an angular sector bigger than a meshing period by a factor of ε. This can be seen in figure 3.6, where the instantaneous flow is plotted against the angular position of the gears. The dashed line corresponds to the instantaneous flow rate with unity contact ratio and the continuous one to the real flow rate. In this figure, the effect of the relief grooves has not been taken into account in the representation of the instantaneous flow.

In the part of the cycle in which both gears make contact in two points, the volume trapped between the gear teeth is gradually varied as the gears rotate. If special design measures are not taken in order to allow drainage from the trapped fluid to the suction side of the pump, then this fluid may only be compressed or flow out through the gaps in the pump, which results in high pressure rise. This high pressure load in the inter-tooth is applied periodically, resulting in high levels of vibration, noise, and occasionally, failure of some of the pump components (e.g. the bearing and the pump body). In order to minimize the pressure rise in the trapped volume, relief grooves are provided in the internal faces of the compensation plates. This consist in slots which allow some oil to pass from the pressure to the suction side, thus decompressing the trapped volume.

The oil volume enclosed between both contact points is connected to the pressure port through the corresponding relief groove during the compression phase (the first half of the cycle, when this volume decreases), and to the suction port through the other relief groove when the volume increases. In an ideally designed pump, the relief grooves cause an instantaneous drop of the flow rate at $u = D - L/2$ being D the distance between both contact points. This effect is shown in figure 3.7.

Nevertheless, special designs of the relief grooves in combination with a control of the backlash between gears, can reduce the amplitude and period of the flow pulsation. Two different types of relief grooves are shown in figure 3.8 and the instantaneous flow rate for each of them is plotted. It can be seen that if no backlash between gears is achieved, and a special groove geometry is designed, the flow pulsation amplitude can be greatly reduced and the period halved.

After integrating the instantaneous flow rate, the volumetric capacity of the pump (the volume of fluid that the pump can impel for a full rotation of the gears), C_v, is obtained as

$$C_v = 2\pi b \left(r_a^2 - r^2 - \frac{r_b^2 \pi^2}{3z^2} \right) \tag{3.2}$$

being r_b the radius of the base circle.

In a gearing cycle, the pump impels two times (one for each gear) the volume of fluid trapped between two teeth and the casing (the inter-teeth volume, V_{it}). Furthermore, during the gearing cycle, the contact point follows the gearing line from the suction side to the pressure side, and at the end of the cycle it jumps back to the pressure side to start a new cycle. In this instant, the volume of oil located between both the initial and the final contact point positions (the squeeze volume, V_{sq}) which belonged to the pressure side, becomes part of the suction side, becoming an assumed

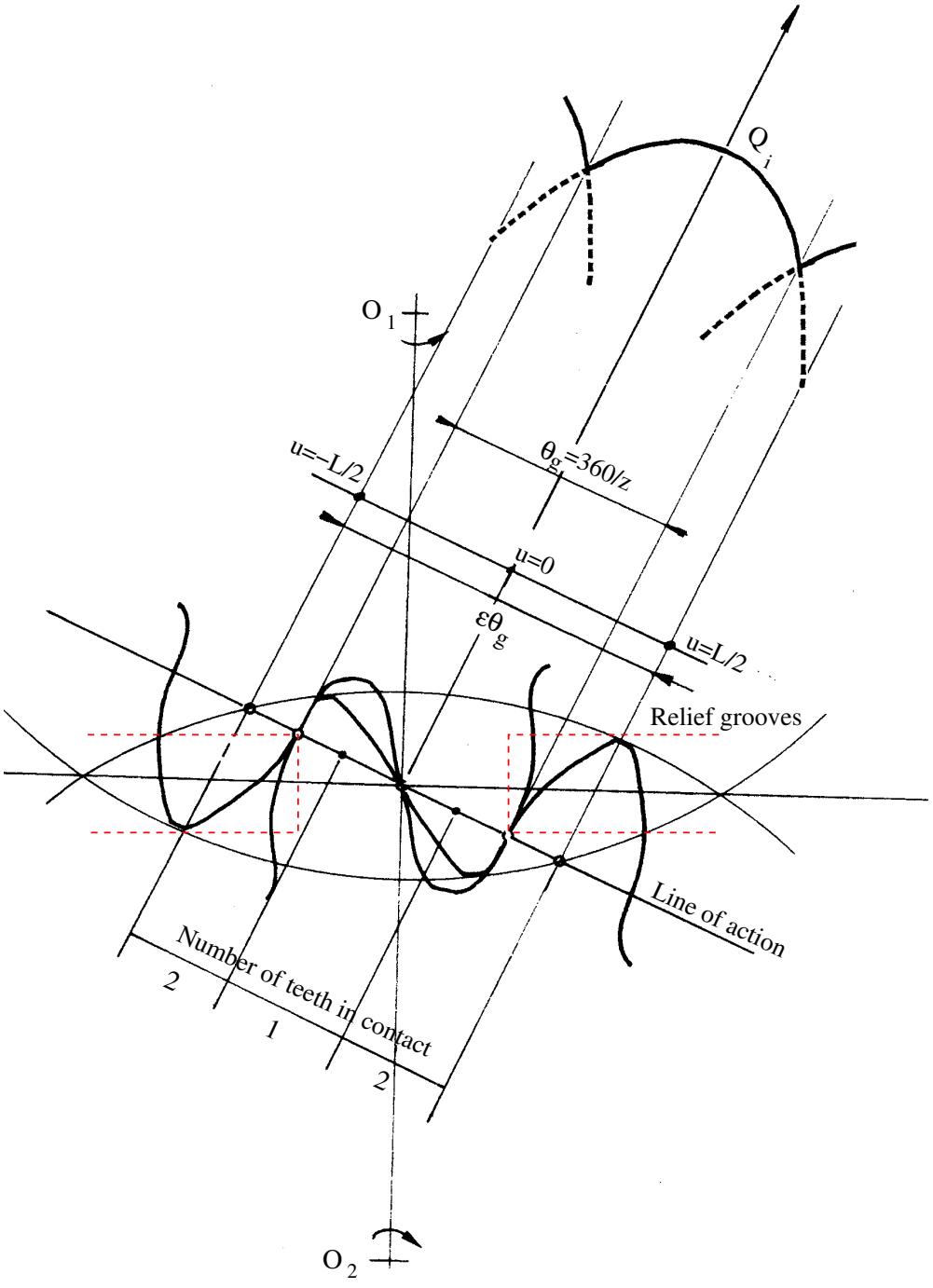

Figure 3.6: Scheme showing the gear contact region and the flow rate in a case where contact ratio is greater than unity.

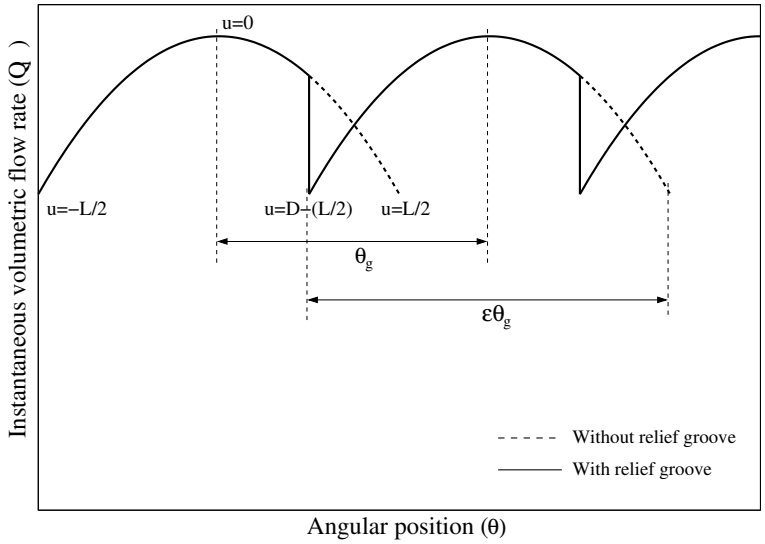

Figure 3.7: Instantaneous flow rate of an external gear pump with and without relief grooves.

back-flow. Both the inter-teeth and the squeeze volumes are shown in figure 3.9. Therefore, the volumetric capacity of the pump, given in equation 3.2, can also be written as:

$$C_v = 2zV_{it} - zV_{sq} \tag{3.3}$$

The theoretical mean flow rate of a pump, Q_{th}, results:

$$Q_{th} = \frac{C_v \omega}{2\pi} = \omega b \left(r_a^2 - r^2 - \frac{r_b^2 \pi^2}{3z^2} \right) \tag{3.4}$$

The flow rate irregularity index is defined as the amplitude of the flow rate pulsation divided by the mean flow rate. Ivantysyn et al. [39] derived and expression in order to express it as a function of the number of teeth and the pressure angle, Ψ, which is defined in appendix A:

$$\delta = \frac{Q_{th\,max} - Q_{th\,min}}{Q_{th}} = \frac{\pi^2 \cos^2 \Psi}{4\left(z + 1 - \frac{\pi^2}{12}\cos^2 \Psi\right)} \tag{3.5}$$

For the case where both gears are not identical, similar expressions have been deduced by Manring et al. [60]. In this analysis, an ideal pump has been considered by assuming:

- The fluid is incompressible.
- Fluid leakage is neglected.
- The pump parts are rigid and inflexible.
- No cavitation/aeration exists.

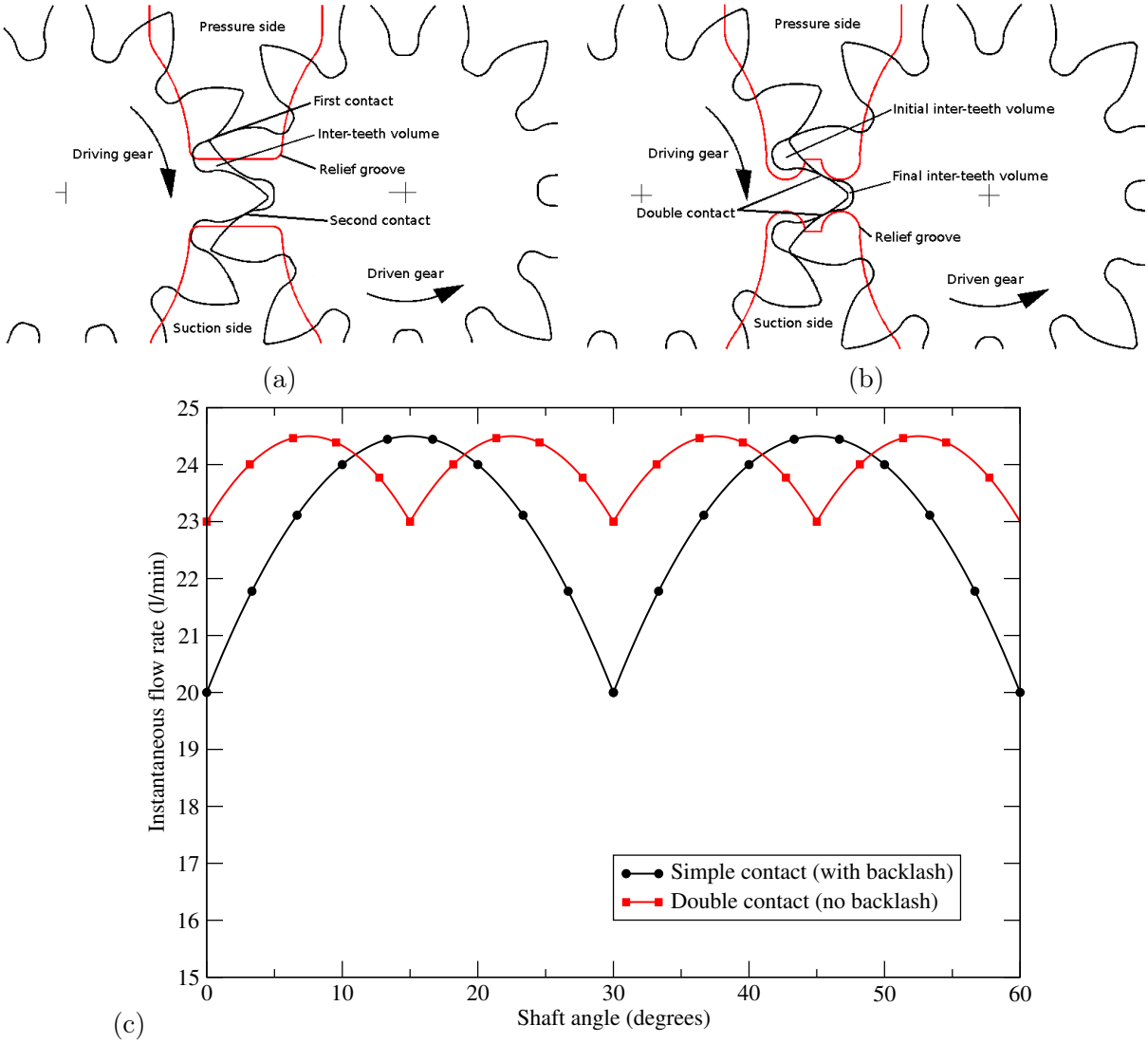

Figure 3.8: (a) Standard relief groove with backlash between gears. (b) Optimized design of the relief grooves with no backlash between gears. (c) Instantaneous flow rate of a Roquet pump using each of the designs.

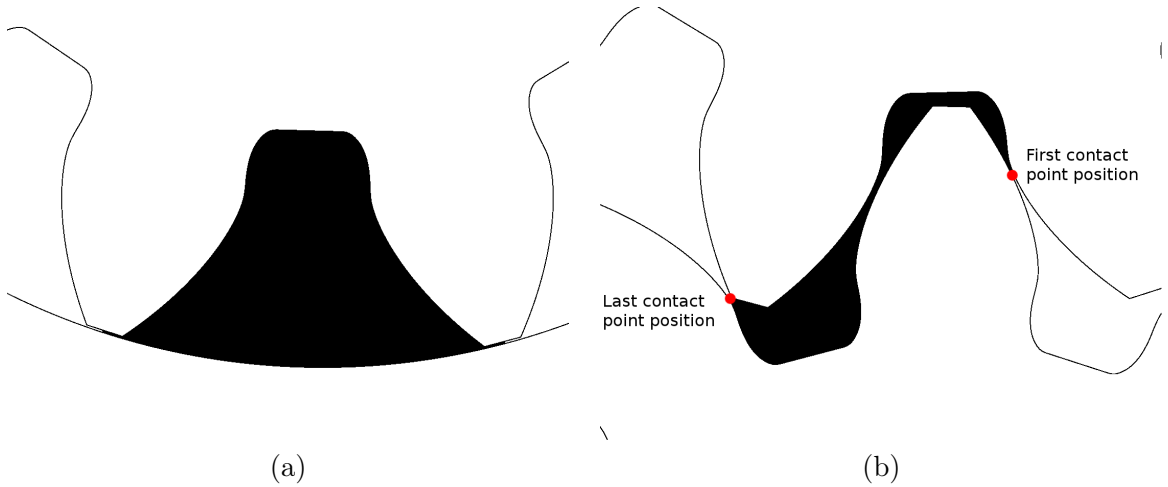

Figure 3.9: (a) Inter-teeth volume, V_{it}, and (b) squeeze volume, V_{sq}.

All these effects contribute to diminish the real volumetric capacity of the pump. The volumetric efficiency of a pump is defined as the relation between the real and the theoretical mean flow rates.

$$\eta_v = \frac{\langle Q_i \rangle}{Q_{th}} \tag{3.6}$$

For a real pump, the flow rate $\langle Q_i \rangle$ has to be referred to the delivery pressure, in order to take into account fluid compressibility. The volumetric efficiency is a function of the pump characteristics, but also of the working conditions (rotation speed and pressure jump), the working fluid (viscosity, density and bulk modulus) and of the fluid temperature (as it affects viscosity).

The total efficiency is defined as the hydraulic energy obtained from the pump divided by the mechanical energy given, and can be expressed as the product of the mechanical and the volumetric efficiencies, being the mechanical efficiency:

$$\eta_m = \frac{\left(\frac{V_m \Delta p}{2\pi}\right)}{T_m} \tag{3.7}$$

where V_m is the volume displacement in one revolution, Δp the pressure jump, and T_m the torque applied to the shaft. Combining equations 3.4, 3.6 and 3.7, the pump efficiency can be written as:

$$\eta = \eta_m \eta_v = \frac{\langle Q_i \rangle \Delta p}{\omega T_m} \tag{3.8}$$

3.5 Real suction capability

A number of causes contribute to reduce the suction capability of gear pumps. These causes will be divided in three types: leakages (i.e. fluid that escapes from the pressure to the suction side), compressibility of the fluid, and cavitation. Therefore, the volumetric efficiency can be written in terms of the volumes of fluid displaced for a complete shaft revolution:

$$\eta_v = \frac{C_v - V_{leak} - V_{comp} - V_{cav}}{C_v} \tag{3.9}$$

- Leakage (V_{leak}): there are three leakage sources, which are shown in figure 3.10 and will be analyzed in subsections 3.5.1, 3.5.2 and 3.5.3:
  - Relief groove leakage: fluid from the meshing inter-teeth volume of the pressure side leaks to the suction side through the volume trapped between contact points, due to the effect of the relief grooves.
  - Side plate or axial leakage: fluid leaks through internal passages between the gears and the side plates, towards the drain, the adjacent inter-teeth volumes, and the suction.
  - Tooth tip or radial leakage: fluid moves through the teeth and the casing towards the adjacent inter-teeth volumes.
- Compressibility (V_{comp}): Loss of volumetric efficiency due to the compressibility of the fluid will be examined in subsection 3.5.4.

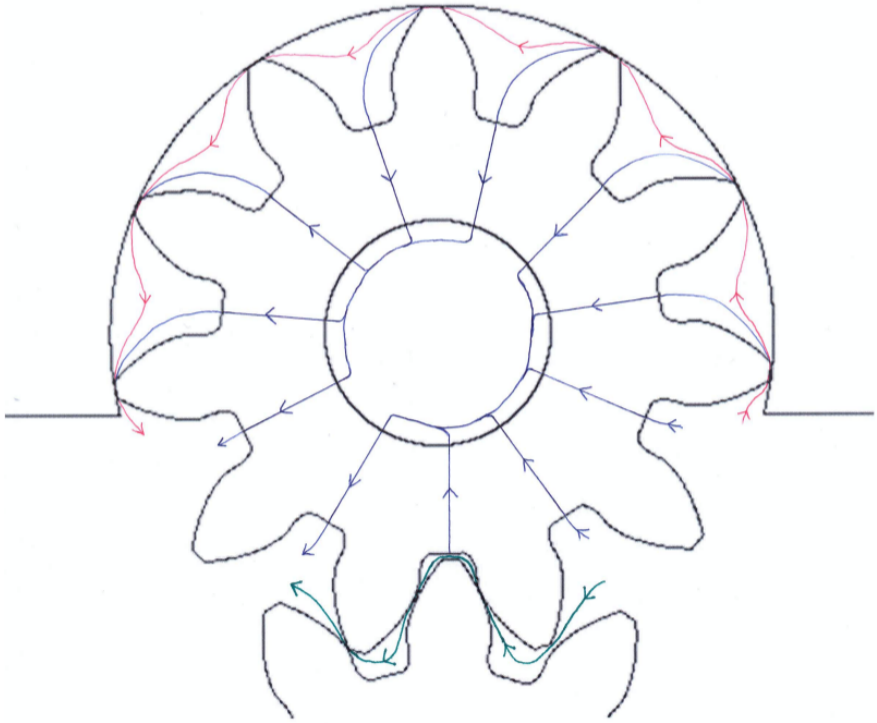

Figure 3.10: Leakage paths in a gear pump. Green line represents the leakage through the relief grooves. Red lines represent radial leakage. Blue lines represent axial leakage.

- Cavitation: Losses due to cavitation will be analyzed along this thesis.

3.5.1 Relief groove leakage

Gear pumps, which are generally used as a power source in hydraulic systems, have a contact ratio greater than one. This ensures a positive drive between meshing gears, but leads to trapping in the space enclosed by the contacting teeth surfaces of the driving and driven gears.

The design and position of the relief grooves has a great influence on the performance of the gear pump. The oil leakage that passes from the pressure to the suction side through it decreases the volumetric efficiency of the gear pump. The flow passing through the high pressure recess can be estimated, according to Borghi et al. [7] by means of the following equation:

$$Q_{rec} = C_d A_r \sqrt{\frac{2\,|\Delta p_{rec}|}{\rho}} \tag{3.10}$$

being C_d the discharge coefficient, A_r the flow area across the recess, Δp_{rec} the pressure drop across the recess, and ρ the fluid density.

3.5.2 Side plate leakage

The leakage through the lateral clearances between the gears and the compensation plates (towards the drain, the adjacent inter-teeth volumes and the suction) are schematized with blue lines in figure 3.10. These leakages are generally considered to form the largest portion of the total internal leakage

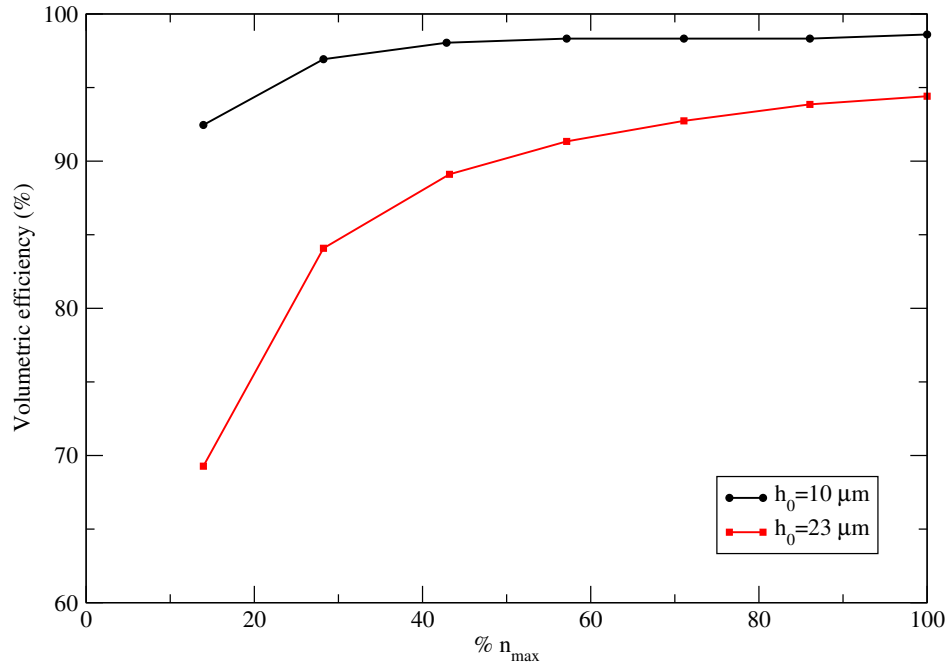

Figure 3.11: Predicted volumetric efficiency against rotational speed at maximum working pressure for 10 μm and 23 μm lateral clearances. From Borghi et al. [7].

in high pressure gear pumps. A pump with fixed side plates, in which the clearance between the side plate and the gears face is constant (around 0.03 to 0.04 mm) usually have a volumetric efficiency as low as 75-80%, and can only operate up to 50-100 bar pressure jump. Therefore hydraulically balanced pumps are in most cases employed. As explained in section 3.3, compensation plates press against the gears as they are fed with working pressure at a certain area (shown in red in figure 3.5) at the rear side. The pressurized area and the seal per-load should be adjusted to obtain the desired axial force, which should be such that the lines of action of the forces acting at both sides are coincident, in order to avoid tilting of the compensation plates.

The lateral clearance height can be determined by imposing the equilibrium of the compensation plates, which are subjected to the the pressure distribution inside the lubricating gaps themselves and to the high pressure exerted on the rear surface. This clearance, which is a function of working pressure and rotational speed, as well as of the tilt angle of the compensation plate, has been studied by Borghi et al. [7]. Figure 3.11 shows how the height of the lateral clearances can greatly affect the volumetric efficiency.

Figure 3.12 has been taken from the catalog of Roquet PLA-family gear pumps (with geometry similar to that of the pump analyzed in this thesis), and shows the measured volumetric efficiency for two different pumps. It can be seen that, up to 175 bar, volumetric efficiency decreases when increasing the working pressure. As a prevailing laminar flow can be assumed in these gaps, the leakage flow through the axial gaps is mainly a Poiseuille-type one. When the delivery pressure increases, the volumes of fluid lost through the lateral clearances also increase, as the clamping force exerted by the compensating plates is unable to reduce the axial gap sufficiently to compensate the effect of pressure (although it damps it, as otherwise the efficiency drop would be approximately linear). At higher delivery pressures, volumetric efficiency is kept constant in the smaller pump and increases in the bigger one, as the hydrostatic force exerted on the compensation plates becomes

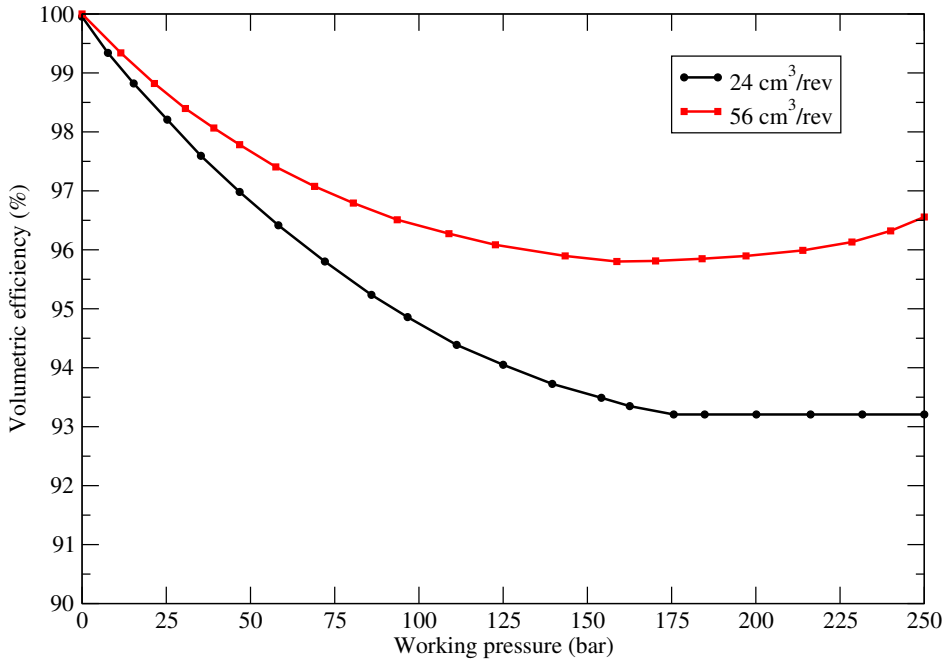

Figure 3.12: Measured volumetric efficiency against working pressure at 1500 rpm of two Roquet gear pumps. Taken from the manufacturer's catalog.

big enough to reduce the gap sufficiently to reduce the axial leakage. This figure also shows that volumetric efficiency is higher in bigger pumps (the ones with higher volumetric capacity), as losses become relatively smaller in them.

3.5.3 Gear tip leakage

There are two different contributions to the leakage across the clearance between the tip of a tooth and the casing. One is produced by the pressure drop across the tip, Q_{pd}, which produces a reverse flux, towards the suction side, and the other is produced by the viscous drag of the tooth, towards the pressure side, Q_{vd}. Therefore, the gear tip leakage flow is $Q_{tip} = Q_{pd} - Q_{vd}$, being the first effect dominant.

In an ideal pump, the pressure around the casing is generally assumed to rise lineally across each tooth tip. For a gear with a number of teeth n_t adjacent to the casing, the pressure drop across the tip of each of these teeth would be,

$$\Delta p_{tooth} = \Delta p / n_t \tag{3.11}$$

In real pumps the pressure jump is concentrated almost on one tooth in each gear due mainly to the eccentric positions of the gears during meshing. The force exerted by the pressurized fluid pushes the gears towards the casing in the pressure region, drastically reducing the tooth tips height. Moreover, in compensated pumps, the circumferential groove on the balancing plate forces delivery pressure on the inter-teeth volumes affected by the groove, as shown in figure 3.5.

The leakage due to this pressure difference corresponds to the Poiseuille flow between two parallel plates:

$$Q_{pd} = \frac{\Delta p_{tooth} h_t^3 b}{12\mu} \tag{3.12}$$

being h_t the tip clearance height.

The forward flow due to the dragging of the gear corresponds to a Couette flow:

$$Q_{vd} = \frac{bh_t V_{tip}}{2} \tag{3.13}$$

being V_{tip} the teeth tip velocity.

In practice, the prediction of this flow is not as simple, as the eccentricity of the axes makes the tip clearance height a function of the tip angular position. The radial displacement of the gear's axes and the orbits that they describe in a gearing cycle has been studied by Gutés [29].

The volumes of fluid lost through the tooth head are higher for lower delivery pressure values because the load due to the inter teeth volume pressure distribution, which pushes the gears towards the suction, is lower in this case, and therefore the height of the clearance located nearby the suction port (where the pressure jump between inter-teeth volumes is found), is higher.

In order to minimize the clearance, pumps are generally designed so that gears scratch the inner surface of the casing, so the radial clearance is only caused by the wear of the casing. Axial and radial leakages are the main causes that contribute to diminish the volumetric efficiency of gear pumps.

3.5.4 Compressibility of the fluid

The term V_{comp} of equation can be estimated as

$$V_{comp} = \frac{2zV_{sq}\Delta p}{B} \tag{3.14}$$

Equation 3.14 considers that the relief grooves are long enough to avoid the squeeze volume pressurization before the communication between the squeeze volume and the groove starts. The pressure transition in the inter-teeth volume occurs as soon as the volume passes over the groove.

3.6 Flow ripple modeling

Hydraulic pumps create a flow ripple due to its meshing mechanism. When inter-teeth volume increases in the suction side, a depression in the suction cavity appears in order to fill it with oil. The suction capability, or capacity to fill in the cavities in between gear teeth, has a great influence in pump efficiency. In the literature we can find several different mathematical models to predict it.

Gutbrod [27, 28] has studied the suction capability of external gear pumps. He derived equations for calculating the geometric displacement and the flow ripple of a gear pump from the geometric dimensions of the gear and the involute shape of the teeth. The model derived by Wilson [95] and extended by Schlösser [74] and Thoma [84] is based on leakage and friction coefficients. Zarotti and Nervegna [99] studied the leak and torque losses. They developed an expression with nine coefficients to describe the torque loss. Their model takes into account non-linear effects in pressure, speed and displacement. Dorey [17] suggested a more flexible model, suitable for widely varying performance conditions, by the use of non-linear coefficients that should be adjusted for each specific design.

Svedberg [82] and Wiklund [94] derived the following theoretical equation from the Navier Stokes equations:

$$p_{in} - p_v + \frac{\rho v_{in}^2}{2} = k_2 \theta^{2/3} \rho \omega^2 + k_1 \tag{3.15}$$

being θ the angular displacement of the gears and k_1 and k_2 experimental coefficients.

Inlet velocity has to be measured at least twice at different inlet pressures in order to calculate the experimental coefficients k_1 and k_2. Then the expression can be used and it will give us the connection between speed and inlet pressure. Coefficients k_1 and k_2 are unique for each pump.

Myllykylä [64] has studied the suction capability of large external gear pumps (with flows from 200 l/min up to 4000 l/min). His aim was to formulate design and calculation rules for lubricating pumps to simulate normal industrial usage. He defined the suction capability as the point where cavitation starts. He defined this point as the one in which the flow decreases by 2% from the value it has when suction pressure is atmospheric. From his experiments, he stated that noise begins to rise as cavitation starts, and amplifies as the number and size of bubbles increases. According to his measurements, the main phenomena that affects suction capability are the tip speed of the inlet chamber and the fluid properties (such as viscosity). Myllykylä also made a simplified mathematical model, from where he obtained the following theoretical formula:

$$p_{in} - p_v = \frac{2\rho m}{\theta_{op} r_a} v_{tip}^2 + \frac{z \rho m^2}{r_a^2} v_{tip}^2 - k_3 \mu v_{tip} \tag{3.16}$$

being m the modulus of the gear, v_{tip} the speed of the gear tips, k_3 an experimental coefficient that depends on the shape of the casing, and θ_{op} the angular displacement of the gear from the instant when the inter-teeth volume opens to the suction side of the pump to the instant when it gets completely covered by the gear casing. This coefficient describes the area which allows oil to flow into the tooth space.

In equation 3.16 we see that both the acceleration of the oil and the centrifugal force form the term that is proportional to the square of the tip speed. The shearing stress forms the term proportional to the tip speed and the constant term is the vapor pressure of the oil. Myllykylä [64] proposed to use experimental correction coefficients in order to obtain a bigger value for the acceleration of the oil:

$$p_{in} - p_v = k_6 \frac{2\rho m}{\theta_{op} r_a} v_{tip}^2 + k_5 \frac{2\rho}{0.5z + 1} v_{tip}^2 + (k_4 - k_3 \mu)\, v_{tip} + p_s \tag{3.17}$$

where the new experimental coefficients k_4 and k_5 depend on the shape of the pump casing and on the shape of teeth respectively, k_6 is a correction coefficient related to the acceleration of the oil, and p_s is an experimental constant pressure that depends on the shape of the casing.

From his study, he founded out that the tip speed of the gear and the shape of the pump casing have a strong effect on suction capability. When the flow path is wide and straight, the pump has a good suction capability, while, if the flow has to make sharp changes in its direction, cavitation starts at a higher inlet pressure.

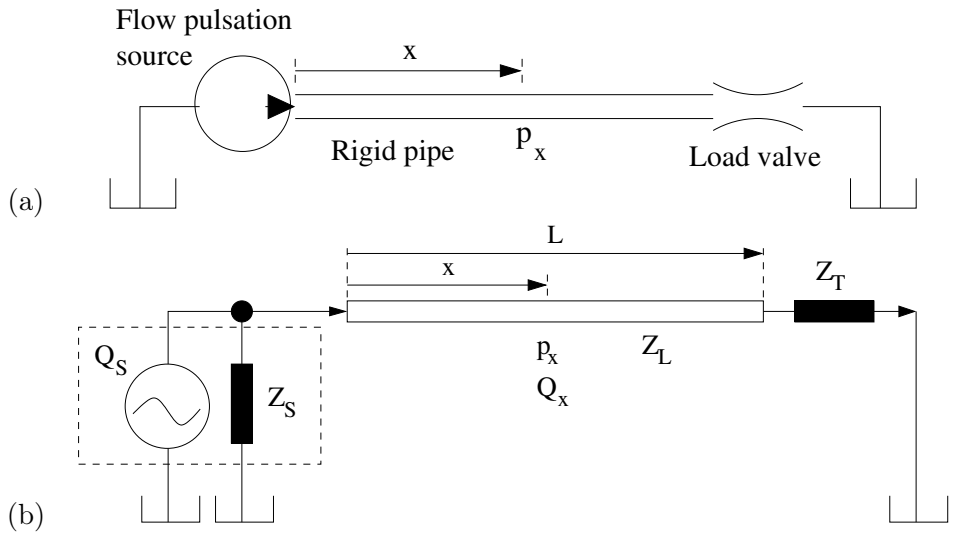

Figure 3.13: Idealized hydraulic circuits. (a) Simple circuit scheme. (b) Scheme using the impedance notation.

3.7 Pressure ripple modeling

The flow ripple, which is inherent to all positive displacement pumps, interacts with the circuit to create a pressure ripple. This pressure ripple has partial reflections when it arrives to the end of the line. The final result of the multiple reflections gives a complex stationary wave. In recent years there has been an increase in the research related to pressure ripple behavior, as well as the interaction of the different components of hydraulic systems. The main efforts have been focused on the pump's impulsion line, where the values of pressure ripple are important.

The mathematical model used to describe the relationship between pressure and flow is based on a solution of the wave equations for one-dimensional flow. These equations are:

$$c^2 \frac{\partial^2 p\,(x,t)}{\partial x^2} = \frac{\partial^2 p\,(x,t)}{\partial t^2} \tag{3.18}$$

$$c^2 \frac{\partial^2 Q\,(x,t)}{\partial x^2} = \frac{\partial^2 Q\,(x,t)}{\partial t^2} \tag{3.19}$$

being c the wave propagation velocity, $p\,(x,t)$ and $Q\,(x,t)$ the pressure and flow in the system as a function of position and time.

A solution in the form of a converging series can be adopted. In an idealized circuit, as the one shown in figure 3.13, Viersma [89] derived from this model an equation which calculates the pressure, p_x, at any point x along a pipeline connected to a positive displacement pump as:

$$p_x = \frac{Q_S Z_S Z_L}{Z_S + Z_L} \frac{e^{-j\beta x} + R_T e^{-j\beta(2L-x)}}{1 - R_S R_T e^{-j2\beta L}} \tag{3.20}$$

being Q_S the flow pulsation at $x = 0$, Z_S the source impedance, Z_L the impedance of the rigid pipe of length L, R_S the source reflection coefficient, and R_T the termination reflection coefficient. The

wave propagation coefficient, β, is defined as

$$\beta = \frac{\omega}{c}\xi(\omega) \tag{3.21}$$

being ω the angular frequency of the wave, and $\xi(\omega)$ the attenuation coefficient.

The coefficients R_S and R_T can be derived from the impedances by making use of the following expressions,

$$R_S = \frac{Z_S - Z_L}{Z_S + Z_L} \qquad R_T = \frac{Z_T - Z_L}{Z_T + Z_L} \tag{3.22}$$

where Z_T is the impedance of the system's load valve.

From the work developed at the University of Bath, the International Standard ISO10767 was published. It suggests an experimental method to evaluate the flow pulsations, Q_S, and the internal impedance, Z_S, of a pump. This method, called the "secondary source" method (Edge and Johnston [19]), needs the presence of a secondary source in the suction line which has to generate pressure ripple in order to be able to calculate the one created by the pump.

As we have said, most of the work has been focused on impulsion lines, where the main pressure is high and the pressure peaks are considerable (pressure fluctuations of 5 bar peak to peak are usual). In the suction lines, with the main pressure is close to atmospheric, the pressure ripple is of less amplitude but it can diminish the pressure to sub-atmospheric conditions and lead to aeration, with the dissolved air coming out of solution.

Some attempts have been done to implement the secondary source method to suction lines. Freitas [23] and Jones [42] studied the suction characteristics of positive displacement pumps. In the implementation of the secondary source method there are some difficult points. In the suction line, being the mean pressure near to atmospheric, the ripple created by the secondary source can lead to undesirable effects such as aeration or even cavitation. Moreover, depending on the secondary source we use, it may provoke the entrance of air into the suction line. Jones [42], in order to avoid the entrance of air, used a flexible hose attached to an electromagnetic vibrator as a secondary source, which gives a ripple without running the risk of provoking the entrance of air in the suction line. The results he obtained show a good agreement with those obtained using a rotary valve as a secondary source.

3.8 Performance of non-balanced gear pumps

In previous sections the volumetric efficiency of hydraulically balanced external gear pumps with contact ratio higher than unity and pressure relief grooves has been analyzed. Nowadays, almost all the pumps that can be found in practical applications fall into this category, as non-balanced gear pumps provide lower efficiencies, higher noise and vibration levels, and its use is limited to relatively low working pressures. The reference pump to be studied, both numerically and experimentally, in this thesis, also falls into this category. Nevertheless, the numerical modeling of all the internal leakages is too complicated, so some simplifications should be made. In chapter 4 all these simplifications will be explained in detail, and it will be justified how, despite how drastic they may seem, they are useful from the point of view of the scope of our work: the study of the influence of cavitation in volumetric efficiency.

In the simplified model that will be used for the numerical simulations, the position of the gear's shafts will be fixed, which implies that the radial clearances will remain constant and equal for every teeth. The radial clearance height of the simulated pump will be considerably bigger ($77\,\mu$m) than the values typically found of real pumps. Furthermore, the fact of employing a fully two-dimensional model has several implications regarding volumetric efficiency:

- The absence of axial gaps, therefore no axial leakage will be considered.
- The absence of pressure relief grooves, therefore, in order to avoid the excessive pressurization of the squeeze oil, the pump will be simulated with unity contact ratio.
- The absence of the circumferential grooves that communicate the inter-teeth volumes, therefore these volumes will communicate just through the radial clearances, and the pressure distribution along them will be linear, following equation 3.11.

Therefore, in our simulations of a non balanced gear pump, the only leakage source will be given by the radial clearances. As it was shown in subsection 3.5.3 the flow through them is given by $Q_{tip} = Q_{pd} - Q_{vd}$ where Q_{pd} represent the Poiseuille-type flow given by equation 3.12 due to the pressure drop, and Q_{vd} the Couette-type flow given by equation 3.13 due to the gear tip's viscous drag effect. In a first approximation, the term Q_{vd} can be neglected with respect to Q_{pd}. If we neglect the contribution of fluid compressibility and cavitation, which are much smaller than that of the gear tip leakage, and take into account equations 3.12 and 3.4, the volumetric efficiency can be approximated by:

$$\eta_v = \frac{\langle Q_i \rangle}{Q_{th}} = 1 - \frac{Q_{pd}}{Q_{th}} = 1 - K_e \frac{\Delta p}{\mu\omega} \tag{3.23}$$

The coefficient K_e is a function of the pump geometry, its clearances, and its size or capacity. Despite the strong limitations of this model, it gives a qualitative idea of the volumetric efficiency dependencies. It can be seen in equation 3.12 that K_e increases with the third power of the clearances height, therefore the importance of keeping them as low as possible through compensation mechanisms. From equation 3.23 we can conclude the following:

- The higher the pressure differential across the pump, the lower the volumetric efficiency.
- At higher speed of operation, the pump is more efficient.
- Pumps operate at higher efficiency with more viscous fluids. Therefore high temperatures reduce volumetric efficiency.
- Pumps with a small value of K_e, which can be achieved by reducing leakage clearances, are more efficient.
- The flow rate of a pump running at small values of $\Delta P/(\mu\omega)$ is less sensitive to changes in the systems.

Chapter 4

Numerical modeling of external gear pumps including cavitation effects

4.1 Introduction

In the previous chapter, the morphology and working principles of external gear pumps have been explained, with special attention to the causes that contribute to reduce the volumetric efficiency. The scope of this thesis is to analyze how cavitation affects to the volumetric efficiency, and to understand the role played the shape of the inlet chamber in this reduction. This will be done by means of Computational Fluid Dynamics (CFD) simulations of the reference pump and of four alternative pumps in which the geometry of the inlet chamber is modified.

The problem to be solved is inherently three-dimensional, due to the axial clearances, the relief and circumferential grooves, and to the circular pipes through which the fluid enters and exits the pump. Moreover, the exact movement of the gears is not known a priori as they are subjected to axial forces that determine the axial clearance height and the tilt angle, and to radial forces that make the axis describe a certain orbit within the horizontal plane. This makes the simulation of the leakage flow through the axial and radial clearances especially difficult. Moreover, the grid employed for the numerical simulation is subjected to very complex deformations along a gearing cycle, especially in the zone around the contact between gears. Depending on the angular position of the gears, two or one contact points appear between them. The numerical simulation of these contacts and the deformation of the volume trapped between them constitute a complex problem.

For these reasons, some assumptions will be made, which will simplify considerably the simulations, but will also prevent us from predicting realistic values of the volumetric efficiency, as some major contributions will not be taken into account (like axial leakage) or will not be simulated realistically (like tip clearance leakage). Nevertheless the simulations will not be aimed to predict realistic values of the volumetric efficiency, but to investigate the effect of cavitation on it.

In this chapter, the algorithms involved in the numerical simulations (like numerical discretization schemes, turbulence modeling, multiphase and cavitation modeling, or mesh deformation algorithms) will be presented and its use will be justified. Boundary conditions and convergence criteria will also be presented. Finally, all the assumptions will be explained and justified from the point of view of the scope of this thesis.

4.2 State of the art

In this section the main advances in the field of numerical simulation of external gear pumps are mentioned. Also, the main contributions in the field of numerical modeling of cavitating flows are cited.

Vande Voorde et al. [90] use a structured mesh in each time step for the simulation of a compressor of two external gears, solving Laplace equation for a certain potential function in each time step, with appropriate boundary conditions. Another technique commonly employed is superposition, as shown in the study of Bruce et al. [10]. In this case, volumes associated to stationary and moving meshes are meshed separately. Along the simulation, both are superimposed freely, and the information is transferred from one mesh to another by interpolation. This technique has the inconvenient of producing a high numerical diffusion due to interpolation errors when used to simulate multiphase flows. Strasser [80] simulates a external gear pump by using a dynamic non-structured mesh. With this technique, the mesh is adapted, through a spring-based algorithm, to the new geometry in each time step. Furthermore, in order to keep the mesh quality above a certain limit, cells are created and agglomerated where necessary. This method has the disadvantage of requiring a too small time step to adapt the mesh without greatly reducing its quality. Houzeaux and Codina [35] take advantage of the periodicity of the flux and build ten different meshes for each period. The simulation was performed by interpolating the solutions for each time-step to the next mesh. Although the meshes can have an high quality, this method has the inconvenient that the time step is quite large (in their case a tenth of the gearing period) unless a high number of meshes are constructed. Also, the use of interpolation, again, produces high diffusion when applied to cavitating flows. Moreover, among these different approaches, only the last one correctly deals with the problem of the contact point between gears. The three first works consider that if the gap between gears is sufficiently small, the leakage is negligible. That can be acceptable if the pressure difference between inlet and outlet is not too high. However, this issue can not be avoided when the pressure difference is important. In the simulation by Houzeaux and Codina [35] the contact is already integrated in the mesh, since there is no actual movement of a gear relative to the other.

Castilla et al. [12] use a hybrid method between the one presented by Strasser [80] and the one by Houzeaux and Codina [35]. As in the first method, the mesh is deformed and locally remeshed, but, also, the mesh is replaced after a defined number of time steps in order to avoid high distortion. Ten different meshes are used in each gearing period, as in the second method. This allows to have a mesh of considerable quality at any instant, as well as a controllable time step. Moreover, the contact point is modeled by introducing a tiny wall, from one to another gear, closing the tiny gap at the theoretical position of the contact point. During the mesh deformation, the wall keeps attached to the same points of the gears, so it does not follow the line of action. Nevertheless, this is not a big problem, as, after one tenth of gearing cycle, mesh is replaced and contact point position corrected, so the wall position does never separate too much from the theoretical position of the contact point. This was the method initially followed in our study, but, as it will be shown in section 4.11, the errors associated to mesh interpolation and the error in the position of the contact point is not acceptable when cavitation is modeled.

Among the many studies about cavitation modeling, we should name the "Full Cavitation Model" of Singhal et al. [78], which uses a transport equation to determine the bubble radius, and vapo-

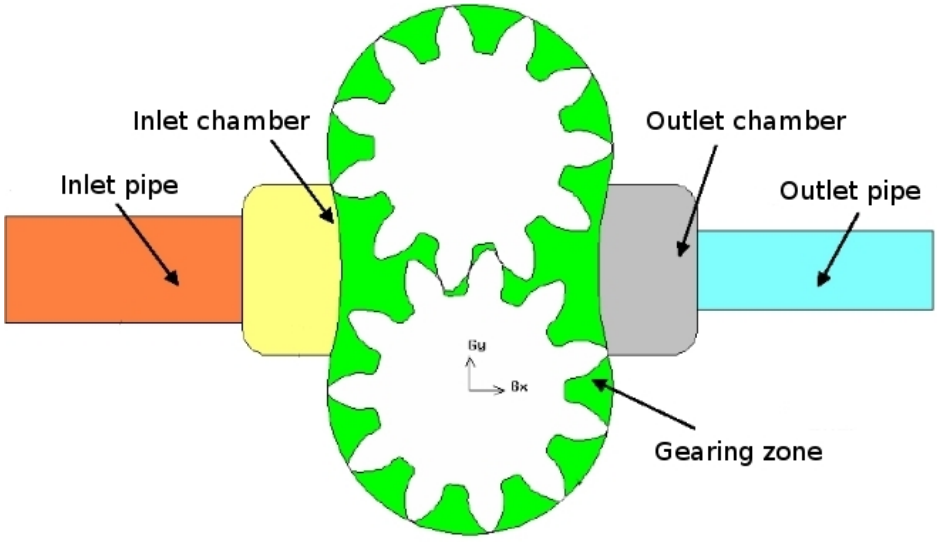

Figure 4.1: Computational domain of the reference pump with the defined zones

rization/condensation source terms to model mass transfer between the two phases. This model can take into account the effect of non-condensible gases and a slip velocity between phases. The model developed by Schnerr and Sauer [75], similar to the last one, differs in how mass transfer is modeled, and in that it is not able to take into account the effect of non-condensible gases. Zwart et al. [101] use a very similar approach to model cavitation, except for the expression that relates the number of bubbles with the volume fraction of air. The effect of turbulence in the generation and growth of bubbles has been studied by Keller et al. [48]. Zhou and Wang [100] have applied the "Full Cavitation Model" to a hydrodynamic profile together with a RNG $k - \varepsilon$ turbulence model.

4.3 Reference pump

In this section, the geometry of the reference pump will be described. Mesh details, as well as the numerical schemes used in the simulations and the physical modeling of cavitation and turbulence will be described in further sections. The alternative geometries, with different inlet chambers, will be presented in the results chapter, but their morphology, as well as the simulation parameters and numerical methods employed are the same as in the reference one.

The reference pump analyzed is the model 1PLA66, by Pedro Roquet. This pump is hydrostatically balanced and can operate up to a maximum continuous pressure of 200 bar at 2300 rpm. Its minimum rotational speed is 500 rpm at 100 bar and 700 rpm at 175 bar.

The computational domain has been divided in five regions, as shown in figure 4.1. Table 4.1 presents the geometrical and operational characteristics of the pump, as well as the properties of the mineral oil selected as fluid.

The theoretical volumetric flow rate, shown in table 4.1 has been calculated from equation 3.2.

Width of the chambers	31.8 mm
Length of the chambers	16.8 mm
Diameter of the gears	53.6 mm
Distance between centers of gears	45.1 mm
Number of teeth	11
Height of the gears	36 mm
Theoretical volumetric capacity	44 cm^3/rev
Modulus	4.1 mm
Pressure angle	23.85°
Density	885 Kg/m^3
Dynamic viscosity	0.028 Pa·s
Bulk modulus	1.5 10^9 Pa
Surface tension	0.0289 N/m
Vapor pressure	0 Pa

Table 4.1: Geometrical and operational characteristics of the reference pump and properties of the mineral oil.

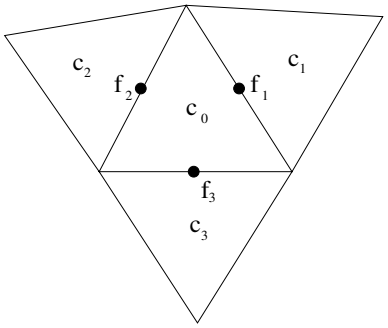

Figure 4.2: Scheme of a triangular cell and its neighboring cells.

4.4 Numerical schemes

For the numerical simulation the commercial Finite-Volume based code ANSYS Fluent 12.0 has been used. With the Finite-Volume Method (FVM), the balance equation for each physical magnitude is solved in each discrete volume using an integral formulation. The balance equation for a magnitude ϕ is

$$\frac{\mathrm{d}}{\mathrm{d}t}\int_V \rho\phi\,\mathrm{d}V + \int_{\partial V} \rho\phi\,(\vec{v}-\vec{v}_g)\cdot\vec{n}\,\mathrm{d}S = \int_{\partial V} \tau_\phi \nabla\phi\cdot\vec{n}\,\mathrm{d}S + \int_V \sigma_\phi\,\mathrm{d}V \tag{4.1}$$

where V is the cell volume, ∂V is the boundary of the cell, ρ the density of the fluid, $\vec{v}$ the flow velocity, $\vec{v}_g$ is the velocity of the deforming grid in ∂V, τ_ϕ the diffusion coefficient for the magnitude ϕ and σ_ϕ the source term. Since a two-dimensional flow has been considered, the volume of the cell is actually its area, and the area of the boundary is actually the length.

Considering the two dimensionality of the flow and the spatial discretization schematized in Fig 4.2, the equation 4.1 is formulated as

$$\frac{\mathrm{d}}{\mathrm{d}t}\left(\rho_c\phi_c S_c\right) + \sum_{i=1}^{3} \rho_{f_i}\phi_{f_i} l_i\left(\vec{v}_{f_i}-\vec{v}_{g_i}\right)\cdot\vec{n}_i = \sum_{i=1}^{3} \tau_{\phi_{f_i}} l_i \nabla\phi_{f_i}\cdot\vec{n}_i + \sigma_{\phi_c} S_c \tag{4.2}$$

where the sub-index c refers to the cell considered and sub-index f to the faces (edges) surrounding

the cell. S_c refers to the area of cell c and l_i to the length of edge i, which is part of the boundary of the cell. The time derivative is calculated with a first-order implicit scheme, since this is the only method that our software allows with dynamic mesh. Hence

$$\frac{\mathrm{d}}{\mathrm{d}t}\left(\rho_c \phi_c S_c\right) = \frac{\left(\rho_c \phi_c S_c\right)^{n+1} - \left(\rho_c \phi_c S_c\right)^{n}}{\Delta t} \tag{4.3}$$

In order to discretize the convective term of equation 4.2 in the continuity equation ($\phi = 1$ and both diffusive and source terms are null) an upwind second order scheme is used. Hence,

$$\phi_{f_i} = \phi_c + \nabla \phi_c \cdot \vec{r} \tag{4.4}$$

where $\vec{r}$ is the vector that goes from the center of edge i to the center of the neighboring cell. The gradient is calculated with the Green-Gauss node-based method:

$$\nabla \phi_c = \frac{1}{S_c} \sum_{i=1}^{3} \bar{\phi}_{f_i} l_i \vec{n}_i \tag{4.5}$$

where

$$\bar{\phi}_{f_i} = \frac{\bar{\phi}_{1_i} + \bar{\phi}_{2_i}}{2} \tag{4.6}$$

and $\bar{\phi}_{1_i}$ and $\bar{\phi}_{2_i}$ refer to the values in the extreme nodes of edge i, and are calculated as the weighted value of ϕ in the cell surrounding the node, following the method originally proposed by Holmes and Conell [34] and by Rauch and Batira [70].

In order to solve the momentum equations ($\phi = u$ and $\phi = v$), the body-force-weighted pressure interpolation has been used to model the pressure in the boundaries, as recommended in the code's documentation when body forces are important. This way, we calculate the boundary forces assuming that the gradient, in the face normal direction, of the difference between pressure and body forces, is constant. Furthermore, in these equations the spatial discretization follows a QUICK scheme, which is based on a weighted average of a second-order discretization and a centered interpolation of the variable, in which the weight coefficients are solution dependent. This way, the solution of the downstream cell is taken into account. This scheme allows us for a higher precision in the regions in which the mesh is structured (inlet and outlet pipes) and becomes identical to the second order upwind scheme in the rest of the computational domain, where mesh is non-structured.

To solve the equations, a pressure-based coupled scheme has been selected, since the segregated one was unable to correctly solve the continuity equation in regions with high density gradients, as the ones in which jets appear due to the separations of the gears, in the suction side of the gearing zone. This coupling is achieved by means of an implicit discretization of the pressure gradients in the momentum equations, and of the mass fluxes through the faces.

4.5 Turbulence modeling

The flux has been modeled as fully turbulent, due to the strong shear that appears, especially in the gearing zone and in the suction chamber. One of the simplest widely-used approximations

to simulate turbulent flux is obtained by the Reynolds averaging of the Navier-Stokes equations (RANS). Equations are averaged by decomposing all variables in a time-averaged part plus a time-dependent fluctuating part. Lets refer to the time-averaged part with capital letter and to the fluctuating part with an apostrophe (e.g. $u_i = U_i + u_i'$ for the velocity). After introducing this decomposition in the Navier-Stokes equations and averaging, new unknowns appear in the equations, involving the time-averages of the products of the fluctuating parts. For this reason, the system must be completed with additional equations (i.e. a closure model is needed).

Amongst these closure models, two-equation models are the simplest complete ones. They include two extra transport equations to represent the turbulent properties of the flow, which allows them to account for history effects like convection and diffusion of turbulent energy.

The selected model has been the standard $k - \varepsilon$ (Launder and Spalding [55]) since its has been proved its good performance in modeling turbulent fluxes in external gear pumps (Castilla et al. [12]). In this model, one of the transported variables is the turbulent kinetic energy, k, which determines the energy contained in the turbulence, and the second is the rate of dissipation of the turbulence energy per unit mass, ε, which determines its length-scale.

The basis for all two equation models is the Boussinesq eddy viscosity assumption, which postulates that the Reynolds stress tensor, τ_{ij}, is proportional to the mean strain rate tensor, S_{ij}, and can be written in the following way:

$$\tau_{ij} = 2\mu_t S_{ij} - \frac{2}{3}\rho k \delta_{ij} \tag{4.7}$$

being

$$S_{ij} = \frac{1}{2}\left[\frac{\partial U_i}{\partial x_j} + \frac{\partial U_j}{\partial x_i}\right] \tag{4.8}$$

Where μ_t is a scalar property called the turbulent (or eddy) viscosity which is computed from the two transported variables. The last term in equation 4.7 is included for modeling incompressible flow to ensure that the definition of turbulent kinetic energy, k, is obeyed:

$$k = \frac{\overline{u_i' u_i'}}{2} \tag{4.9}$$

The same equation can be written more explicitly as:

$$-\rho\overline{u_i' u_j'} = \mu_t \left(\frac{\partial U_i}{\partial x_j} + \frac{\partial U_j}{\partial x_i}\right) - \frac{2}{3}\rho k \delta_{ij} \tag{4.10}$$

This assumption is a huge simplification which allows one to think of the effect of turbulence on the mean flow in the same way as molecular viscosity affects a laminar flow. It also makes it possible to introduce intuitive scalar turbulence variables like the turbulent energy and dissipation.

The definition of the turbulence dissipation rate, ε, is:

$$\epsilon = 2\nu \left\langle s_{ij} s_{ij} \right\rangle = \nu \left\{ \left\langle \frac{\partial u_i}{\partial x_j} \frac{\partial u_i}{\partial x_j} \right\rangle + \left\langle \frac{\partial u_i}{\partial x_j} \frac{\partial u_j}{\partial x_i} \right\rangle \right\} \tag{4.11}$$

The integral length scale, l, is a physical quantity describing the size of the large energy-containing eddies in a turbulent flow. It is often used to estimate the turbulent properties on the inlets of a

CFD simulation. Since the turbulent length scale is a quantity which is intuitively easy to relate to the physical size of the problem, it is easy to guess a reasonable value for it. In the $k-\varepsilon$ model the integral length scale can be computed as:

$$l = \frac{k^{3/2}}{\varepsilon} \tag{4.12}$$

The model transport equation for k is derived from the exact equation, while the model transport equation for ε is obtained using physical reasoning and bears little resemblance to its mathematically exact counterpart. In the derivation of the $k-\varepsilon$ model, the assumption is that the flow is fully turbulent, and the effects of molecular viscosity are negligible.

The turbulence kinetic energy, k, and its rate of dissipation, ε, are obtained from the following transport equations:

$$\frac{\partial}{\partial t}(\rho k) + \frac{\partial}{\partial x_i}(\rho k u_i) = \frac{\partial}{\partial x_j}\left[\left(\mu + \frac{\mu_t}{\sigma_k}\right)\frac{\partial k}{\partial x_j}\right] + G_k + G_b - \rho\varepsilon - Y_M + S_k \tag{4.13}$$

$$\frac{\partial}{\partial t}(\rho \varepsilon) + \frac{\partial}{\partial x_i}(\rho \varepsilon u_i) = \frac{\partial}{\partial x_j}\left[\left(\mu + \frac{\mu_t}{\sigma_k}\right)\frac{\partial \varepsilon}{\partial x_j}\right] + C_{1\varepsilon}\frac{\varepsilon}{k}(G_k + C_{3\varepsilon}G_b) - C_{2\varepsilon}\rho\frac{\varepsilon^2}{k} + S_\varepsilon \tag{4.14}$$

In these equations, G_k represents the generation of turbulent kinetic energy due to the mean velocity gradients, calculated as

$$G_k = -\rho\overline{u_i' u_j'}\frac{\partial u_j}{\partial x_i} = \mu_t S^2 \tag{4.15}$$

where S is the modulus of the mean rate-of-strain tensor, defined as

$$S \equiv \sqrt{2 S_{ij} S_{ij}} \tag{4.16}$$

G_b is the generation of turbulence kinetic energy due to buoyancy, which is negligible in our case, since no gravity effects are taken into account. Y_M represents the contribution of the fluctuating dilatation in compressible turbulence to the overall dissipation rate, and is negligible in liquids. $C_{1\varepsilon}$, $C_{2\varepsilon}$ and $C_{3\varepsilon}$ are constants. σ_k and σ_ε are the turbulent Prandtl numbers for k and ε, respectively. S_k and S_ε are source terms that will be null in our case.

The turbulent viscosity, μ_t, is computed by combining k and ε:

$$\mu_t = \rho C_\mu \frac{k^2}{\varepsilon} \tag{4.17}$$

where C_μ is a model constant which in the standard version of the $k-\varepsilon$ model has a value of 0.09.

The model constants $C_{1\varepsilon}$, $C_{2\varepsilon}$, $C_{3\varepsilon}$, σ_k and σ_ε have the following values,

$$C_{1\varepsilon} = 1.44 \quad C_{2\varepsilon} = 1.92 \quad C_{3\varepsilon} = -0.33 \quad \sigma_k = 1.0 \quad \sigma_\varepsilon = 1.3$$

which have been determined from experiments with air and water for fundamental turbulent shear flows including homogeneous shear flows and decaying isotropic grid turbulence. They have been found to work fairly well for a wide range of wall-bounded and free shear flows (Launder [55]).

Both equations have been discretized by means of a second-order upwind scheme.

For the near-wall flow modeling, the standard wall functions (Launder [55]) have been modified. This was done because, in a small region surrounding the theoretical contact point position, the distance between the walls of each gear becomes so small (and hence the mesh so fine), that excessively low values of y^+ are obtained ($y^+ \lesssim 5$). In those regions, wall functions become too imprecise and the turbulence model used in the laminar sublayers may not take into account the low Reynolds number effects, leading to convergence errors. The wall functions modified to take into account these regions distinguish two different zones, depending on the Reynolds number based on the wall-normal distance to the nearest wall, y, calculated at the cell centers, Re_y,

$$Re_y = \frac{\rho y \sqrt{k}}{\mu} \tag{4.18}$$

In the fully turbulent region ($Re_y > Re_y^*$; $Re_y^* = 200$), the standard $k-\varepsilon$ model is used, while, in the viscosity-affected near-wall region ($Re_y < Re_y^*$), the one-equation model of Wolfshtein [96] is employed. In the one-equation model, the k equation is kept unmodified. However, the modified turbulent viscosity, $\mu_{t,w}$, is computed from

$$\mu_{t,w} = \rho C_\mu l_\mu \sqrt{k} \tag{4.19}$$

where the length scale that appears in equation 4.19 is computed from Chen and Patel [15]:

$$l_\mu = y C_l^* \left(1 - e^{-Re_y/A_\mu}\right) \tag{4.20}$$

The two-layer formulation for turbulent viscosity described above is used as a part of the enhanced wall treatment, in which the two-layer definition is smoothly blended with the high-Reynolds-number μ_t definition from the outer region, as proposed by Jongen [43]

$$\mu_{t,enh} = \lambda_\varepsilon \mu_t + (1 - \lambda_\varepsilon)\, \mu_{t,w} \tag{4.21}$$

Finally, a blending function, λ_ε, is defined in such a way that it is equal to unity away from walls and is zero in the vicinity of the walls. The blending function has the following form:

$$\lambda_\varepsilon = \frac{1}{2}\left[1 + \tanh\left(\frac{Re_y - Re_y^*}{A_w}\right)\right] \tag{4.22}$$

The constant A_w determines the width of the blending function. By defining a width such that the value of λ_ε will be within 1% of its far-field value given a variation of ΔRe_y, the result is

$$A_w = \frac{|\Delta Re_y|}{\tanh^{-1}(0.98)} \tag{4.23}$$

The ε field in the viscosity-affected region is computed from

$$\varepsilon = \frac{k^{3/2}}{l_\varepsilon} \tag{4.24}$$

The length scale that appears in equation 4.24 is computed from Chen and Patel [15]:

$$l_\varepsilon = yC_l^* \left(1 - e^{-Re_y/A_\varepsilon}\right) \tag{4.25}$$

For the blending of ε a procedure similar to the μ_t-blending has been used, in order to ensure a smooth transition between the algebraically-specified ε in the inner region and the ε obtained from solution of the transport equation in the outer region. The constants in equations 4.20 and 4.25 are taken from Chen and Patel [15]:

$$C_l^* = \kappa C_\mu^{-3/4} \quad A_\mu = 70 \quad A_\varepsilon = 2C_l^*$$

4.6 Multiphase flow modeling

In order to model multiphase flow, the mixture model, proposed by Ishii [38] has been used. This model uses a single-fluid approach.

This means that it can model two or more immiscible fluids by solving a single set of momentum equations and tracking the volume fraction of each of the fluids throughout the domain. Flow is therefore modeled as a mixture of vapor (air) and liquid (oil), where the volume fraction of vapor, α, and liquid, α_l, may take any value between 0 and 1, as far as the sum is 1 ($\alpha = 1-\alpha_l$). This way, the vapor volume fraction, α, appears as a new unknown. The mixture model solves the continuity and the momentum equations for the mixture, plus an extra continuity equation for the vapor volume fraction. It is also able to deal with relative velocities if phases are moving at different velocities, by solving an algebraic expression. As the cavitation that appears in gear pumps is traveling cavitation (cavities move continuously with the local velocity of the flowing liquid), we will consider a unique velocity for both phases.

Furthermore, according to the code's documentation [1], this model is recommended for homogeneous multiphase flow with a big coupling between phases and phases moving at the same speed.

It should be noted that, by assuming air to be the only vaporous phase (as we are not considering oil vapor), we are considering the effect of aeration, but we will not be able to model the effect of vaporous cavitation. This is justified by taking into account that cavitation begins with nuclei with diameters ranging from $10^{-7} - 10^{-5}$ m which grow explosively as they pass through regions where the pressure drops below the vapor pressure, and that for gaseous cavitation, growth is limited by molecular diffusion timescales, being therefore much slower than aeration.

The continuity equation for the mixture is

$$\frac{\partial}{\partial t}(\rho_m) + \nabla \cdot (\rho_m \vec{v}) = 0 \tag{4.26}$$

being ρ_m the mixture density,

$$\rho_m = \alpha\rho_v + (1-\alpha)\,\rho_l \tag{4.27}$$

The subscripts l and v stand for the properties of pure liquid and pure vapor.

The momentum equation for the mixture can be obtained by summing the individual momentum equations for all phases. When no relative velocity between phases is considered, it can be expressed

as,

$$\frac{\partial}{\partial t}\left(\rho_m \vec{v}\right) + \nabla \cdot \left(\rho_m \vec{v}\vec{v}\right) = -\nabla p + \nabla \cdot \left[\mu_m \left(\nabla \vec{v} + \nabla \vec{v}^T\right)\right] \tag{4.28}$$

where μ_m is the dynamic viscosity of the mixture, which is also obtained as a volume-weighted average:

$$\mu_m = \alpha \mu_v + (1 - \alpha)\, \mu_l \tag{4.29}$$

Finally, the volume fraction equation for the secondary phase (vapor) can be obtained from the continuity equation

$$\frac{\partial}{\partial t}\left(\alpha \rho_v\right) + \nabla \cdot \left(\alpha \rho_v \vec{v}\right) = \dot{m}_{lv} - \dot{m}_{vl} \tag{4.30}$$

being $\dot{m}_{ij}$ the mass transfer rate from phase i to phase j.

The QUICK scheme, previously described, has been used for the spatial discretization of this equation.

4.7 Cavitation modeling

As seen in chapter 2, the dynamics of bubble inception, growth and collapse are complex and depend on a variety of factors, including surface tension, viscous effects, and noncondensable gas content. The cavitation region is made up of a large number of bubbles, which collapse as they are swept into regions of higher pressure. The large accelerations and pressures generated by the final stage of collapse are responsible for much of the noise and damage generated by cavitating flows. Not surprisingly, there are no cavitation models which attempt to account for all of these complexities.

The simplest models do not account for the cavitation rate at all. Instead, the volume fraction is post-processed from the pressure field using the Rayleigh-Plesset equation. With this methods the density changes induced by cavitation do not affect the flow solution. A second strategy for modeling cavitating flows is to assume a barotropic equation of state to express the mixture density as a function of local pressure. An example is presented by Coutier-Delgosha et al. [16]. This modeling approach is attractive because it can be integrated into a single-phase CFD code without much effort. However, these approaches are overly simplistic in their assumption of equilibrium thermodynamics.

There are models, however, which do account for non-equilibrium effects. Most of these models are based upon the Rayleigh Plesset equation, which describes the growth and collapse of a single bubble subjected to a far-field pressure disturbance. Examples of such models are given by Schnerr and Sauer [75], Gerber [25], Zwart et al. [101], and Senocak and Shyy [77]. The details of the models developed by these and other researchers vary, but they share the common feature of modeling the vapor composition by using a continuity equation having a source term which can be traced back to the Rayleigh Plesset equation.

Before choosing a model for our simulations we have tested the models given by Schnerr and Sauer [75] and by Zwart et al. [101]. Since, in a multiphase numerical simulation, global accomplishing of the continuity equation with cavitation is not as easy as in a single-phase one, a two-dimensional venturi geometry has been tested with both models in order to find out which one works better

from the point of view of continuity. After analyzing the results, the model given by Zwart et al. [101] has been chosen. Details of this simulations will be presented in section 4.8.

The cavitation model employed in our simulations, is the one developed by Zwart et al. [101]. It accounts for all first-order effects (i.e., phase change, bubble dynamics, turbulent pressure fluctuations, and noncondensable gases), as well as for the compressibility of the liquid phase.

To close the system of equations, an additional relation is needed, since we have introduced a new variable, α. The vapor is assumed to consist of n_b spherical bubbles per unit volume, all of them of radius R. Being V_b the bubble volume, the vapor volume fraction can be expressed as:

$$\alpha = V_b n_b = \frac{4}{3}\pi R^3 n_b \tag{4.31}$$

In a flowing liquid with zero velocity slip between the fluid and bubbles, the bubble dynamics equation can be derived from the generalized Rayleigh-Plesset equation as it was explained in chapter 2:

$$\frac{p_B - p_\infty}{\rho_l} = R\frac{\mathrm{d}^2 R}{\mathrm{d}t^2} + \frac{3}{2}\left(\frac{\mathrm{d}R}{\mathrm{d}t}\right)^2 + \frac{4\nu_l}{R}\frac{\mathrm{d}R}{\mathrm{d}t} + \frac{2\sigma}{\rho_l R} \tag{4.32}$$

Neglecting the second order terms and the surface tension force, equation 4.32 is simplified to

$$\frac{DR}{Dt} = \sqrt{\frac{2}{3}\frac{p_B - p_\infty}{\rho_l}} \tag{4.33}$$

Taking into account that vapor phase is modeled as incompressible (ρ_v is constant), the rate change of mass of a single bubble can be expressed as:

$$\frac{\mathrm{d}m_B}{\mathrm{d}t} = \rho_v \frac{\mathrm{d}V_B}{\mathrm{d}R}\frac{DR}{Dt} = 4\pi R^2 \rho_v \sqrt{\frac{2}{3}\frac{p_B - p_\infty}{\rho_l}} \tag{4.34}$$

By combining equations 4.31 and 4.34 and assuming liquid's density constant (it's compressibility can be neglected for cavitation purposes), the net mass transfer rate from liquid to vapor, R_{lv}, can be expressed as

$$R_{lv} \equiv \dot{m}_{lv} - \dot{m}_{vl} = \frac{3\alpha\rho_v}{R}\sqrt{\frac{2}{3}\frac{p_B - p_\infty}{\rho_l}} \tag{4.35}$$

This model has been derived assuming vaporization (bubble growth), and that bubbles do not interact with each other (which is only realistic in the earliest stages of cavitation). Zwart et al. [101] purposed the following expressions to take into account condensation and bubble interaction:

$$R_{lv} = \begin{cases} F_{vap}\frac{3r_{nuc}(1-\alpha)\rho_v}{R}\sqrt{\frac{2}{3}\frac{p_B - p_\infty}{\rho_l}} & p < p_v \\ F_{cond}\frac{3\alpha\rho_v}{R}\sqrt{\frac{2}{3}\frac{p_B - p_\infty}{\rho_l}} & p > p_v \end{cases} \tag{4.36}$$

Model parameters F_{vap} and F_{cond} have been tuned experimentally by Zwart et al. [101] for various test cases.

For the case of unsteady cavitation, they employed the experimental results of Stutz and Reboud [81] with water passing through a venturi-type geometry. They characterized the cavitation cloud

shedding frequency at the venturi throat by means of a Strouhal number, defined as

$$St = \frac{f L_c}{U_{in}} \tag{4.37}$$

where f is the frequency, L_c is the average cavity length, and U_{in} is the inlet velocity. They found $F_{vap} = 0.4$ and $F_{cond} = 0.001$ to work well for this transient cavitation case. Nevertheless, found out that these coefficients should be very carefully tuned in transient cases, as the cloud shedding frequency in the venturi was highly dependent on them.

The parameter r_{nuc} represents the nucleation site volume fraction. Assuming that the dissolved air volume agrees with Henry's law at atmospheric pressure, r_{nuc} should take the Bunsen's coefficient value, $r_{nuc} = 0.09$. The initial bubble radius, R, is also a parameter of the model.

In order to tune the cavitation model parameters, we have simulated the venturi test case employed by Zwart et al. [101] both with water and mineral oil. We have also reproduced the cavitation experiments with mineral oil in a long orifice performed by Yamaguchi [98]. These results will be presented in section 4.8.

4.8 Comparison of cavitation models

Simulations including cavitation effects have required more strict convergence criteria than the ones without them, in order to avoid global mass flow imbalance. The cavitation model selected, as well as its parameters, can also greatly influence mass flow imbalance.

We define the mass flow imbalance, M_i, as the relative mean mass flow difference between inlet and outlet within a gearing cycle:

$$M_i = \frac{\left|\overline{\dot{m}}_{in} - \overline{\dot{m}}_{out}\right|}{\overline{\dot{m}}_{in}} \tag{4.38}$$

We have checked that simulations including cavitation effects, unlike the ones without them, presented a mass flow imbalance of around 1% when all scaled residuals were set to 10^{-3} (the recommended value in the code's documentation), despite the simulation was converged according to the selected criteria, which will be explained in section 4.9. Reducing the residuals obviously reduces the mass flow imbalance, but increases the computational time of the simulation, which was already long.

Furthermore, Zwart et al. [101] demonstrated that in unsteady cases, a careful tuning of the model constants (very especially the vaporization constant, F_{vap}, and the condensation constant, F_{cond}) is a must. They tuned these constants by simulating a venturi nozzle with water and comparing the shedding frequency of the cavity that generates at the throat with the one taken from the experimental results of Stutz and Reboud [81].

In order to analyze the influence of the residuals criteria, the cavitation model selected, and to properly tune its parameters, two different test cases have been numerically simulated and compared to experimental data: a two-dimensional venturi nozzle and a circular orifice. Results will be presented in the following subsections.

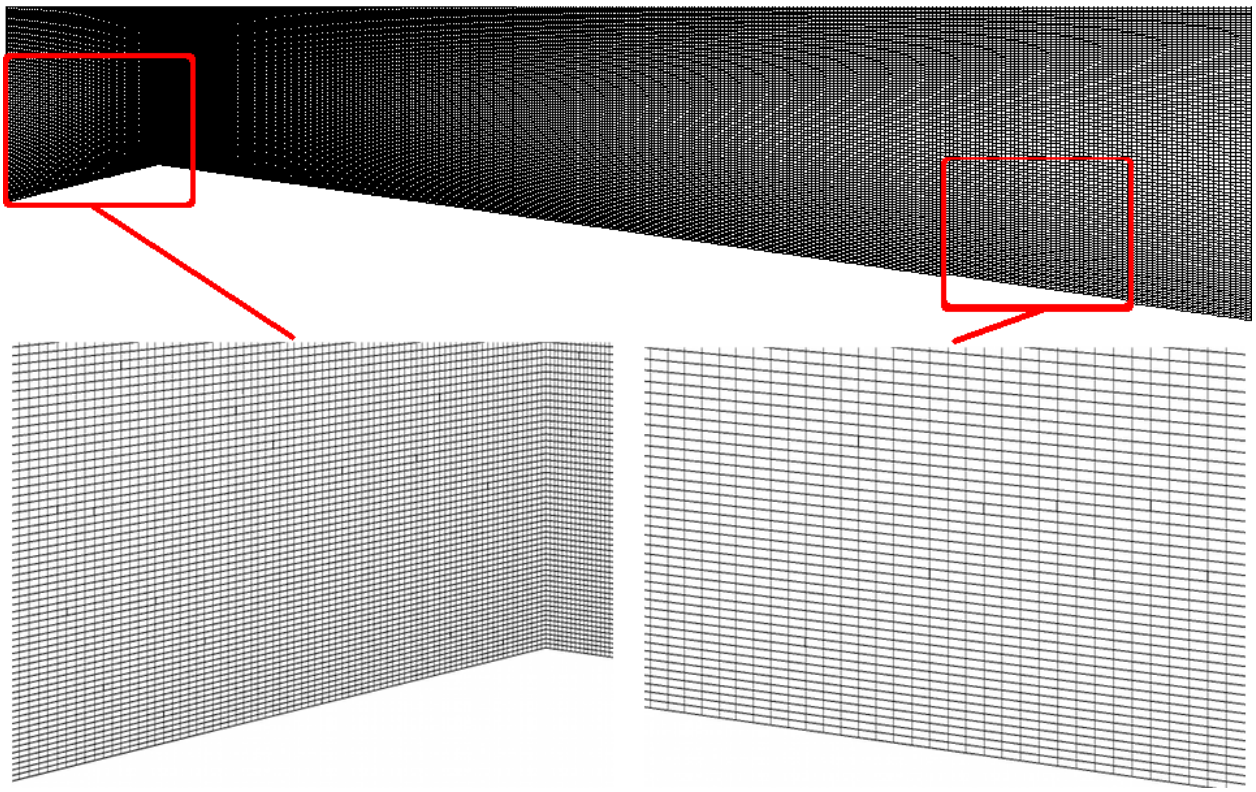

Figure 4.3: Mesh of the venturi nozzle.

4.8.1 2D venturi nozzle

In the validation of the cavitation model performed by Zwart et al. [101] it was shown that the empirical constants of their model are highly dependent on the type of cavitation that takes place. They adjusted these constants by simulating the following experimental test cases: a hydrofoil and an inducer, both with steady cavitation, and a venturi nozzle, with transient cavitation. The model constants had to be readjusted for the transient case, changing in one or more orders of magnitude with respect to the values taken in the steady cavitation cases. This sensitivity of the model constants, along with the fact that Zwart et al. employed water in all their test cases, suggested we do further testing on the cavitation models.

A two-dimensional venturi nozzle similar to the one used in the model validation by Zwart et al. [101], was simulated, using mineral oil as fluid. In the validation of the cavitation model performed by Zwart et al. [101] using water, the model constants were adjusted to $F_{vap} = 0.4$ and $F_{cond} = 0.001$, by comparing the cloud shedding frequency against that obtained experimentally by Stutz and Reboud [81].

Two cavitation models were tested: the one proposed by Schnerr and Sauer [75], and the one proposed by Zwart et al. [101].

The mesh has 52290 cells and is shown in figure 4.3. The boundary conditions were set to an inlet velocity of 16 m/s, an outlet pressure of 20 kPa, and no-slip condition at the venturi walls. Time step was 10^{-4} s. The throat length is $D_t = 0.0625$ m. The inlet length is $1.25D_t$, the outlet length is $2D_t$, and the total length of the nozzle is $8D_t$. The throat is at a distance D_t from the inlet.

Table 4.2 shows the mass flow imbalance and the cloud shedding frequency obtained for each

Cavitation model	Residuals	Mass flow imbalance (%)	Frequency (Hz)
Schnerr and Sauer	10^{-3}	0.118	20.60
	10^{-4}	0.016	39.62
	10^{-5}	0.001	42.01
Zwart et al.	10^{-3}	0.775	12.19
	10^{-4}	0.175	6.60
	10^{-5}	0.142	6.88

Table 4.2: Mass flow imbalance and cloud shedding frequency in a venturi nozzle with Schnerr and Sauer and Zwart-Gerber-Belamri cavitation models, using hydraulic oil as working fluid.

cavitation model tested using different convergence criteria for the scaled residuals.

These simulations show that mass flow imbalance is always lower with the model from Schnerr and Sauer. Regarding the cloud shedding frequency, a low convergence criteria yields a completely wrong prediction of the unsteady characteristic of the flow. When convergence criteria is made more restrictive, shedding frequency converges to a certain value, but this value is very different depending on the cavitation model selected. The shedding frequency can be easily controlled in the model from Zwart et al. by adjusting the constants F_{vap} and F_{cond}, but it can't be controlled in the model from Schnerr and Sauer. Therefore, unless we can be certain that the shedding frequency of the model from Schnerr and Sauer is correct, we would be obliged to use the model from Zwart et al., despite its higher mass flow imbalance, after correctly tuning the model constants.

As mentioned above, the model constants selected for our test case were taken from Zwart et al. adjustment for a test case very similar to ours, but with water instead of oil. In order to check whether the same constants can suit our case with oil, we have repeated the venturi simulation with Zwart et al. model and the scaled residuals convergence criteria set to 10^{-5} using water as working fluid. This simulation yields a shedding frequency of 6.89 Hz, which is very similar to the one of 6.88 Hz obtained with oil. Therefore, we can assume that the model constants obtained by Zwart et al., $F_{vap} = 0.4$ and $F_{cond} = 0.001$, for unsteady cavitation are not highly dependent on the working fluid, and can therefore be used in our case.

Regarding the convergence criteria, it is clear that 10^{-3} is not an small enough residual from both the point of views of mass flow imbalance and unsteady behavior. We have chosen to use the 10^{-4} criteria, as the mass flow imbalance and the unsteady behavior seem to be acceptable and are not very far from the ones obtained with the 10^{-5} criteria. On the other hand, each simulation already takes around 3 to 4 weeks time to be computed in a Pentium Core i7 processor with 6 Gb RAM, and going to 10^{-5} would make simulations considerably longer.

The volume fraction of oil in our venturi nozzle at a certain instant is shown in figure 4.4. The cavity attached to the nozzle throat due to the expansion that takes place can be clearly seen. This cavity grows up to a maximum length and then gets detached from the throat.

Finally, Zwart et al. [101], in the validation of their model (in which they employed the standard $k - \varepsilon$ turbulence model, as we do), used a modified turbulent viscosity, following the example of Coutier-Delgosha et al. [16] in order to reduce the eddy viscosity in the cavitating regions. This way, in regions with higher vapor volume fractions (lower mixture densities) the turbulent viscosity

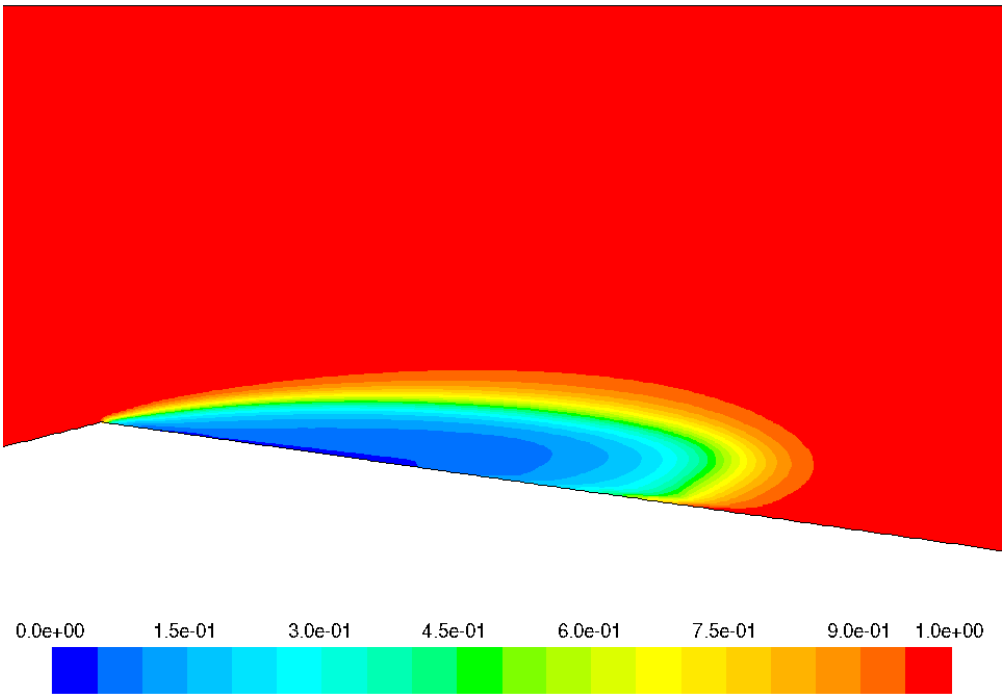

Figure 4.4: Instantaneous liquid volume fraction in a venturi nozzle with hydraulic oil. Cavitation model: Zwart et al. Convergence criteria: all scaled residuals should drop below 10^{-4}.

of the mixture is artificially reduced. The modified turbulent viscosity takes the form

$$\mu_{tm} = f(\rho) C_\mu \frac{k^2}{\varepsilon} \tag{4.39}$$

where

$$f(\rho) = \rho_v + \left(\frac{\rho_v - \rho_m}{\rho_v - \rho_l}\right)^n (\rho_l - \rho_v) \tag{4.40}$$

being ρ_v , ρ_l and ρ_m the vapor, liquid and mixtures densities respectively, and n an empirical exponent that should be tuned. This modified turbulence model was introduced via a user-defined function and was employed in our test cases taking $n = 5$, following Zwart et al. [101] procedure. Initially, it was also used in the simulations with the gear pump, but, in this case, a considerably higher mass flow imbalance was observed with the modified turbulent viscosity than without it: 0.505% with modified turbulent viscosity and 0.262% without it, at 1500 rpm. In addition, Zwart [102] found out that this custom modification of turbulent viscosity seems rather ad-hoc and not universal. Therefore, the standard turbulent viscosity was finally taken for the gear pump simulations.

4.8.2 Circular orifice

In order to better tune and validate the parameters of the model selected, some experimental data of unsteady cavitation in hydraulic oil is needed. The experiments of cavitation in long orifices performed by Yamaguchi [98] have been used. In his experiments, Yamaguchi tests cavitation in sharp-edged and round-edged long orifices with mineral oil at different low Reynolds numbers. We have numerically reproduced some of these experiments with sharp-edged orifices.

Set	R (μm)	r_{nuc}	F_{vap}	F_{cond}
A	10	0.09	0.4	0.001
B	0.57	0.09	0.4	0.001
C	1	0.09	50	0.01

Table 4.3: Constant sets of the cavitation model tested. The meaning of each constant can be found in section 4.7.

In these experiments, the pressure at the downstream tap of the orifice, p_{out}, is gradually reduced. When it drops below a certain value, bubbles appear at first in the separation zone at the sharp inlet edge. As p_{out} is further reduced, cavitation developed gradually and then flow choking occurs. Under the choking conditions, cloud shedding disappears and volume of air is kept constant, without high frequency fluctuations.

Yamaguchi performed a series of experiments at different Reynolds numbers ranging from 2000 to 5000 and annotated the critical cavitation numbers at which incipient cavitation took place, k_i, and at which choking occurred, k_c. Here, the cavitation number is defined as,

$$k = \frac{p_{out} - p_v}{p_{in} - p_{out}} \tag{4.41}$$

For the simulations, the axis-symmetric solver was used. The orifice is 20 mm long and has a diameter of 4.52 mm. Velocity inlet boundary conditions were imposed at inlet, in order to simulate two different Reynolds numbers: $Re = 2400$ and $Re = 4000$. Different pressure outlet boundary conditions were imposed for each Reynolds number, in order to simulate a range of cavitation numbers for each of them. As the Reynolds numbers are small, flux was simulated laminar. At both ends of the orifice, stagnation chambers, with a diameter 5 times that of the orifice, have been placed. Mesh is structured and has approximately 130.000 faces, of which 35.000 belong to the orifice region.

For the discretization, second order spatial schemes have been used. Multiphase flow has been modeled with the mixture model and no-slip condition, as in the pump simulations. The cavitation model employed was the one of Zwart et al. [101] and the scaled residuals convergence criteria was set to 10^{-4} for all variables, following the conclusions of our tests with the venturi nozzle, presented in the previous subsection. The time step for all these unsteady simulations has been taken $\Delta t = 2{\cdot}10^{-5}$ s, which yields $(T_r/\Delta t)_{Re=2400} = 55.55$ and $(T_r/\Delta t)_{Re=4000} = 33.33$ being T_r the residence time of a fluid particle inside the orifice. Three different sets (A, B and C) of the cavitation model constants have been tested. These model constants are detailed in table 4.3.

Three different initial bubble radii have been employed. The one of set C (1 μm) is the default one included in the cavitation model, and also the one employed by Zwart et al. [101] in their venturi model validation. The ones of set B (0.57 μm) and C (10 μm) represent the orders of magnitude between which an air bubble can be found in equilibrium conditions with mineral oil. Nucleation site volume, r_{nuc}, has been kept the Bunsen coefficient for oil ($r_{nuc} = 0.09$). Vaporization and condensation model constants in sets A and B are taken as the ones employed by Zwart et al. [101] in the venturi validation. In set C, they are taken as the default values of the model, which were taken from the calibration with steady cavitation cases performed by Zwart et al. [101].

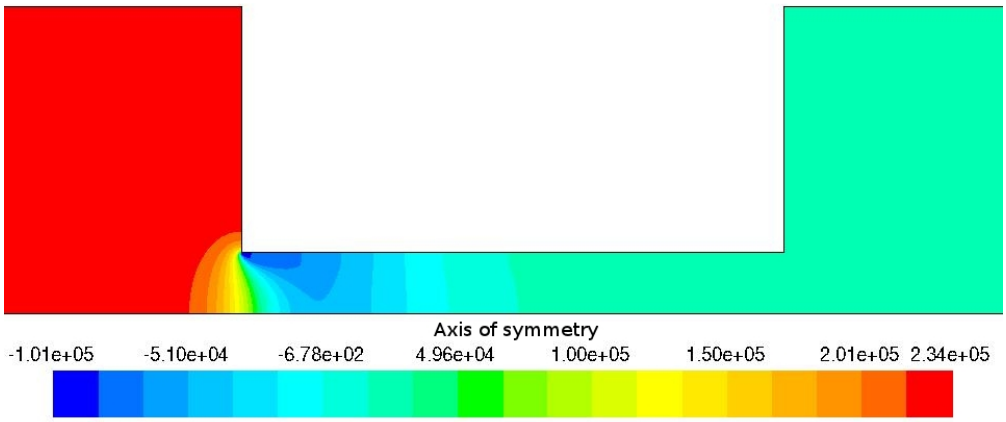

Figure 4.5: Pressure contours (Pa) for $Re = 2400$, $k = 0.6$, and cavitation model constants from set A.

The computational domain with pressure contours for $Re = 2400$, $k = 0.6$ and cavitation model constants from set A are shown in figure 4.5.

In figure 4.6 the experiments performed by Yamaguchi [98] are represented by the red and black lines, showing the experimental incipient and choking cavitation numbers for a range of Reynolds numbers. As outlet pressure is gradually reduced, so does the cavitation number. Therefore, cavitation should start to appear when cavitation number drops below the black line, and after further reducing the outlet pressure, choking should take place when crossing the red line. Along with this data, the different conditions simulated with each set of model constants are also presented in the same figure.

In table 4.4 the average relative volume occupied by air in the $Re = 2400$ simulations is shown. Although the cavitation number is not exactly the same for each $Re - k$ point, because small differences in the inlet pressure appear for a given outlet pressure, a representative number (the average) has been adopted for each case. These four cases can be clearly identified in figure 4.6. The simulations at $k = 0.60$ should present no cavitation. The ones at $k = 0.52$ should present no cavitation either, although a very small amount of vapor would be acceptable since it is near the cavitation inception point. The ones at $k = 0.46$ are a bit below the inception point and therefore some cavitation with cloud shedding should be expected. Finally, the ones at $k = 0.37$ should present a considerable amount of volume of air with choking conditions.

From the table, it is clear that with the model parameters of set C, a considerable cavitation is predicted, independently of the cavitation number, which does not agree with the experiments. The air volume predicted for sets A and B seem to be reasonable, with negligible cavitation for $k = 0.6$, very small for $k = 0.52$, and developed cavitation for $k = 0.46$ and $k = 0.37$. For developed cavitation situations, set B predicts stronger cavitation than set A. Unfortunately, as cavitation was eye-observed by Yamaguchi, we have no information about the volume of air present in the experiments.

The instantaneous oil volume fraction in the orifice for $Re = 2400$ and $k = 0.46$ is shown in figure 4.7. The cloud-shedding structure that appears in the simulations with parameters from set A seem to be closer to the expected behavior than the structures observed in the simulations with parameters from set B.

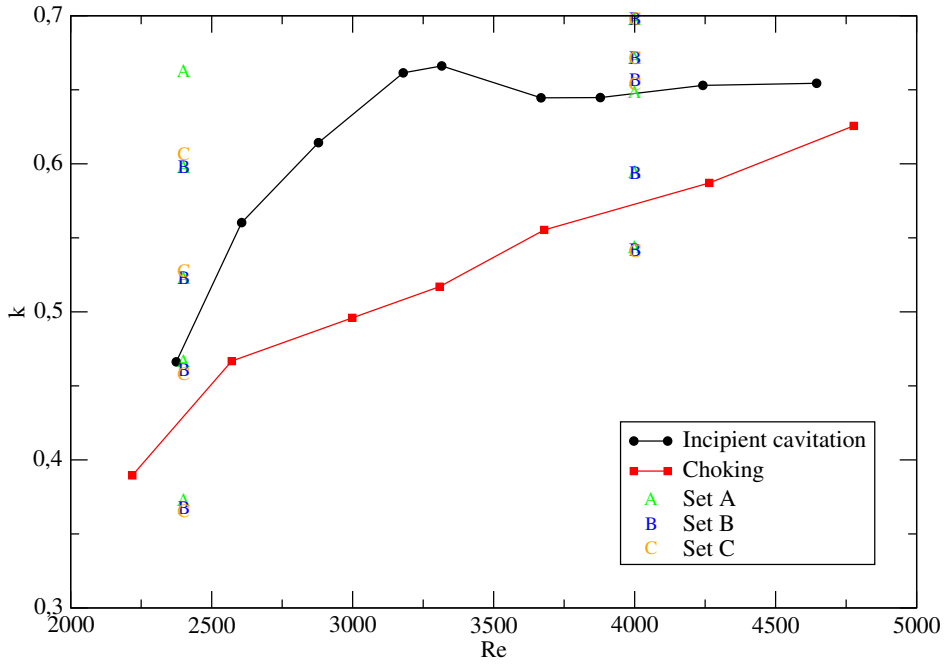

Figure 4.6: Incipient and choking cavitation numbers versus Reynolds. Experiments from Yamaguchi [98] and numerical simulations with different sets of cavitation model parameters.

k	Set	$\langle V_{air}/V_{pipe} \rangle$ (%)
0.60	A	0.13
	B	0.06
	C	29.66
0.52	A	0.37
	B	0.24
	C	29.41
0.46	A	5.91
	B	10.77
	C	27.44
0.37	A	13.61
	B	16.21
	C	26.96

Table 4.4: Relative mean air volume in the simulations at $Re = 2400$.

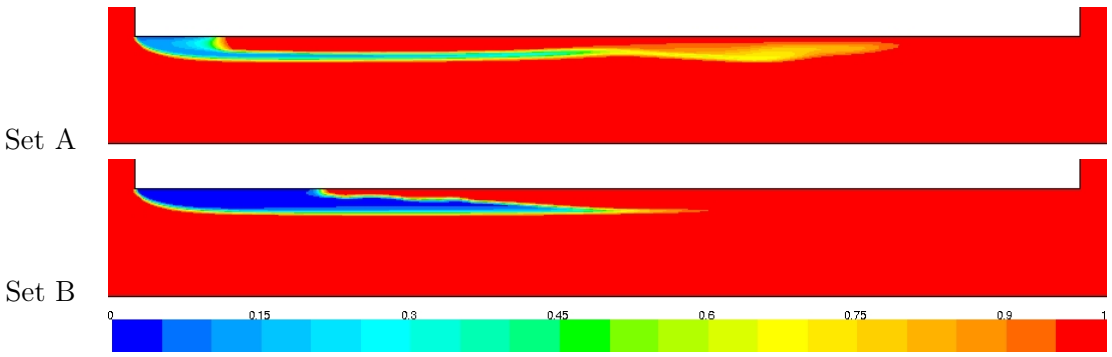

Figure 4.7: Volume of oil contours in the orifice at $Re = 2400$ and $k = 0.46$.

k	Set	$\langle V_{air}/V_{pipe} \rangle$ (%)
0.67	A	0.00
	B	0.00
0.65	A	0.04
	B	0.03
0.59	A	0.28
	B	0.33
0.54	A	1.97
	B	1.97

Table 4.5: Relative mean air volume in the simulations at $Re = 4000$.

As the parameters from set C can be clearly discarded, only the results from sets A and B will be analyzed at $Re = 4000$. In table 4.5 the average relative volume occupied by air in these cases is shown. Again, an average value has has been selected for each $Re - k$ point. According to the experimental data, the selected values of the cavitation parameters should correspond, from higher to lower, to a case with no cavitation ($k = 0.67$), another at the cavitation inception point ($k = 0.65$), another with developed cavitation with cloud shedding ($k = 0.59$), and a last one in choking conditions ($k = 0.54$). It can be seen that volume of air is much lower that in the $Re = 2400$ cases, due to the fact that the cavitation numbers that represent the points under our study are higher. Just above cavitation inception, no air at all is present in the pipe. At the inception point a negligible air volume appears. In the case with developed cavitation, both the model with set A and set B parameters predict some small volumes of air, which do not differ much one from the other. Finally, in the case of lower cavitation number, at which choking conditions should appear, both with set A and set B parameters, 1.97% of the pipe volume is, in average, occupied by air.

In order to check the cloud shedding characteristics and the choking condition, the temporal evolution of the total air volume for the three cavitating cases is plotted in figure 4.8. From these graphs we can see that in all cases, the relative amplitude of the oscillations is always higher with constants from set B. Furthermore, for $k = 0.65$ and $k = 0.59$ the air volume periodically drops to zero with set B constants, while, with constants from set A, a minimum volume of air is always present. For the incipient cavitation case ($k = 0.65$) air volume evolution is rather irregular in both cases, but anyway, the total air volume present is almost negligible. In the case of developed cavitation before choking occurs ($k = 0.59$), a rather periodic shedding frequency of period $0.59\,T_r$ is observed with set A parameters, while with set B parameters air volume oscillates in a much irregular way and a cloud shedding frequency can not be clearly identified. Finally, for the the conditions at which, attending to the experimental data, choking should have occurred ($k = 0.54$), air volume oscillations have become relatively lower in the simulations with set A parameters (as expected in a choked orifice), while in the simulations with set B parameters high amplitude oscillations still appear. In conclusion, the simulations using set A constants reproduce much better the expected behavior of air volume evolution attending to the experimental data available. Therefore, we have selected to use the constants from set A in the numerical simulations of the external gear pump.

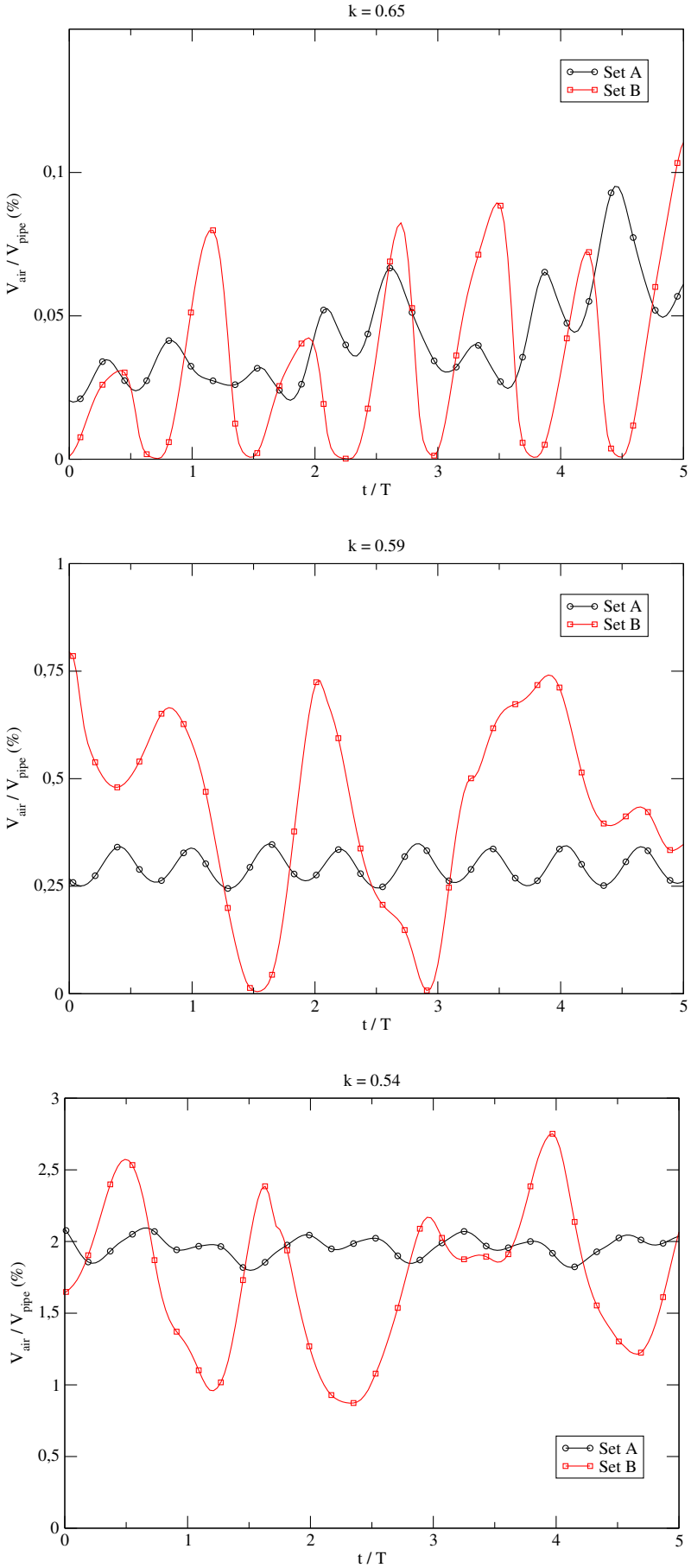

Figure 4.8: Relative air volume in the orifice at $Re = 4000$ for three different cavitation numbers.

4.9 Convergence criteria

The convergence criteria in a time step is met when the scaled residual of each equation reaches a defined value. In this moment, the next time step can be simulated. If after 100 iterations convergence is not reached, the time step is advanced anyway.

After discretization, the conservation equation for a general variable ϕ at a cell P is written as

$$a_p \phi_p = \sum_{nb} a_{nb} \phi_{nb} + b \tag{4.42}$$

being a_p the center coefficient, a_{nb} the influence coefficients for the neighboring cells, and b the contribution of the constant part of the source terms and of the boundary conditions.

The scaled residuals we have used to judge convergence are defined as follows:

$$R^{\phi} = \frac{\sum_{cells P} \left| \sum_{nb} a_{nb} \phi_{nb} + b - a_p \phi_p \right|}{\sum_{cells P} |a_p \phi_p|} \tag{4.43}$$

After checking the periodicity of the solutions at various rotational speeds, we have seen that a simulation can be considered converged when the following conditions are met:

- The scaled residuals of each equation drop below 10^{-4} in all time steps of the gearing cycle.
- Instantaneous relative error between the last two time steps is below 0.015 at any instant for the following magnitudes: inlet mass flow, outlet mass flow, and horizontal velocity in a control point of the inlet chamber, shown in figure 4.9.

$$\left. \frac{\left| \dot{m}_{in}^{n} - \dot{m}_{in}^{n-1} \right|}{\overline{\dot{m}_{in}^{n}}} \right|_{max} < 0.02 \qquad \left. \frac{\left| \dot{m}_{out}^{n} - \dot{m}_{out}^{n-1} \right|}{\overline{\dot{m}_{out}^{n}}} \right|_{max} < 0.02 \qquad \left. \frac{\left| U_x^n - U_x^{n-1} \right|}{\overline{U_x^n}} \right|_{max} < 0.02$$

- Mean relative error of the aforementioned magnitudes is below 0.005.

$$\frac{\left\langle \left| \dot{m}_{in}^{n} - \dot{m}_{in}^{n-1} \right| \right\rangle}{\langle \dot{m}_{in}^{n} \rangle} < 0.005 \qquad \frac{\left\langle \left| \dot{m}_{out}^{n} - \dot{m}_{out}^{n-1} \right| \right\rangle}{\langle \dot{m}_{out}^{n} \rangle} < 0.005 \qquad \frac{\left\langle \left| U_x^n - U_x^{n-1} \right| \right\rangle}{\langle U_x^n \rangle} < 0.005$$

Figure 4.10 shows how these criteria are met for the simulation at 1500 rpm with the reference pump.

4.10 Mesh deformation algorithms and mesh quality analysis

Inlet and outlet pipes consist of stationary structured meshes formed by quad cells. In the inlet and outlet chambers, meshes are stationary, unstructured and formed by triangular cells. In the gearing zone, mesh is dynamic, unstructured and formed by triangular cells.

Following the method suggested by Strasser [80], the curve that separates the gearing zone from the inlet and outlet chambers is tangent to the circular part of the casing, in order to avoid angular boundaries in the dynamic mesh.

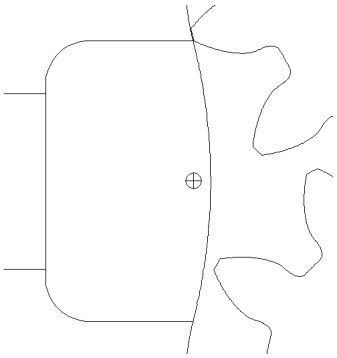

Figure 4.9: Control point inside the suction chamber where the horizontal velocity is measured.

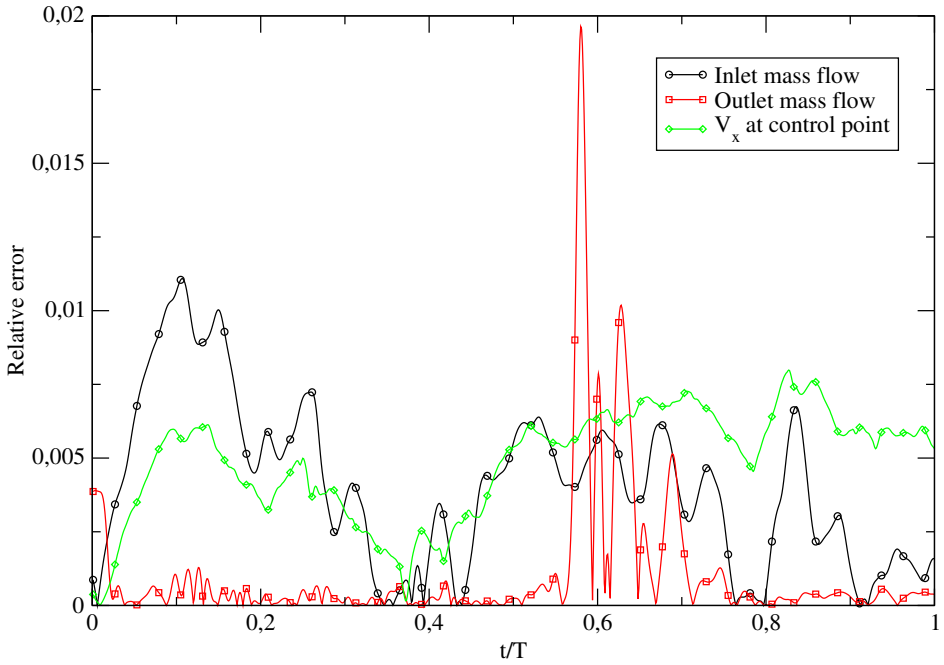

Figure 4.10: Instantaneous relative error in the reference pump at 1500 rpm. Mean values are: 0.0041 for inlet mass flow, 0.0011 for outlet mass flow, and 0.0048 for the horizontal velocity at the reference point.

The geometry and mesh of the inlet chamber of the reference pump is presented in figure 4.11, and the ones of the four modified inlet chambers that will be tested are presented in figures 4.12, 4.13, 4.14 and 4.15. Only the upper half of the chambers is shown. In each figure a detailed view of a particular region of the mesh is shown. The scaling factors employed are the same for all figures. The number of cells of each mesh is also shown in these figures. In the modified pumps the rest of the mesh is very similar to that of the original pump, as only the inlet chamber was changed, so the mesh in pipes and outlet chamber was kept unchanged, and mesh in the dynamic zone was created with analogous parameters to that of the reference pump.

The gearing zone is subjected to very complex deformations. From a geometrical point of view, there is no contact between the boundaries of each gear, neither between gears and casing. However, contact is simulated through changes in viscosity, as it will be explained in the next section. This way, the deforming grid "flows" in a connected domain of constant area so no parts of the flow domain are isolated from the rest. Nevertheless, the geometrical changes that take place in the gearing zone are very severe. This fact leads to very complex mesh deformations and makes it difficult to find a mesh deformation method capable of keeping mesh quality above a certain limit along several gearing cycles.

An Arbitrary Lagrangian-Eulerian (ALE) formulation with local remeshing is employed. The ALE method allows the grid to move with a velocity that is independent from the flow solution, as far as the grid topology is maintained. The use of these kind of algorithms has been employed in gear pumps by Castilla et al. [12], Vande Voorde et al. [90] and Riemslagh et al. [44]. The grid is modified during the computation independently of the flow velocities while keeping fixed connectivity. The prescribed velocity of the boundary nodes are the boundary condition of a problem from which the velocity of every grid node is obtained. The Navier-Stokes equations are reformulated by using relative velocities to each cell.

It has been seen that deforming the grid through the widely-spread spring analogy operator, as done by all authors mentioned above, results in very highly distorted grids after a fraction of a cycle. To avoid this, the methodology followed by Castilla et al. [12] was initially followed. It consists in generating 10 independent grids, one after each 1/10 of a cycle, and interpolating the corresponding solution over the new mesh periodically. This way, mesh quality is kept within acceptable limits. This methodology proved to be inadequate when simulating cavitating flows, as the interpolation and later gradient reconstruction provide inaccurate solutions along several time steps after each interpolation. It was seen that continuity equation was not globally satisfied in those time steps. This happens because, when cavitation is present, continuity residuals become very sensitive to gas volume fraction changes, and the interpolation errors generate these changes, which are only corrected after simulating several more time steps. Consequently, this method makes it impossible to get an accurate solution along a full gearing cycle, as it will be seen in section 4.11.

Finally, an improved Laplacian smoothing method has been used. This method adjusts the location of each mesh vertex to the geometric center of its neighboring vertices. The computation of the node positions works as follows: the position of node i in time step $m+1$, $\vec{x}_i^{m+1}$ is computed as a weighted average between its position in time step m, $\vec{x}_i^m$, and the geometric center of its neighboring vertices, $\overline{\vec{x}_i^m}$,

$$\vec{x}_i^{m+1} = \vec{x}_i^m (1-\beta) + \overline{\vec{x}_i^m}\beta \tag{4.44}$$

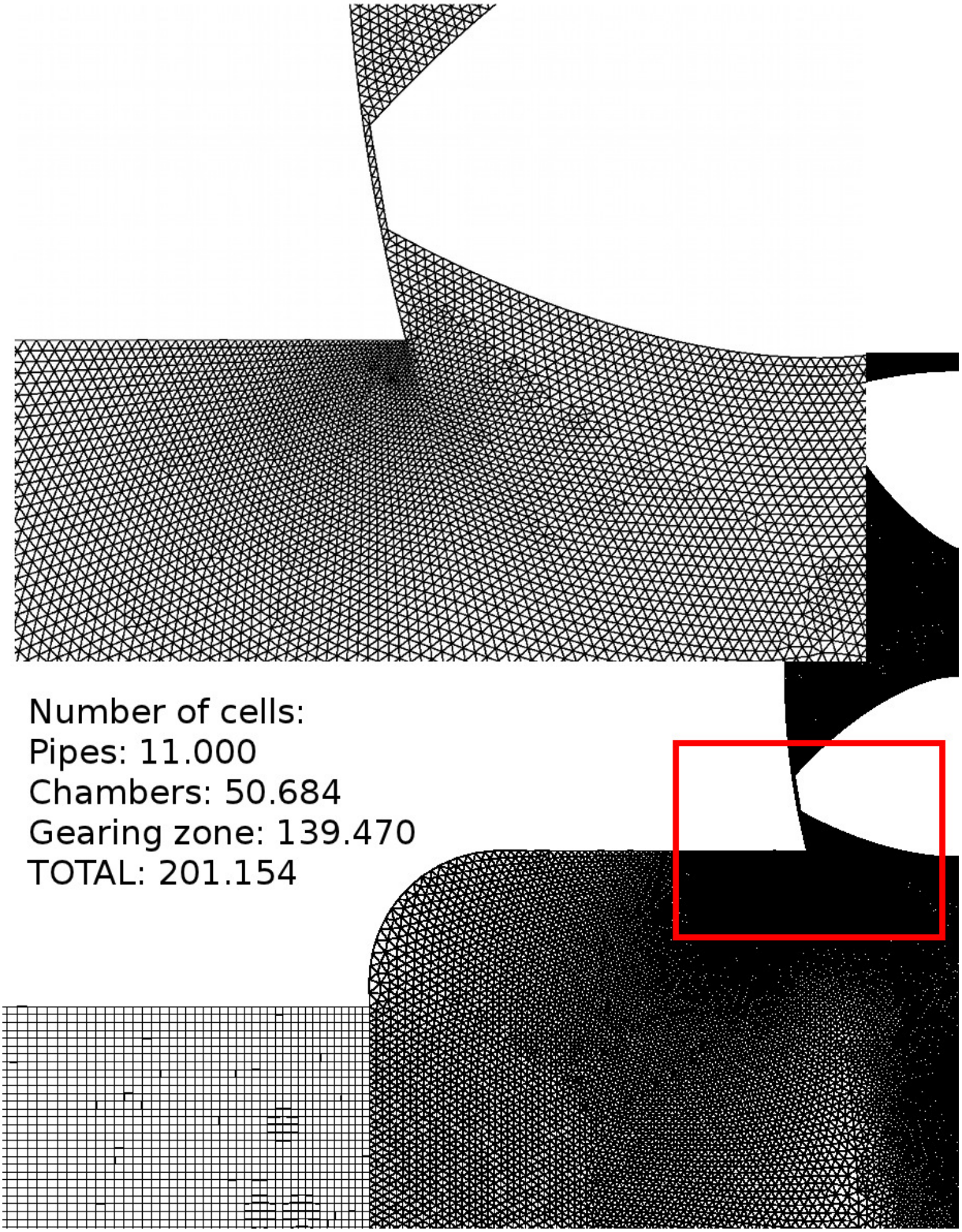

Figure 4.11: Inlet chamber of the reference pump.

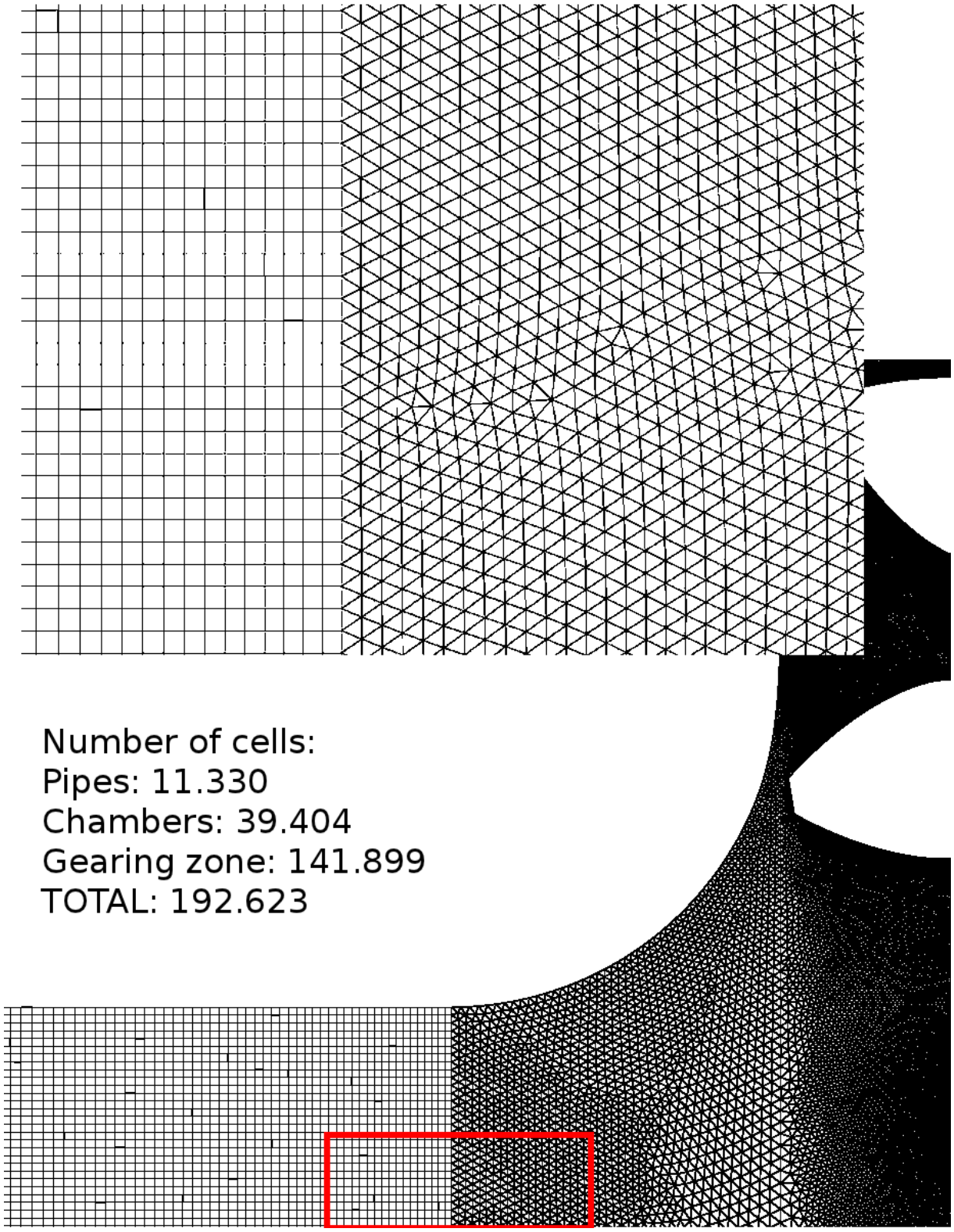

Figure 4.12: Inlet chamber of pump number 1.

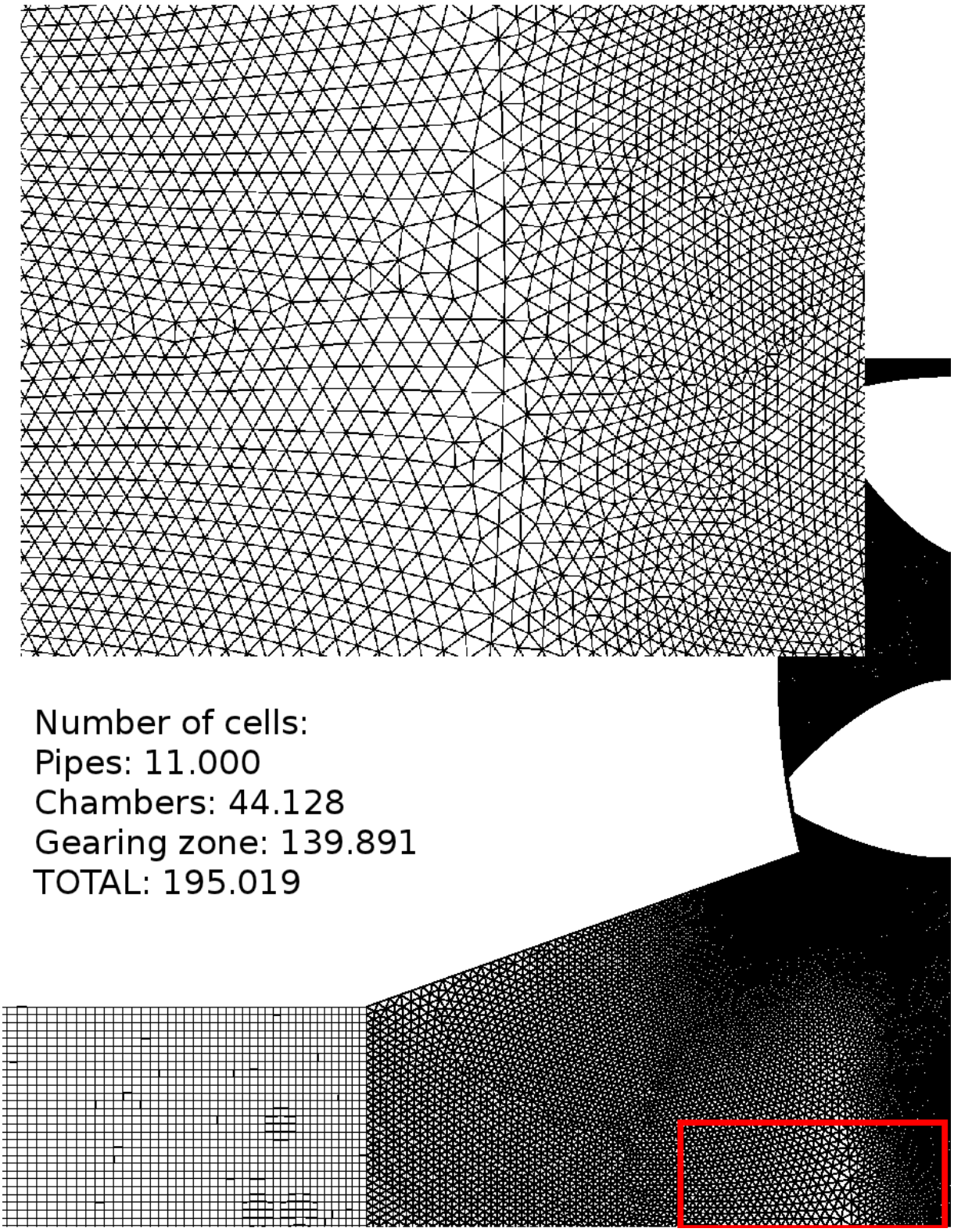

Figure 4.13: Inlet chamber of pump number 2.

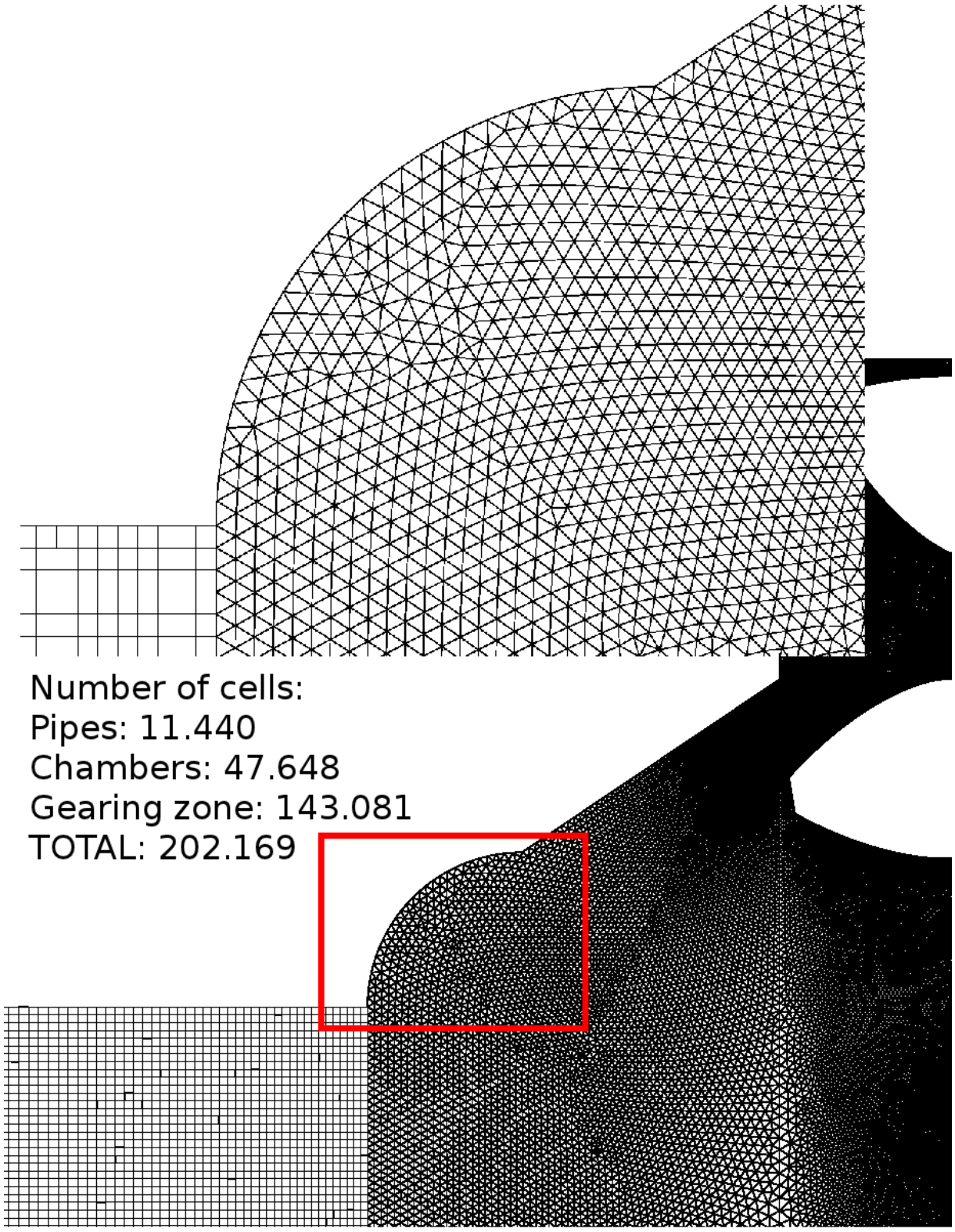

Figure 4.14: Inlet chamber of pump number 3.

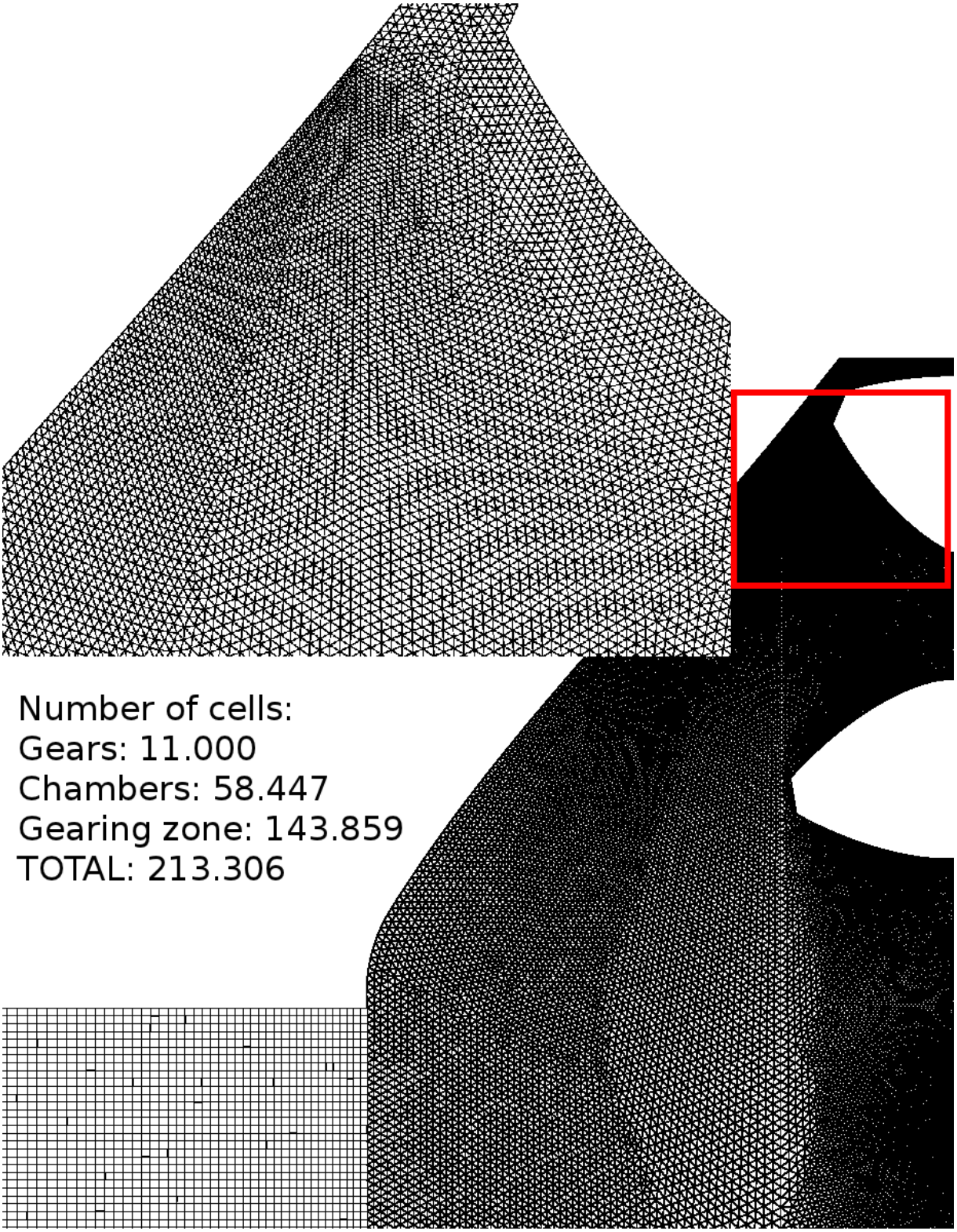

Figure 4.15: Inlet chamber of pump number 4.

Domain	Cell type	Structure	Mesh type
Inlet pipe	Quads	Structured	Stationary
Outlet pipe			
Inlet chamber	Tri	Unstructured	
Outlet chamber			
Gearing zone			Dynamic

Table 4.6: Mesh type in each computational domain.

where

$$\overline{\vec{x}_i^m} = \frac{\sum_j^{n_i} \vec{x}_j^m}{n_i} \tag{4.45}$$

The relaxation factor, β, that appears in equation 4.44 has been taken as $\beta = 0.5$.

It is computationally inexpensive as only a small number of vertices is involved in the determination of the new position of a vertex. It does not guarantee an improvement on mesh quality, since repositioning a vertex by Laplacian smoothing can result in poor quality elements. To overcome this problem, node position is updated only if the maximum distortion (measured through the equivolume skewness) of the cells surrounding node i is improved.

In addition to this, when a group of cells reach a fixed maximum skewness, a local remeshing of those cells takes place.

This smoothing process increases the cell-averaged equivolume skewness of the domain, and the local remeshing increases the total number of elements. Nevertheless, it has been seen that both effects mainly take place along the first three gearing cycles, and later on, both values are kept fairly constant. The equivolume skewness of a cell is defined as

$$Sk = \frac{S_e - S_c}{S_e} \tag{4.46}$$

where S_c is the cell surface and S_e is the surface of a equilateral triangle with the same circumradius.

A mesh sensibility study has been performed with the reference pump. Simulations were performed with a coarse grid, containing 77.236 cells in the gearing zone, and a fine one, containing 156.659 cells. It was shown that the remeshing algorithm quickly changes the number cells in each time step until an equilibrium, between the cells that are created and destroyed when remeshing, is reached, and the number of cells is kept stable after a few meshing cycles. The number of cells of both the initial coarse and fine grids stabilized around 140.000 cells. Therefore, both meshes become very similar and no appreciable difference is found. This interesting effect of coarsening or refining the mesh until a stable number of cells is reached is shown in figure 4.16. Finally, the fine mesh was selected, since, as its initial number of cells in the gearing zone is much closer to the stable value, the degree of refinement in the static zones is more appropriate (while, with the coarse mesh, after the refinement produced by the algorithm, the number of cells in the static zones resulted too low). This way, a much smoother interface, from the point of view of mesh regularity, is got between the static and the dynamic domains. This can be seen in figure 4.17 which represents the same detail of the fine and coarse mesh in the inlet chamber/gearing zone interface, after 10 gearing cycles.

In table 4.6 the type of mesh used in each domain is presented.

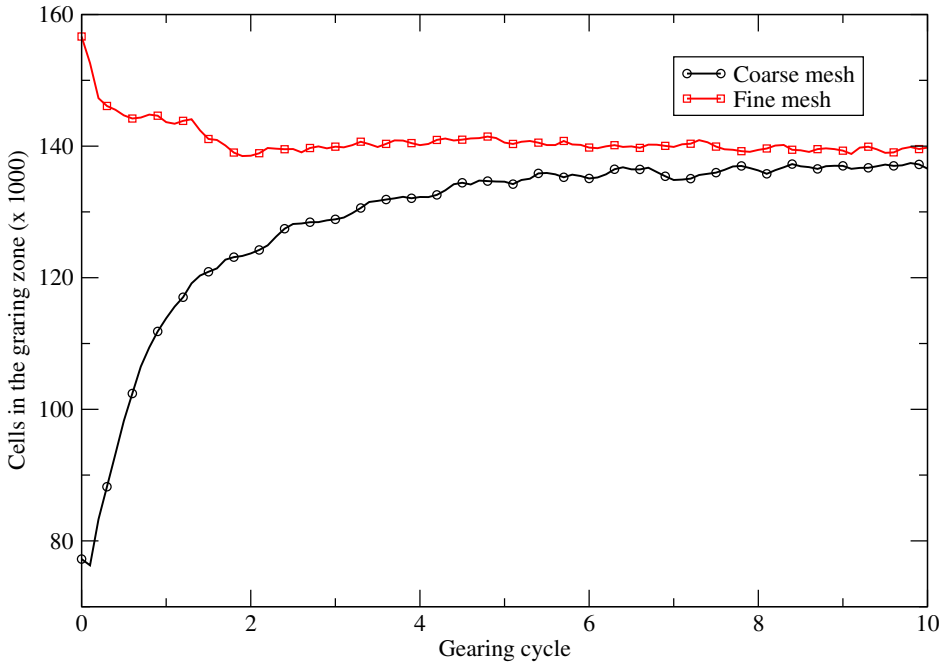

Figure 4.16: Cell number evolution in the gearing zone for the coarse and fine meshes.

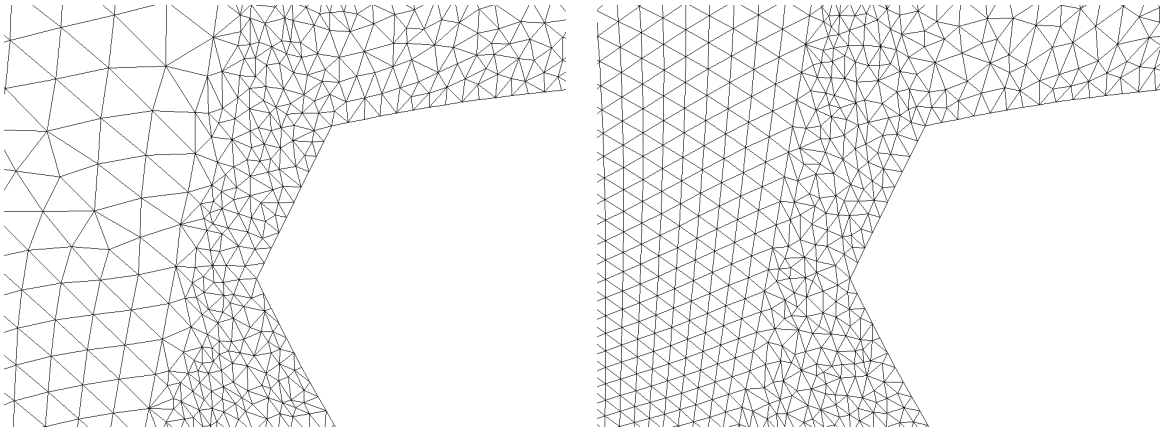

Figure 4.17: Mesh in a region of inlet chamber / gearing zone interface, after 10 gearing cycles. (a) Coarse mesh. (b) Fine mesh.

Domain	Reference pump	Pump 1	Pump 2	Pump 3	Pump 4
Pipes	11.000	11.330	11.000	11.440	11.000
Chambers	50.684	39.404	44.128	47.648	58.447
Gearing zone	139.470	141.889	139.891	143.081	143.859
TOTAL	201.154	192.623	195.019	202.169	213.306

Table 4.7: Number of cells in each region of each pump. The number of cells of the dynamic (gearing) zone refers to the average number of cells along the ninth gearing cycle.

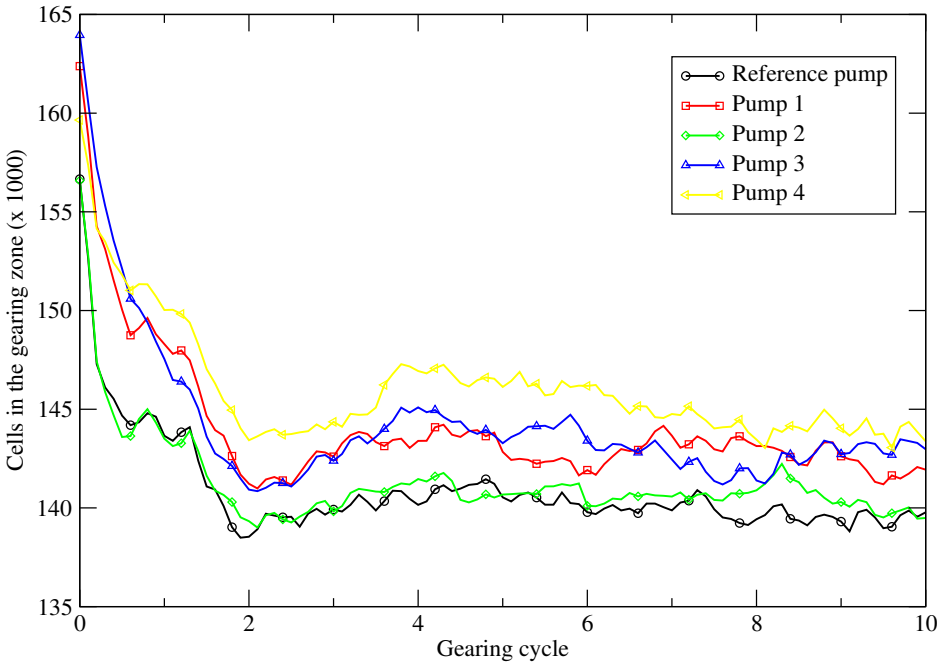

Figure 4.18: Cell number evolution for each pump.

In table 4.7 the number of cells of each zone, for each pump geometry, is presented. The number of cells of the gears zone should be understood as the average in the ninth gearing cycle.

In figure 4.18 the cell number evolution in the first 10 cycles for each mesh is shown.

Strasser [80] reported a maximum skewness of 0.16 with a similar mesh after 15 revolutions. In the present simulation, skewness grows until reaching approximately this same value, in the first gearing cycles, and then is fairly maintained. This happens with the fine mesh as well as with the coarse one, as shown in figure 4.19.

Finally, figure 4.20 shows a detail of the original mesh of the reference pump, and the same detail after 10 gearing cycles.

The mesh deformation process is identical in all simulations as the time step has been adjusted so that every gearing cycle becomes divided into 1000 time steps.

4.11 Simulation of the contact between gears

Due to the two-dimensional nature of the simulation, decompression slots cannot be simulated. Therefore, the simulations have been performed with unitary contact ratio, in order to avoid the

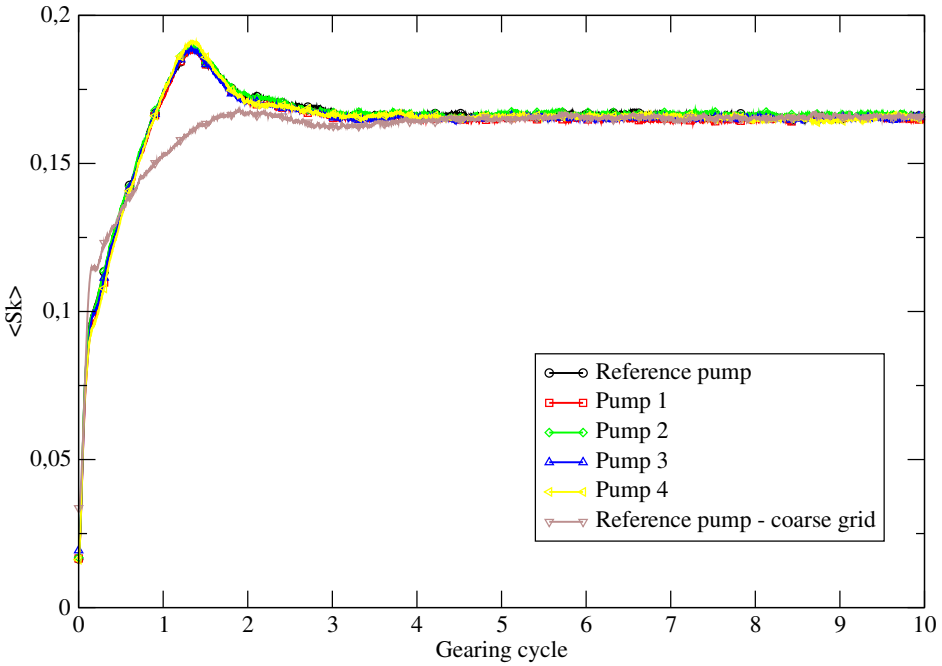

Figure 4.19: Average equivolume skewness evolution for each pump.

presence of fluid trapped into diminishing volumes, as this would rise the pressure of the involved fluid too much, leading to convergence problems. Therefore only one contact point has been simulated.

A geometrical simulation of the contact point would imply dynamic topological changes, by continuously connecting and disconnecting regions of the dynamic domain with time-depending area, thus complicating even more the mesh deformation process. Moreover, because of the tolerances of the grid, it is complicated to assure instantaneous tangential contact of the two moving boundaries.

The first approach was to use the technique employed by Castilla et al. [12]. Ten different grids were built. After simulating 1/10 of a cycle, the mesh was replaced by the next one and the solution was interpolated. Mesh was deformed by means of a spring-based method. This way, mesh quality was kept within acceptable limits. Contact point was simulated by placing a tiny wall in the small gap between gears at the contact point position. During mesh deformation this wall deforms with the mesh, and the contact point position separates slightly from the theoretical position. When mesh is substituted, contact point position is corrected. Figure 4.21 shows the wall position in the original mesh and in the deformed one after 1/10 of gearing cycle, just before substitution. Unlike what happened in the work by Castilla et al., in our simulations with cavitation, the errors associated to data interpolation, after mesh substitution, lead to unrealistic results along several time steps after each mesh replacement. Furthermore, the discontinuous movement of the contact point due to mesh replacement, which leaves a group of cells with high pressure on the suction side after correcting the contact point position, also affect negatively to the results. This can be seen in figure 4.22, which shows the outlet mass flow rate at 1000 rpm when using this method. In it, the effect of mesh substitution every 1/10 of a cycle can be clearly appreciated.

For this reason, a new approach has been chosen. The contact point has been simulated by continuously adjusting the dynamic viscosity of the liquid in a small region centered in the theoretical position of the contact point, which is just the center of this clearance. This approximation

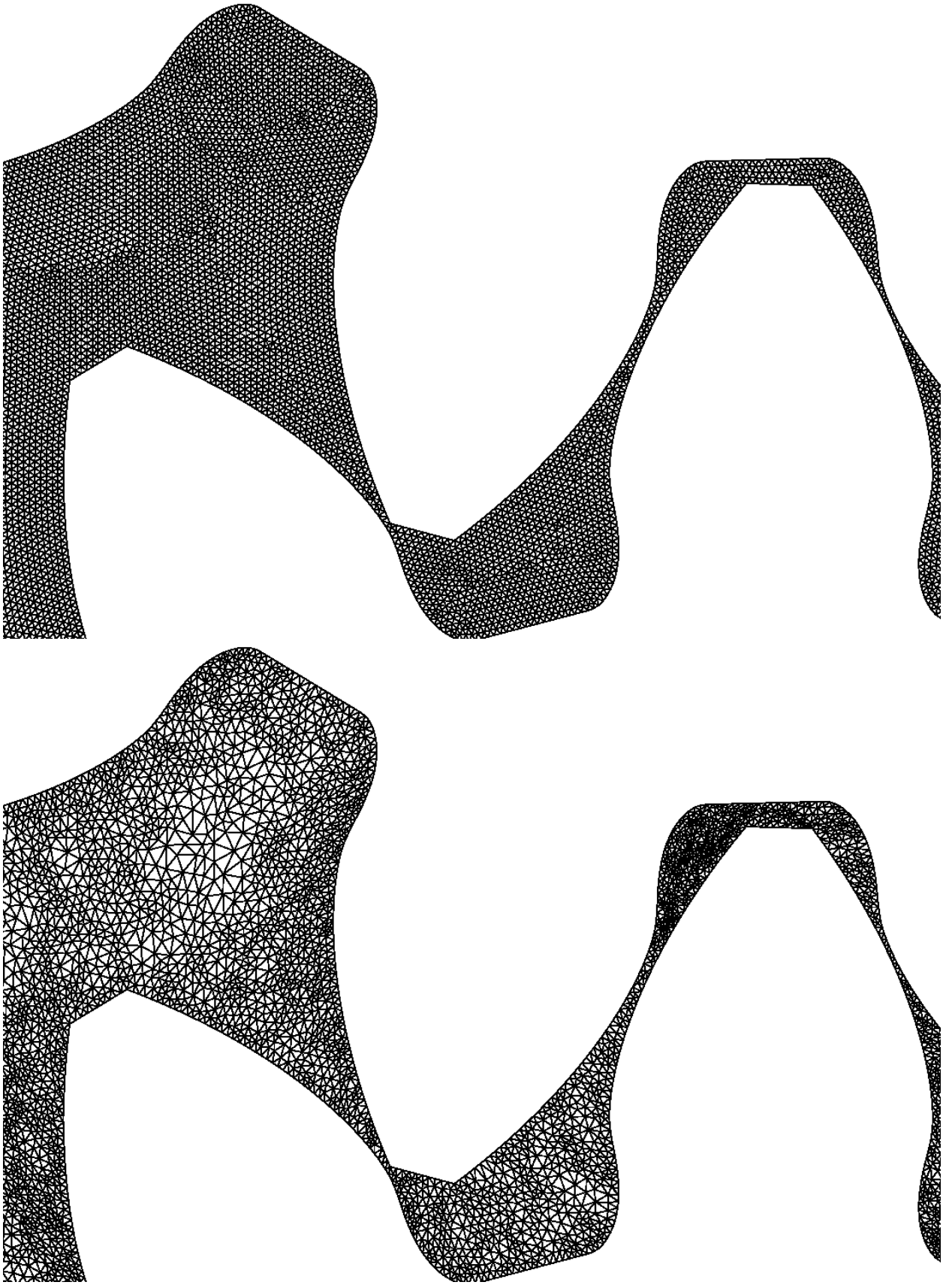

Figure 4.20: Detail of original and deformed mesh, after 10 gearing cycles.

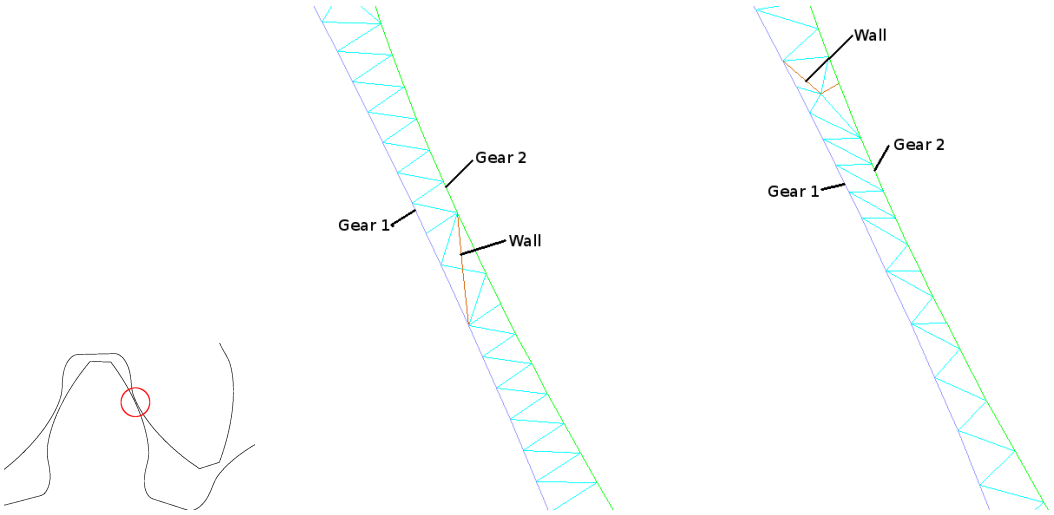

Figure 4.21: Contact point modeling by the use of a tiny wall in the gap between gears. (a) Original mesh. (b) Deformed mesh before replacement.

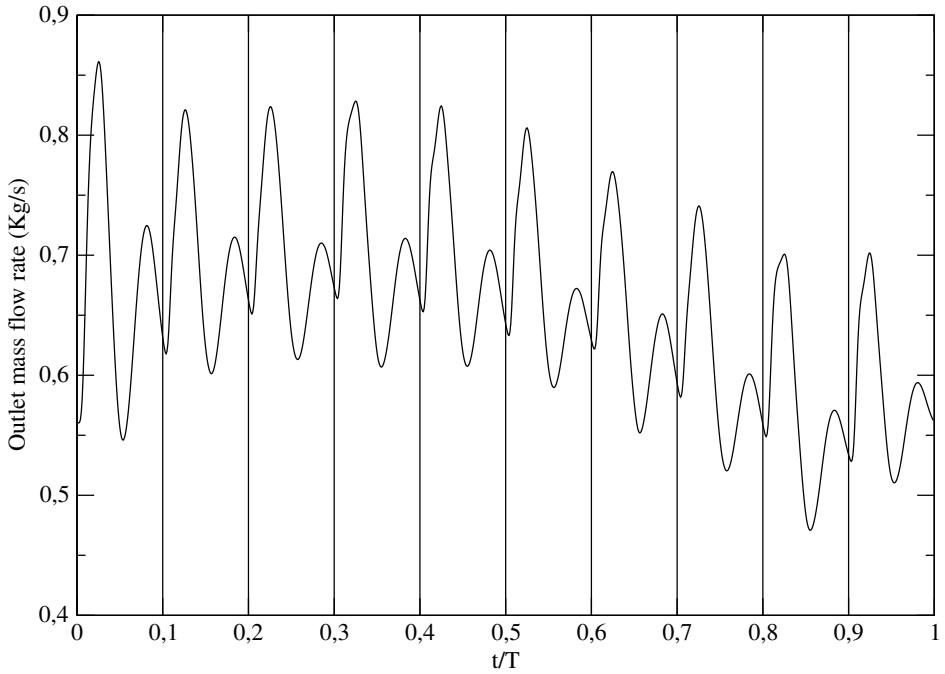

Figure 4.22: Outlet mass flow rate at 1000 rpm in a simulation with cavitation effects when mesh is replaced every 1/10 of a gearing cycle.

```
IF first iteration of time step
  FOR nodes in gear 1
    Get node position
    IF node position is within correct region
      FOR nodes in gear 2
        Get node position
        Get distance between nodes of each gear
        IF distance < min distance
          Get cell index of contact point
  Get position of cell centroid
  FOR all cells in domain
    Get cell centroid
    Mark the ones within a certain distance to contact point
    Reset viscosity to 0.028
  FOR all marked cells
    Set a linear variation of viscosity
```

Figure 4.23: Pseudo-code of contact point simulation through viscosity

is geometrically acceptable as the clearance is very small compared to the length of the gears ($d_{CP} = 74\,\mu$m). Assuring that, in each moment, the viscosity of the fluid is several thousand times higher than the real one only in this contact point region, the fluid acts as a solid spot, preventing oil to flow through the clearance, therefore simulating the effect of the contact point.

A user-defined function which is executed by the code prior to each time step has been programmed. Firstly, this function resets liquid's phase viscosity to its real value in all the domain, to undo the changes applied in previous time steps. Then, it searches for the nearest pair of points of both gears. This search is performed within a time-dependent prescribed region in which the desired contact point is known to be, in order to assure that the simulated contact point is the desired one. Afterwards, the cell that surrounds the middle point of the segment formed by these points is identified. In this cell, liquid's phase dynamic viscosity is changed to a very high value ($\mu_{max} = 100\,\text{Pa}\cdot\text{s}$). To avoid numerical problems related to strong gradients or checkerboard patterns, the cells within a small area around this position, within a radius $d_a = 8.5\,d_{CP}$ are also identified, and a distribution of viscosity, linear with the distance to the central cell, is imposed in them, in order to gradually return the viscosity to its normal value, μ_{oil}. Therefore, the viscosity in this area, as a function of the distance to the theoretical contact point position, d, takes the form:

$$\mu\,(r) = \mu_{max} - \frac{\mu_{max} - \mu_{oil}}{d_a} d \tag{4.47}$$

The pseudo-code of this process is shown in figure 4.23, and the code is presented, along with all other used-defined functions employed, in appendix C.

The modified viscosity in the contact point region is shown in figure 4.24.

We have checked that this way mass flux through the contact point position remains null at every time step.

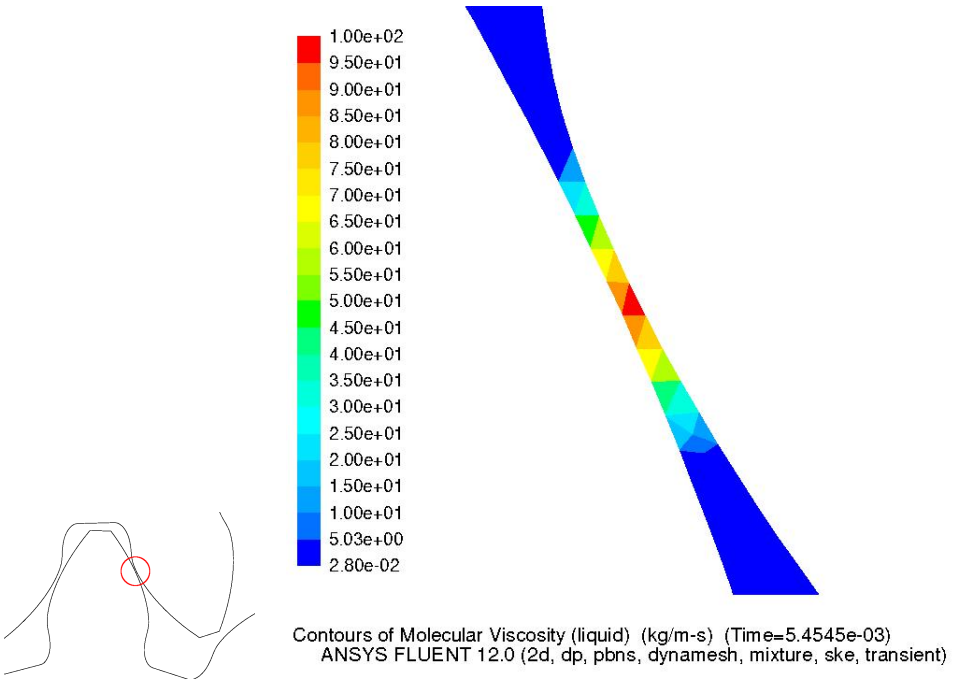

Figure 4.24: Dynamic viscosity imposed in the contact point position in order to simulate its effect.

4.12 Boundary conditions

As it was explained in the previous chapter, the pressure ripple in the suction pipe is small compared to that in the pressure pipe (although it can seriously affect the performance due to aeration). For this reason, pressure can be set constant in the inlet, but not in the outlet, for which an impedance will be simulated through the boundary condition.

Reference inlet pressure has been set to 0 bar.

An average pressure jump of 10 bar has been imposed. In order to allow for pressure fluctuations, the outlet boundary condition imposes that instantaneous pressure jump is proportional to outlet dynamic pressure through a loss factor, $k_{L,out}$, that represents the impedance of the discharge circuit:

$$k_{L,out} = \frac{\Delta p}{\frac{1}{2}\rho v_{out}^2} \tag{4.48}$$

being $\Delta p = 10\,\text{bar}$ the time-averaged pressure jump (this unrealistic low value has been selected because of experimental limitations and will be justified in section 4.13), and v_{out} the time-averaged outlet velocity, which is estimated from the theoretical volumetric capacity of the pump, the rotational speed, and the outlet area.

Inlet and outlet turbulent boundary conditions have been fixed through the hydraulic diameter and the turbulent intensity (defined as the ratio of the root-mean-square of the velocity fluctuations to the mean flow velocity).

The hydraulic diameter is defined as

$$D_h = \frac{4A}{P} \tag{4.49}$$

being A the inlet or outlet area and P its perimeter. With the dimensions of our inlet and outlet pipes this yields an inlet hydraulic diameter of $D_{h\,in} = 25.7\,\text{mm}$ and an outlet one of $D_{h\,out} = 21.2\,\text{mm}$.

rpm	Δt (μs)	v_{in} (m/s)	$Re_{D_h in}$	I_{in} (%)	v_{out} (m/s)	$Re_{D_h out}$	I_{out} (%)	$k_{L,out}$
500	10.909	0.524	421	7.518	0.699	462	7.430	4631.8
1000	5.455	1.048	842	6.894	1.397	924	6.814	1158.0
1500	3.636	1.572	1263	6.553	2.096	1387	6.477	514.6
2000	2.727	2.096	1684	6.322	2.794	1849	6.248	289.5
2500	2.182	2.619	2105	6.148	3.493	2311	6.076	185.3
3000	1.818	3.143	2526	6.009	4.191	2773	5.939	128.7

Table 4.8: Numerical parameters and boundary conditions employed for each simulated rotational velocity.

According to the code's documentation, in fully-developed duct flows an approximate relationship between the integral length scale, l, and the physical size of the duct is $l = 0.07D_h$.

The turbulence intensity at the core of a fully-developed duct flow can be estimated from the following formula derived from an empirical correlation for pipe flows:

$$I = 0.16Re_{D_h}^{-1/8} \tag{4.50}$$

Being Re_{D_h} the Reynolds number based on the hydraulic diameter,

$$Re_{D_h} = \frac{vD_h}{\nu} \tag{4.51}$$

where time-averaged inlet or outlet velocity, v, is again estimated from the theoretical volumetric capacity of the pump, the rotational speed, and the area.

In all solid surfaces, no-slip velocity condition has been imposed.

Finally, table 4.8 shows the main numerical parameters and boundary conditions employed for each rotational velocity that has been simulated: the numerical time step, the inlet and outlet velocities, the Reynolds numbers and turbulence intensities, and the outlet loss factor.

4.13 Limitations of the numerical simulations

Due to the nature of our numerical simulations, some leakage factors that contribute to reduce the volumetric efficiency of the real pump cannot be properly simulated, or even not be simulated at all. Since our interest is centered in the influence of cavitation, this fact should not stop us from performing the simulations, as long as our simplifications do not significantly modify the cavitating behavior of the pump, which is the case. Results will become useful after comparison against analogous single-phase simulations which will not include cavitation effects.

Therefore, it should be noted that the values of volumetric efficiency that will be obtained do not represent the actual volumetric efficiency of the real three-dimensional pump, but will nevertheless be useful from the point of view of understanding the complex phenomenology involved in the flow that takes place inside it. These simplifications, which are outlined in figure 4.25 have been presented along this chapter, and are summarized below:

- In the real pump, inlet and outlet pipes are circular. This provokes a three-dimensional expan-

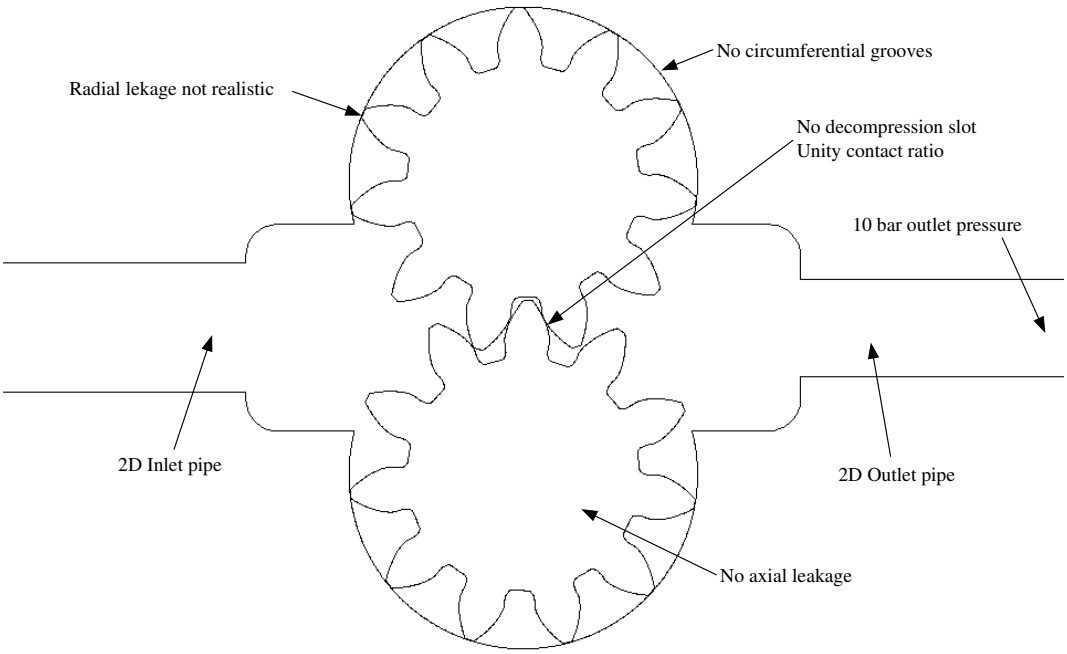

Figure 4.25: Simplifications made in the numerical simulations.

sion of the flow when it enters into the suction chamber and a three-dimensional compression when it leaves the outlet chamber. In our numerical simulations, pipes are modeled as two-dimensional. Therefore the flow predicted near the entrance of the inlet chamber and near the exit of the outlet chamber is not supposed to correctly reproduce the one that would be expected in the middle plane of the real pump. This should not affect greatly the cavitating behavior of the simulated pump, as cavitation takes place mainly in the suction side of the meshing region, which is far from the entrance to the inlet chamber, so the effect of the three-dimensional expansion should have been almost completely damped. This will be proved in chapter 5 after an experimental validation.

- As the simulation is two-dimensional, the axial leakage through the clearance between the gears and the compensation plates cannot be simulated. This leakage represents an important contribution to the volumetric efficiency, and therefore this effect itself would make the volumetric efficiencies obtained to be far from the ones of the real pump. From the point of view of cavitation, the effect of this leakage flow is negligible.

- The effect of the pressure relief grooves cannot be predicted with a two-dimensional simulation. This has forced us to perform the numerical simulations using unity contact ratio, in order to avoid the high pressure rise that would take place in the volume trapped between the two contact points. This affects the flow pulsation pattern and the leakages through the trapped volume, but does not affect greatly the cavitation behavior of the pump. The way in which the contact point has been simulated was presented in section 4.11.

- It is also impossible to take into account the effect of the circumferential grooves of the

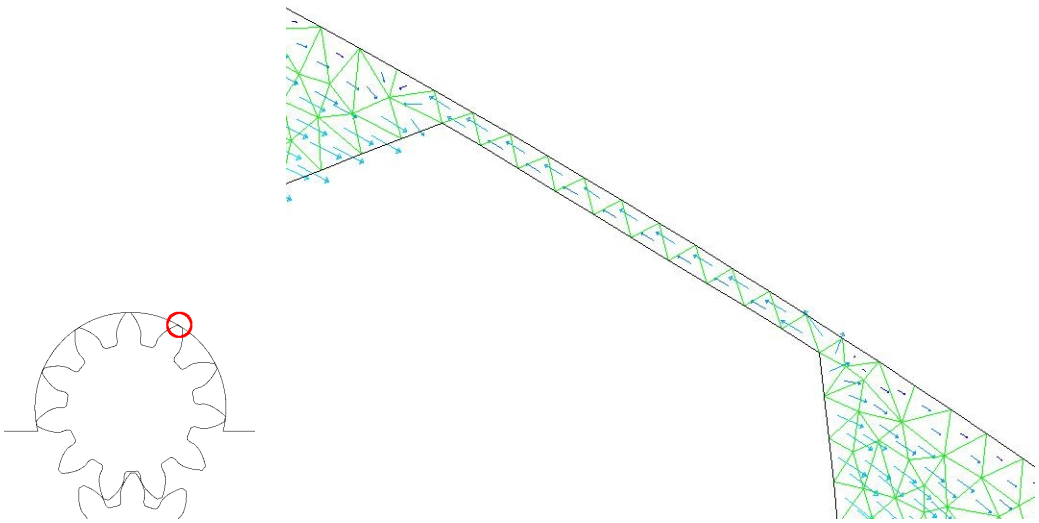

Figure 4.26: Mesh and velocity field in the gear tip region.

compensation plate in a two-dimensional simulation. The lack of circumferential grooves causes the inter-teeth volumes to be communicated only through the gear's tip clearances. Taking into account that gear eccentricity is not simmulated, this provides an equal pressure jump among each teeth that is facing the casing. This pressure distribution is given in equation 3.11 and implies that, in our simulations, radial leakage will take place equally at all those gear tips. Once more, from the point of view of cavitation, this effect does not make a big difference.

- In a real pump, gears are subjected to radial forces that cause the axis to displace within the horizontal plane and describe a certain orbit. In our numerical model, a constant clearance of 77 μm is left between the gear tips and the casing. This distance, apart from being constant, is considerably higher that the ones generally found in real pumps. This big value is justified taking into account that the mesh between the housing and the gear tip is only one cell high, being the cells in these zones among the smaller ones of the whole domain. Reducing the clearance height would also lead to reducing the size of the smaller cells, thus drastically increasing the Courant number of the simulation and therefore the computational time required, which is already very long. Furthermore, in order to properly simulate the flow in this passage, a finer mesh in that zone would be required. A detail of the grid in this zones and the velocity field simulated is shown in figure 4.26. The leakage flow, going from the higher to the lower pressure inter-teeth volume can be seen, although its numerical value may not be exact due to the locally poor mesh resolution.

  In addition, a relatively big clearance of constant height will cause the volumetric efficiencies obtained in the simulations to drop far below the high values of those of the real pump at 10 bar, shown in figure 3.12. Once more, the gear tip leakage shouldn't affect greatly the cavitating behavior, as long as the cavitation remains near the gears meshing zone, and does not propagate between the gears and the housing (which only at very high operating velocities may occur).

  A simple way of avoiding the gear tip losses is by simulating the effect of sealing the clearance by imposing viscosity changes, in a similar way as it has been done to simulate the contact

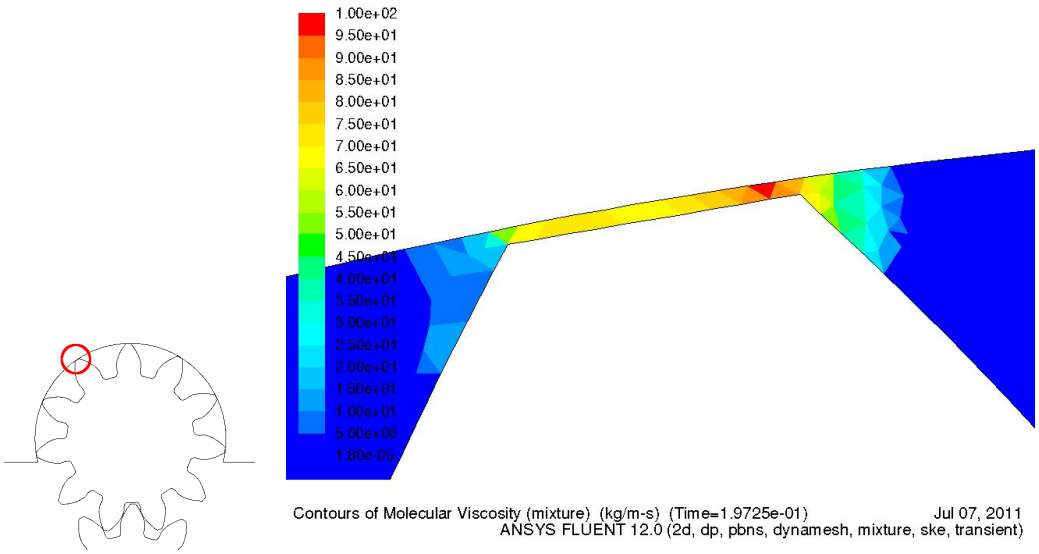

Figure 4.27: Dynamic viscosity imposed in the gear tip clearance in order to avoid leakage.

point between gears. This has been programmed and some results using this technique will also be presented in the chapter 6. The user-defined functions to do that are shown in appendix C and the viscosity in the clearance zone is shown in figure 4.27.

- The operating conditions of the simulations, with a pressure jump of only 10 bar, are far from the typical operating conditions for these type of pumps (which are around 100 bar). This value has been selected for two reasons: Firstly, because of the big clearances between the gear tips and the casing, which amplify the effect of the pressure jump on the gear tip leakage, thus decreasing considerably the volumetric efficiency. By keeping a low pressure jump, we avoid having an excessive leakage, which would mask the effect of cavitation on volumetric efficiency. Secondly, because results will be validated against experiments that require the pump casing to be made in methacrylate, which is not able to resist higher operating pressures. Despite cavitation should not be much affected by the pressure jump, since it takes place in the suction side, a simulation at 100 bar pressure jump has also been performed in order to study any possible influence.

Chapter 5

Experimental analysis of the suction chamber of an external gear pump by Time-Resolved Particle Image Velocimetry

5.1 Introduction

In this chapter, the technique of Time-Resolved Particle Image Velocimetry (TRPIV) will be presented and applied in order to experimentally characterize the unsteady velocity field in the middle plane of the suction chamber of our reference gear pump. This flow field will be used for a qualitative validation of the numerical simulations that have been presented in the previous chapter and which results will be discussed in the following chapter.

In section 4.13, the simplifications involved in the numerical simulations were summarized. The purpose of the TRPIV experiments is to assure that, despite these simplifications, the numerical two-dimensional flow field at the inlet chamber is sufficiently similar to the one of the middle plane of the real gear pump. If we can assure a sufficiently realistic flow field without cavitation, we can be confident that, with an appropriate cavitation model, the results of the simulation will be useful enough to understand the effect of cavitation on the volumetric efficiency of the pump. As TRPIV in multiphase flows present some extra difficulties, validation will be done at a low rotational speed (500 rpm), where cavitation is absent or negligible.

The reason for choosing Particle Image Velocimetry (PIV) as the experimental technique is that it has gained significant popularity in the past decade, becoming the most extended velocimetry technique when a instantaneous velocity field, instead of the velocity at one point, is to be measured. Furthermore, it has already been successfully applied in the suction chamber of external gear pumps.

In this chapter, the principles of PIV will be explained. The state of the art of PIV techniques applied to the characterization of the flow field of external gear pumps will be presented. The experimental setup used for our experiments will be described, as well as the experimental procedure and the

algorithms used to process the images. Finally, the results will be presented and compared to those obtained in the two-dimensional numerical simulations, and conclusions will be given.

5.2 Principles of Particle Image Velocimetry

The development of Particle Image Velocimetry (PIV), a non-intrusive measurement technique which allows for capturing velocity information of the whole flow field in fractions of a second by observation of particles immersed in the fluid, has begun in the eighties of the last century. While the method of adding particles or objects to a fluid in order to observe its flow is likely to have been used from time to time through the ages, no sustained application of the method is known. The first to use particles to study fluids in a more systematic manner was Ludwig Prandtl, who did so in the early 20th Century.

In the last two decades, a rapid development of cameras, lasers, optics and software has contributed to extend it more and more, to the point that it has become one of the most widely spread experimental techniques for measuring flow velocity. Very especially, improvements in high speed digital photography, with CCD sensors capable of taking pairs of images within a few hundred nanoseconds has made PIV so popular. Extensive information about the fast development of PIV in the last twenty years can be found in Adrian [40].

Unlike other velocimetry techniques, as hot wire anemometry or laser Doppler velocimetry, it has the ability to capture the instantaneous 2D 2-component flow field instead of the the flow field in a single point. Some variants of PIV, which use a multiple camera arrangement, can analyze 2D 3-component (Stereo-PIV) or even 3D 3-component (Tomographic-PIV) velocity fields. With cameras capable of taking picture frames in continuous mode with a high repetition rate (this is generally achieved with CMOS sensors), unsteady velocity fields can also be characterized.

Another advantage of PIV is its high accuracy, since particle displacement between two images can typically be accurate down to 10% of one pixel on the image plane.

Small tracer particles have to be added to the flow. These particles have to be illuminated in a plane at least twice within a short time interval. To do this, a laser light sheet should be created. The light scattered by the particles has to be recorded on a sequence of frames. The displacement of the particle images between the light pulses has to be determined through evaluation of the PIV recordings. Laser pulses should be synchronized with the camera trigger using synchronizer. The time delay between pulses, which depends on the mean flow velocity and the magnification at imaging, together with the determined displacement of the particles, gives the velocity field. The image post-processing required to obtain the particle displacements is based in cross-correlation between pairs of images. Figure 5.1 briefly sketches a typical setup for PIV recording in a gear pump.

The typical sub-systems involved in the experimental setup of a PIV system will be now briefly described. Detailed information can be founded in Raffel et al. [59].

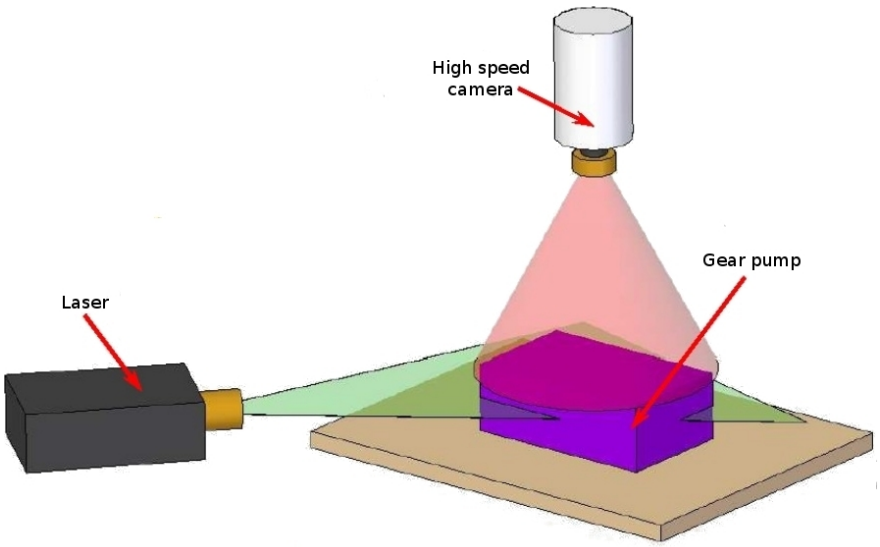

Figure 5.1: Experimental arrangement for Particle Image Velocimetry.

5.2.1 Seeding particles

A good election of tracer particles and its seeding mechanism is of major importance in any PIV setup. The main aspects to consider when selecting them will be analyzed.

Proper tracer particles must be small enough to follow (trace) fluid motion and should not alter fluid or flow properties. The tracing ability and the dispersion characteristics depends on the size and shape of the particles and the densities of particles and fluid flow. The particle density should be as close as possible to the one of the flow, in order to minimize the effect of buoyancy forces over them.

If we assume spherical particles in a viscous fluid at very low Reynolds numbers, Stokes's law gives us the drag force over the particle of diameter D_p

$$\vec{F}_D = 3\pi D_p \mu \vec{v} \tag{5.1}$$

where D_p is the particle diameter.

Assuming no vertical acceleration of the fluid, the vertical velocity of the particle, w_p, that appears due to gravitational forces is

$$w_p = D_p^2 \frac{\rho_f - \rho_p}{18\mu} g \tag{5.2}$$

being ρ_f and ρ_p the fluid and particle densities.

Analogously, the velocity lag of the particle within a flow with uniform acceleration $\vec{a}$ is given by

$$\vec{v}_{lag} = \vec{v}_p - \vec{v} = D_p^2 \frac{\rho_f - \rho_p}{18\mu} \vec{a} \tag{5.3}$$

Therefore, the tendency of particles to attain velocity equilibrium with the fluid linearly decreases with the difference of densities and with the square of the particle diameter.

If the fluid acceleration is not constant or Stokes drag does not apply, the equations of the particle motion become more difficult to solve. Nevertheless, this results give a good qualitative idea of the

influence of particle size and densities in the ability of particles to track the fluid velocity.

Moreover, getting an optimum particle concentration uniformly distributed along the flow domain is critical to the success of obtaining the velocity field. It is very important to make sure that all regions of the fluid domain get seeded with enough number of particles. For doing this, the seeding source must be placed cleverly, so that the particles mix with the flow well. The tracking capability of particles also affects uniformity, as the ones with finite inertia are known to disperse non-uniformly in a turbulent flow.

In order to be able to apply the cross-correlation to obtain the displacement vectors from the images, particle concentration should be within two limits. Beyond these limits, velocity fields may be obtained through the use of other techniques, yielding different experimental methods. Depending on particle concentration, three methods can be distinguished:

- Particle tracking velocimetry (PTV): it is possible to distinguish individual particles in an image as well as to identify the same particle in two different images.
- Particle image velocimetry (PIV): it is possible to distinguish individual particles in an image but no to identify the same particle in two different images.
- Laser speckle velocimetry (LSV): it is not possible to distinguish individual particles in an image.

Moreover, an excessive particle concentration or size may lead to interaction between particles, which would affect their tracking ability.

When turbulence wants to be measured, additional considerations regarding the particle size should be taken into account. In this case, seeding particles need to be smaller than the smallest turbulence scale if one wants to identify all the structures in the vicinity of the flow. The smallest fluid length scale is called the Kolmogorov length scale, and it is related to the size of the smallest eddy. The Stokes number, St, indicates the degree of coupling between the particle phase and the fluid. It is defined as the ratio of the particle response time to the Kolmogorov time scale:

$$St = \frac{\tau_p}{\tau_k} \tag{5.4}$$

being τ_p the particle response time, which is obtained from the integration of equation 5.3 the relaxation time of the particle motion in a uniform accelerated fluid, and τ_k the Kolmogorov time scale:

$$\tau_p = D_p^2 \frac{\rho_f - \rho_p}{18\mu} \tag{5.5}$$

$$\tau_k = \left(\frac{\nu}{\varepsilon}\right)^{1/2} \tag{5.6}$$

If $St \to 0$, we can assume that the particles behave like tracers, while, when $St \to \infty$, the particles are completely unresponsive to the fluid flow.

At the same time, particles must be large enough to be visible by the camera. As laser sheet leads to a low energy density, particle scattering efficiency is important. The scattering cross section C_s is

defined as the ratio of the total scattered power P_s, to the laser intensity I_0 incident on the particle.

$$C_s = \frac{I_s}{I_0} \tag{5.7}$$

It is often more effective and economical to increase the image intensity by properly choosing the scattering particles than by increasing the laser power. The scattering cross section depends on the ratio of the refractive index of the particles to that of the surrounding medium, the ratio of the particle size to the laser wavelength, the particle shape and orientation, and also on polarization and observation angle (the camera should be, if possible, orientated in the direction towards which this intensity is maximum).

For spherical particles with diameters larger than the wavelength of the incident light λ, Mie's scattering theory can be applied [87]. The Mie scattering can be characterized by the normalized diameter, q, defined by

$$q = \frac{\pi D_p}{\lambda} \tag{5.8}$$

Figure 5.2 shows the light scattering diagrams of 1 μm and 10 μm oil particles in air. It can be seen that scattering quickly increases with particle size (the average intensity roughly increases with q^2), and that forward scatter (in the 180° direction) is maximum. Therefore it would be preferable to record in forward scatter, but, due to the limited depth of field, recording at 90° is most often used. Lets call I_{s180} the forward scatter intensity and I_{s90} the 90° scatter intensity (which usually interests us). A more detailed parametric analysis of particle scattering characteristics throw the following conclusions:

- The ratio I_{s180}/I_{s90} decreases with increasing normalized diameter q, with values roughly in the range 10^{-1}-10^{-3} for scattering particles useful in PIV.

- The resulting intensity of the scattered light for a given light sheet intensity will depend on the combined influences of C_s and I_{s180}/I_{s90}, which exhibit opposing tendencies with increasing particle size. In general, larger particles will still give stronger signals.

- The scattering efficiency, and the ratio I_{s180}/I_{s90}, strongly increases with the ratio of the refractive index of the particles to that of the fluid. Hence particles in air provides stronger 90° scattering than in water.

In conclusion, for a given refractive index and laser wavelength, larger particles are able to scatter more light. Therefore an optimum particle size should represent a compromise between the tracing and the scattering characteristics of the particles.

In addition, a uniform particle size is desirable in order to avoid excessive intensity from larger particles and background noise from the smaller ones. Particles that naturally exist in the flow seldom meet the above requirements. Hence, in PIV applications, it is often necessary to seed the flow with a chosen tracer particle. The particles are either premixed with the whole fluid (e.g. stirred) or released in situ by a seeding source.

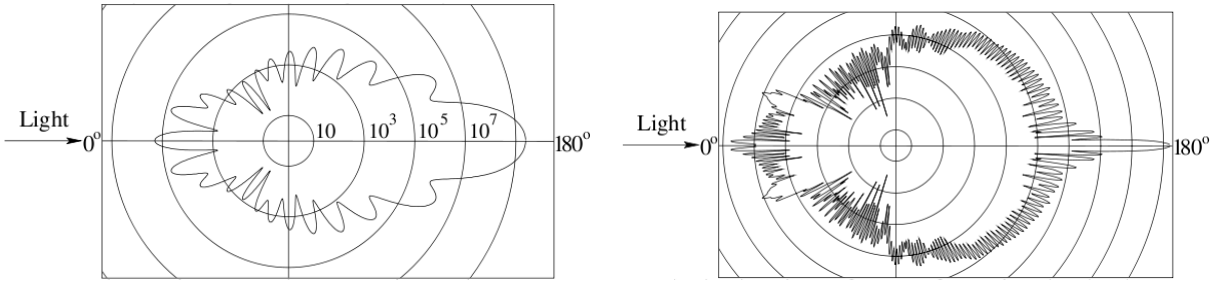

(a) (b)

Figure 5.2: Light scattering by an oil particle in air. (a) 1 μm particle, (b) 10 μm particle. Intensity scales are the same. Adapted from Raffel et al. [59].

5.2.2 Laser and light sheet

Lasers are widely used in PIV, because of their ability to emit monochromatic light with high energy density, illuminating and recording the tracer particles without chromatic aberrations. Furthermore, laser light can be easily guided through mirrors or optical fiber through the test region, and then be bundled, through a system of lenses, into thin light sheets.

Many types of laser can be employed in PIV. An explanation of the physical principles of lasers, together with a detailed description of the light source requirements for PIV, the main parts of a PIV laser system, and information about the most commonly used lasers, can be found in Raffel et al. [59].

Flash lamp pumped Neodym-YAG lasers (Nd:YAG) are the most common solid-state systems for conventional PIV applications where high pulse energies at moderate repetition rates are required. In these lasers, the beam is generated by Nd^{3+} ions within YAG (yttrium-aluminum-garnet, $Y_3Al_5O_{12}$) crystal bars. At standard operating temperatures, this laser only emits the strongest wavelength, 1064 nm (infrared). For safety reasons, the laser beam is filtered to isolate the 532 nm harmonics (this is green light, the only harmonic which can be seen by the naked eye). They are optically pumped using a flash-tube or laser diodes. As all solid-state lasers, they can be pumped with white light (most commonly through xenon lamps). Nd:YAG lasers have a high amplification and good mechanical and thermal properties.

Nd:YAG laser operates in both pulsed and continuous mode. Pulsed Nd:YAG lasers are typically operated in the so called Q-switching mode: an optical switch is inserted in the laser cavity waiting for a maximum population inversion in the neodymium ions before it opens. Then the light wave can run through the cavity, depopulating the excited laser medium at maximum population inversion. Q-switches normally consist on a polarizer and a Pockels cell, which changes the quality of the optical resonator depending on its voltage. In this Q-switched mode, high energy is achieved in short duration pulses. For this reason, the Q-switched mode is of higher interest in PIV, as high energy per pulse is needed to illuminate the whole plane of interest sufficiently so that a picture of the particles can be taken in very short time fractions. A typical Nd:YAG laser for PIV concentrates from 20 to 400 mJ energy per pulse in 4 to 15 ns duration pulses. Typical repetition rate is around 10 Hz. For TRPIV, this repetition rate may be, in many cases, too low, but for standard PIV it is not the repetition rate but the separation between two pulses within a pair what is critical. To get this double pulse, double oscillator arrangements are commonly employed. This way, two

independent beams are generated in different oscillators, and are guided through an arrangement of mirrors through a single output beam aperture.

The essential element for generating a thin light sheet of high intensity from a circular beam is a cylindrical lens, which expands the laser into a plane. Nevertheless, additional elements are usually necessary in order to obtain a high quality light sheet. A diverging lens is often situated before the cylindrical lens to avoid focal lines and focal points, as otherwise the air may become ionized, or dust particles might be burnt affecting the beam quality. At least one additional spherical lens has to be used for focusing the light into an appropriate thickness. The minimum thickness is on the order of the wavelength of the laser light and occurs at the focal point of the spherical lens. This is the ideal location to place the analysis area of the experiment. More complex arrangements can be set. A detailed description of some of the most common ones can be found in Raffel et al. [59].

5.2.3 Camera

To perform PIV analysis on the flow, two exposures of laser light are required upon the camera from the flow. In the case of TRPIV, each pair of pulses is used to evaluate an instantaneous velocity field, so the camera should be continuously triggered in order to temporally resolve the flow. Originally, with the inability of cameras to capture multiple frames at high speeds, both exposures were captured on the same frame and this single frame was used to determine the flow, through auto-correlation. Faster digital cameras using CCD (charge coupled device) or CMOS (complementary metal-oxide-semiconductor) sensors were developed since then. This has allowed the development of double-triggered and high speed cameras, so that each exposure can be isolated on its own frame for a more accurate cross-correlation analysis. An in-depth comparison of each type of sensor can be found in Hain et al. [30].

A double-exposure camera is capable of recording two frames within a very short inter-frame period. After recording, both frames are transferred to the host system and the camera is prepared for the next image pair. Inter-frame times of below 500 ns are possible, but inter-pair times can be quite substantial, in the order of 0.1–0.5 s, depending on the image transfer system. Consequently, double-exposure cameras are well suited for high speed repeatable flow events, or when only an instantaneous flow field is desired. This cameras use interline transfer CCD sensors, in which the information recorded on each pixel in the first frame of the pair is almost immediately transfered into adjoining storage sites, being later transfered both frames to the camera's internal memory.

For TRPIV, a high speed video system should be used, which can usually record up to 5000 fps at full sensor resolution and much higher rates at reduced image sizes. This is generally achieved through CMOS sensors.

5.2.4 Mathematical Background of Statistical PIV Evaluation

Statistical evaluation of the images is based in dividing the image in small regions called interrogation areas (IA) and cross-correlating each of them with its correspondent in the next image. This results in the most probable displacement vector for that particular particle pattern. Displacement can be estimated with sub-pixel accuracy by appropriately fitting the peak shape. The process is repeated

for all interrogation areas of the image pair resulting in a complete vector diagram of the flow studied. Finally, erroneous vectors should be identified and appropriately corrected. Extensive information can be found in Raffel et al. [59]. Nevertheless, the basics will be here briefly exposed.

Firstly, images are divided into square regions of size NxN pixels, the so-called interrogation areas (IA). They should be selected containing a relatively small number of particles. In principle, an area containing only one single particle would be ideal, but it is hard to find that single same particle back in the second image, especially in a densely seeded flow as for PIV recordings. The probability for a good analysis result is highest when the interrogation area contains about 8-10 particle images (Keane and Adrian [47]).

The mean value of velocity in an IA at time t is calculated by cross-correlating the image intensities of that IA at time t and $t + \Delta t$. The cross-correlation function results:

$$R_c(i,j) = \sum_{k=-M}^{M} \sum_{l=-M}^{M} I_g(k,l)\, I'_g(i+k, j+l) \tag{5.9}$$

The functions I_g and I'_g represent the grey intensity values as extracted from the first and second image respectively, where I_g has the IA size, NxN and I'_g has a bigger size $(2M+N)\,\mathrm{x}\,(2M+N)$. Essentially the function I_g is linearly 'shifted' around in the sample I'_g without extending over its edges. By applying this operation a correlation plane of size $(2M+1)\,\mathrm{x}\,(2M+1)$ is formed. This is shown graphically in figure 5.3, being $N = 4$ and $M = 2$. For shift values at which the sample particle images align with each other, the sum of the products of pixel intensities will be larger than elsewhere, resulting in a high cross-correlation value at this position. After normalization, the new image is a visible representation of the two-dimensional probability-density function of the level of matching between the two sub-images. The highest value in the correlation plane can then be used as a direct estimate of the particle image displacement.

The alternative to calculating the cross-correlation directly using equation 5.9 is to take advantage of the correlation theorem which states that the cross-correlation of two functions is equivalent to a complex conjugate multiplication of their Fourier transforms. Using the fast Fourier transform (FFT) reduces the number of operations required from $O\left[N^2\right]$ to $O\left[N \log_2 N\right]$. Then the product is transformed back to the real domain using an inverse FFT. Fourier analysis needs interrogation area formats of a power of 2. Both forms of cross-correlating are shown in figure 5.4.

All $R(i,j)$ values apart from the one representing the displacement vector form the noise of the correlation function. This occurs because the displaced pattern in the second image is not identical to the pattern of the first one. The main reasons for this are:

- Background noise: which can be attenuated by filtering the images before performing the cross-correlation analysis.
- Out of plane displacements: a particle can escape from the laser sheet between the first and the second frame due to three-dimensional effects. Therefore, we must have enough thickness of the laser sheet and assure that the flow is highly two-dimensional in the analyzed plane.
- Local low or high illumination close to the image border, or crippled interrogation areas next to the image border. Several boundary treatment methods have been developed to overcome

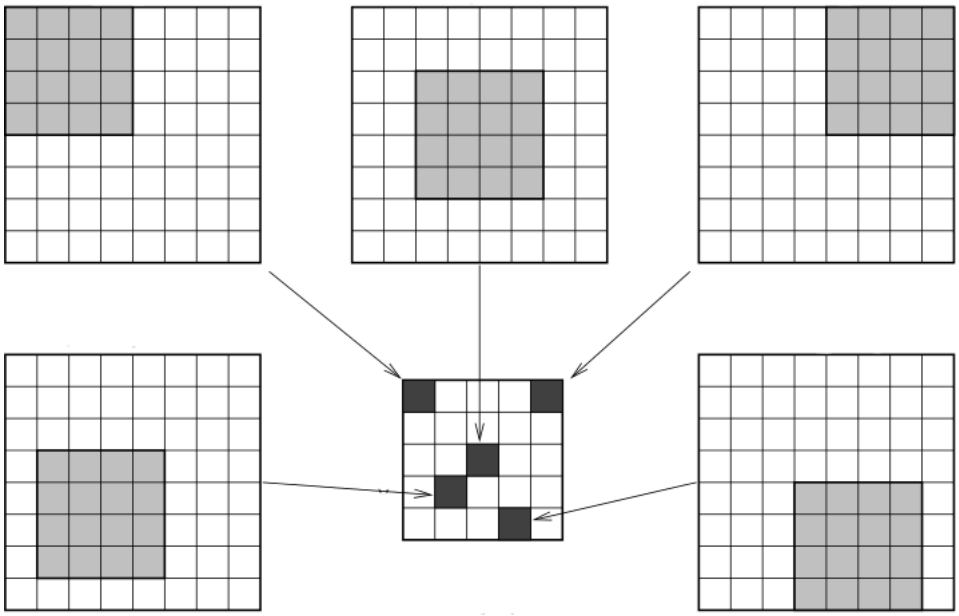

Figure 5.3: Cross correlation technique. Each pixel in the correlation plane is calculated from the sum of the products of all individual overlapping pixels from the interrogation area from image 1 (light grey) and the sub-image from image 2 (white). Adapted from Raffel et al. [59].

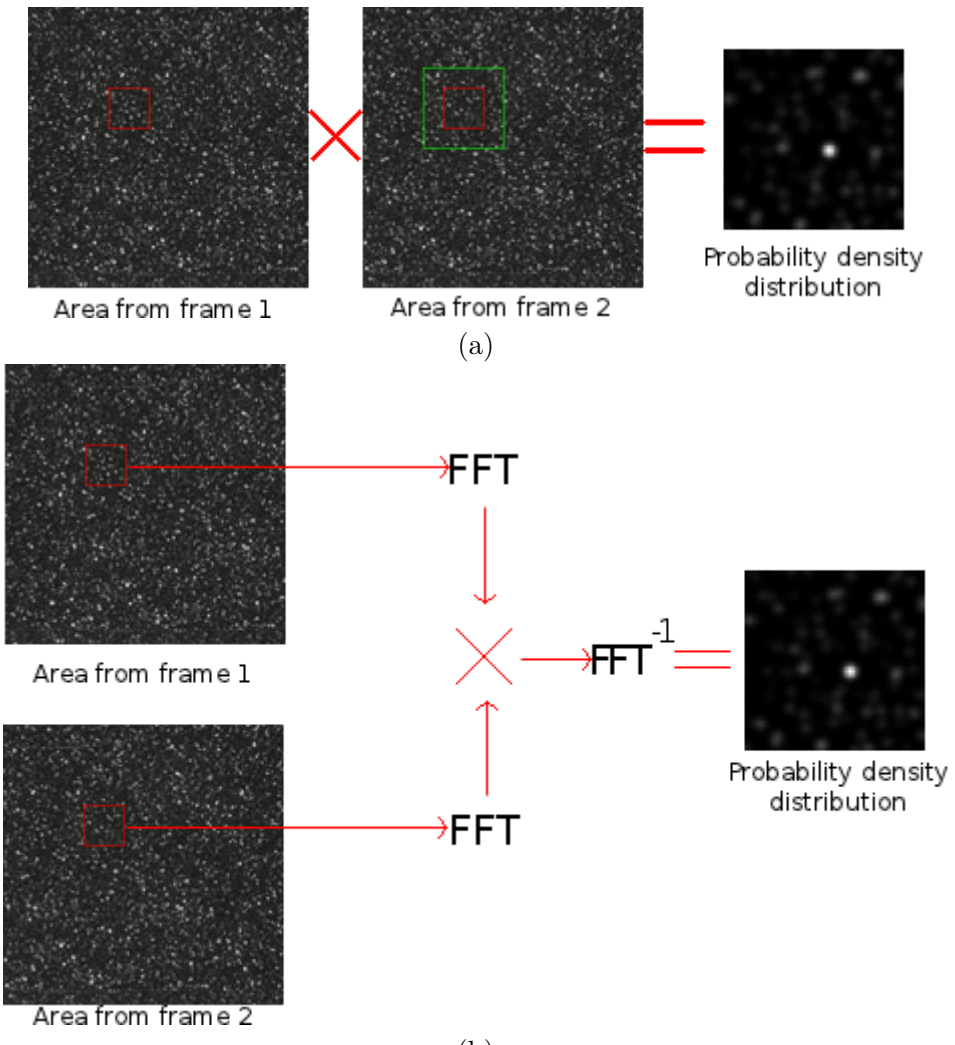

Figure 5.4: (a) Cross-correlation by convolution filtering. (b) Cross-correlation by Fourier analysis.

this issue (e.g. Usera el al. [66]).

- In-plane displacements: If the interrogation window is not large enough, particles may shift to another IA between two consecutive frames. The highest measurable velocity is constrained by particles traveling further than the size of the interrogation area within the time Δt. As a rule of thumb, the maximum displacement should be no larger than 1/4 of the IA side, so that no more that 25% of the particles are loss through in-plane displacements.

- It should be noted that the cross-correlation method inherently recovers linear shifts only. No rotations or deformations can be recovered by this first order method. IA should therefore be small enough to avoid big velocity gradients within them. As a rule of thumb, the maximum difference between the displacements of any pair of particles in an IA should be no larger that 5% of the IA side. For this reason, it is common to find spurious vectors in the vortex cores.

The high intensity peak in the result image has to be located to know the particle displacement. Because the peak is usually larger than one pixel, all pixel information of the peak can be used to calculate the peak position, and obtain sub-pixel accuracy. Methods used so far are centroiding, center of gravity B/W, center of gravity weighed to grey value, Gaussian curve fitting, and parabolic curve fitting. Centroiding, in which all the pixels of the peak outline are used to calculate it's center, works well for larger peaks but is not very accurate for small ones, and the same is true for calculation of the center of gravity B/W (after thresholding). Calculation of the center of gravity weighed to grey value, in which lighter pixels contribute more than darker ones, gives good and accurate results for average size peaks (3 pixels diameter) and even better for larger peaks. Gaussian and parabolic curve fitting are accurate on average size peaks (3 pixels) but are less reliable on smaller or larger peaks. Depending on the peak size and the method used, accuracies of less than one tenth of a pixel are possible.

The process of selection of an interrogation area, cross-correlation, peak-finding, and calculation of the velocity vector, is repeated over the whole image, resulting in a complete vector representation of the flow field. To obtain more velocity information out of the images, adjacent interrogation areas are often overlapping. Any overlap is in principle possible, but one should keep in mind that a high degree of overlap also means that the same information is sampled multiple times, resulting in over-sampling. An overlap of 50% is recommendable because of a good balance between information density and over-sampling (Hinsch [46]).

When excessive noise is present, the maximum correlation value can occur at a position different from that representing the true displacement, yielding an spurious velocity vector. These vectors usually stand out clearly with respect to the surrounding vectors due to their very different orientation and magnitude. This enables relatively easy recognition to the observer as well as to any automated validation routine. Automated validation routines usually compare every vector with the surrounding one's and use statistical parameters (as the standard deviation or a histogram distribution function) to discriminate between correct and erroneous vectors. Once the spurious vectors are recognized, they should be replaced by new vectors, which should represent the local flow velocity as close as possible.

5.3 State of the art

The turbulent flow in the suction chamber of a gear pump has been observed with TRPIV by Castilla et al. [13] and by Ertürk et al. [20]. As far as the author knows, these are the only experimental studies of the flow inside a gear pump by using a non-intrusive experimental technique. Our experiments are based in those ones, but include two major improvements:

In the aforementioned experiments, small air bubbles were used as tracing particles, instead of small solid particles or water drops, as usually reported in most PIV experiments. This was necessary as the metal-metal contact between teeth can lead to material erosion and, eventually, damage the transparent casing of the gear pump, while the use of water drops can produce oxidation of the steel gears. Nevertheless, some disadvantages of using water drops were reported: (a) the size of the bubble is not easily controllable, (b) the density ratio is very large, and (c) the presence of gas in a liquid can reduce the velocity of sound and hence make the flow become compressible at relatively low velocity. After carefully analyzing the effects of these disadvantages, they concluded that, if the size of the bubbles is smaller than 0.3 mm and the quantity does not exceed the number of 15 to 20 bubbles per interrogation area, the effects of buoyancy and compressibility are not important. In our study, air bubbles have been substituted by solid particles especially designed to fulfill the requirements of our experiments.

Moreover, in the aforementioned experiments the pump was driven by an oleohydraulic motor, which was in turn driven by an hydraulic power-pack. This scheme had the disadvantage that it was not possible to select a certain rotational speed with precision, neither to keep it stable. In our study these problems are solved as the gear pump is driven by an electric motor which is connected to a variable frequency drive.

Finally, in the experiments by Castilla et al. [13], the camera was used as master time-base and an output synchronization signal generated by it was used to trigger the laser. Both in their experiments and in the ones performed by Wernet [91], using the same laser as ours, it was reported that the behavior of the output signal was rather unstable. Therefore an external synchronizer has been used for our study.

5.4 Experimental arrangement

The reference pump presented in section 4.3 has been analyzed with TRPIV in a test bench. In this section, the experimental setup and the characteristics of each of its parts will be explained. A general view of the test bench is shown in figure 5.5.

For the experimental tests, the reference gear pump has been modified by substituting its casing with one completely made in methacrylate in order to allow light to pass through the suction chamber and film the flow in the interior. The dimensions and properties of the hydraulic fluid have already been presented in table 4.1. The test pump is shown in figure 5.6.

The suction chamber is illuminated from its right side. In order to allow illumination from this side, a relaxation chamber, also made in methacrylate, has been placed upstream the inlet pipe. This way, the fluid firstly enters the relaxation chamber by two opposite lateral pipes that are connected to the elevated tank, which does not interfere with the light sheet, as it can be seen in figure 5.5.

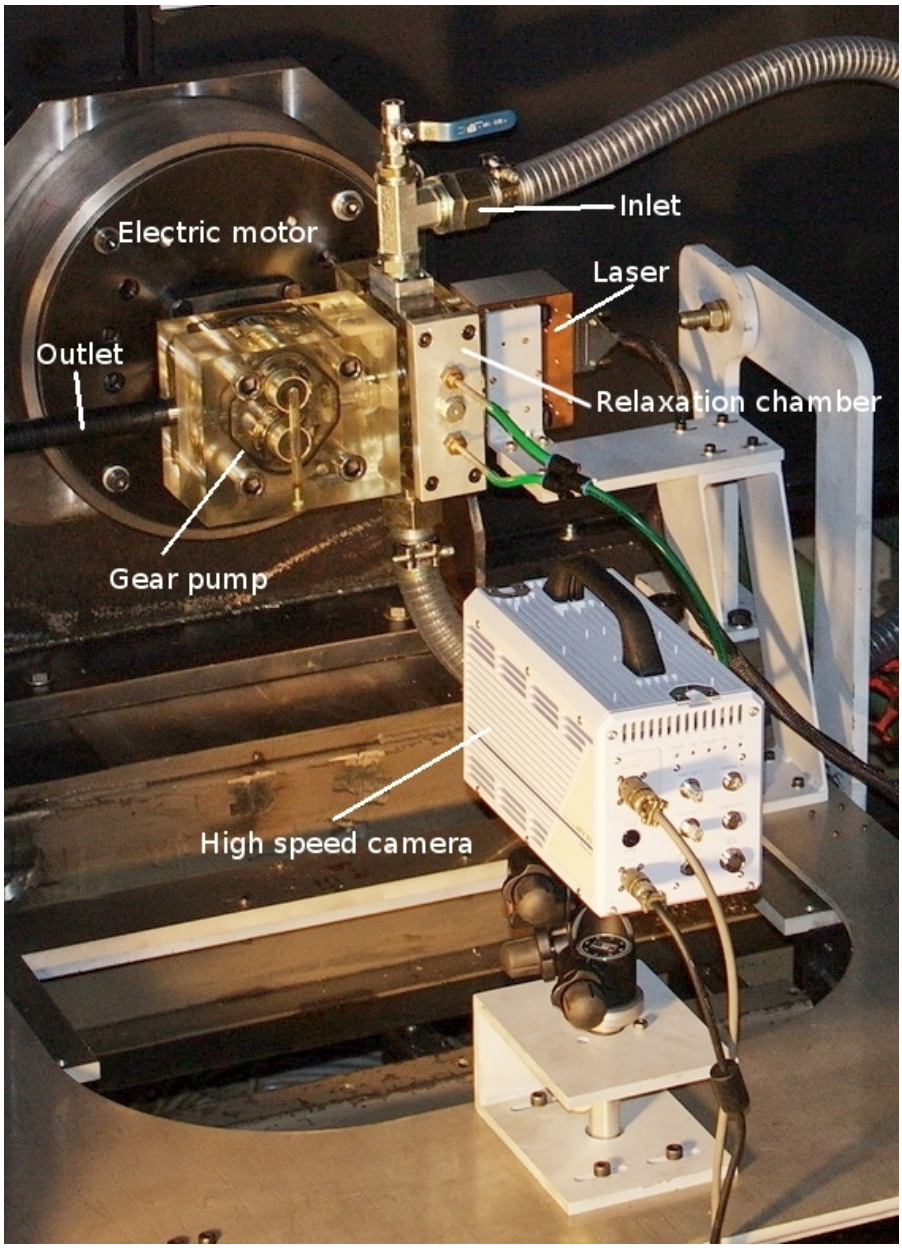

Figure 5.5: Test bench and experimental arrangement.

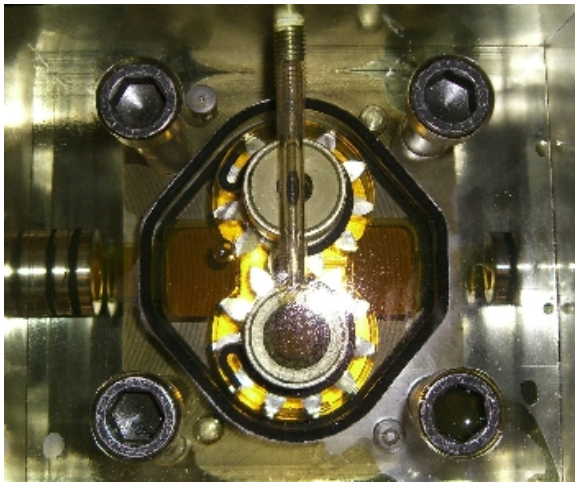

Figure 5.6: Reference pump with methacrylate casing to be tested.

Center wavelength	805 ± 5 nm
Max. output peak power	250 W
Max. operation current	280 A
Pulse length	10 - 100 μs
Max. Pulse energy	2.5 mJ at 10 μs
	25 mJ at 100 μs
Max Frequency	5 kHz
Laser beam dimensions	12 x 0.7 mm at output

Table 5.1: Specifications of Monocrom LU80250-FSAC laser.

5.4.1 Tracing particles

A new kind of solid tracer particles has been designed and produced at the Rovira i Virgili University of Tarragona by Ertürk. These particles, which do not damage the gear teeth, are spherical and can absorb the working fluid, matching with its density. They are within $5-10\,\mu$m in diameter and have very good light scattering characteristics. Further information is not yet available as they are under patent process.

5.4.2 Camera

The high velocity digital camera used in the experiments was the Photron Ultima APX-RS. It uses a 10-bit monochrome CMOS sensor with 17.5 μm square pixels in a 1024 x 1024 pixel arrangement. Its has a global electronic shutter which gives exposure times from 16.7 ms to 2 μs independent of frame rate and overexposure protection. This camera can record up to 3000 frames per second at full resolution and 250.000 at limited resolution and has a buffer memory of 2 Gb.

5.4.3 Laser

We used for the experiments the laser Monocrom LU80250-FSAC. It is a 800 nm (infrared) laser which main features are given in table 5.1. It is a diode laser, which means that the active medium is a semiconductor similar to that found in a light-emitting diode, that is powered by injected electric current. Laser diodes are arranged in a bar, which makes it possible to produce the necessary laser sheet with optical elements that are encapsulated in the laser box. Therefore, the laser box is directly placed in front of the gear pump without the need for additional optical elements between laser and pump. The fact of being infrared requires us to be extremely careful when performing the experiments, as the laser beam cannot be seen but it can produce serious damage if reflected towards the eyes. Apart from wearing IR protection glasses, the whole bench is surrounded by black walls and a black curtain, which is closed before turning on the laser.

5.4.4 GPIV software

For image processing, the GPIV software has been used. GPIV is an open source software for recording and analyzing images obtained from PIV measurements, which runs under the GNU/Linux environment. All software is written in ANSI-C and it is issued under the GNU General Public

Rotational speed	500 rpm
Pressure jump	1.1 bar
Frequency rate	3000 fps
Temporal resolution (Δt)	1/3000
Resolution	1024 x 1024 pixels
Image resolution	61.54 (μm/pixel)
Camera optics	Sigma 105 mm f/2.8
Extension tubes	34 mm
Laser output power	95 W
Laser pulse length	20 μs
Number of images recorded	2048
Time recorded	0.68 s
Revolutions recorded	5.69
Gearing period (T_g)	0.01091 s
Reynolds number based on gears diameter	4755

Table 5.2: Experimental parameters employed in the TRPIV test.

License. It has been developed by Gerber van der Graaf [88] and it has been successfully used, among others, by Castilla et al. [13] for studying the turbulent flow in the suction chamber of an external gear pump, Cadalfach et al. [11] for the study of convection in large tunnels and Guiseppe et al. [26] for the study of air cavities. The code can be downloaded from the software's web site[1].

Although the software is capable recording and pre-processing the images, we have limited its use to the image interrogation process. Data acquisition has been done with the camera's own control software, while pre and post processing has been done with Matlab.

5.5 Experimental procedure and image processing technique

Experimental measurements have been taken at the LABSON facilities at the Universitat Politècnica de Catalunya in Terrassa in collaboration with the Rovira i Virgili University of Tarragona.

Measurements have been taken in the middle-plane of the pump working at 500 rpm an 1.1 bar, with a frame rate of 3000 frames per second. This frame rate assures the sufficient temporal resolution to capture the large scales of the flow, in which we are interested. This happens because it yields a time step between measurements smaller than the Taylor microscale of the flow, as shown by Usera et al. [66] and Ertürk et al. [20].

The main features of the experimental setup are shown in table 5.2.

When performing TRPIV in flows with a cyclic behavior, a ensemble phase-lock average is needed to substantially reduce the errors. Therefore, it is necessary to carefully identify all images that are exactly in the same phase.

Taking a look to table 5.2 it can be seen that a gearing period does not include an integer number of inter-frame periods ($T_g = 32.73\Delta t$). Nevertheless, after 11 gearing periods (this is, a full revolution) we can again find pictures which are in the same phase as the first one ($11T_g = 360\Delta t$). Therefore, a gearing cycle is characterized with 33 frames, and frame number n is in phase with frame number

[1] http://gpiv.sourceforge.net

```
for i=1:34;
    for j=0:360:1800;
        filename=strcat('exp_22_500rpm_',num2str(i+j),'.png');
        if j==0;
            matref=imread(filename);
        elseif j==360;
            m2=imread(filename);
            corr=m2-matref;
            imwrite(corr,strcat('exp_22_500rpm_corr_',num2str(i+j),'.png'));
            corr=matref-m2;
            imwrite(corr,strcat('exp_22_500rpm_corr_',num2str(i),'.png'));
        else
            m2=imread(filename);
            corr=m2-matref;
            imwrite(corr,strcat('exp_22_500rpm_corr_',num2str(i+j),'.png'));
        end
    end
end
```

Figure 5.7: Matlab code employed for image filtering.

$n+360m$ being m any integer. We find out that with the total number of frames recorded, we have six different gearing cycles with in-phase information, so each final instantaneous velocity field will be calculated as the average of six different velocity fields.

In order to eliminate undesired light reflections and to homogenize the median illumination, the images are preprocessed before using them to calculate the velocities. Common background can be easily eliminated by subtracting the illumination of one image to the one of another in-phase image. This has been done with a Matlab script that is shown in figure 5.7. Figure 5.8 shows an original image and the same image after applying the clean-up mask process. It can be seen that the filtered image shows a homogeneous illumination at the region of interest, and the high intensity reflections near the gears disappear.

Once the clean-up mask has been applied to all images, the region of interest is selected. As we are only interested in validating the numerical simulations, results in the near-wall regions or in the gearing zone are not needed. Otherwise, a dynamic mask should have been placed, following the moving boundaries, and some boundary treatment method should have been used, as explained in subsection 5.2.4. The region of interest, of size 520 x 520 pixels, in which the interrogation scheme has been applied, is marked in figure 5.9. The velocity vectors obtained from interrogation windows that fully or partially intersect with the solid boundaries has been discarded.

The interrogation windows size, NxN, should be such that N is a power of 2, in order to be able to apply the FFT. Also, as stated in subsection 5.2.4, the sizes must be chosen in such a way that the particle displacements remain within 1/4th of the interrogation area's in order to keep the in-plane errors at a minimum. Taking these factors into account, as well as the maximum estimated velocities and the temporal resolution, we decided to use 32 x 32 pixel interrogation areas.

Instead of performing a straight-forward estimation, iterative interrogation methods are often applied to increase the accuracy of the method. This means that a first calculation of the displacement vector is used as an estimator. The Image Deformation iterative method (Scarano [73]) has been

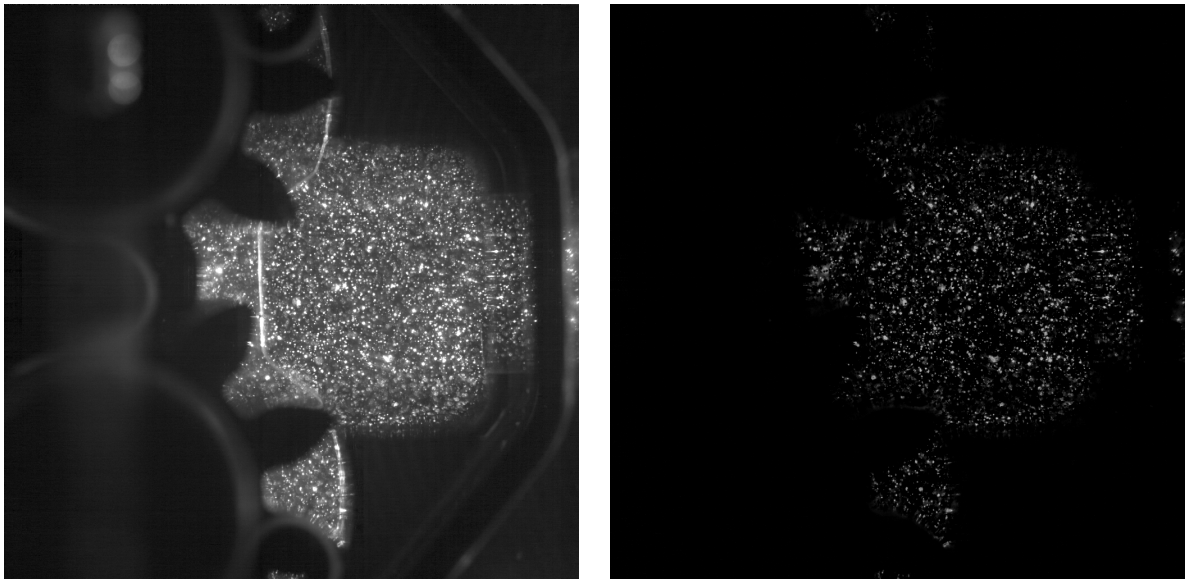

(a) (b)

Figure 5.8: (a) Original image. (b) The same image after clean-up mask process.

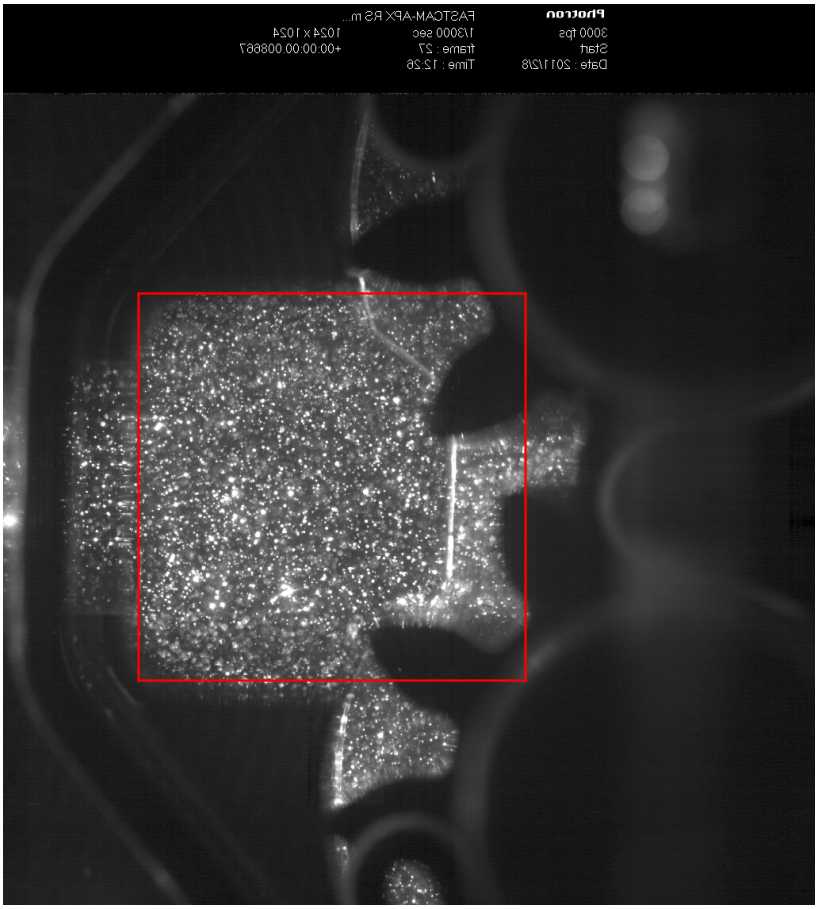

Figure 5.9: Interest domain for PIV interrogation.

employed. Now, the images of a pair are deformed following the particle displacements obtained from the initial PIV estimators or from the previous iteration step. The first image is deformed in positive direction with half the magnitudes of the estimators and the second image in negative direction. In this way, both deformed images will show the particle positions at the moment in-between the recordings. As a convergence criterion for this iterative procedure, the cumulative difference between the PIV estimators from the current and the previous iteration should drop below 0.25.

In order to obtain sub-pixel accuracy, we have fitted with Gaussian curves the maximum peak in the correlation plane, making use of two adjoining points in each direction. The use of Gaussian estimators, which has become wide-spread, typically work best for correlation peaks formed from particle images in the 2–3 pixel diameter range, which is our case. The reason why Gaussian estimators are most frequently employed, is that the particle images themselves, if properly focused, describe Airy intensity functions which are approximated very well by a Gaussian intensity distribution. By the use of this interpolation scheme, accuracy is easily increased up to 1/10 of a pixel.

Finally, a data validation process is required, in order to identify and replace spurious vectors (also called outliers). Outliers are identified by using a Normalized Median Test (Westerweel and Scarano [92]). Lets consider the velocity vector associated to a certain grid point and its eight nearest surrounding vectors. The normalized median is defined as the ratio between the median residual with the considered data point included and the median residual of the surroundings (with the considered data point excluded). Therefore, the velocity vector in certain a grid point $\vec{v}_0$ will be considered valid when

$$\frac{|\vec{v}_{med} - \vec{v}_0|}{r_{med} + \varepsilon_0} < \varepsilon_{th} \tag{5.10}$$

being $\vec{v}_{med}$ the median of the nine vectors within the 3x3 grid centered in the vector being checked, r_{med} the median of the eight r_i residuals of the surrounding vectors, which are defined as $r_i = |\vec{v}_{med} - \vec{v}_i|$ $(i = 1, \ldots, 8)$, ε_0 an additional term which represents the acceptable fluctuation level due to cross-correlation, and is taken $\varepsilon_0 = 1$ px. The threshold value, ε_{th} has been taken $\varepsilon_{th} = 2$ as recommended by Westerweel and Scarano [92].

Westerweel and Scarano [92] demonstrated that this method yields a rather universal probability density function for the residual such that a single threshold value can be applied to effectively detect spurious vectors. Normalized median test results in a very powerful validation scheme, and is especially well suited for iterative PIV interrogation schemes such as the one employed in our case.

Finally, the resulting velocity fields have been phase-averaged as already explained. The phase-averaged velocity field in time step n, $\vec{v}^n_{av}$, results

$$\vec{v}^n_{av} = \frac{1}{6}\sum_{i=0}^{5} \vec{v}^{n+360i} \qquad n = 1, \ldots, 33 \tag{5.11}$$

5.6 Experimental results and conclusions

In this section, the results obtained from the TRPIV experiments will be compared against those obtained by means of a numerical simulation, with no cavitation effects. This comparison will be made from a qualitative point of view, as the simplifications involved in the numerical model are

too restrictive to perform a quantitative comparison. Nevertheless, a qualitative agreement of the fluid flow structures in the inlet chamber would imply that, despite its limitations, the numerical model is suitable for the prediction of the cavitating behavior of the pump, as long as the cavitation models employed are appropriate.

The numerical simulation represents a two-dimensional approach to the prediction of the real three-dimensional flow structures that take place in the real pump. All the numerical algorithms used in these simulation, as numerical discretization schemes, turbulence modeling, multiphase and cavitation modeling, or mesh deformation algorithms, have been detailed in chapter 4. The two-dimensionality of the numerical model implies some important simplifications with respect to the real three-dimensional pump that has been tested. In section 4.13 these simplifications are presented and justified from the point of view of the scope of this thesis: understanding the influence of cavitation in the volumetric efficiency.

In figure 5.10 the experimental and numerical streamlines at the inlet chamber are compared each 1/10th of a gearing cycle. The rotational velocity of the pump is 500 rpm, which is low enough to avoid important cavitation effects that would make more difficult the experimental procedure. The experimental streamlines correspond to those at the middle plane of the pump, which is a plane of symmetry. The main conclusions are exposed below:

- Matching between numerical and experimental streamlines is very poor at the entrance zone of the inlet chamber at all instants. This is an expected effect and can be easily explained: The real inlet pipe is circular, and the simulated one is two-dimensional, equivalent to a rectangular pipe with its width equal to the diameter of the circular pipe and its height equal to the depth of the gears. As the cross area of the real pipe is smaller than that of the simulated one, and volumetric flows are equal (fixed by the rotational speed of the pump), the inlet velocity is higher in the real pump than in the numerical simulation. This explains the fact that the experimental streamlines show the jet entering more directly into the center of the chamber, due to its inertia, than those obtained from the numerical simulations.

- In the external zones of the chamber, two main vortices are predicted by the numerical simulation. Upstream these vortices, secondary structures appear, in order to fill the remaining volume up to the rounded corners. Depending on the instant and the corner considered, these structures can take different forms. If we fix our attention in the upper corner, we can see that at $0T_g$ the main vortex becomes smaller and the volume left by it, near the corner, becomes filled by the fluid that enters the chamber close to the walls of the pipe. Then, this fluid flows towards the center of the chamber before entering the gearing zone. From $0T_g$ to $0.5T_g$ this structure remains stable with a size slightly smaller than that of the main vortex. From $0.6T_g$ to $0.7T_g$, a secondary vortex appears next to the front wall of the chamber. This vortex grows as the former structure shrinks and later collapse into a new secondary vortex (this can be better appreciated in the lower corner).

  Regarding the experimental results, we can appreciate that these secondary structures do not appear. As the inlet velocity is higher in the real pump, the flow cannot bend so easily just after entering the chamber due to its inertia. For this reason, the main vortices fully fill the lateral volumes of the chamber, and therefore they are bigger than those predicted by the numerical simulation.

- As we advance towards the center of the chamber, separating from the three-dimensional expansion of the circular jet, flow patterns begin to match considerably well. Near the meshing zone (which is a region of our interest as cavitation should take place there) it can be seen that flow separates into two parts, each one directed towards one of the gears. The numerical simulations predict reasonably well the point in which this separation takes place.

- The position of the core of the main vortices predicted numerically is slightly downstream their real position. This is because these vortices are smaller than the real ones, as it has been explained above, and are pushed downstream by the secondary structures that are predicted between them and the front wall of the chamber. Nevertheless, this position is reasonably well matched by the numerical simulation.

These conclusions indicate that there is a poor matching of the flow patterns in the region where the expansion of the entering jet takes place, as we are comparing a three-dimensional expansion with higher velocity with a two-dimensional one with lower velocity. These limitations are being studied by using PIV and three-dimensional CFD in a thesis currently in preparation by Ertürk. The following articles are related to this thesis: Ertürk et al. [21, 20]. Nevertheless, in the part of the chamber that is farther away from the entrance of the flow (and therefore closer to the gear's meshing region), where the cavitation effects are more likely to take place, the three-dimensional effect of the expansion at the real pump has been very much damped by the two-dimensional geometry of the chamber, and the agreement between numerical and experimental results is accurate enough to consider our numerical model valid for the study of the influence of cavitation in the volumetric efficiency of external gear pumps.

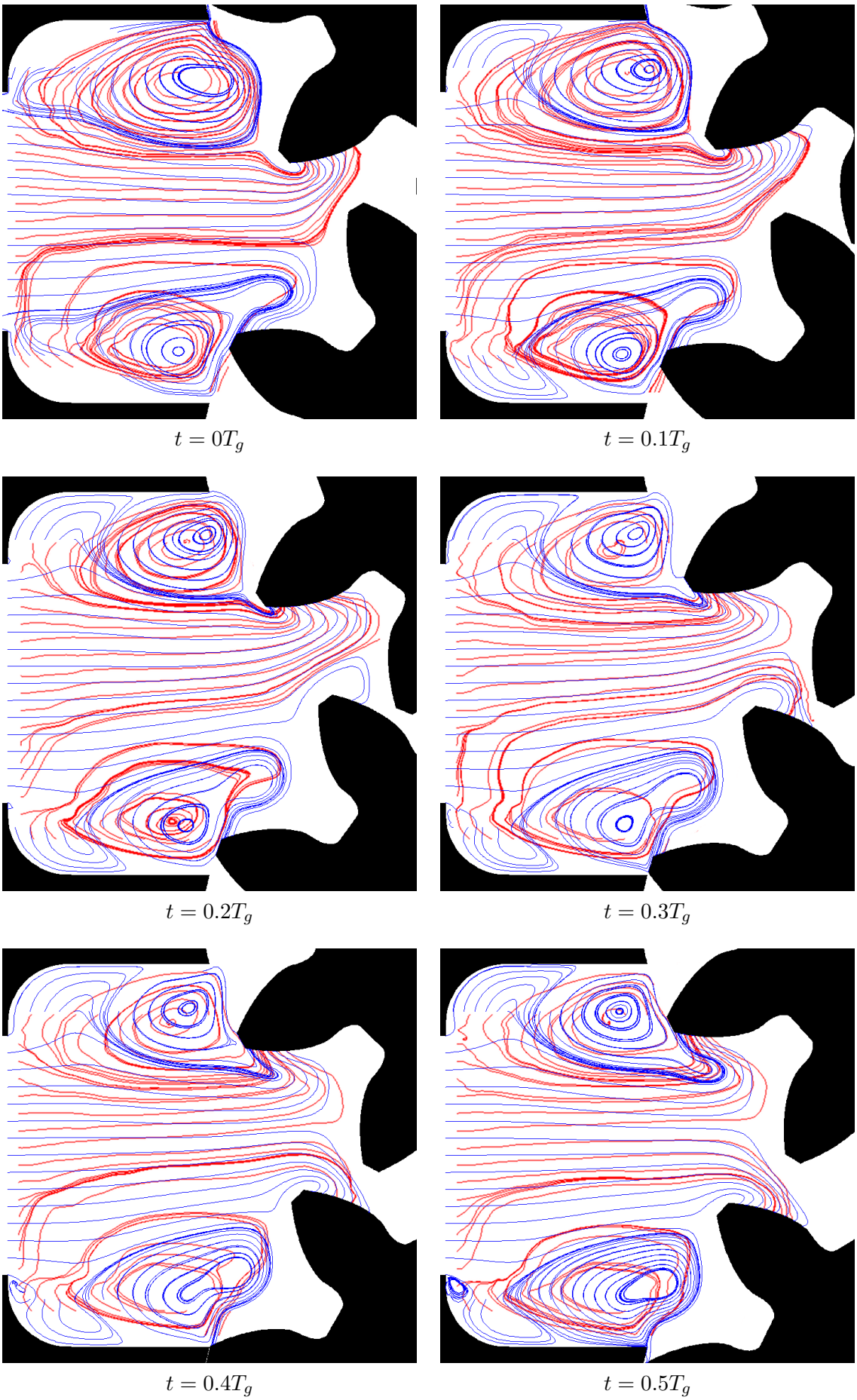

Figure 5.10: Streamlines in the inlet chamber. Red line: PIV. Blue line: CFD.

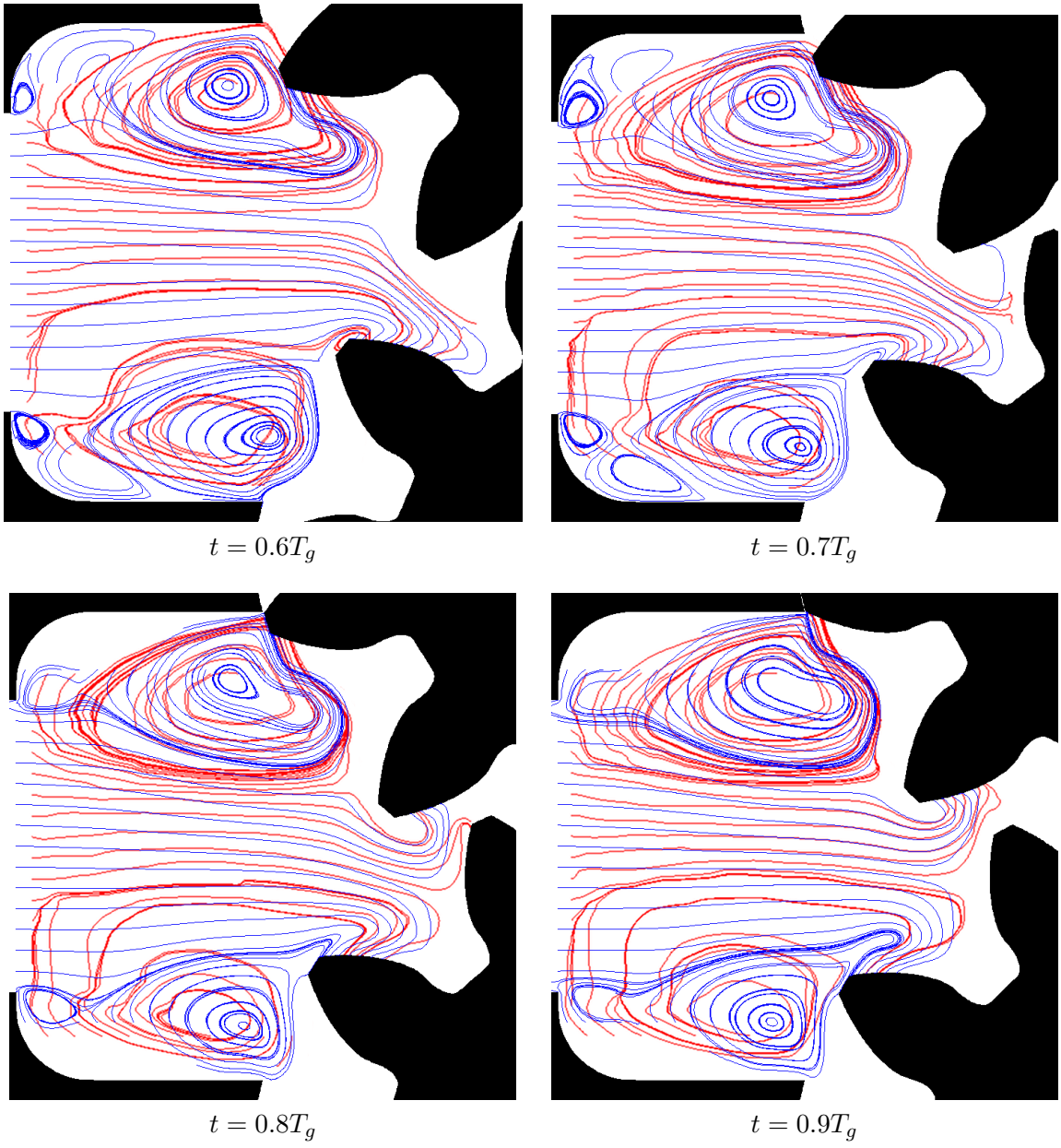

Figure 5.10: Streamlines in the inlet chamber. Red line: PIV. Blue line: CFD.

Chapter 6

Results of the numerical simulations

6.1 Introduction

In this chapter, the results of the numerical simulations performed in a two-dimensional model of an external gear pump, both including and excluding cavitation effects, will be presented. The numerical and physical parameters employed in the simulations, and the boundary conditions, have been presented in chapter 4. The fact of using a two-dimensional simplified model for the study of the three-dimensional hydraulically balanced pump forces us to cope with some limitations. These limitations have been presented and discussed in section 4.13 and it has been concluded that the values of volumetric efficiency that we may expect to obtain from the numerical simulations may be far from the real ones but, nevertheless, they should be useful enough to study the influence of cavitation in the volumetric efficiency by comparing simulations including cavitation effects against others not including them.

To validate the suitability of the numerical model, experiments by means of Time-Resolved Particle Image Velocimetry (TRPIV) have been performed, and results have been compared to those obtained from the numerical simulations. The experimental procedure has been presented in section 5.5, and the results, from which it can be concluded that the numerical model is appropriate for the aim of this thesis, is presented in section 5.6.

The effect of the inlet chamber geometry will also be studied. In section 4.10, four chamber geometries, different from that of the reference gear pump, have been presented, and the results of the simulations with these chambers will be analyzed.

Firstly, in section 6.2, the effect of cavitation on volumetric efficiency will be studied by analyzing simulations performed with the reference gear pump, with and without cavitation effects, at different rotational speeds, ranging from 500 to 3000 rpm in increments of 500 rpm. These speeds are representative of the typical operation ones of this pump. In these simulations, a constant inlet pressure, and an outlet pressure loss factor are set, as described in section 4.12. This coefficient is calculated for each case in order to always obtain a mean pressure jump of no less than 10 bar. This pressure jump, which is far below the typical operating pressures of this pump, was selected in order to better compare with the experimental results. Since, for flow visualization, the pump employed in the test rig was made in methacrylate, it had to be operated at a low pressure. Furthermore, since the simulated pump has a relatively big tip clearance, as explained in section 4.13, performing the

simulations with a higher operating pressure would lead to very low volumetric efficiencies caused by a high gear tip leakage, thus masking the effect of cavitation in volumetric efficiency, in which we are mainly interested.

In order to better understand the effect of the pressure jump in cavitation and volumetric efficiency, the simulations at 1000 rpm with and without cavitation effects have been repeated with a mean pressure jump of 100 bar and results are presented in section 6.3. It will be seen that the physical phenomena of cavitation is not much affected by the operating pressure of the pump, since it takes place mainly in the suction side, in which the same inlet pressure is imposed. On the other hand, the volumetric efficiency becomes greatly affected by the gear tip leakage, therefore justifying our election of a low operating pressure.

In section 6.4 the alternative inlet chambers are presented. Simulations allowing cavitation effects have been repeated for all of them at the same rotational speeds as with the reference chamber. Simulations not allowing cavitation effects have also been performed for all the inlet chambers but at only 1500 rpm. The main objective of this section is study the influence of the inlet chamber geometry on the volumetric efficiency of the pump considering cavitation effects.

So far, all simulations have a constant pressure inlet boundary condition. The reason for not using a loss factor in the inlet is that absolute pressure is as low as 1 bar and therefore flow perturbations are not supposed to be important. In section 6.5 an inlet loss factor, equivalent to that used for outlet boundary condition, has been used. This factor has been used to decrease the inlet mean pressure, therefore simulating the effect of the pump absorbing fluid from a deposit placed at a lower level. It will be seen that this effect allows cavitation to propagate towards the inlet of the pump therefore decreasing volumetric efficiency and radically changing the way in which cavitation affects to the suction characteristics of the pump.

Finally, in section 6.6, some simulations with the reference pump and cavitation effects, have been repeated, but sealing the gear's tip clearances through setting high viscosity in the small areas between them and the casing, as described in section 4.13. This will help us to better understand the effect of cavitation on volumetric efficiency, as the gear tip leakage will be canceled.

In appendix B a summary of all the simulations that have been performed, along with its main results are shown. In this table, the volumetric efficiency and the mean air volume compared to the total volume of the gear pump are shown.

Along this chapter, several plots will represent the evolution of a variable along the gearing cycle. We have considered the gearing cycle starting at the point at which the contact point is at its maximum x position (the nearest to the pump outlet). Along the cycle the contact point follows the line of action advancing towards the suction side of the pump, and the cycle ends at the instant, in which the contact point jumps back to the pressure side. In order to help us to relate each instant of the gearing cycle with the gears meshing position and the contact point position, table 6.1 shows these positions at each 1/10 of the gearing cycle.

t/T_g	0	0.1	0.2	0.3	0.4
	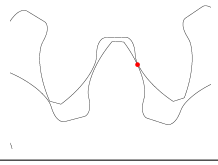	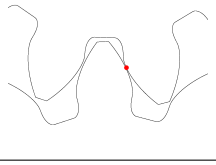	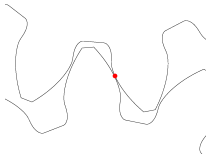	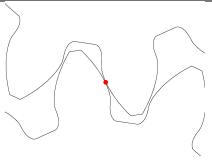	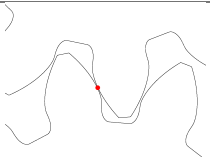
t/T_g	0.5	0.6	0.7	0.8	0.9
	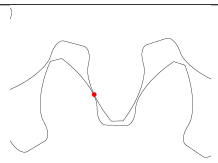	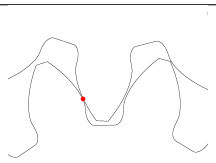	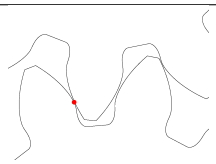	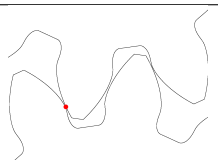	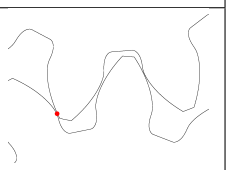

Table 6.1: Gears and contact point (in red) position at each 1/10 of a gearing cycle.

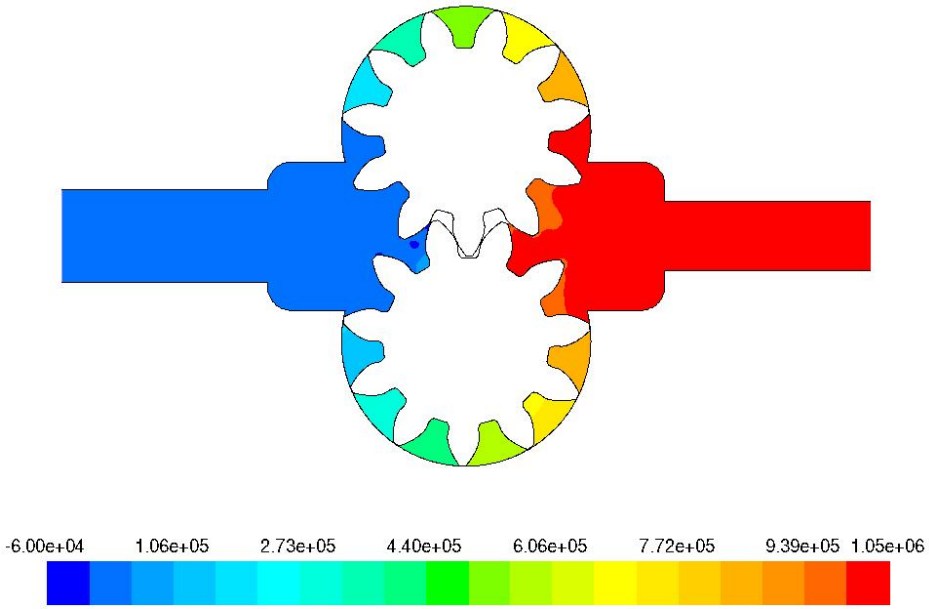

Figure 6.1: Gauge pressure contours with cavitation effects (Pa) at 1500 rpm. $t/T_g = 0.5$.

6.2 Reference gear pump

In this section the results of the simulations with the reference gear pump, at a range of rotational velocities (from 500 rpm to 3000 rpm in 500 rpm increments) will be analyzed. In all cases a mean pressure jump of 10 bar between inlet and outlet is imposed, using a constant pressure boundary condition at the inlet, and a pressure loss factor at the outlet, as explained in section 4.12, to allow for pressure fluctuations. In appendix B the cases analyzed and their main results are shown.

Figure 6.1 shows the pressure contours at 1500 rpm at $0.5T_g$. It can be seen that the pressure jump from one inter-teeth volume to the next one is kept approximately constant, as stated by equation 3.11.

In figure 6.2 the outlet pressure evolution along the gearing cycle with and without cavitation effects is compared for all the operating velocities that have been simulated. Despite cavitation takes place mainly in the suction side of the pump, it can be seen how its effect clearly affects the pressure

ripple at the outlet. At low rotational speeds, the effect of cavitation is hardly appreciated, except for a slight pressure increase at the end of the gearing cycle, at around $0.8 - 0.9T_g$. When no cavitation effects are simulated, as the rotational speed increases, the effect of the sudden jump of the contact point position at the end of the gearing cycle can be appreciated in the high frequency pressure fluctuation that takes place at the beginning of the cycle. This fluctuation is clearly damped when cavitation is taken into account. Even at low rotational speeds, when the the high frequency fluctuation does not appear, the pressure irregularity is reduced in about 50% due to cavitation, which damps the pressure pulsation associated to the contact point jump.

On the other hand, a pressure fluctuation associated to cavitation begins to appear at 1000 rpm, at around $0.6 - 0.7T_g$. This fluctuation becomes important at high operating velocities (starting from 1500 rpm) and can become higher than the one associated to the contact point position jump with no cavitation effects, causing a pressure pulse higher than the one damped by cavitation. This time period corresponds to the opening of an inter-teeth volume towards the suction side of the pump, and its effect will be explained later, when analyzing the flow and air volume evolution. At the highest rotational speeds, smaller pressure fluctuations associated to cavitation start to appear also in the first half of the cycle.

Therefore, despite cavitation damps the pressure fluctuation associated to the contact point jump, it also creates, at high working speeds, new fluctuations which can become higher than the aforementioned.

Figure 6.3 shows the inlet volumetric flow compared to the mean theoretical one (given by the volumetric capacity of the pump) at each simulated rotational speed, comparing the cases with and without cavitation effects. Regarding the cases with no cavitation effects, it can be seen that a flow pulsation at the beginning of the cycle appears due to the jump of the contact point position. This flow peak very slightly increases in amplitude when increasing the pump velocity. As the damping time of this perturbation is almost independent of the rotational speed, its relative duration linearly increases with it. At 3000 rpm the perturbation is still not completely damped by the end of the gearing cycle. This ripple is superimposed over an approximately parabolic curve, as the one predicted by the instantaneous theoretical flow rate given by expression 3.1. It is a water hammer effect produced by the jump in the contact point position. We have checked that the period of this perturbation is four times the period of an acoustic wave that travels from the inlet to the meshing region, which means there exists a 90° phase shift between the inlet and the meshing region. Besides the important increase in the flow irregularity produced by this water hammer, it is a source of noise and vibrations.

In the same figure, regarding the effect of cavitation, it can be seen that even the smallest amount of cavitation, which appears at 500 rpm, is enough to completely damp the water hammer associated to the jump of the contact point position, as the amount of air present in the inlet chamber by the end of the gearing cycle avoids the effect of a sudden oil volume rise at that instant. Cavitation also makes the curve to completely separate from the one representing the cases in which no cavitation is allowed (except in the final part of the cycle at 500 rpm). As it occurred with the outlet pressure, cavitation vanishes the peaks associated to the contact point jump, but is responsible for new peaks which are associated to the variations in air volume. In all cases two peaks can be seen, at different positions, within the gearing cycle for each rotational speed. The amplitude of these

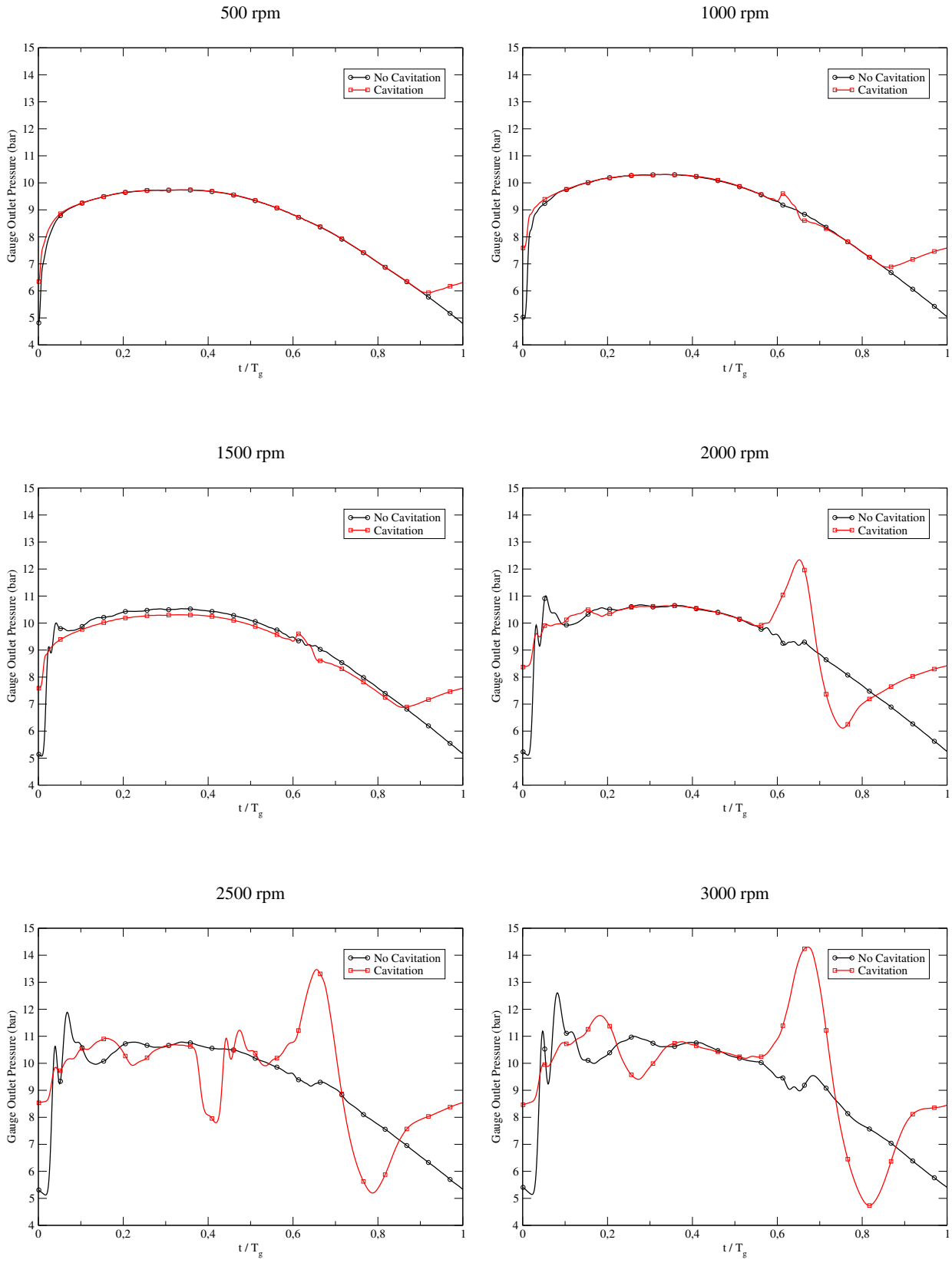

Figure 6.2: Gauge outlet pressure evolution at different rotational speeds, with and without cavitation effects.

peaks is comparable, thus smaller, to the one of the flow ripple present without cavitation effects, at 500 rpm and 1000 rpm. Above 1000 rpm, while increasing the rotational speed, despite the air volume increases, the flow pulsation amplitude decreases. This seems to be related to the relative air volume variations, as inlet flow increases when air volume decreases and vice versa, and at higher rotational speeds the volume occupied by air is kept relatively more stable along the gearing cycle than at the lower ones. This point will be clarified later, when analyzing the air volume evolution.

Figure 6.4 shows the outlet volumetric flow compared to the mean theoretical one at each simulated rotational speed, comparing the cases with and without cavitation effects. As outlet pressure is proportional to the outlet velocity squared, as imposed by the outlet boundary condition, these curves can in fact be obtained from the ones of figure 6.2 and therefore the analysis already done for the outlet pressure applies for the outlet flow rate.

The analysis of air volume evolution and the cavitating structures can throw some light on the flow and pressure pulsations already commented. In figures 6.5, 6.6, 6.7, 6.8, 6.9 and 6.10 the contour plots of fraction of oil volume, in the region where cavitation is present, are shown for 500, 1000, 1500, 2000, 2500 and 3000 rpm respectively, each 1/10 of a gearing cycle.

At 500 rpm some air is found at very small zones, where the minimum pressures are reach, especially near the contact point region at the suction side, due to the opening volume. At $0.3T_g$ also a cavitation cloud starts to appear from the gear tip of the lower gear, partially filling with air the inter-teeth volume of the upper gear. In the period $0.5 - 0.6T_g$ that same volume increases considerably, while the area through which the flow should pass in order to fill still remains small. Therefore, the cavitation cloud grows and almost totally fills that inter-teeth volume. Later on, from $0.7T_g$ until nearly the end of the cycle the cloud disappears and the pump operates with a very small amount of air. In this time range, the inlet flow coincides with the one obtained without cavitation effects. It is interesting to see how even the small amount of air present in this case is enough to completely damp the flow and pressure fluctuations associated to the jump of the contact point position between two gearing cycles.

At 1000 rpm cavitation clouds appear not only in the same regions as at 500 rpm, but also at the gear tip of the upper gear in the time range $0.1-0.3T_g$, which creates another cavitation cloud in the corresponding volume that partially fills it up to $0.3T_g$. The cloud that fills this inter-teeth volume grows not only by the effect of the volume opening, but also by the effect of flow separation when passing through the gear tip facing the inlet chamber. This effect creates a recirculation bubble of low pressure. Therefore, this cloud grows from both sides. Regarding the cloud that appears closer to the contact point, it is seen that it has a higher air content than at 500 rpm, and completely fills the volume. Due to this bigger air content and to the fact that the gears rotate quicker, it takes a higher fraction of the period for the cloud to dissipate, and thus we find that it has not completely disappeared by the end of the cycle, as it can be seen in the figure at $0.9T_g$. At 1000 rpm a significant volume of air is found in the meshing zone at any instant, although this amount changes significantly from one instant to another.

As the rotational speed increases, the air volume created in the inception phases of cavitation continues to grow due to the lower pressures that appear in the opening volumes. The time associated to the opening volumes phenomena that causes cavitation becomes shorter and comparable to the time associated to the dissipation of the cavitation clouds. Therefore, with increasing velocity, a

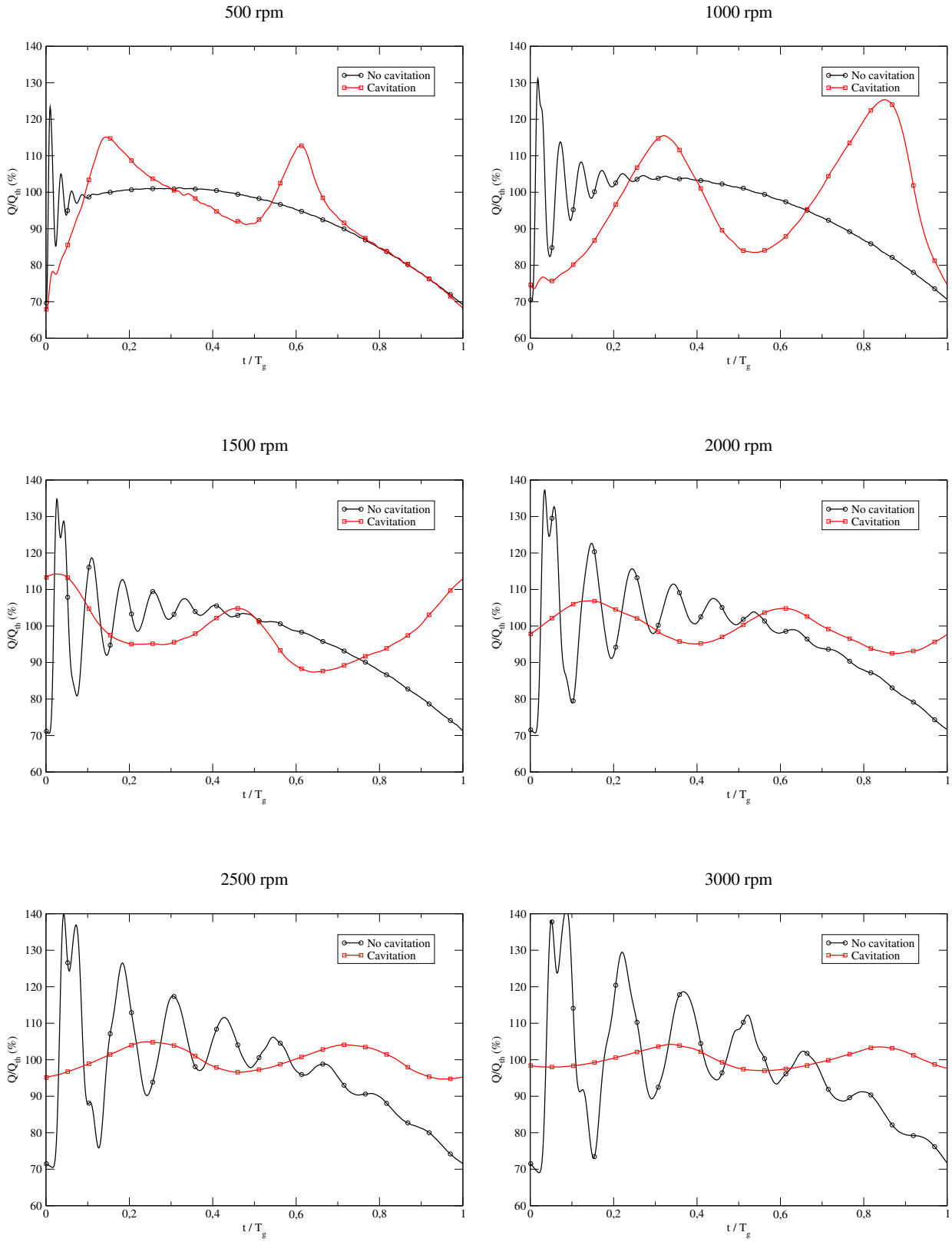

Figure 6.3: Inlet flow rate of the reference gear pump at different rotational speeds with and without cavitation effects.

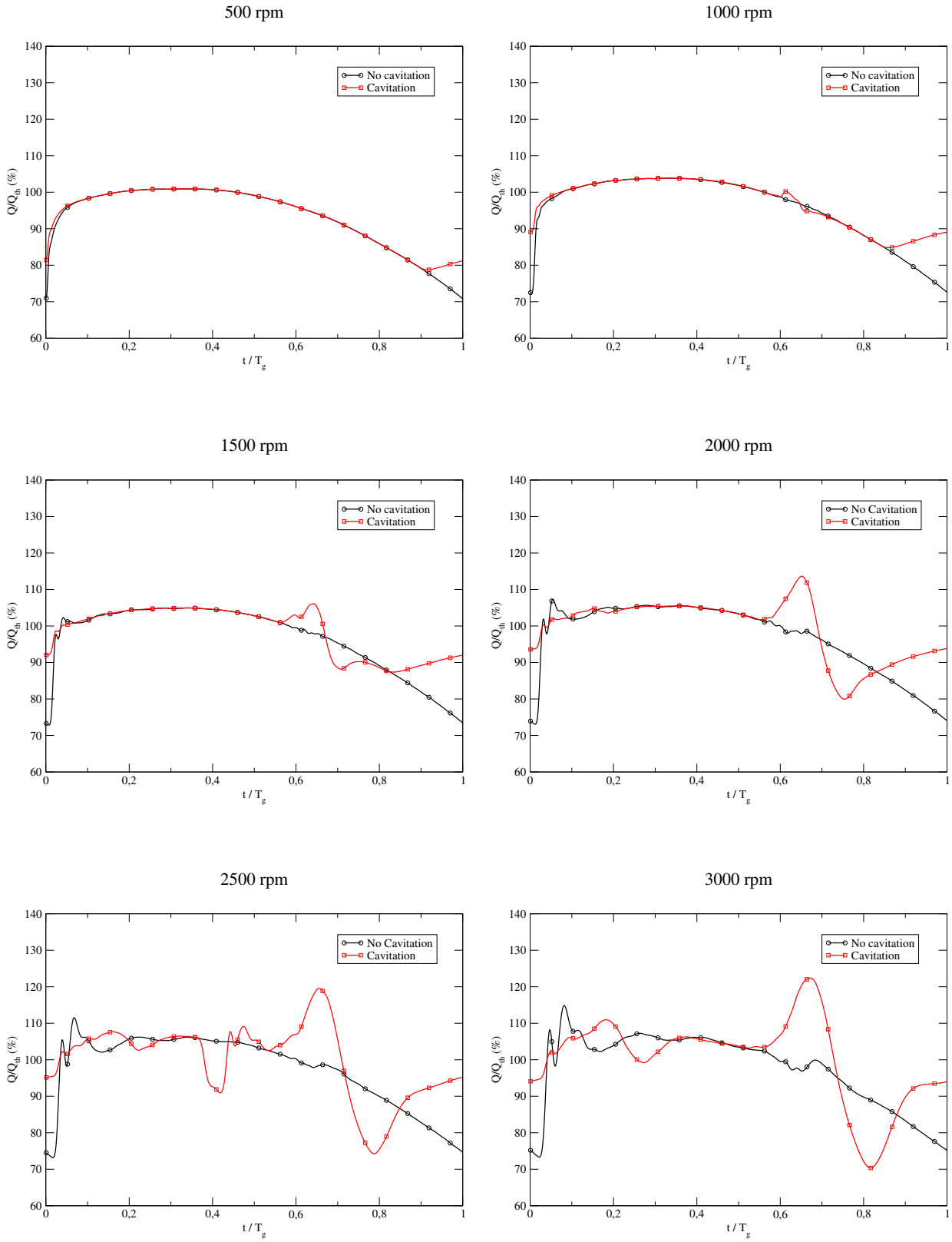

Figure 6.4: Outlet flow rate of the reference gear pump at different rotational speeds with and without cavitation effects.

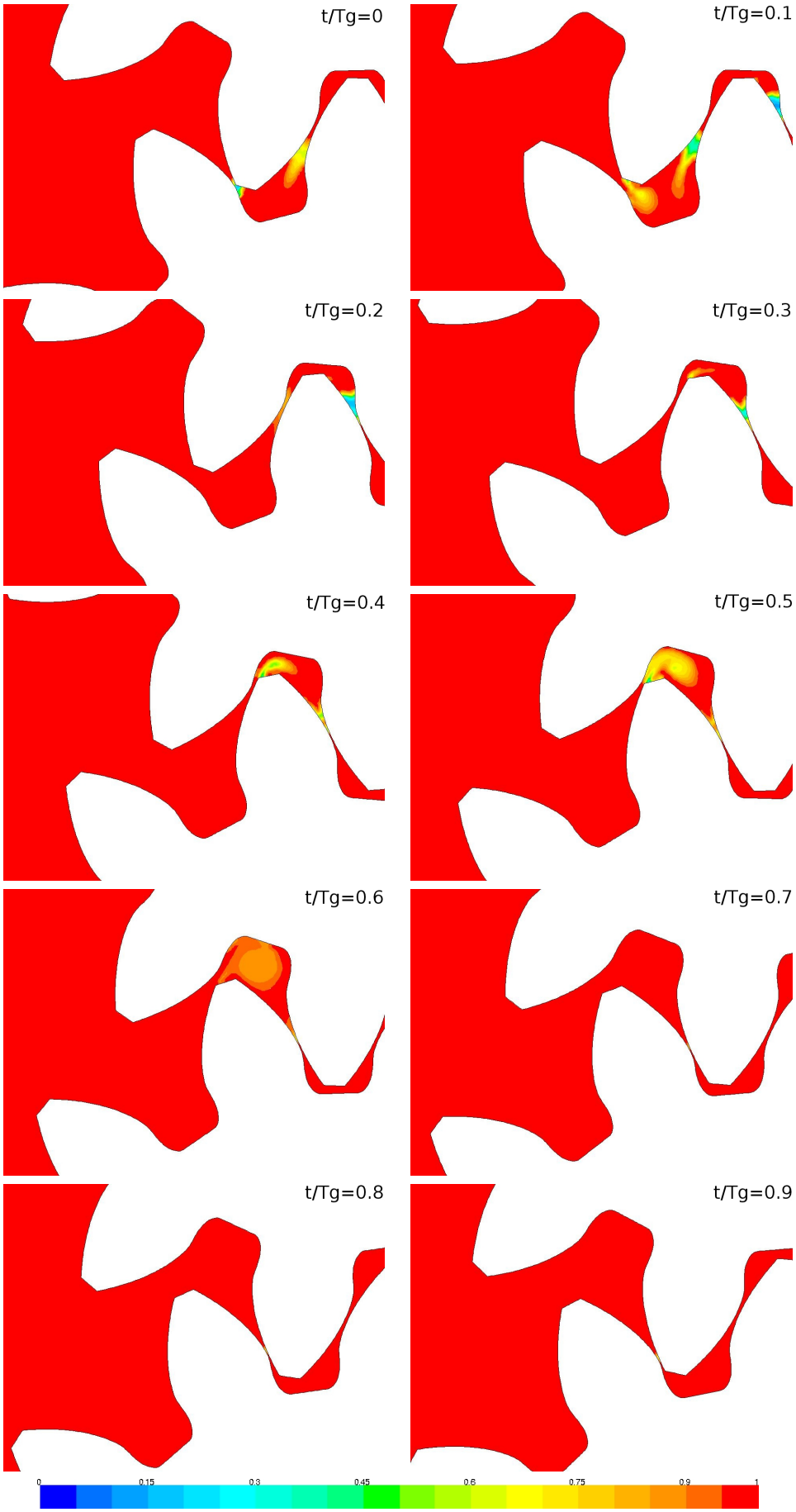

Figure 6.5: Volume fraction of oil at 500 rpm each 1/10 of a gearing cycle.

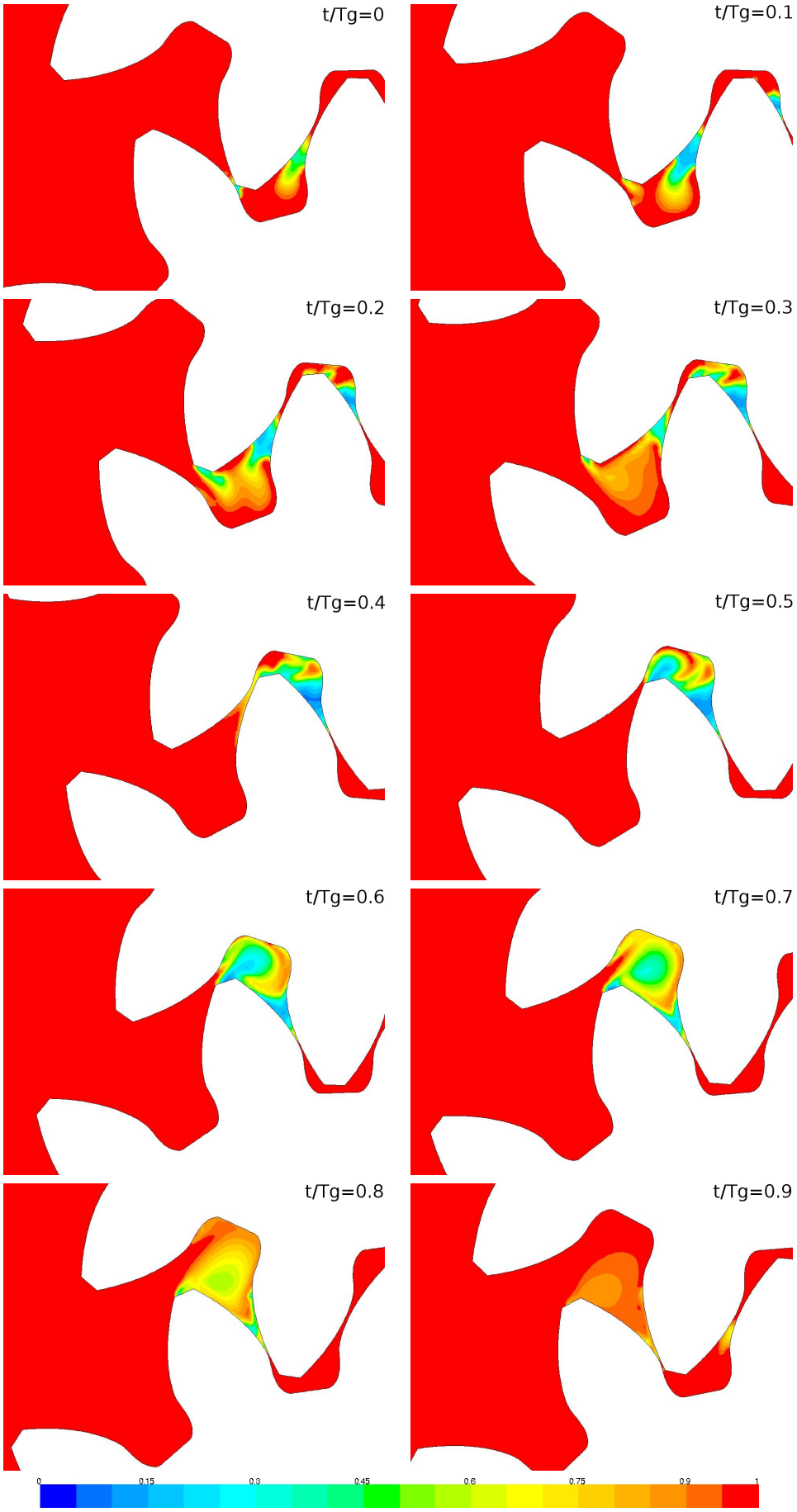

Figure 6.6: Volume fraction of oil at 1000 rpm each 1/10 of a gearing cycle.

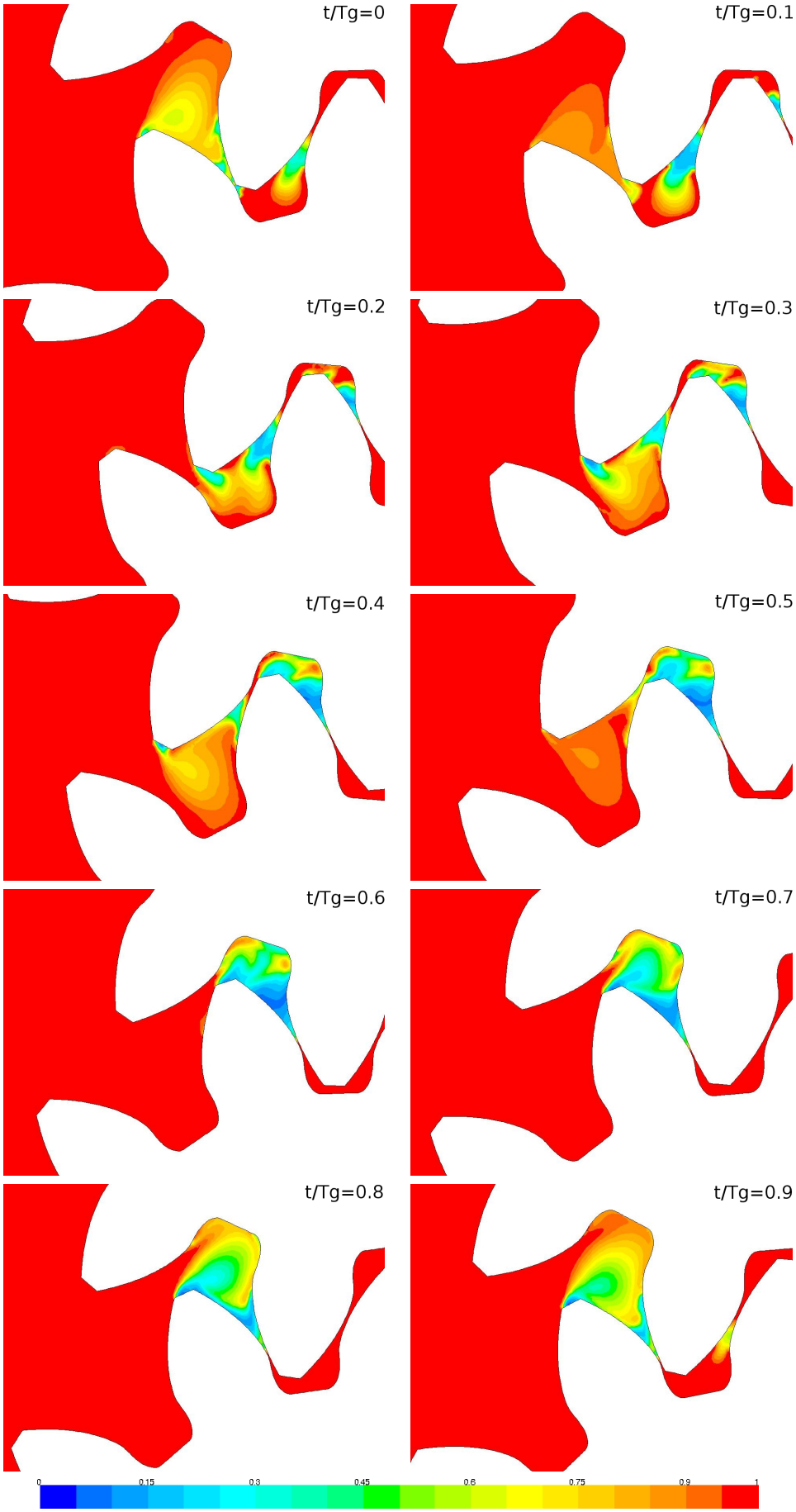

Figure 6.7: Volume fraction of oil at 1500 rpm each 1/10 of a gearing cycle.

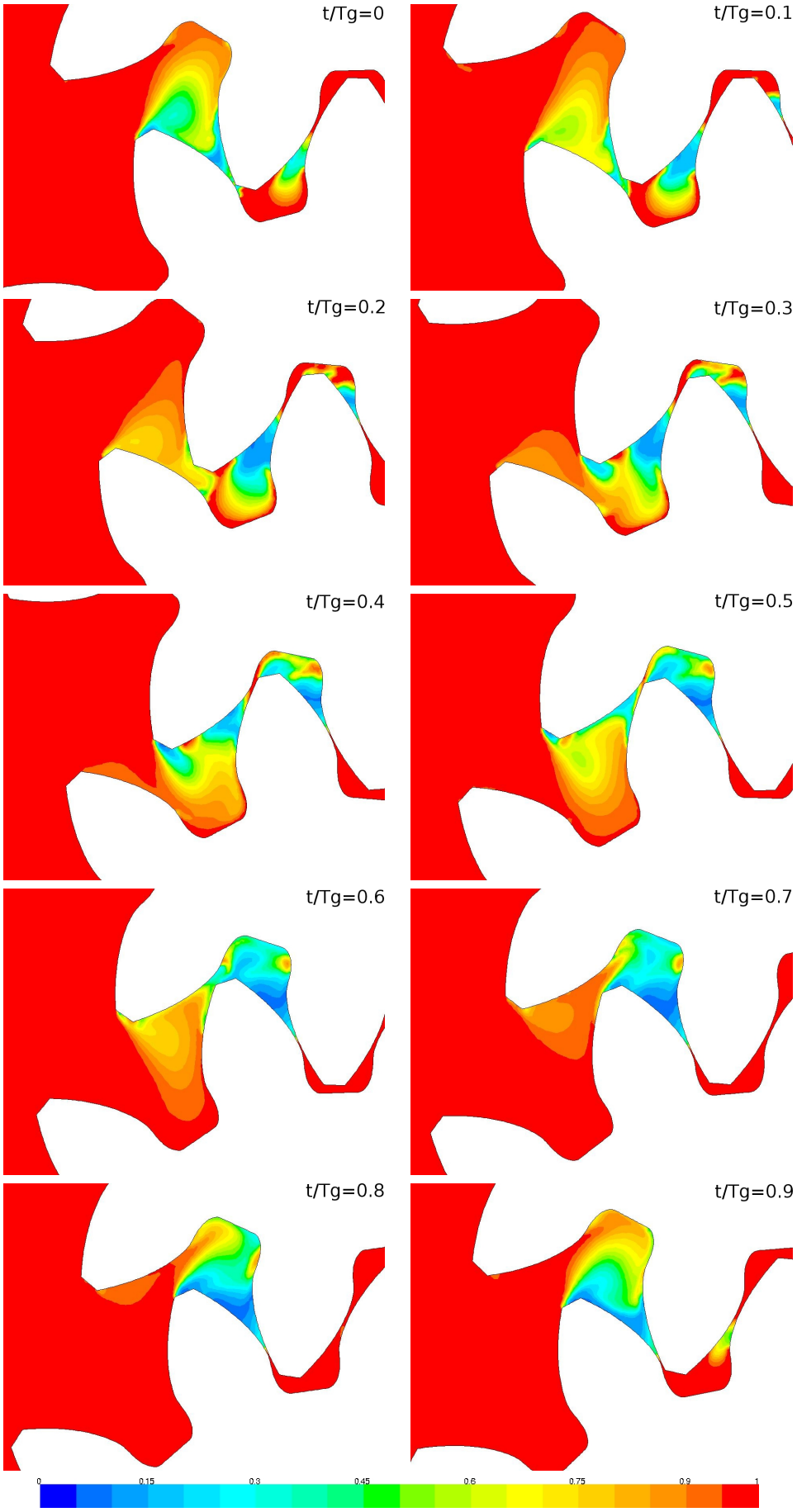

Figure 6.8: Volume fraction of oil at 2000 rpm each 1/10 of a gearing cycle.

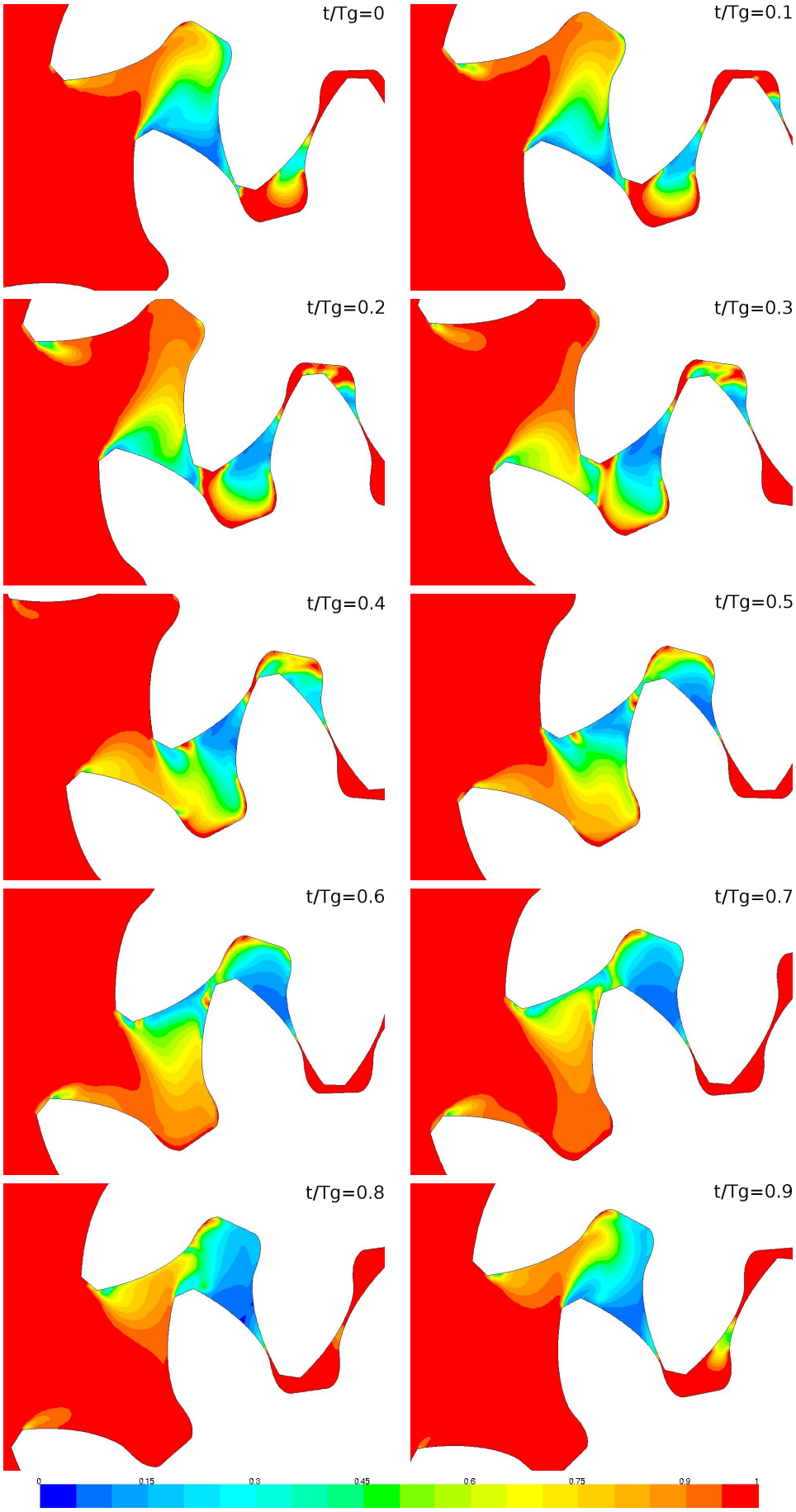

Figure 6.9: Volume fraction of oil at 2500 rpm each 1/10 of a gearing cycle.

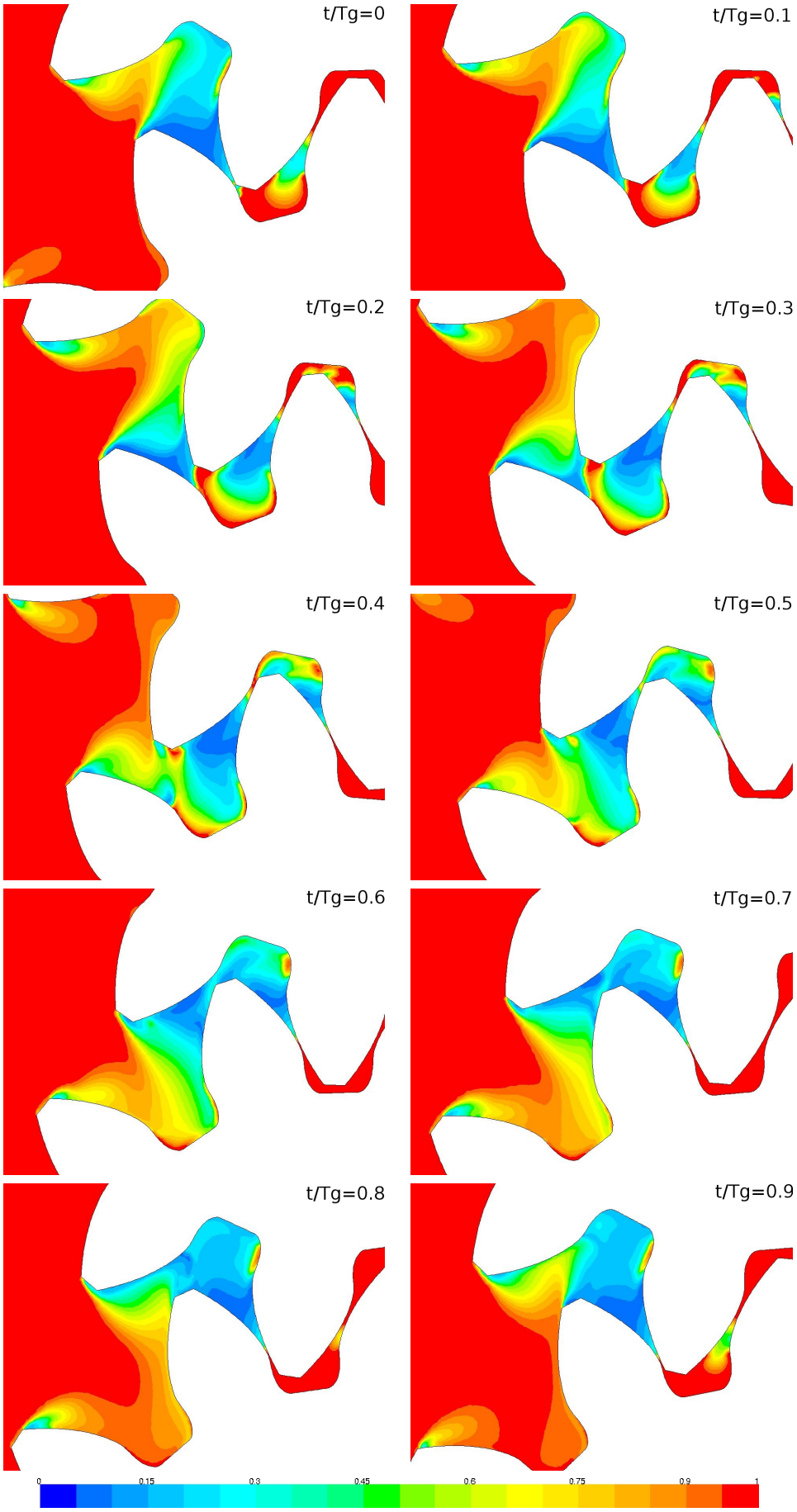

Figure 6.10: Volume fraction of oil at 3000 rpm each 1/10 of a gearing cycle.

cloud formed by a cavitation mechanism is each time further away from dissipating when a new cavitation mechanism appears, causing a more stable content of the air volume.

At $0.9T_g$ it can be seen that a cavitation cloud appears in the meshing region downstream the contact point. This cloud is caused by the jet that passes through the backlash clearance in order to fill the increasing volume adjacent to the contact point, at the pressure side. It acts as a virtual contact point, blocking the backward oil flow by filling the opening volume with air, and it is therefore responsible for the increase of outlet flow rate that was seen in figure 6.4 between $0.8T_g$ and $0.9T_g$. As it was seen in section 3.4, the effect of having a contact ratio higher than unity is that of bringing forward the new flow period up to the instant in which the second contact point takes place, reducing the flow irregularity. This effect was shown in figure 3.6. In figure 6.4 it is seen that the effect of this virtual contact point is equivalent.

At 1500 rpm, the physical phenomena is found to be similar to the one at 1000 rpm, but the volume of air is kept more stable. This can be clearly seen by comparing the instants $0.9T_g$ at both velocities. While at 1000 rpm only a small cloud with around 20% of air still remains from the one that appeared at $0.3 - 0.6T_g$, at 1500 rpm a bigger zone with around 50% of air volume remains. The volume of air that can be seen around the backlash clearance at $0.9T_g$ is now bigger than at 1000 rpm.

At 2000 rpm more air volume is found and the cavitation clouds that fill the inter-teeth volumes are more stable. The cloud that at 1500 rpm was almost completely dissipated by $0.5T_g$ now remains until $0.7T_g$ approximately. Also, due to the higher velocity of the flow, new cavitation clouds caused by flow separation on the teeth advancing towards the inlet chamber appear. This can be seen at the tip of the upper gear in the range $0.7 - 0.8T_g$, where a cavitation cloud that did not exist at 1500 rpm appears now. The volume of air in the backlash region at $0.9T_g$ continues to grow.

At 2500 rpm the air already fills not only the opening volumes next to the contact point but also the contiguous one at any instant. The cavitation due to flow separation can now be observed even at the teeth tips that are further away from the meshing region, almost completely facing the inlet chamber. This can be observed at $0.1 - 0.4T_g$ in the upper gear and at $0.6 - 0.9T_g$ in the lower one. With the increasing rotational speed, the virtual contact point formed by the cavitation cloud at the backlash region appears earlier in the gearing cycle and it can be already appreciated at $0.8T_g$.

Finally, at 3000 rpm, it is seen how the cavitating region continues extending towards the suction chamber, and the air content of the clouds attached to the gear's tips caused by flow separation continues to increase. The volume of air that appears at the right side of the contact point by the end of the gearing cycle also continues to increase.

With the help of these figures we have seen that the air that appears in the pressure side before the end of the gearing cycle justifies the separation between the curves of the simulations with and without cavitation effects that was seen in the outlet pressure and flow evolution (figures 6.2 and 6.4). This fact damps the effect of the jump in the contact point position therefore reducing the flow irregularity. But it was seen that another separation between these two curves takes place at around $0.6 - 0.7T_g$ from 1000 rpm onwards in the way of a single pulse, and also earlier at 2500 and 3000 rpm. This separation of both curves can not be explained by the presence of air in the pressure side as no air is found at those instants. We believe this effect to be related to the bubble

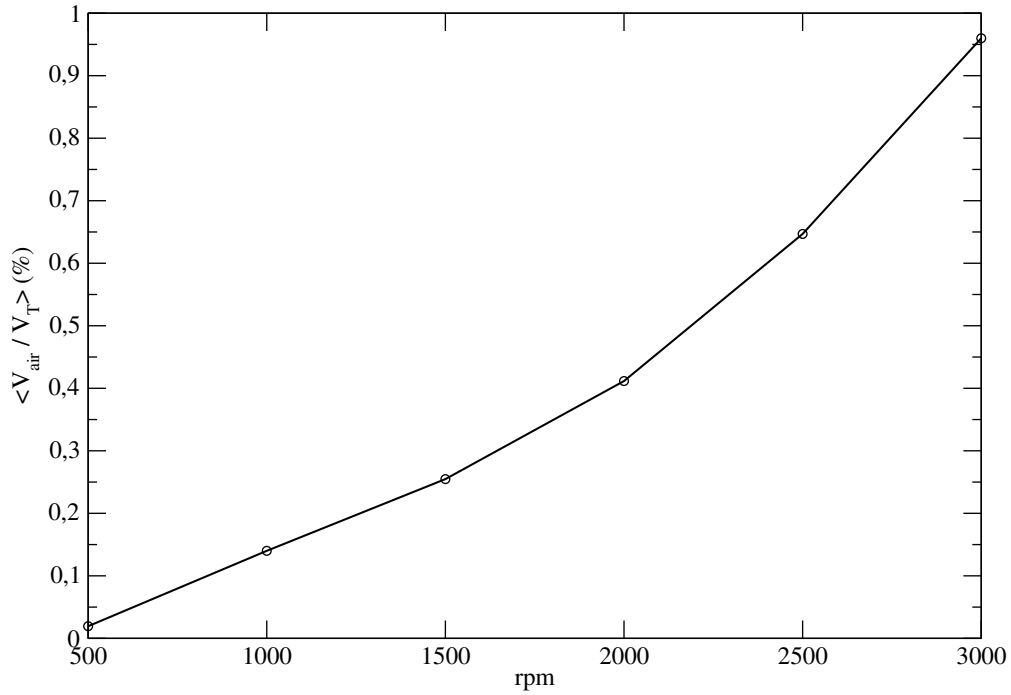

Figure 6.11: Relative mean volume of air against operating velocity.

collapse rate of the cavitation model, which is influenced by the fact of assuming constant density for the air phase. A further study of this fact is purposed as future work.

In figure 6.11 it is shown how the mean air volume quickly increases with the rotational speed, in a nearly parabolic manner.

In figure 6.12 the evolution of the volume of air divided by the total volume of the pump is shown for each rotational speed, along with their mean value. Firstly, it is seen how the mean volume of air increases with increasing rotational speed, from 0.02% at 500 rpm to 0.96% at 3000 rpm. It is also seen how at the lower rotational speeds, two peaks associated to the opening volumes mechanisms can be identified, since the cavitation clouds have more time to dissipate before a new cavitation mechanism appears. These peaks are displaced to the right at 1000 rpm with respect to 500 rpm as the physical time needed for bubble growth corresponds to a lower non-dimensional time. At higher speeds, only a peak around $0.7T_g$ is clearly seen at all rotational speeds, and the relative volume of air is kept more stable along the gearing cycle.

Figure 6.13 shows the time derivative of the total volume of air divided by the mean air volume for each case. Since the 500 rpm case has a very small air content and the derivative is noisy, its peaks are not shown in the graph in order to better appreciate the other curves. It can be seen how the air volume variation becomes relatively smaller when increasing the rotational speed, as already seen in the oil volume contour plots and in figure 6.12. It is more interesting to compare this figure to figure 6.3. By doing this it can be seen that the non-dimensional times at which the maximums of the derivatives appear, match rather precisely with the ones at which the maximum flow rates take place, and vice versa. This means that inlet flow is pushed backwards by the effect of bubble growth, reducing the flow rate, and it is favored by the effect of bubble implosion, which creates an extra suction force on the flow that increases the flow rate. It is also seen that the lower the derivatives become while increasing velocity, the flatter the flow rate curves. Therefore, the

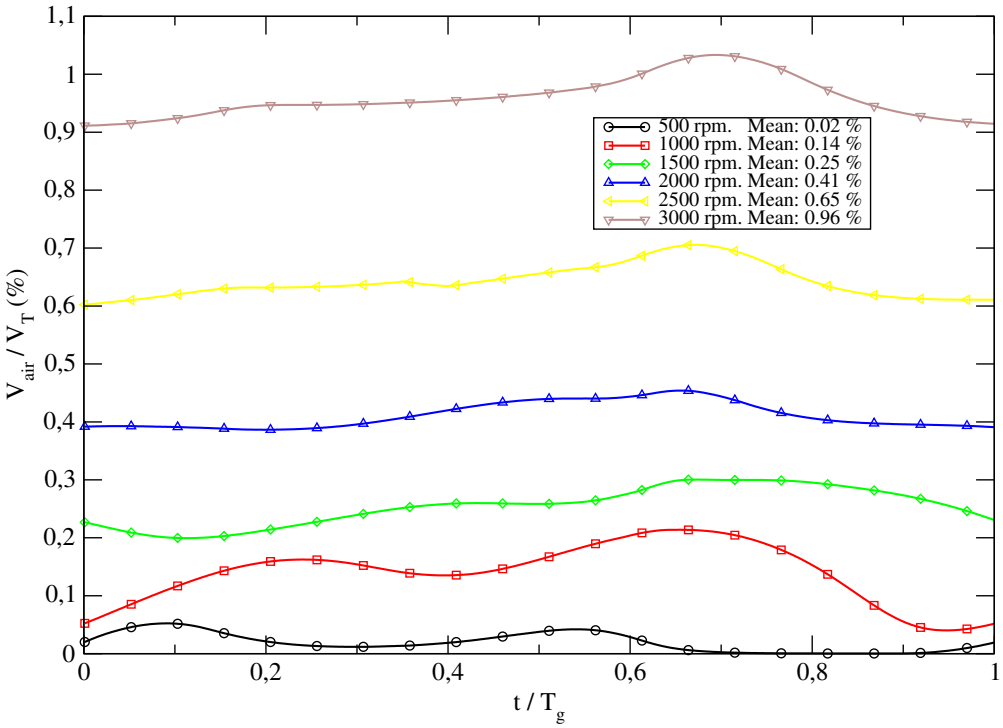

Figure 6.12: Relative volume of air evolution at different rotational speeds.

more stable air content that we can find at high velocities, the smaller the inlet flow irregularity. In order to better appreciate this fact, in figure 6.14, the relative inlet flow rate evolution at 1000 rpm is presented together with the relative air volume and the air volume time derivative. In this figure it is seen how the positive peaks of the flow rate coincide with the negative ones of the time derivative of the air volume.

Lets now analyze the volumetric efficiency of a pump with cavitation. It was seen in figure 6.4 that an increase in the outlet flow rate takes place at around $0.9T_g$ (earlier for high rotational speeds) and by analyzing the volume of oil contour plots it was seen and that this is caused by the effect of adding a virtual contact point in the backlash region due to cavitating jet that appears in the backlash clearance in order to fill the opening volume. This increase in the flow rate contributes to increase the volumetric efficiency. Furthermore, this fact may provide efficiencies higher than 100%, as the effect of cavitation is not considered in the definition of the theoretical volumetric capacity of the pump used to define the volumetric efficiency. In other words, the effect of having a cavitation cloud at the backlash clearance before the end of the gearing cycle blocks a backward flow which is assumed to be present in the definition of the theoretical volumetric capacity through the term V_{sq} of equation 3.3 which represents the volume shown in figure 3.9(b). When cavitation is considered, the volume of oil present in the squeeze volume by the end of the gearing cycle, when the contact point jumps back to the pressure side, is smaller than the squeeze volume itself, as part of it is filled by air, as shown in figure 6.15. Therefore, the volumetric flow of oil that passes back to the suction side is reduced by cavitation. It is important to notice that this back-flow is not associated to any leakage source, but is assumed when defining the theoretical volumetric capacity of the pump. Therefore, by using the standard definition of volumetric capacity, in a case with cavitation, volumetric efficiency can eventually become higher than unity. Taking this into account, the fact of obtaining values higher than unity should not prevent us from using the volumetric efficiency

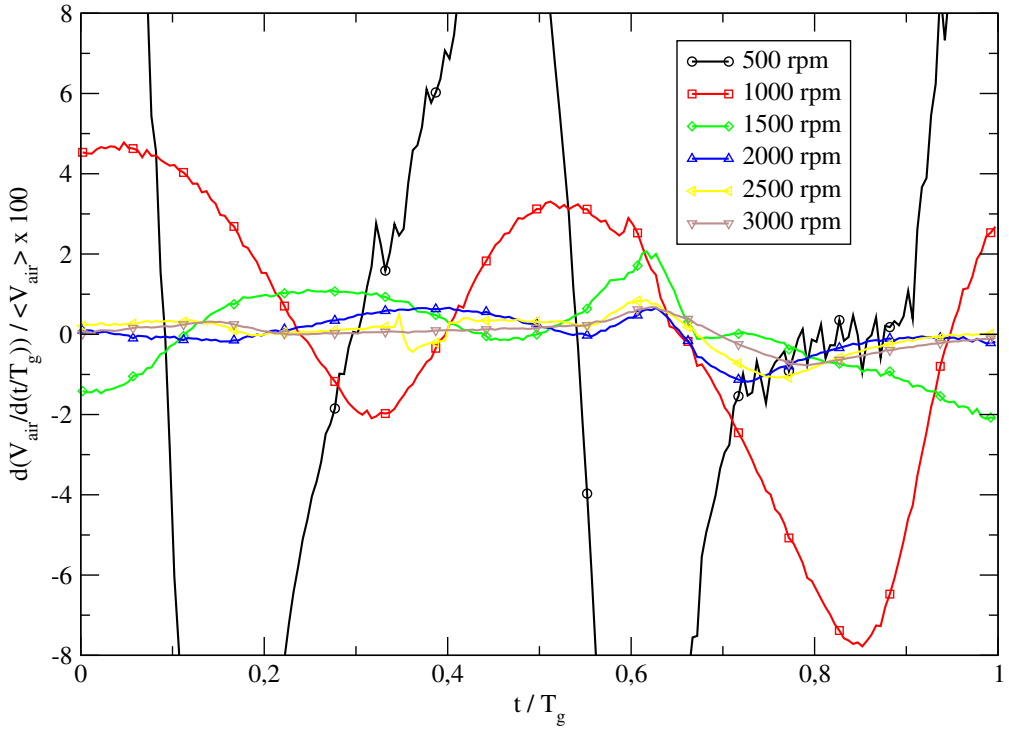

Figure 6.13: Derivative of air volume with respect to the non-dimensional time divided by the mean air volume at different rotational speeds.

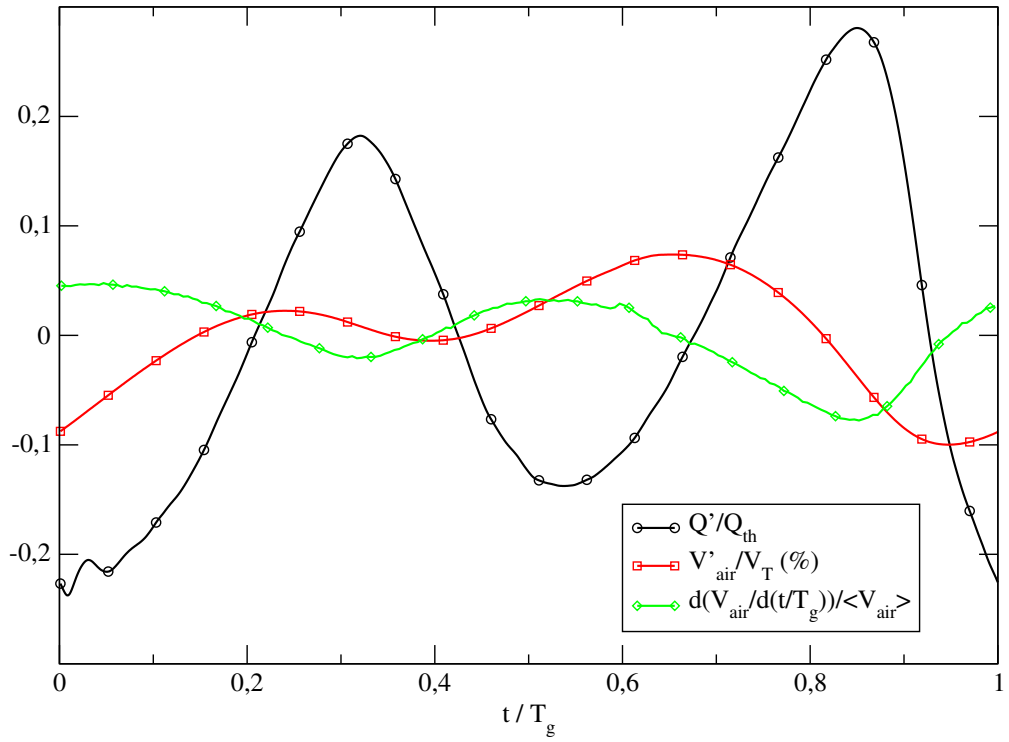

Figure 6.14: Relative inlet flow rate, relative air volume, and non-dimensional derivative of the relative air volume at 1000 rpm. All curves have been shifted to zero mean in order to better compare their behavior.

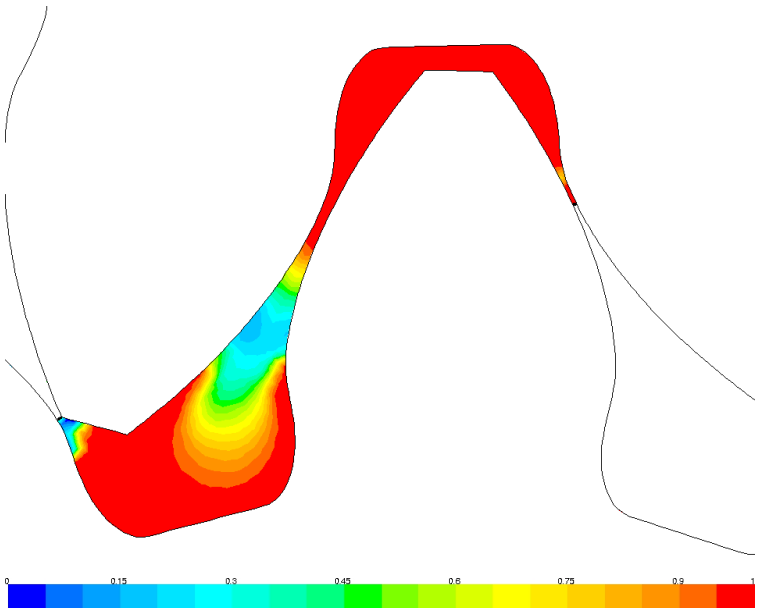

Figure 6.15: Volume fraction of oil in the squeeze volume at 1500 rpm in the beginning of a gearing cycle.

in the way we have defined it, as the value of the theoretical volumetric capacity employed is just a reference value with which to non-dimensionalize the mean flow rate per revolution and will be the same for all cases. Nevertheless, in order to avoid calling "efficiency" to a number that can be greater than unity, we will call it, from now on, "volumetric ratio", κ_v. Therefore, the volumetric ratio will be defined in the same way as the volumetric efficiency was, but assuming that it can take values higher than unity. For better accuracy, the mean value between the inlet and outlet flow rates has been taken, although the difference between both, due to numerical errors, has been found to be in all cases below 0.1%.

In figure 6.16 the volumetric ratios for all the cases, with and without cavitation effects, are shown. The suction capacity of the pump without cavitation effects shows to be as one would expect taking into account the loss factors exposed in chapter 3, together with the limitations of our numerical model. We can also see that efficiency increases with the rotational speed, due to the flow drag effect, which is proportional to the gear tip velocity (equation 3.13).

Regarding the simulations allowing cavitation, not so intuitive results appear. Firstly, we appreciate that volumetric ratio continues to increase with the rotational speed, in a very similar way as it did when no cavitation effects were allowed. Therefore, we can say that an increase in the air content does not necessarily reduce the volumetric ratio. On the contrary, we have seen that the instantaneous flow rate depends on the derivatives of the volume of air, and at higher rotational speeds, these derivatives become lower due to the inertia of the cavitation clouds to dissipate. Furthermore, we see that at any rotational speed, the volumetric ratio when allowing cavitation is higher than the one obtained when not allowing it. Table 6.2 shows that the increase in the volumetric ratio due to cavitation ranges from 0.65% at 500 rpm to 2.53% at 3000 rpm. This can be understood by taking into account the effect of the cavitation cloud that takes place before the end of the gearing cycle at the backlash clearance and acts in a similar way as a second contact point, increasing the flow rate from the instant in which it appears. This fact compensates for part

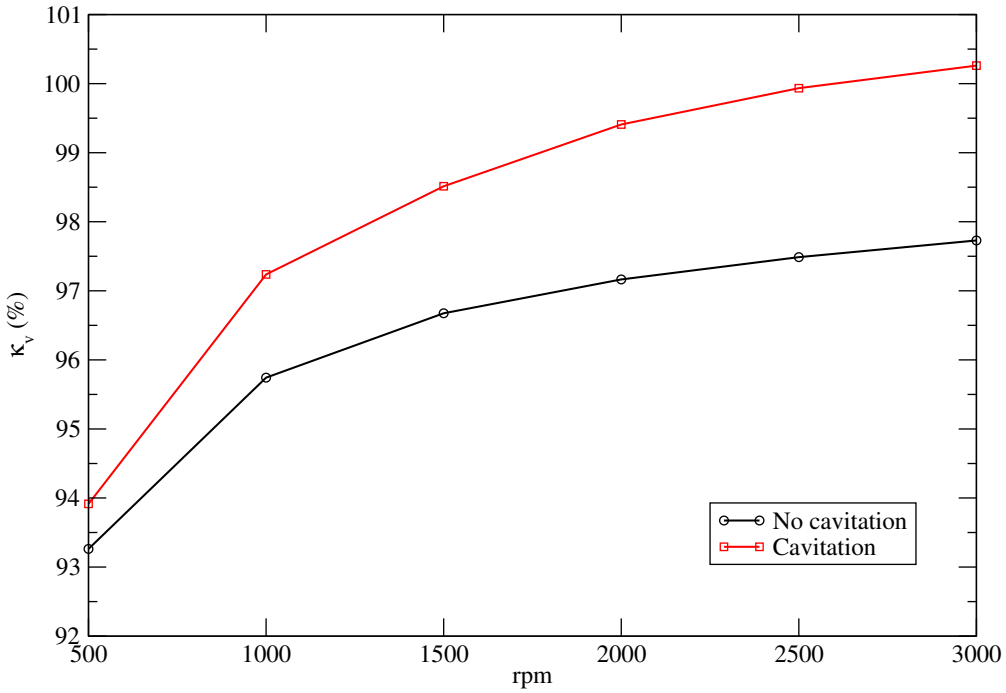

Figure 6.16: Volumetric ratio against operating velocity with and without cavitation effects.

rpm	$\kappa_{v,cav}$ (%)	$\kappa_{v,nocav}$ (%)	$\Delta\kappa_v$ (%)
500	93.91	93.26	0.65
1000	97.23	95.74	1.49
1500	98.51	96.67	1.84
2000	99.41	97.16	2.24
2500	99.93	97.49	2.45
3000	100.26	97.73	2.53

Table 6.2: Volumetric ratios of the reference pump with and without cavitation effects and their increase due to cavitation.

of the leakage factors and can even over-compensate them, so that a volumetric ratio higher than unity may be achieved in some case, as it occurs in our simulation at 3000 rpm, which volumetric ratio is 100.26%.

Once that we have seen that the effect of the cavitation cloud located in the backlash region by the end of the gearing cycle is positive from the point of view of increasing the volumetric ratio, we can analyze the effect of the cavitation that takes place outside it. For doing this, we will calculate a modified volumetric ratio by subtracting, from the real volumetric flow rate, the back-flow air that passes through the squeeze volume in a revolution, which corresponds to the one trapped inside the squeeze volume by the end of the gearing cycle, $V_{air,sq}$, multiplied by the number of gears, z. This modified volumetric ratio, which does not account for the beneficial effect of the air trapped in the squeeze volume is,

$$\kappa_{v,mod} = \kappa_v - z\frac{V_{air,sq}}{C_v} \tag{6.1}$$

It should be noticed that in the definition of the theoretical volumetric capacity the compressibility of the oil is not taken into account. Therefore if we wanted to discount from the volumetric ratio the real back-flow through the squeeze volume, the term $V_{air,sq}$ in equation 6.1 would have to be

rpm	$V_{air,sq}/V_{sq}$ (%)	κ_v (%)	$\kappa_{v,mod}$ (%)
500	4.01	93.91	93.21
1000	8.89	97.24	95.68
1500	11.71	98.51	96.46
2000	13.29	99.41	97.08
2500	14.63	99.93	97.37
3000	15.90	100.26	97.47

Table 6.3: Volumetric ratio of the reference pump at different operating velocities, and modified volumetric ratio (according to equation 6.1) subtracting the effect of the volume of air trapped in the squeeze volume at the beginning of the gearing cycle.

substituted by $V_{sq} - (m_{oil,sq}/\rho_{oil})$, being ρ_{oil} the reference oil density. This way both the effects of cavitation and compressibility of the oil would be subtracted from the volumetric ratio at a time. As we are interested only in subtracting the effect of cavitation, equation 6.1 will be employed. Nevertheless, the effects of cavitation and compressibility of oil cannot be completely separated, as the air content affects the pressure field in the squeeze volume and therefore the oil density. Anyway, since the effect of compressibility is small, this modified volumetric ratio should be adequate for our need.

Table 6.3 shows the values of the real and modified volumetric ratios of each simulated case, and the relative volume of air that passes from the pressure to the suction side through the squeeze volume. It is seen that at higher rotational speeds, the volume contained in the squeeze volume by the end of the gearing cycle increases.

In figure 6.17 both the real and the modified volumetric ratios are plotted, along with the ratios of the cases in which cavitation is not simulated. It is seen that the modified volumetric ratio drops very slightly below the volumetric ratio of the cases where no cavitation is simulated, being the difference between both almost negligible at all rotational speeds. Therefore it is concluded that the air that appears in the squeeze volume has a noticeable beneficial effect on volumetric ratio, which increases with the pump speed (at higher velocities more air appears in the squeeze volume) while the rest of the air, located in the suction chamber, has an almost negligible effect on the volumetric ratio.

It is important to notice that the inlet boundary condition imposes a constant atmospheric pressure. Therefore cavitation can only appear locally at the low pressure zones of the meshing region due to the opening volumes or at the gear tips facing the inlet chamber, due to flow separation, but it is unable to propagate further towards the inlet. If the pump had to suck from an oil tank placed at a lower level, thus decreasing its inlet pressure, cavitation would be able to extend towards the pump inlet and its consequences regarding the volumetric ratio would change drastically, as it will be seen in section 6.5.

In conclusion, the following points regarding the cavitation and suction characteristics of the reference pump should be noticed:

- A flow pulsation appears associated to the jump in the contact point position between two consecutive gearing cycles when cavitation is not simulated. This pulsation corresponds to a water hammer and increases the flow irregularity.

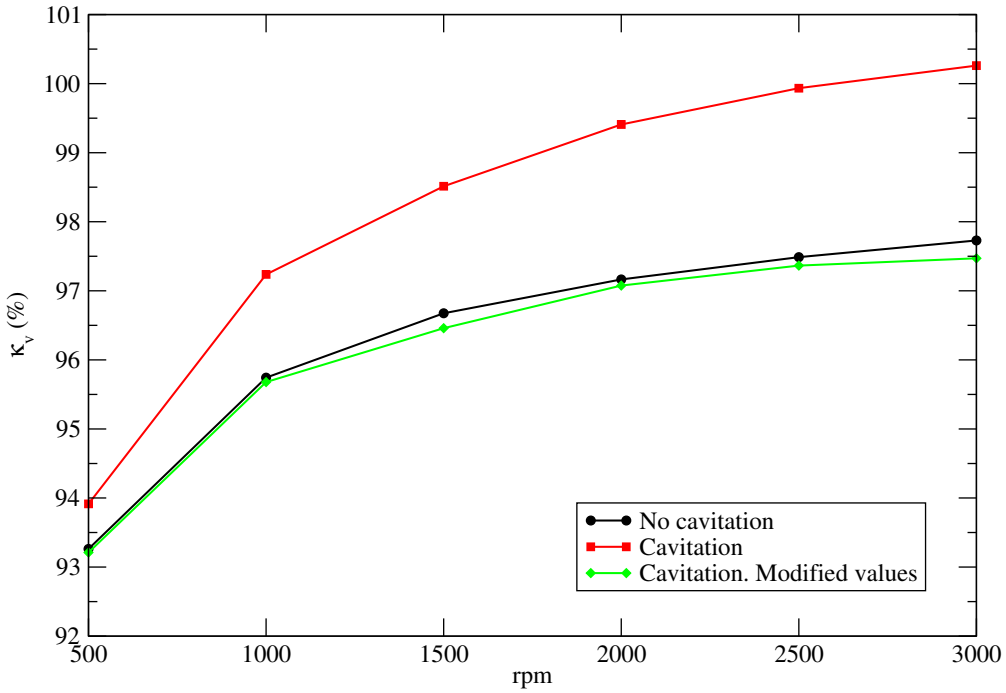

Figure 6.17: Volumetric ratio against operating velocity with and without cavitation effects, and modified volumetric ratio (according to equation 6.1) subtracting the effect of the volume of air trapped in the squeeze volume at the beginning of the gearing cycle.

- Even the smallest air content very effectively damps the water hammer fluctuations associated to the jump in the contact point position.
- Flow and therefore pressure oscillations due to cavitation are noticed at the outlet.
- The main cavitation mechanism is the low pressure that appears in the volumes opening towards the suction side in the meshing region, in order to fill them. At relatively high rotational speeds, flow separation at the gear's tips that advance towards the inlet becomes another source of cavitation.
- The mean air volume rapidly increases with the rotational speed, as flow velocity also increases. The higher the pump speed, the shorter the time for cavitation clouds to dissipate before a new cavitation mechanism takes place, and therefore the more stable the air volume content becomes.
- The inlet flow increases with positive net mass transfer rate from vapor to liquid and vice versa. Therefore, the more stable the air content, the lower the inlet flow irregularity.
- Before the end of a gearing cycle, some amount of gas appears at the backlash clearance between the gears due to the oil jet that takes place in order to fill the increasing volume that is found next to the contact point. This cloud acts as a virtual second contact point, blocking the backward oil flow and therefore increasing the outlet flow rate.
- The effect of this virtual contact point is that of increasing the volumetric efficiency, which may even become larger than unity, as the cavitation mechanisms are not taken into account when defining the theoretical volumetric capacity of the pump (for this reason we have renamed the volumetric efficiency as "volumetric ratio").

- When allowing cavitation, the volumetric ratio increases with the rotational speed, in a similar way as it does without cavitation effects.
- The volumetric ratio with cavitation is considerably higher than without it (with differences ranging from 0.65% at 500 rpm to 2.53% at 3000 rpm). These differences are mainly caused by the effect of the air generated at the backlash clearance.
- The air content which appears in the suction chamber has a very small effect on the volumetric ratio of the pump.

6.3 Outlet pressure effect

In section 6.2 we have seen that the inlet flow perturbation caused by cavitation propagates towards the pressure side, necessarily through the gear's tip clearances. It should be noticed that a mean pressure jump of 10 bar has been imposed, which corresponds to an absolute pressure of 11 bar at the outlet. Taking into account that typical operating pressures in the pressure side of real pumps are much higher and tip clearances are generally smaller, we suppose that in practical cases outlet pressure and flow ripples should not be so much affected by cavitation.

In order to check this, we will present the results of simulating the gear pump at 1000 rpm, with and without simulating cavitation, when imposing a mean pressure jump of $\Delta p = 100\,\text{bar}$. This outlet boundary condition has been imposed, as in the prior cases, by calculating the corresponding loss factor from equation 4.48, which now takes the value $k_{L,out} = 11580$.

In figure 6.18 the gauge outlet pressure evolution has been plotted for the numerical simulations with and without cavitation effects. It is clear that in this case cavitation does not affect the outlet pressure at all. Unlike what was seen at 10 bar, the negative pressure peak associated to the contact point position jump is not damped now. Neither appears any pressure perturbation associated to the change in air volume around $0.6 - 0.7T_g$. The flow perturbation of the suction side of the pump cannot easily propagate through the outlet when a 100 bar pressure is imposed, despite the relatively wide tip clearances.

Once seen that the large outlet perturbations observed in section 6.2 should not worry us much, as they disappear at higher working pressures, lets analyze now the volume of air and the flow rate at the inlet.

In figure 6.19 the volumetric flow rate compared to the mean theoretical one is shown both at the inlet and at the outlet of the pump. The flow behavior at the inlet is totally analogous (except for a slightly noisy pattern) to that shown in figure 6.3 for the 1000 rpm case, where cavitation completely damps the initial ripple associated to the jump in the contact point position and two flow peaks appear, at the approximate positions $0.3T_g$ and $0.8T_g$. This means that increasing the outlet pressure does not seem to affect the flow pulsation patterns at the inlet. Regarding the outlet, on the contrary, flow remains unaffected by cavitation (as could be deduced from the outlet pressure curve through the boundary condition). It is also seen how the higher outlet pressure reduces the flow (and pressure) irregularity.

The volume fraction of oil contour plots for this case are shown in figure 6.20. It can be seen that, in the suction side, the cavitation behavior stays very similar to that shown in figure 6.6 for the

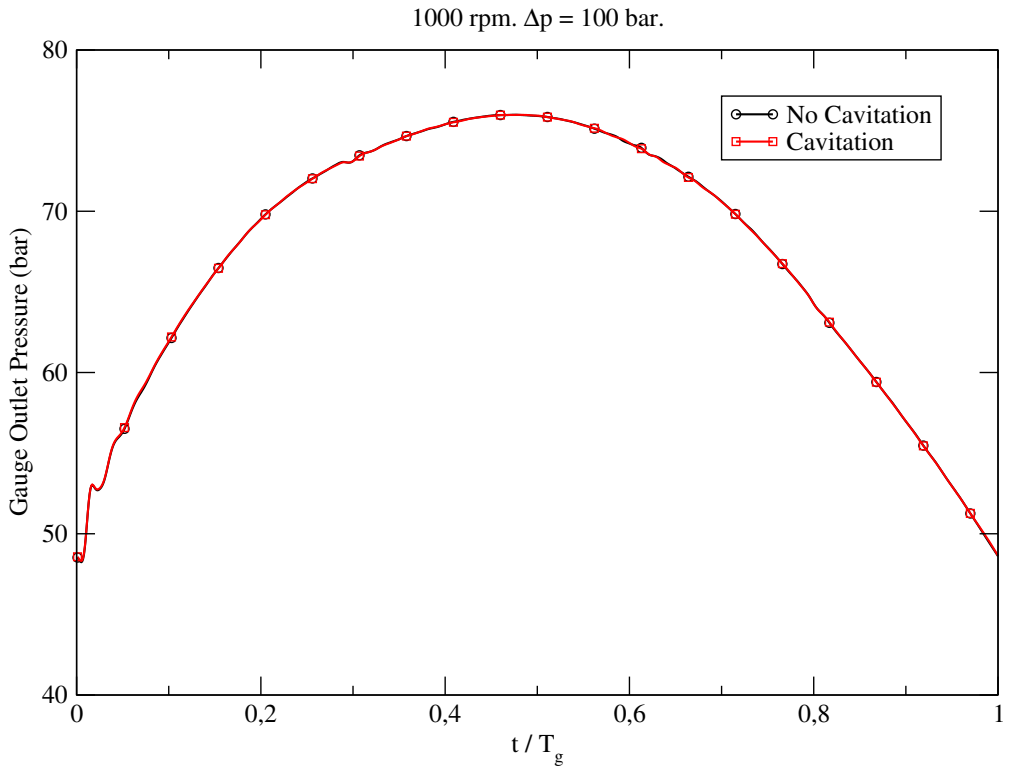

Figure 6.18: Gauge outlet pressure evolution at 1000 rpm and 100 bar pressure jump with and without cavitation effects.

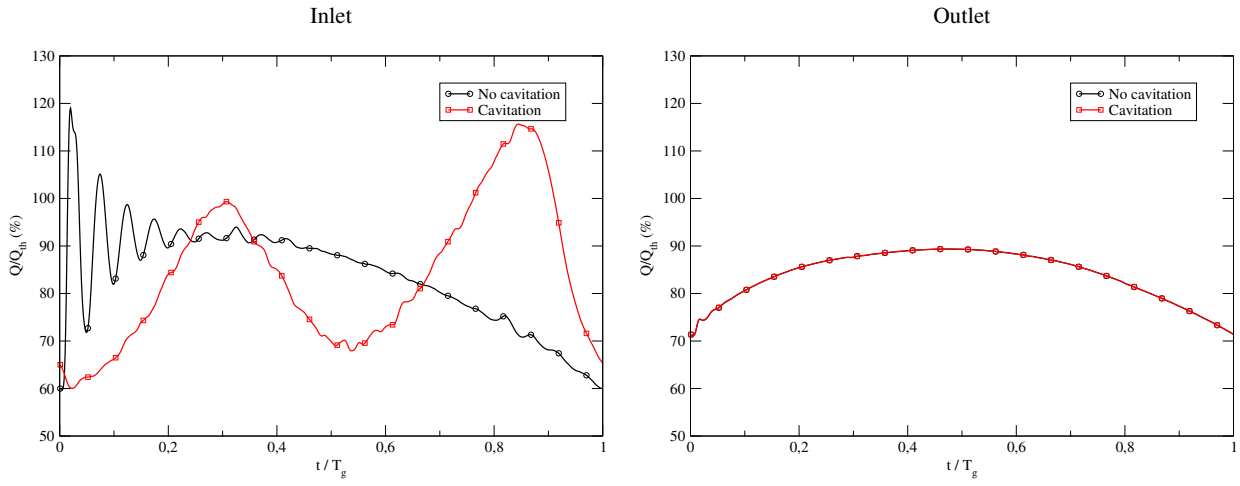

Figure 6.19: Inlet and outlet flow rates at 1000 rpm and 100 bar pressure jump with and without cavitation effects.

10 bar pressure jump case. Therefore the same comments about cavitation mechanisms, volume of air, and dissipation characteristic times that were done for that case apply here. As the inlet pressure is kept unchanged, these results should not surprise us. Nevertheless, it is seen that the small cavitation cloud that was appreciated at the backlash clearance at $0.9T_g$ (in figure 6.6) and acted as a virtual contact point, can't be seen now. As the region in which this cloud appeared belongs to the pressure side, and now our outlet pressure is much higher, the pressure drop that takes place at the jet that passes through the backlash clearance is not enough to reach cavitation conditions.

Figure 6.21 shows the relative air volume evolution for the case with a 10 bar mean pressure jump and the one with a 100 bar one. It can be seen that volume of air evolution has the same tendency in both cases, and that the peaks appear at the same positions. Once more, the derivative of the volume of air shows to be directly related to the flow rate shown in figure 6.19. The effect of a higher outlet pressure is just very slightly noticed on the suction side where the main relative volume of air only diminishes from 0.140% at 10 bar to 0.132% at 100 bar, which is an almost negligible difference.

Once we have observed that the effect of high outlet pressure doesn't affect too much to the cavitation characteristics or the pump, neither to the inlet flow rate pattern, lets observe the volumetric ratios. In table 6.4 these values are shown and compared to those obtained with a 10 bar mean pressure jump. We can see that both allowing and preventing cavitation, volumetric ratio drops in more than 10% when a 100 bar pressure jump is applied. So, while the instantaneous flow pattern keeps very similar from one case to another, the mean value of the volumetric flow drops very much, due to the tip clearance leakage flow given by equation 3.12 (which is proportional to the pressure jump). Also, we can see that while, at 10 bar, cavitation increases the volumetric ratio in 1.5%, at 100 bar, the difference becomes almost negligible (only 0.03% more efficiency with cavitation).

The very strong effect of the gear tip leakage on the volumetric ratio due to high pressure jumps has been used to justify the selection of a low working pressure for our simulations (as it was assumed that cavitation takes place mainly in the suction side). Nevertheless, fact of finding very similar volumetric ratios with or without cavitation when simulating a high working pressure, is mainly related to the absence of a cavitation cloud on the backlash clearance (which acted as a virtual contact point at low pressure therefore increasing the outlet flow). In conclusion, we have seen that the beneficial effect of cavitation requires the presence of a cavitating jet at the pressure side, and is therefore subjected to relatively low working pressures.

In most of the oleohydraulic applications of external gear pumps the working pressure is not as low at 10 bar. Nevertheless, low working pressure gear pumps can be found in combination with piston pumps that work in low inlet pressure conditions. These pumps are employed to provide a sufficiently high inlet pressure to the piston pump in order prevent the risk of cavitation. Moreover, the study performed at low working pressure has helped us to understand how cavitation affects the volumetric displacement performance of external gear pumps.

In conclusion, the following points regarding the mean outlet pressure imposed should be noticed:

- The strong effect of cavitation on outlet flow and pressure ripples seen at low operating pressure disappears when a higher outlet pressure is imposed.

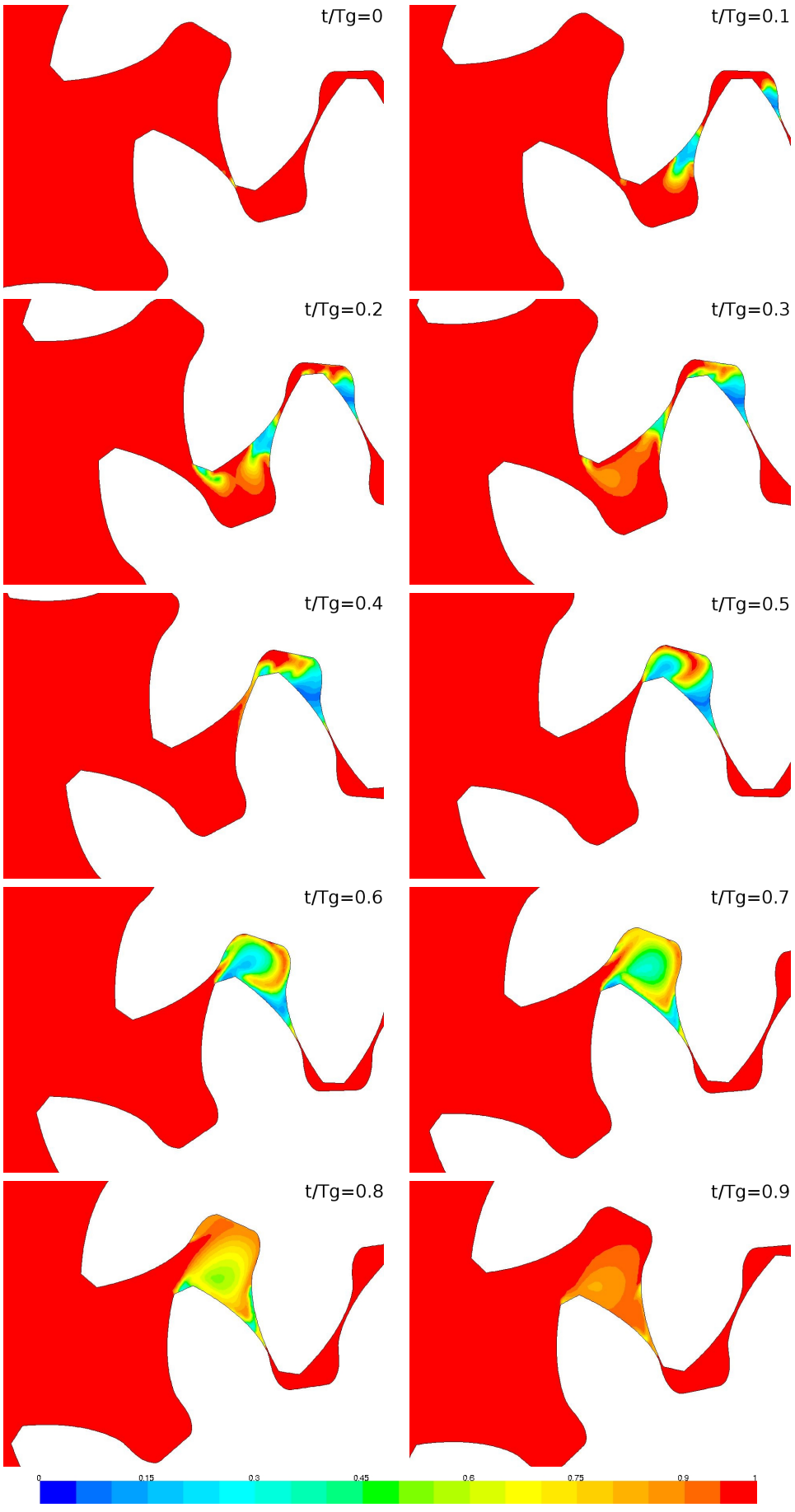

Figure 6.20: Volume fraction of oil at 1000 rpm and 100 bar pressure jump each 1/10 of a gearing cycle.

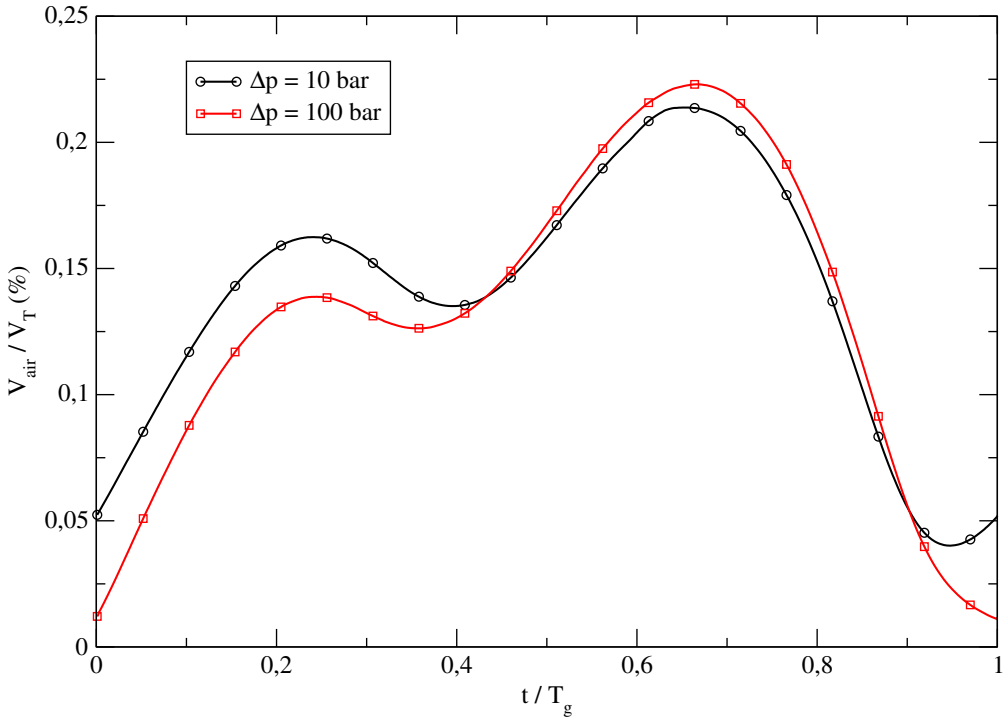

Figure 6.21: Relative volume of air evolution at 1000 rpm with 10 bar and 100 bar pressure jumps.

	$\Delta p = 10\,\text{bar}$	$\Delta p = 100\,\text{bar}$
No cavitation	95.74	83.91
Cavitation	97.24	83.94

Table 6.4: Volumetric ratios (%) at 1000 rpm for 10 bar and 100 bar pressure jumps with and without cavitation effects.

- Inlet flow and pressure ripples, volume of air evolution, and the morphology and air content of the cavitation clouds, are not significantly affected by the mean outlet pressure, with the exception of the cavitating jet that was found in the backlash clearance, which may not be present at high working pressure.

- Volumetric ratio is highly reduced at high operating pressure because of the gear tip leakage, especially in our case in which the tip clearance width is relatively high. This fact is independent from cavitation.

- The volumetric ratios at high operating pressure are very similar with or without cavitation, as the virtual contact point created by the cavitating jet at the backlash clearance at low operating pressure, which acted as a virtual contact point, is no longer present at high operating pressure.

6.4 Alternative inlet chambers

In this section, four alternative inlet chambers will be presented and numerically simulated. The influence of the inlet chamber geometry in cavitation and volumetric ratio will be studied. Each inlet chamber has been simulated at the same rotational speeds as the reference one, which was

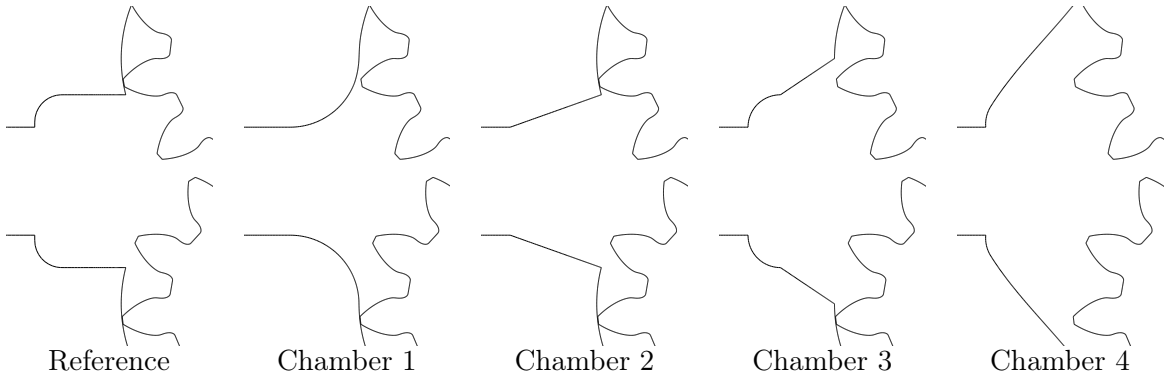

Figure 6.22: Inlet chambers.

Inlet chamber	Pump total volume (cm^3)
1	144.38
2	145.06
Ref	148.23
3	150.63
4	157.34

Table 6.5: Total volume of each gear pump.

analyzed in section 6.2, allowing cavitation. They have also been simulated at 1500 rpm preventing cavitation, in order to check up to which extent the change in the suction characteristics from one inlet chamber to another is related to cavitation. As with the cases analyzed in section 6.2, a mean pressure jump of 10 bar is imposed.

The meshes used for simulating the alternative inlet chambers were already presented in figures 4.12, 4.13, 4.14 and 4.15. The chamber geometries are presented in figure 6.22. The total volume of each gear pump is shown in table 6.5. Chambers are ordered from smaller to bigger, being numbers 1 and 2 smaller than the reference one and 3 and 4 bigger. Figure 6.23 shows the streamlines in all the inlet chambers at 1500 rpm and $0.5T_g$ with cavitation effects. It can be seen that the lateral vortices adapt their size and geometry to the chamber shape in such a way that the flow pattern in the central region, through which the meshing region is filled, remains very similar in all cases.

One one hand, it can be thought that these vortices may help to damp the flow and pressure perturbations that travel upstream from the gearing region, therefore reducing the irregularity and increasing the volumetric ratio. On the other hand, it can also be thought that, the more directly flow is guided into the pump, the bigger the inlet velocity should be, therefore, more efficiently filling the inter-teeth volumes and increasing the volumetric ratio. In this section we will try to clarify if any of these suppositions is realistic.

Firstly, the inlet and outlet flow rates obtained when cavitation is not simulated will be analyzed. Figure 6.24 shows these flow rates for the reference chamber and the four alternative ones at 1500 rpm. Having an inlet chamber bigger than the reference one slightly damps the amplitude of the water hammer that travels upstream just at the first peak after the contact point position jump, as the amplitude of the first pressure peak is smaller for chambers 3 and 4 than for the others. At the rest of the peaks the flow pulsation amplitude remains unchanged. A more noticeable effect associ-

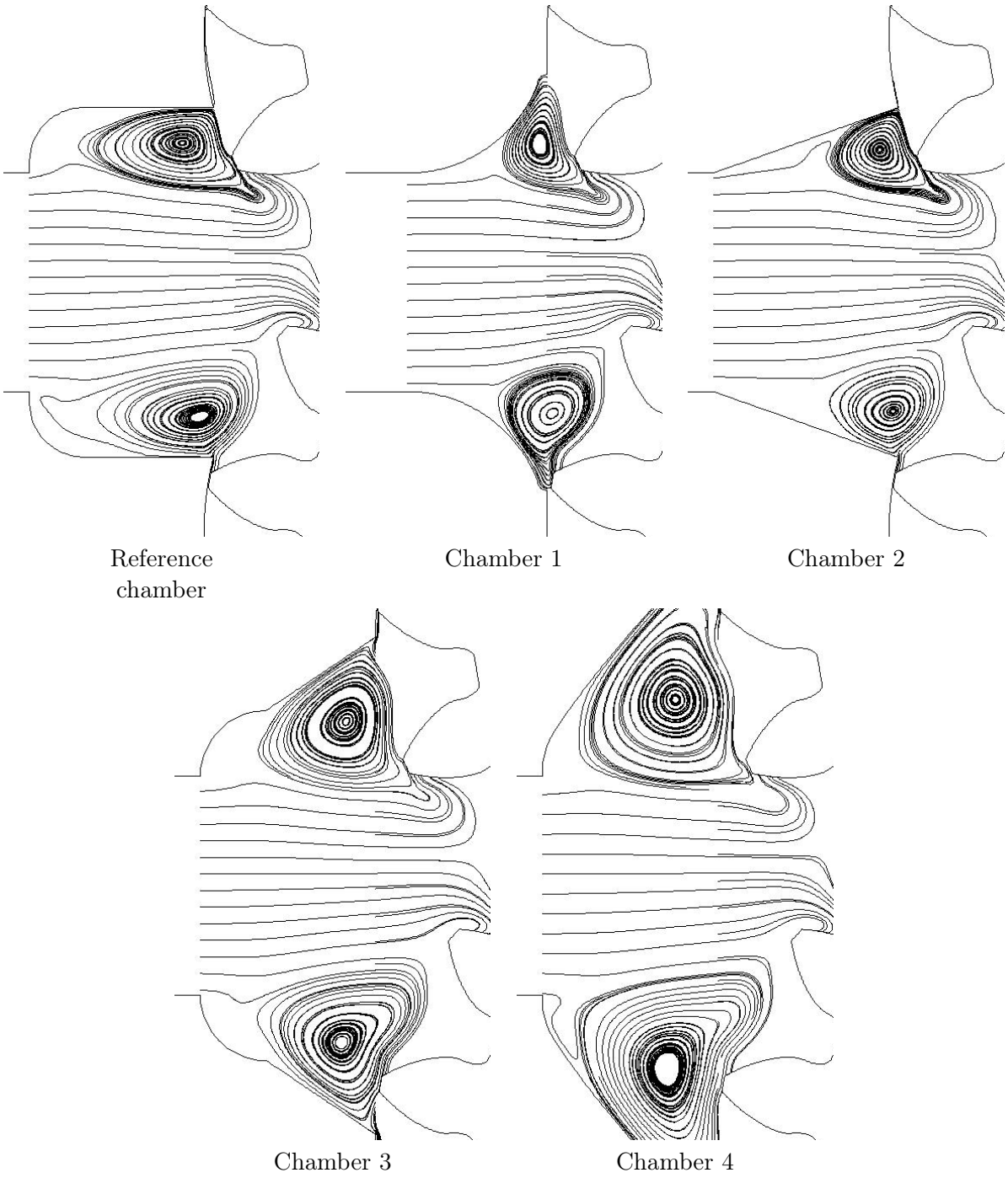

Figure 6.23: Streamlines in the inlet chambers at 1500 rpm and $t/T_g = 0.5$ with cavitation effects.

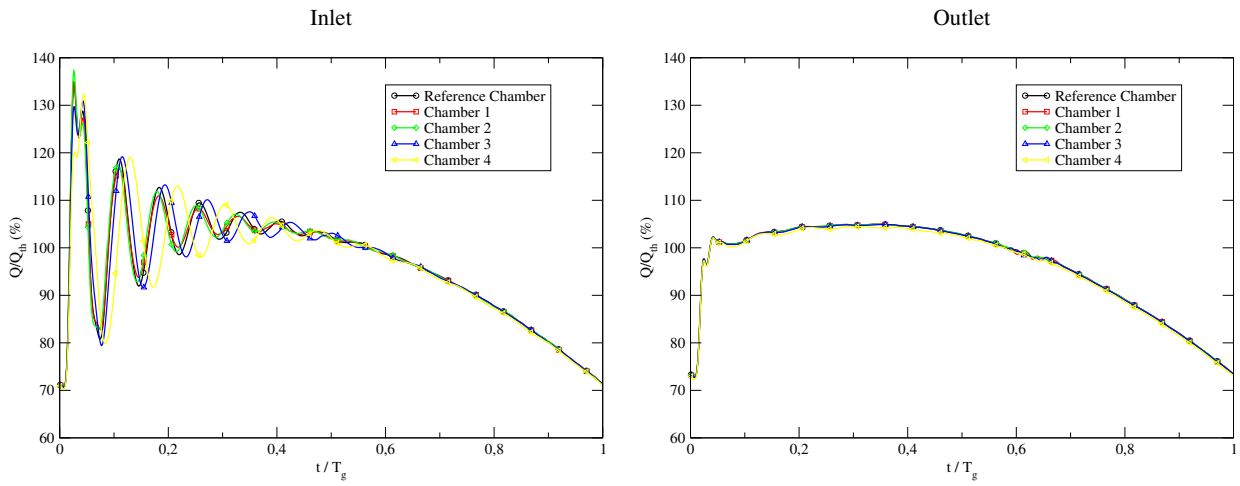

Figure 6.24: Inlet and outlet flow rates of all the pumps at 1500 rpm with no cavitation effects.

ated to the bigger inlet chambers is a reduction on the frequency of the water hammer. The smaller frequency corresponds to chamber 4 and the next smaller one to chamber 3. All perturbations can be considered almost totally damped by $0.5T_g$. Regarding the chambers that are smaller than the reference one (chambers 1 and 2), the inlet flow remains almost unchanged with respect to the one of the reference pump. Therefore, it seems that, independently from the influence of cavitation, a bigger inlet chamber has a damping effect on the upstream water hammer perturbation, which is appreciated mainly in a frequency reduction, but very slightly in the amplitude of the perturbation.

Regarding the outlet flow, it is observed that the fact of changing the inlet chamber has no effect on the outlet flow ripple. The outlet pressure evolution has not been plotted as it is analogous to the flow one (as imposed by the boundary condition), and therefore also independent from the inlet chamber.

In figure 6.25 the inlet flow rate of all the pumps at different rotational speeds with cavitation effects is shown. It is seen that the inlet flow ripple is rather independent from the inlet chamber geometry. Therefore, the same effects that were observed and commented in section 6.2 for the reference chamber are also present in the new geometries.

In figure 6.26 the relative volume of air evolution of all the pumps at different rotational speeds is shown. The origin and scale of the vertical axis has been adjusted for each speed in order to better appreciate the evolution of the variable. It is seen that the effect of having one chamber or another is only noticed on a small shift of the curve, but not on its shape. This means that bubble growth and implosion phenomena, which phases were commented for each rotational speed in section 6.2 is similar for all the inlet chambers. This is not surprising, as bubble growth and implosion takes place locally, in the meshing region, which is relatively far away from the inlet chamber walls. The only appreciable difference from one chamber to another is a shift in the mean value, which will be better analyzed with the help of the next figures.

Figure 6.27 shows the relative volume of air at each rotational speed for the different inlet chambers. We can see that the bigger the chamber, the lower the relative volume of air. This is only caused by the fact that we are dividing by a higher volume. In fact, if we plot, in figure 6.28, the absolute mean air volume, we can see that the difference from one chamber to another is negligible. Therefore, again we can say that the cavitation process is almost not dependent on the shape or volume of

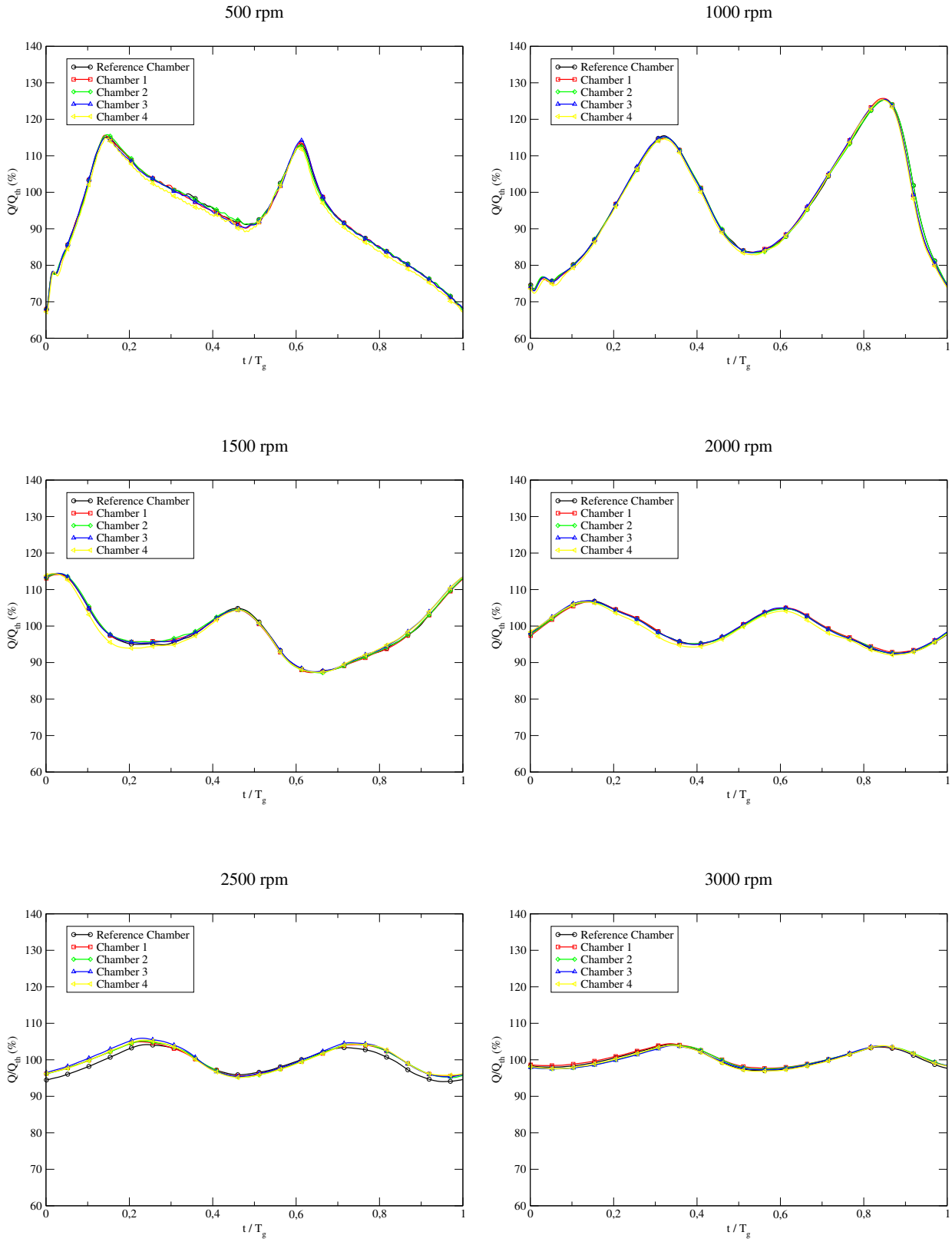

Figure 6.25: Inlet flow rate of all the pumps at different rotational speeds with cavitation effects.

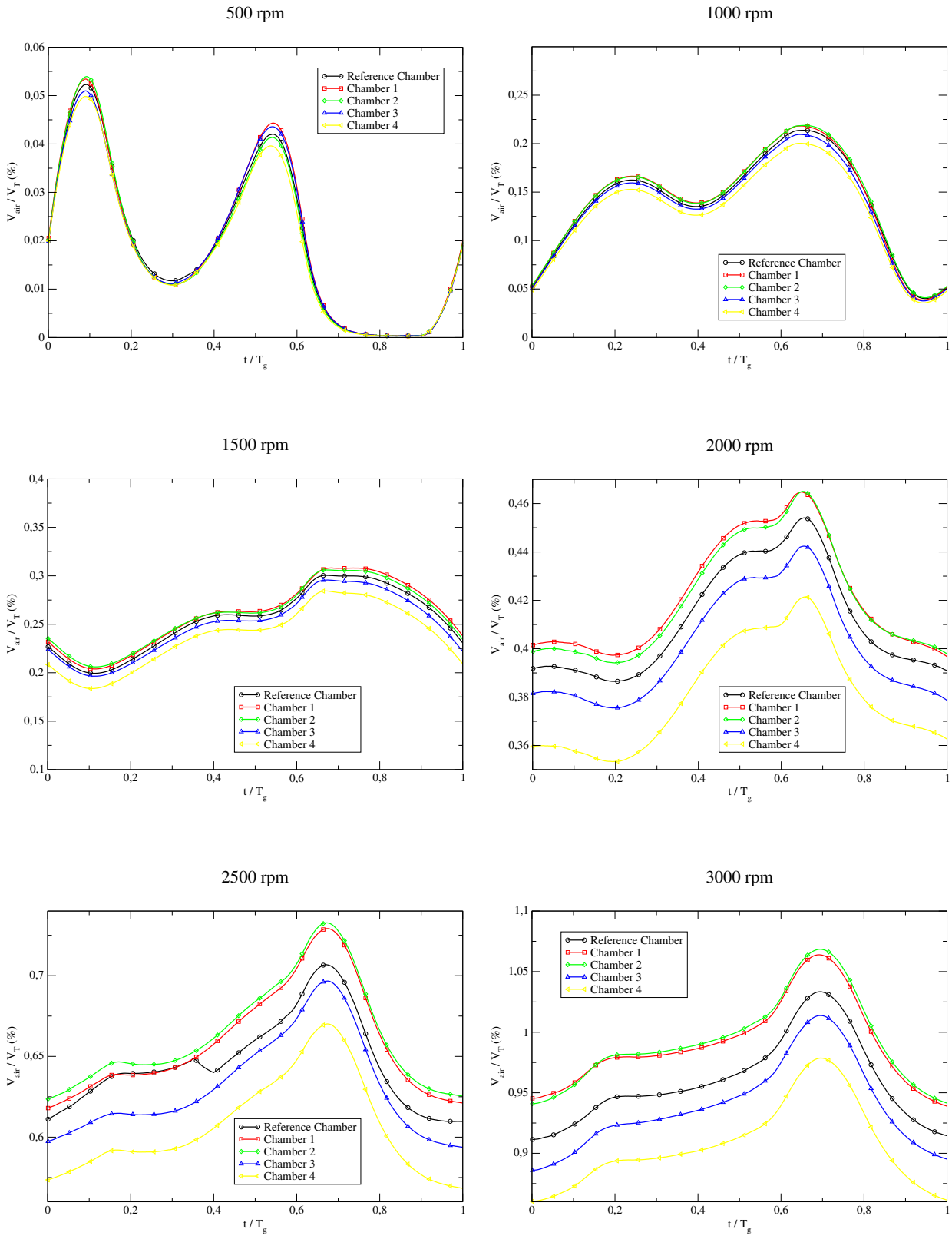

Figure 6.26: Relative volume of air evolution of all the pumps at different rotational speeds.

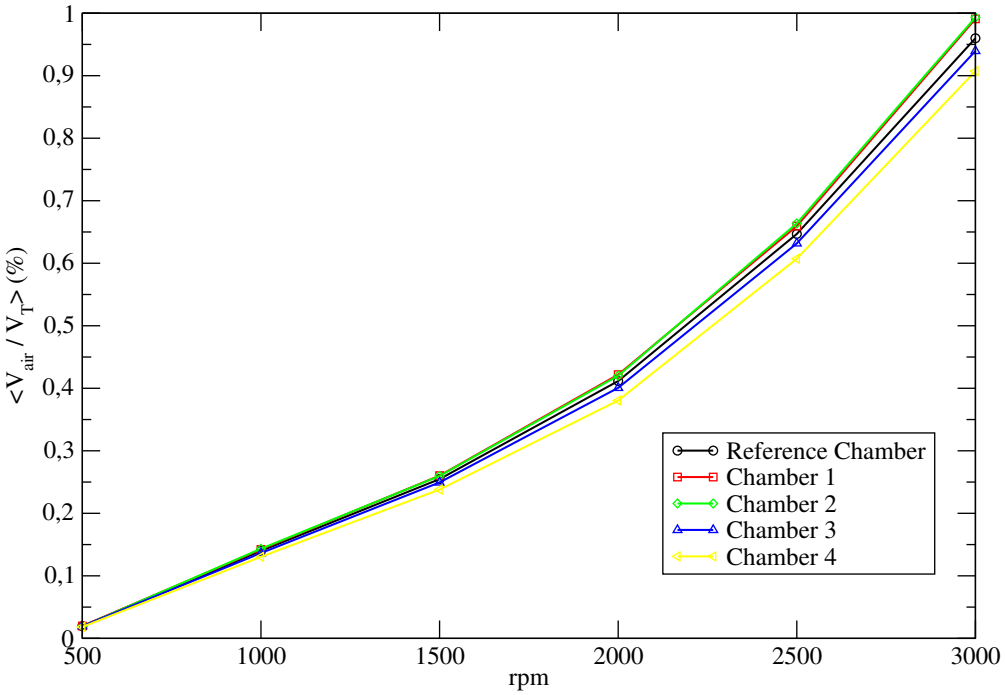

Figure 6.27: Relative volume of air of all the pumps against rotational speed.

the inlet chamber, as both the mean value and the evolution of the volume of air is, for a given rotational speed, very similar in all cases. The reason why the shape of the chamber does not affect to its air content is that we are simulating with a constant inlet pressure. When cavitation is related to a variable lower inlet pressure, the shape of the inlet chamber should influence the air content. In our case, cavitation is only related to the gear's meshing action and does not extend upstream sufficiently to appreciate an influence of the chamber geometry.

In figure 6.29 the volumetric ratio at each rotational speed for the different inlet chambers is shown. It is seen that for inlet chamber 4 (the bigger one) volumetric ratio is lower than for any other chamber at all speeds (around 1% lower than the reference gear pump at speeds below 2000 rpm, and around 0.3% lower at higher speeds). For the rest of the chambers we find that volumetric ratio is almost the same as for the reference one at all speeds, except for the slightly higher volumetric ratio of chamber 3 at 2500 rpm and of chamber 1 at 3000 rpm.

In section 6.2 we showed that the influence of cavitation in the volumetric ratio is mainly related to the cavitating jet that may appear in the backlash clearance before the end of the gearing cycle. This is a local phenomenon which depends on the rotational speed and the working pressure of the pump, but shouldn't be affected by the shape of the inlet chamber. Lets compare the volumetric ratios of all chambers with and without cavitation effects. This comparison is shown, for 1500 rpm (the only at which we have simulated all the chambers preventing cavitation), in table 6.6. We can see that the volumetric ratio drop from the reference chamber to chamber 4 is very similar with and without cavitation, although cavitation seems to have a slightly beneficial effect. Therefore, this fact seems not to be much related to cavitation. For the rest of the chambers the volumetric ratio is not much altered from one to another, both allowing or preventing cavitation. Nevertheless, again cavitation seems to have a very slightly beneficial effect, but we cannot assure this, as just for chamber 3 this effect would be slightly above the mass imbalance tolerated according to our

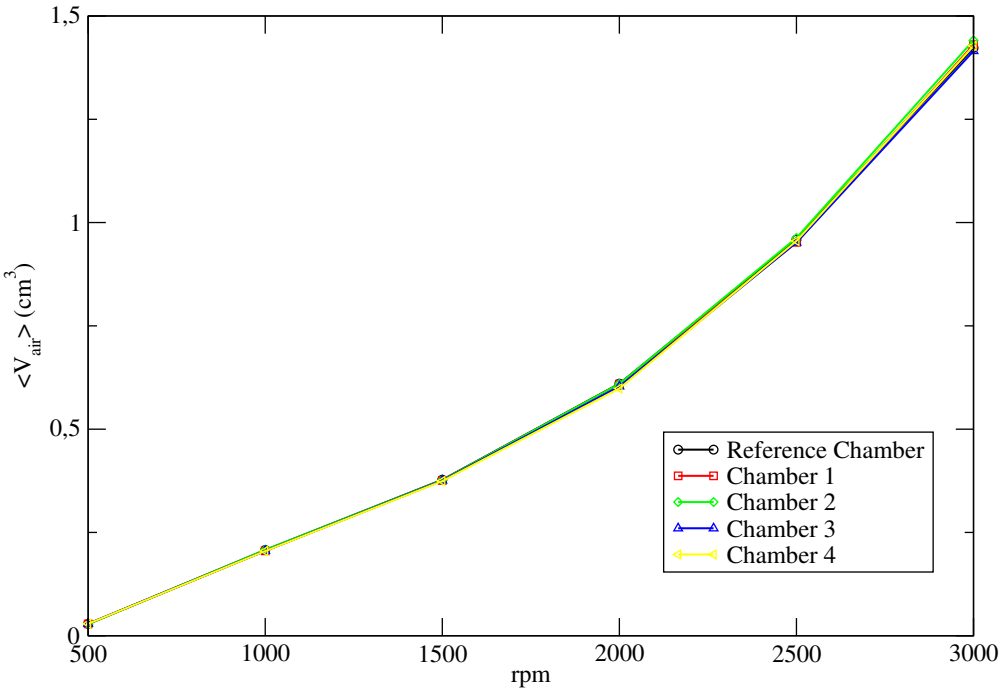

Figure 6.28: Absolute volume of air of all the pumps against rotational speed.

	No cavitation		Cavitation	
Chamber	κ_v (%)	$\kappa_v/\kappa_{v,ref}$ (%)	κ_v (%)	$\kappa_v/\kappa_{v,ref}$ (%)
Reference	96.674	-	98.514	-
1	96.634	99.96	98.505	99.99
2	96.669	99.99	98.603	100.09
3	96.604	99.93	98.652	100.14
4	96.211	99.52	98.171	99.65

Table 6.6: Absolute and relative volumetric ratios of all the pumps at 1500 rpm.

convergence criteria.

The lower volumetric ratio found when using chamber 4 should be then related to gear tip losses. We have seen in subsection 3.5.3 that the main contribution to gear tip leakage is proportional to the pressure jump between two inter-teeth volumes (equation 3.12), and that this pressure jump is the operating pressure jump of the pump divided by the number of teeth adjacent to the casing (equation 3.11). In the pump with inlet chamber 4 a bigger part of the gear is open to the inlet chamber, compared to the others, and therefore the area of the casing adjacent to the gear's tips is smaller, causing a higher pressure jump at both sides of each tip and consequently higher losses. In inlet chamber 2, this area is exactly the same as the one of the reference inlet chamber. In chambers 1 and 3, it is smaller, but as the difference in these cases is very small, this effect is not noticed. Nevertheless, if the effect of circumferential grooves or of gears eccentricity was simulated, all the pressure drop between teeth would be concentrated at a single tooth in each gear, and therefore this effect would not appear.

Lets now try to figure out if the shape of the chamber is related to the acceleration of the fluid when reaching the meshing region. In figure 6.30 the evolution of the horizontal[1] velocity at control

[1]Refers to the direction given by the pipe axis.

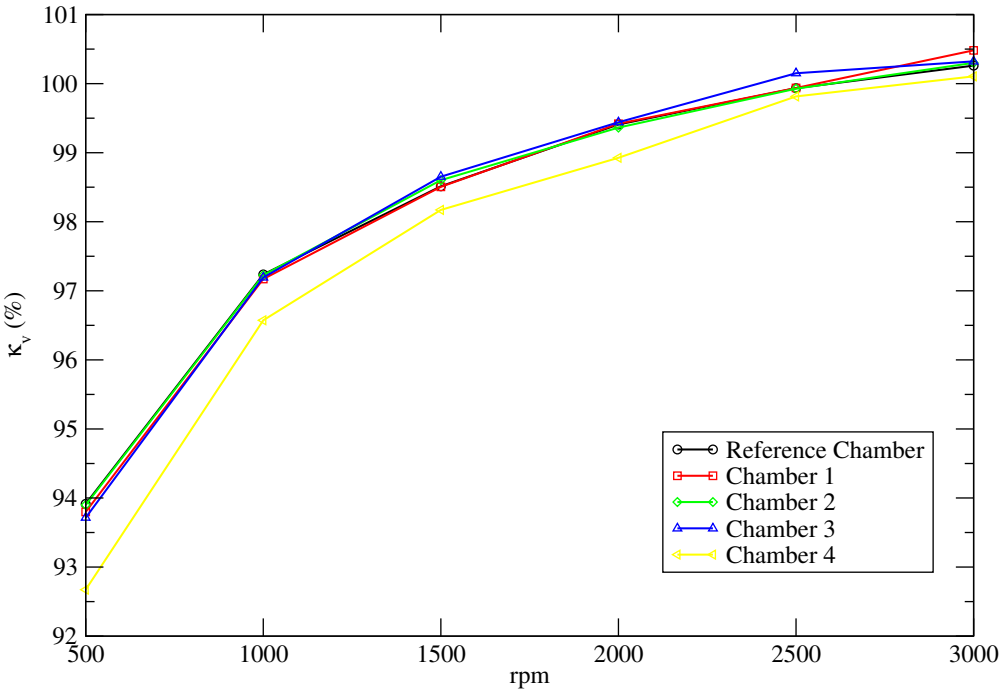

Figure 6.29: Volumetric ratio of all the pumps against rotational speed.

point P is shown. The position of this point was shown, for the reference chamber, in figure 4.9. This point is placed in the symmetry axis of the pipes, 26 mm upstream the pitch point, in all the geometries studied.

The main difference from one inlet chamber to another is found in the mean value of the velocity. The shape of the curves, both allowing or preventing cavitation, is very similar. These shapes are also very similar to the ones of the flow rate curves. When cavitation is prevented, a strong fluctuation associated to the water hammer already studied appears at the beginning of the gearing cycle. The first peak of this fluctuation is especially high compared to the rest, as the control point is close to the contact point. When cavitation is allowed, a more uniform behavior is observed: the peaks associated to the jump in the contact point position disappear (even the first one despite the position of the control point), but other fluctuations associated to the temporal derivative of the volume of air appear. As with the inlet flow rate, it can be seen that the local maximums of this velocity are associated to minimums of the volume of air temporal derivative. Therefore a direct relation between the horizontal velocity at point P and the inlet flow rate is observed. Nevertheless, this relation includes the temporal evolution but not the mean values, as those differ from one inlet chamber to another. The lower velocity is found with chamber 1 and the higher one with the reference chamber. If, for the moment, we only take into account chambers 1 and 2 and the reference one, it seems that up to a certain point the more the chamber opens when approaching the gear's zone, the higher the velocity at the control point. With inlet chamber 3, the limit of this effect seems to be reached, as the chamber continues to open into the gear zone but no higher velocity is obtained at point P. With chamber 4 the velocity at point P continues dropping and it reaches the same level as in chamber 2. In this last case, the effect of a lower volumetric ratio (of flow coming from the gear's tip clearances and pushing backwards) may also have some influence.

In conclusion, the following points regarding the cavitation and suction characteristics of the differ-

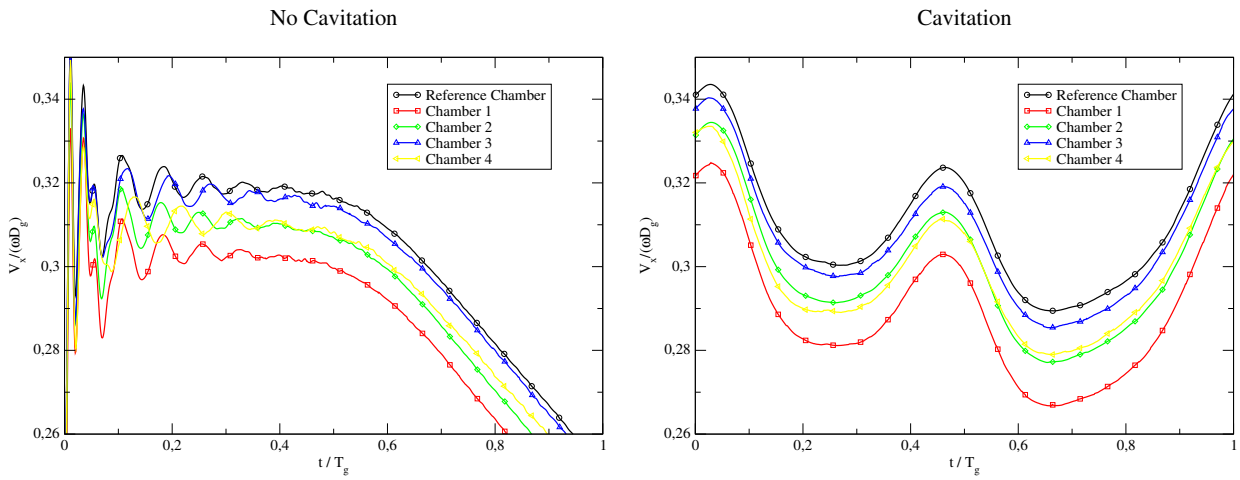

Figure 6.30: Evolution of the non-dimensional horizontal velocity at control point P (shown in figure 4.9) along a gearing cycle at 1500 rpm with and without cavitation effects.

ent inlet chambers should be noticed:

- When preventing cavitation, it is observed that bigger chambers have an effect in reducing the inlet water hammer frequency.
- No significant difference is seen in the outlet when using one or another inlet chamber, both when allowing or preventing cavitation.
- The flow patterns in the central region of the inlet chamber, through which the meshing region is filled, remains very similar for all chamber geometries.
- The evolution of the absolute volume of air and the cavitation clouds morphology and air content are not significantly affected by the inlet chamber geometry.
- The volumetric ratio is very similar for all inlet chambers except for number 4 (the bigger one). The volumetric ratio reduction obtained with this chamber is very similar with and without, and is related to the lower area adjacent to its casing, which increases the pressure jump between teeth and therefore the gear's tip leakage.
- For the smaller chambers, up to the reference one, as the inlet chamber grows in size and opens towards the gearing zone, the acceleration of the fluid reaching the meshing region increases. For the bigger ones, more open chambers have the opposite effect. This acceleration is unrelated to the volumetric ratio.

6.5 Inlet pressure effect

Up to now, a major conclusion extracted from our simulations is that cavitation has a beneficial effect on uniforming the flow rate and that, at low working pressure, it may increase the volumetric ratio through the effect of the cavitating jet at the backlash clearance, which acts as a virtual contact point. This effect is therefore related to the air contained in the squeeze volume. It was seen that the air contained in the inlet chamber doesn't affect much to the volumetric ratio.

In the simulations already presented, we have imposed a constant atmospheric inlet pressure, which means that the inlet pipe and the major part of the inlet chamber should be operating at a pressure near to atmospheric and therefore cavitation cannot take place there. We have therefore simulated one cause of cavitation, which is related to the locally low pressures that appear in the meshing region due to the opening volumes and flow separation at the teeth tips. When a pump operates with a lower inlet pressure (i.e. when absorbing fluid from a tank situated at a lower level) pressures in the inlet pipe and chamber get closer to vapor pressure, and therefore cavitation can appear upstream the gear's meshing region. In this case, if the suction force needed is sufficiently high, the available Net Positive Suction Head (NPSH) would be reached and the pump would be unable to operate. In this section we will analyze this source of cavitation with some simulations in which a lower input pressure is used.

The reference pump has been simulated at 1500 and 3000 rpm with the same conditions as in section 6.2 but using a loss factor also for the inlet boundary conditions. This coefficient is defined in an analogous way as the outlet one defined in section 4.12:

$$k_{L,in} = \frac{|\Delta p|}{\frac{1}{2}\rho v_{in}^2} \tag{6.2}$$

being v_{in} the time-averaged inlet velocity, which is estimated from the theoretical volumetric capacity of the pump, the rotational speed, and the outlet area. This factor represents an inlet impedance that has been calculated in order to obtain a 0.8 bar pressure drop when operating at 3000 rpm. This factor takes the value $k_{L,in} = 18.30$ and will be used for both the simulations at 1500 rpm and 3000 rpm. Therefore, at 3000 rpm, the pump should be operating with a mean inlet absolute pressure of 0.2 bar, which is relatively close to the pump limit, and cavitation should appear much more developed that in the case already presented, with atmospheric inlet pressure. At 1500 rpm this same value of $k_{L,in}$ represents a smaller pressure drop, of only 0.2 bar (the pressure drop is proportional to the inlet velocity squared, and therefore also to the rotational speed squared). The simulations at 3000 rpm have been performed both allowing and preventing cavitation, while the one at 1500 has been performed only allowing cavitation.

In figure 6.31 the inlet and outlet flow rates of these three simulations are presented and compared to those with constant inlet pressure conditions. It should be noticed that the inlet loss factor has been calculated in order to reduce the mean inlet pressure. Therefore, two effects are involved in the simulations with inlet loss factor: a reduction in the inlet mean pressure (of 0.8 bar for the 3000 rpm cases and 0.2 bar for the 1500 rpm ones) and the fact of allowing for an inlet pressure ripple.

Regarding the inlet flow rate at 3000 rpm when preventing cavitation, it can be seen that the water hammer that appeared with constant inlet pressure is still clearly appreciated, although its peak-to-peak amplitude is attenuated in around 25%, while its frequency is kept unchanged. Regarding the outlet, in the same case, it is seen that the inlet pressure has no effect on the flow rate.

At 1500 rpm, allowing cavitation, a very slight attenuation in the inlet flow ripple is appreciated when using an inlet pressure loss factor. The attenuation in this case is smaller than in the previous one, as the mean inlet pressure with loss factor is now just 0.2 bar below that of the case with constant inlet pressure. The outlet flow also remains unchanged in this case.

In order to clarify if cavitation has any effect in this attenuation of the flow ripple, lets take a look at

the inlet flow rate at 3000 rpm allowing cavitation. In this case it is seen that cavitation completely suppresses any flow ripple. In section 6.2 we have seen that the amount of air generated in the meshing region at 3000 rpm was enough to very strongly damp the pressure ripple that appeared when preventing cavitation. Now, as cavitation can extend further towards the inlet of the pump, the higher amount of air completely uniforms the flow rate. Regarding the outlet flow, once again both cases also present very similar fluctuations but now with a slightly lower mean value when an inlet loss factor is used. This difference is caused by the lower volumetric ratio obtained in this case, as it will be seen later.

In figures 6.32 and 6.33 the contour plots of volume fraction of oil are shown for 1500 and 3000 rpm respectively.

At 1500 rpm the contour plots look very similar to those of figure 6.7. In the opening volumes neighboring the contact point almost no difference is observed, and the cavitation clouds that appear are very similar in shape and air content to those of the case with the inlet at atmospheric pressure. This includes the ones that work as a virtual contact point. The main difference is seen in the clouds attached to the gear's tips advancing towards the inlet chamber. In this zone, further away from the meshing region, the pressure drop of 0.2 bar is noticed, and it is responsible for the generation of some cavitation clouds of low air content at the advancing tip of the lower gear at $0.2T_g$ and that of the upper tip at $0.6T_g$, as well as for increasing the amount of air content at the lower gear tip at $0.1T_g$. This shows that the 0.2 bar pressure drop is unimportant compared to the strong suction caused by the opening volumes, but is noticed in the cavitation limit related to gear-tip flow separation. In fact, this limit depends on the inlet velocity (as seen in section 6.2) and the pressure in the inlet chamber, which establishes the pressure drop needed to reach cavitation conditions.

At 3000 rpm we observe that cavitation with a pressure inlet loss factor, which yields a 0.2 bar average pressure, appears to be much more extended towards the inlet chamber when compared to the case with atmospheric inlet pressure (seen in figure 6.10). We have increased the field of view for this case in order to visualize all the cavitation that takes place in the suction chamber. We observe here that air almost completely fills the inter-teeth volumes in the meshing region and even extends to the neighboring volume upstream. Furthermore, high-air-content cavitation clouds at the gear tips due to flow separation appear at all positions, up to the point in which the gear tip reaches the casing. With such a big air cushion filling the meshing region, it can be understood how the volume variations of the suction side due to the gear meshing are not translated into volume of oil fluctuations and therefore the inlet flow remains constant, as already observed in figure 6.31. Moreover, a new effect is seen: due to flow separation, cavitation clouds appear at the corners between the inlet chamber and the casing. Therefore, with a mean inlet absolute pressure of 0.2 bar, relatively smaller accelerations of the fluid become enough to reach the vapor pressure.

This cavitation clouds attached to the inlet chamber corners get trapped between the advancing teeth and the casing when the next gear reaches their position and are carried towards the pressure side. This can be seen in figure 6.34. The trapped air, due to the action of centrifugal forces on the oil, travels to the bottom region of the inter-teeth volumes when being carried towards the pressure side. Before arriving to the suction side, when the tooth tip is close enough to the impulsion chamber, a low-air-density cavitation cloud appears at the top of the inter-teeth volume. This is

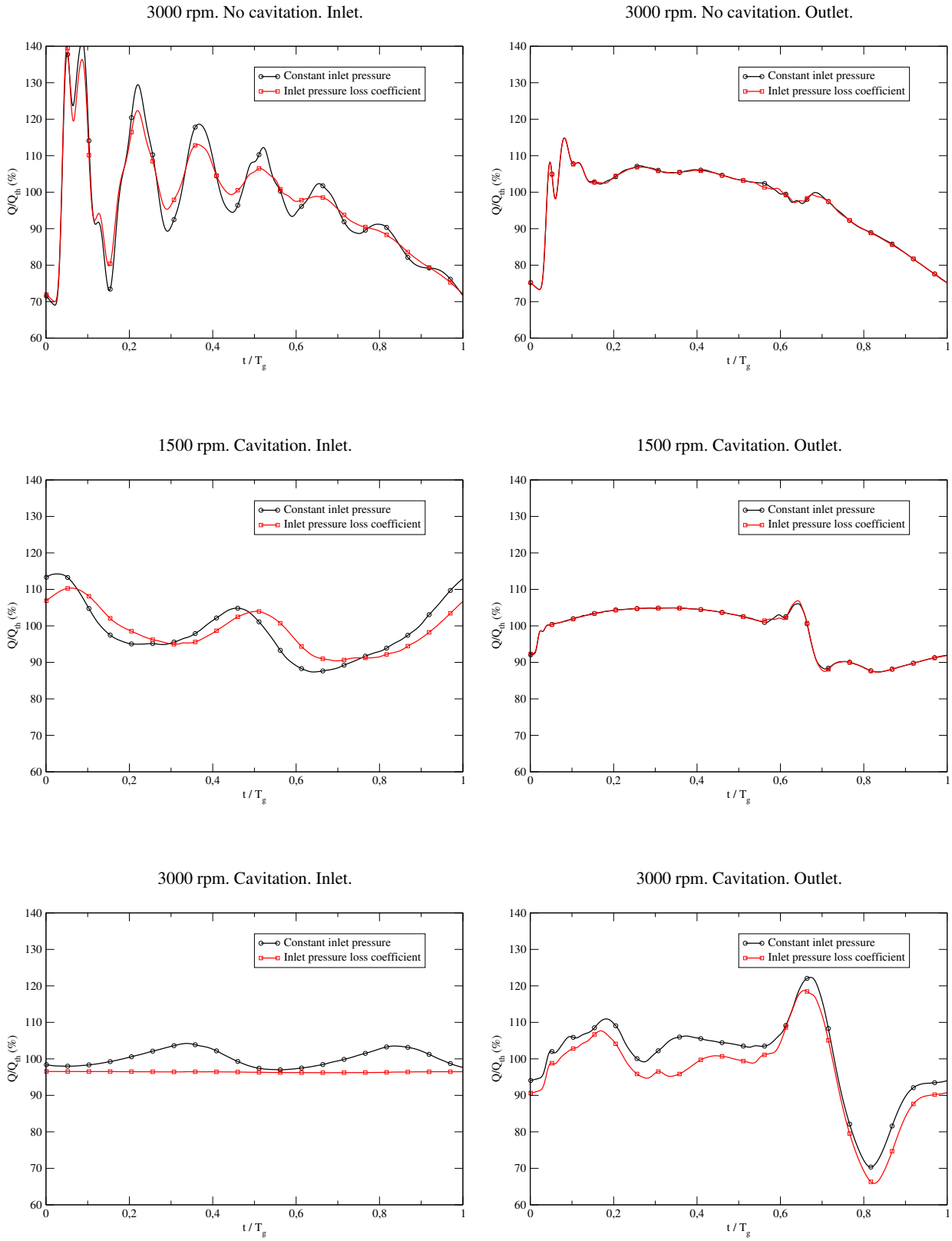

Figure 6.31: Inlet and outlet flow rate of the reference gear pump with constant inlet pressure and inlet pressure loss factor.

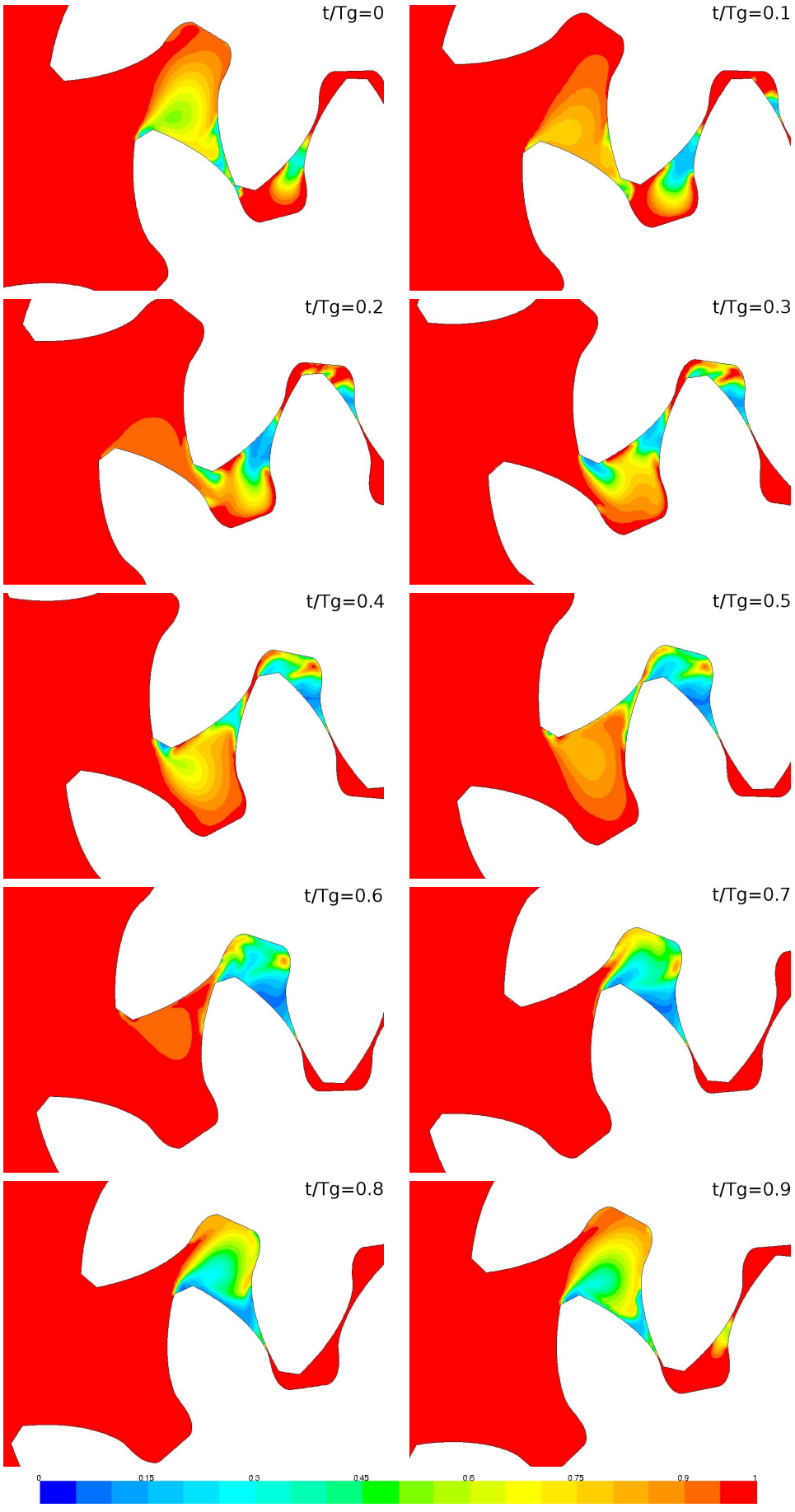

Figure 6.32: Volume fraction of oil at 1500 rpm each 1/10 of a gearing cycle with a pressure inlet loss factor.

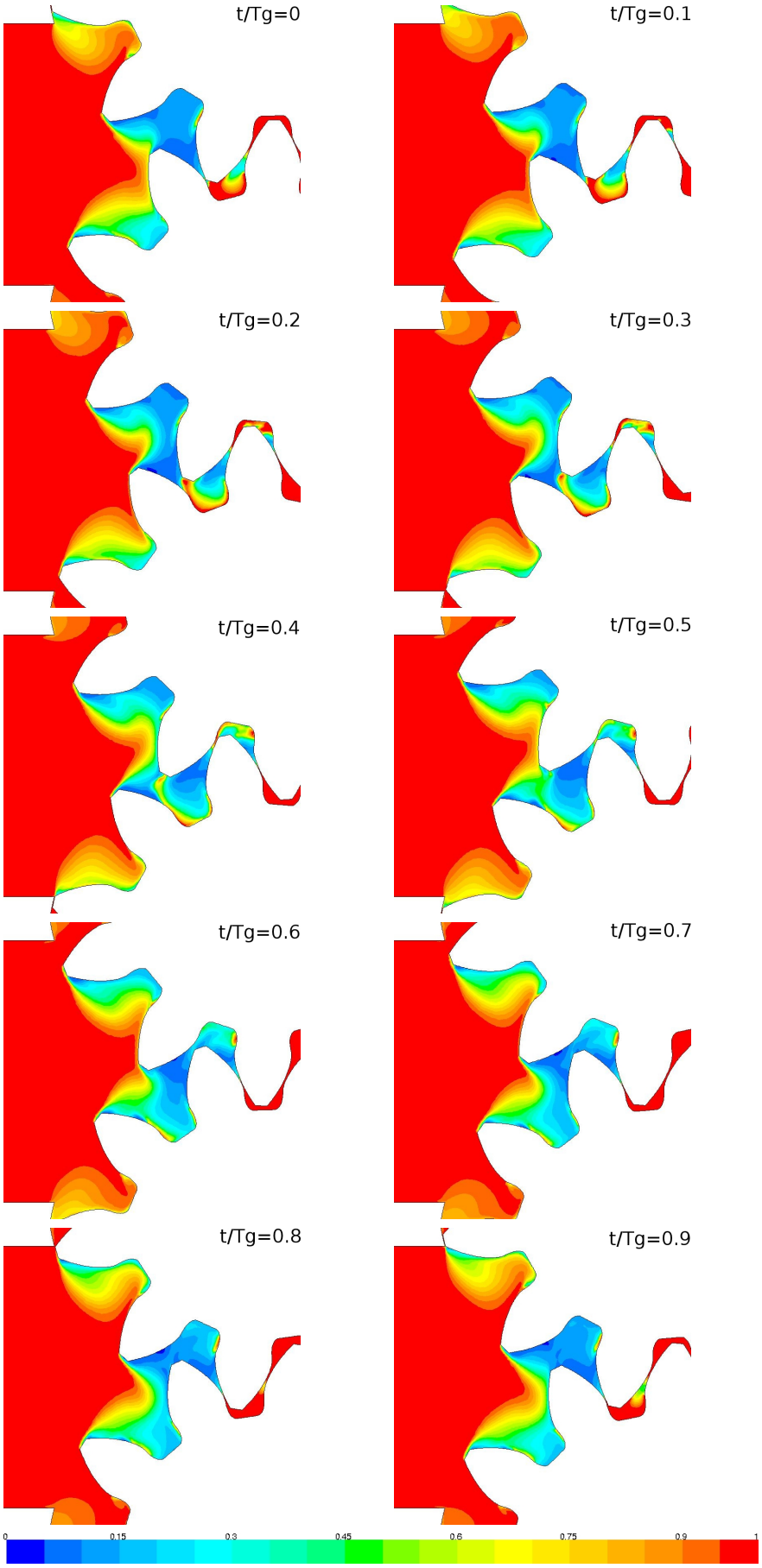

Figure 6.33: Volume fraction of oil at 3000 rpm each 1/10 of a gearing cycle with a pressure inlet loss factor.

		κ_v (%)		$\kappa_{v,mod}$ (%)	
rpm	Cavitation	Constant inlet pressure	Inlet loss factor ($k_{L,in} = 18.30$)	Constant inlet pressure	Inlet loss factor ($k_{L,in} = 18.30$)
1500	Yes	98.51	98.55	96.46	96.47
3000	No	97.73	97.66	-	-
3000	Yes	100.26	96.26	97.47	93.42

Table 6.7: Comparison of volumetric ratios with constant inlet pressure and with an inlet pressure loss factor.

due to the expansion caused by the entraining jet that comes from the impulsion chamber through the gear tip clearance. Nevertheless, we believe that if we had a narrower tip clearance this jet would not appear.

In table 6.7 the volumetric ratios of these cases are compared to those obtained with constant atmospheric inlet pressure. For the cases with cavitation, the modified ratios, given by equation 6.1, are also given. At 1500 rpm the effect is almost not noticed as the loss factor only gives a small pressure drop. At 3000 rpm, when cavitation is not simulated, the volumetric ratio is kept almost constant (only 0.07% below for the pressure loss factor case, despite the slight flow ripple reduction). Finally, at 3000 rpm, when cavitation is simulated, it can be seen how the volumetric ratio decreases in 4% from that with atmospheric inlet pressure. Furthermore, it also drops below that obtained in the same conditions when not simulating cavitation (1.4%). If we look at the modified volumetric ratios, it is seen that the differences between the cases with constant inlet pressure and with an inlet loss factor are kept almost constant. This shows that the cavitation that takes place in the backlash clearance is very little affected by the inlet pressure. In conclusion, in this case, in which a part of the cavitation generated in the suction side of the pump is carried to the pressure side, we can no longer affirm that cavitation increases the volumetric ratio of the pump. On the contrary, at high rotational speeds, as less oil is transported inside the inter-teeth volumes, the flow and therefore the volumetric ratio is reduced.

In figure 6.35 the relative air volume evolution with constant inlet pressure and using an inlet pressure loss factor at 1500 and 3000 rpm is shown. At 1500 rpm it is seen that the behavior in both cases is very similar, but the mean volume is increased in 20% when the inlet loss factor is used. We believe this difference to be mainly caused by the bigger cavitation clouds attached to the gear's tips. At 3000 rpm, the mean volume of air increases in more than 3 times its value when using the inlet loss factor. In the case with loss factor, despite the much higher air content in all parts of the cycle and the constant flow rate shown in figure 6.31, the slight peak observed around $0.7T_g$ can still be noticed.

Regarding the inlet pressure, its evolution can be deduced from the instantaneous flow rate graphs, by using the relation established by the boundary condition. Nevertheless, in order to clarify concepts, this evolution has been plotted in figure 6.36, along with their main values, for the three cases simulated with inlet pressure loss factor. The loss factor was calculated in order to obtain a 0.8 bar pressure drop at the maximum velocity. It should be recalled that when applying the inlet boundary condition, the velocity employed in equation 6.2, v_{in}, is estimated from the theoretical volumetric capacity of the pump. As the real flow rate is lower than the theoretical one, this explains that the real pressure drop obtained was of just 0.79 bar with no cavitation allowed and 0.75 bar

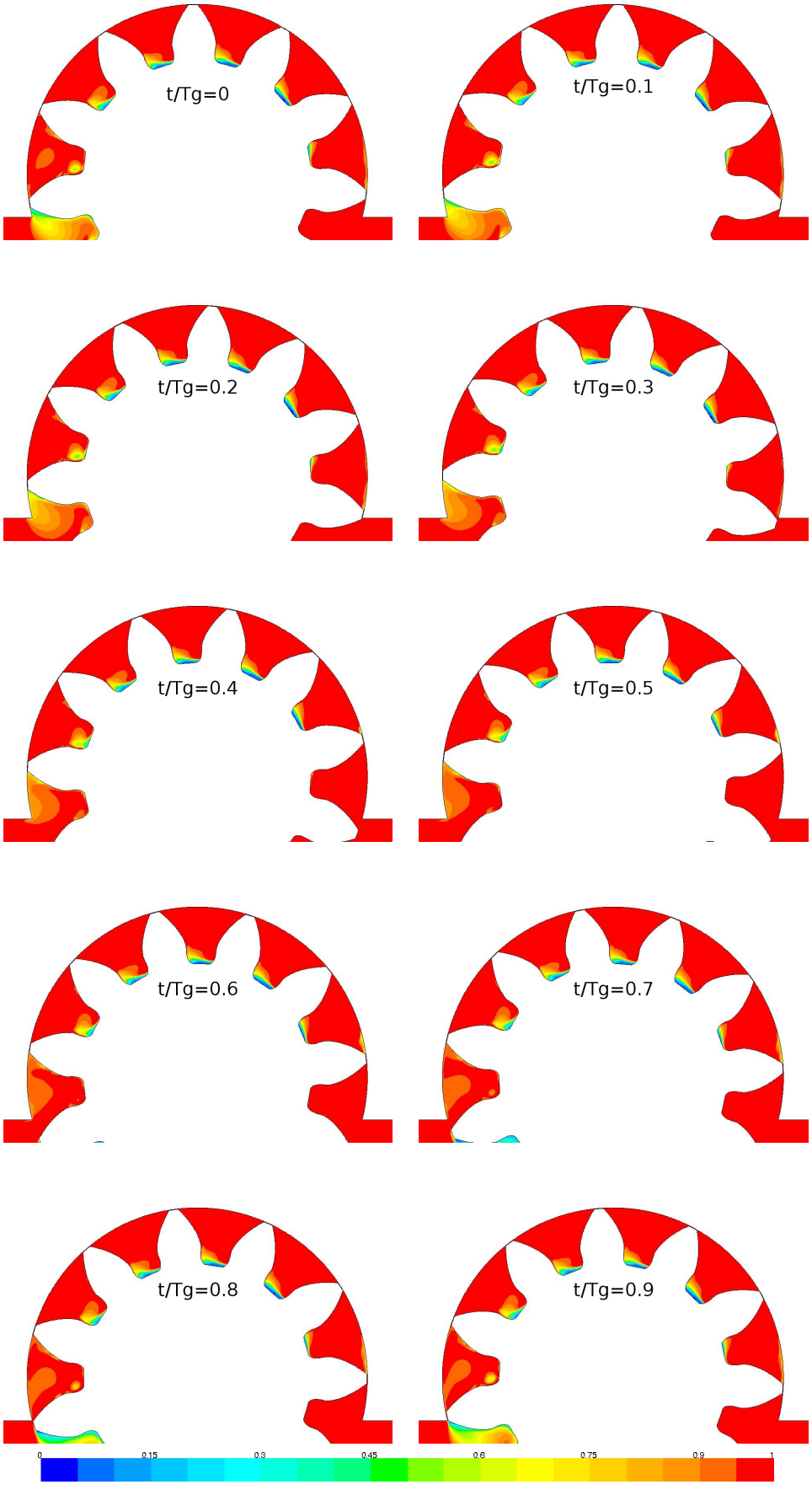

Figure 6.34: Volume fraction of oil trapped between the teeth and the casing at 3000 rpm each 1/10 of a gearing cycle with a pressure inlet loss factor.

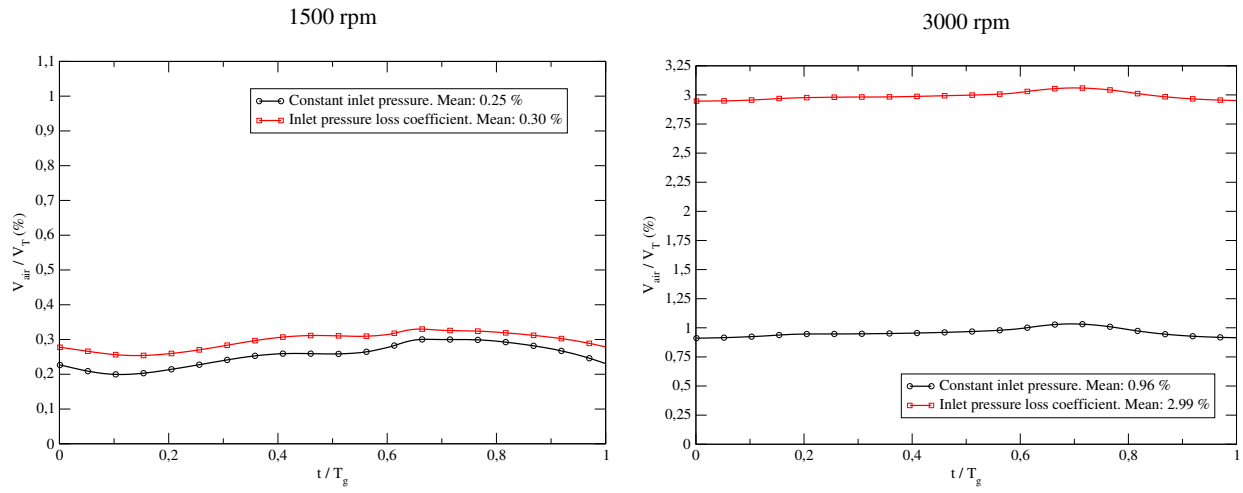

Figure 6.35: Comparison of the relative air volume evolution with constant inlet pressure and with an inlet pressure loss factor, at 1500 rpm and 3000 rpm.

(lower due to the high volumetric ratio drop) with cavitation allowed.

In conclusion, the following points regarding the cavitation and suction characteristics of the reference pump when an inlet pressure loss factor is used, should be noticed:

- Decreasing the main inlet pressure has a small damping effect on the inlet water hammer pulsation when no cavitation is allowed. Otherwise, this damping effect is bigger, and grows with the volume of air generated by cavitation. In this case, at high rotational speeds, the inlet flow may become almost uniform.

- When decreasing the mean inlet pressure, cavitation extends towards the suction chamber. This is especially noticed in the generation of new or bigger cavitation clouds attached to the gear's tips.

- At higher rotational speeds, cavitation clouds are also generated at the corners between the inlet chamber and the casing. At 3000 rpm, these clouds get trapped in the inter-teeth volume and are transported towards the impulsion chamber.

- Decreasing the mean inlet pressure, at 1500 rpm, has a negligible effect on the volumetric ratio despite the increase of 20% in the volume of air. Therefore it remains higher than when not allowing cavitation.

- At 3000 rpm the volume of air increases in over 3 times its original value, and the volumetric ratio drops far below the value that was found when cavitation is not allowed.

- The fact seen in section 6.2, for which an increase in the volume of air does not imply a significant drop in the volumetric ratio is confirmed in this case, as long as cavitation remains in the suction side of the pump and is not transported towards the pressure side. Otherwise, cavitation contributes to highly reduce the volumetric ratio.

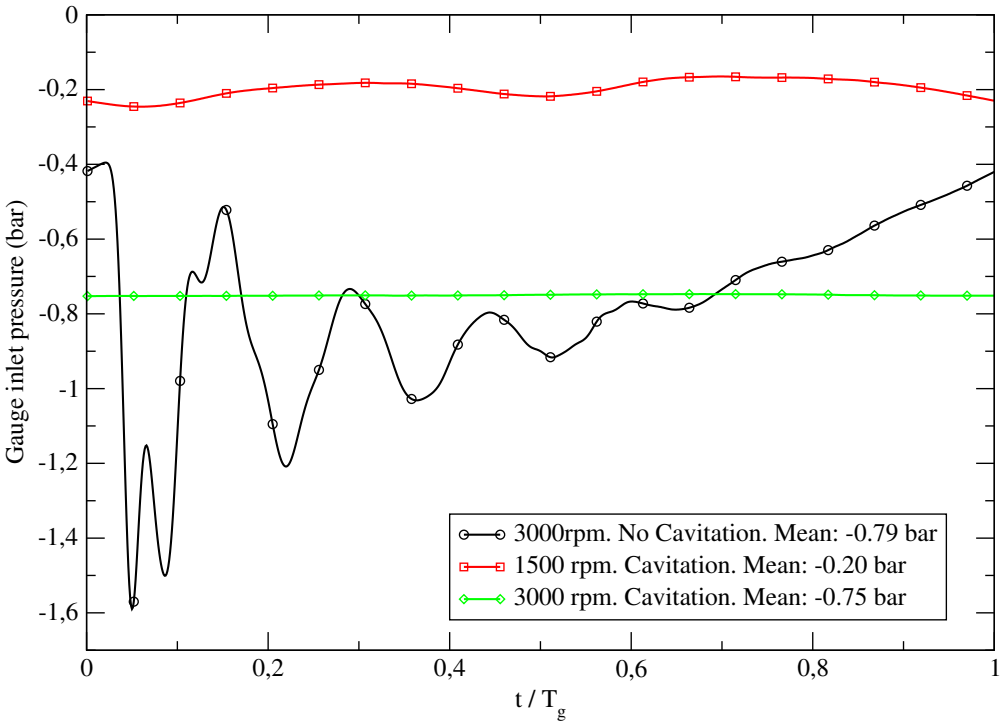

Figure 6.36: Inlet pressure with an inlet pressure loss factor.

6.6 Tip clearance effect

It was seen in section 6.2 that the main effect of the cavitating jet that appears in the backlash clearance is that of increasing the volumetric ratio of the pump (even above 100%). It was also seen that the one of the air contained in the suction chamber (at least for a constant atmospheric inlet pressure) is that of uniforming the inlet flow, damping the water hammer associated to the contact point position jump, while its effect on the volumetric ratio is small.

It is known that losses through the gear tip clearance contribute to diminish the volumetric ratio of the pump. In section 6.3 it was shown that at high working pressures these losses become much higher than at low pressure. Simulations were performed at low pressure in order to prevent the gear tip losses from masking the effects of cavitation. Nevertheless, it was seen that the outlet pressure has a great influence on the cavitation mechanism that affects the volumetric ratio, so that at high working pressure this mechanisms may not take place.

In this section we will repeat the simulations at 2000, 2500 and 3000 rpm with the reference pump, cavitation effects, 10 bar pressure jump, and constant atmospheric inlet pressure, but preventing the fluid from flowing through the gear's tip clearances. This will be done by imposing a very high value of the dynamic viscosity in the tip clearance region at each time step through a user-defined function, as explained in section 4.11. This methodology allows us to concentrate on the influence of cavitation at different working pressures and rotational speeds.

In figure 6.38 the relative volume of air evolution at different rotational speeds, with and without gear's tip clearances, is shown. It is seen that the curves representing the simulations without clearances have a positive shift with respect to the ones with clearances, and that this shift increases with increasing rotational speed. This effect, which may seem strange as we have seen that the

cavitation phenomena is unrelated to the tip leakage, are justified below.

Figure 6.38 compares the contour plots of volume fraction of oil with and without clearances at the beginning of the gearing cycle for the three cases studied. It is observed that both regarding the cavitation cloud's morphology and the amount of air generated, results are very similar. It has been checked that this also happens at any other instant.

In figure 6.39 the contour plots of the volume fraction of oil trapped between a pair of teeth and the casing are shown for the three cases studied at the same non-dimensional time. We appreciate that some cavitation appears near the tooth tip and the casing at the side of the tooth from which the fluid is being dragged. At 3000 rpm part of the air generated in this region is found in the bottom of the inter-teeth volume due to the centrifugal forces acting on the oil. This cavitation that seems to take place in the inter-teeth volumes is a numerical effect that was understood when we checked that the viscosity imposed in the clearances is not high enough to completely cancel the flow through them. Therefore a small amount of leakage still remains in our simulations (of around 25% of the original one) and a jet appears in that region, which is affected by the modified viscosity imposed (as shown in figure 4.27). When increasing even more the viscosity imposed in the clearances numerical instabilities appeared. Nevertheless, some qualitative interpretation of the results obtained in our simulations can be done, by discounting the effect of the air found in the inter-teeth volumes.

We can estimate the amount of air that is transported towards the pressure side due to this numerical effect. Being $V_{air,it}$ the volume of air found in an inter-teeth volume, the volume of air transported to the pressure side in a full revolution would be $2zV_{air,it}$. This volume has shown not to be much dependent on the inter-teeth volume or on the instant considered. We can therefore define a corrected volumetric ratio, $\kappa_{v,corr}$ as

$$\kappa_{v,corr} = \kappa_v + 2z\frac{V_{air,it}}{C_v} \tag{6.3}$$

It should be noticed that, despite this corrected value discounts the unrealistic effect of the air trapped in the inter-teeth volumes, we are still not simulating the pump without tip clearances at all, but just with these leakages strongly reduced. In fact, for a future research, we can think on simulating the effect of different clearances widths by adjusting the value of the viscosity imposed. This way we would be able to simulate more realistic narrower clearances without the need to modify the grids.

In figure 6.40 both the obtained and the corrected values of the volumetric ratio are plotted for each case along with the results previously obtained with tip clearances. Using this corrected value, the volumetric ratios become shifted with respect to the ones with gear tip clearances in an amount ranging from 1.55% to 1.79%, and all of them are found to be above 100%. The effect of the increase in volumetric ratio due to the air trapped in the squeeze volume is noticed in the fact that the volumetric ratio increases with the rotational speed, due to the increasing volume of air present in the squeeze volume at the beginning of the gearing cycle. It is seen that, despite the effect of the gear tip leakage is important from the point of view of obtaining the real volumetric ratio of the pump, it is not dependent on cavitation, and therefore our previous comparisons between simulations with and without cavitation were significant in order to study the effect of cavitation

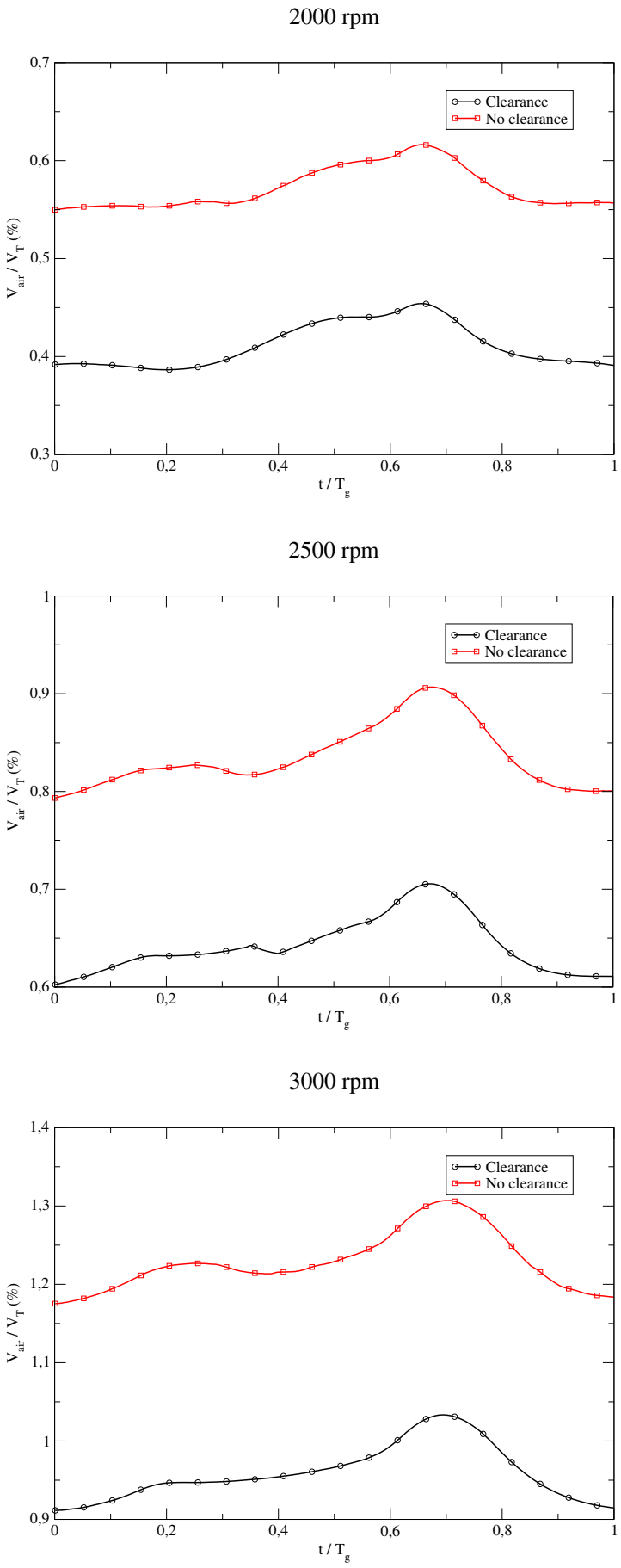

Figure 6.37: Relative volume of air evolution at different rotational speeds, with and without gear's tip clearances.

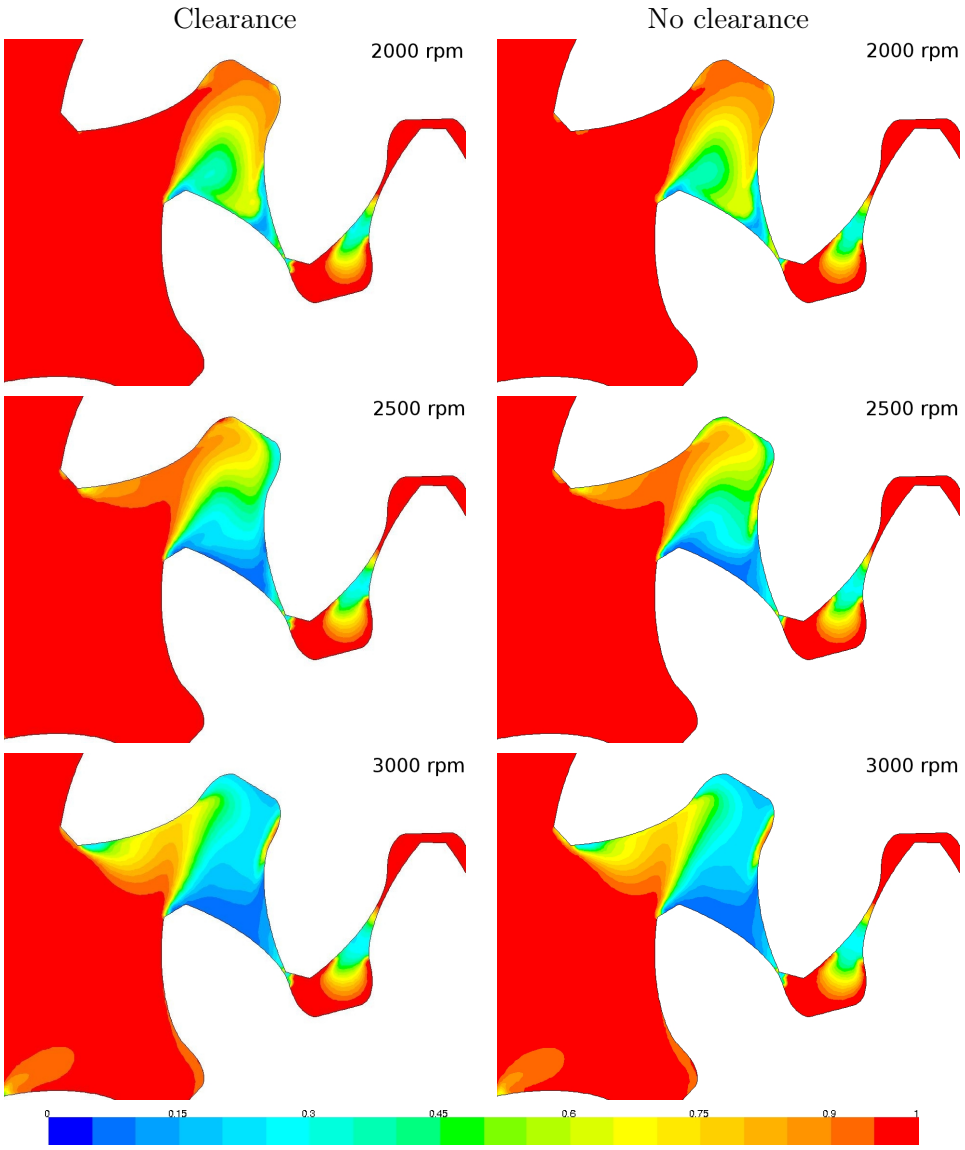

Figure 6.38: Volume fraction of oil at 2000, 2500 and 3000 rpm at $t/T_g = 0$ with and without gear tip clearance.

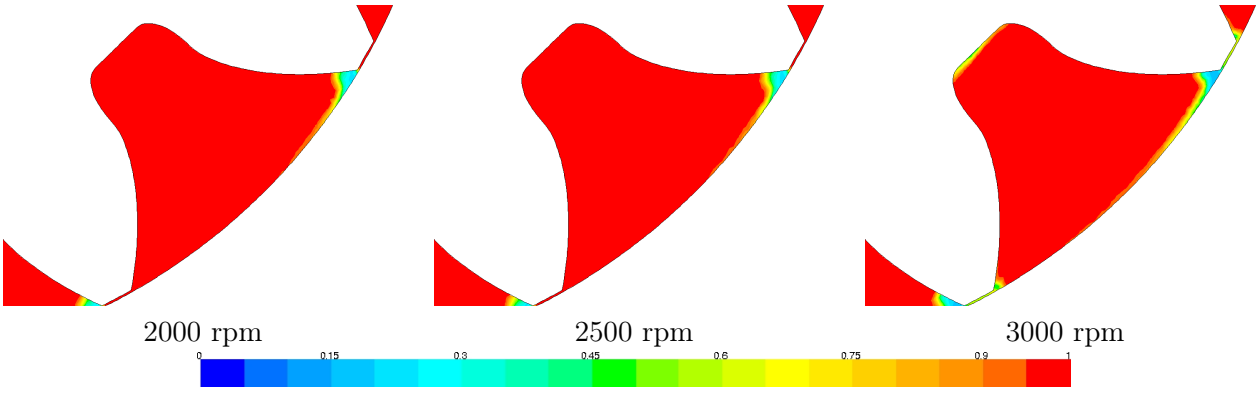

Figure 6.39: Volume fraction of oil trapped between teeth and casing at 2000, 2500 and 3000 rpm without tip clearance.

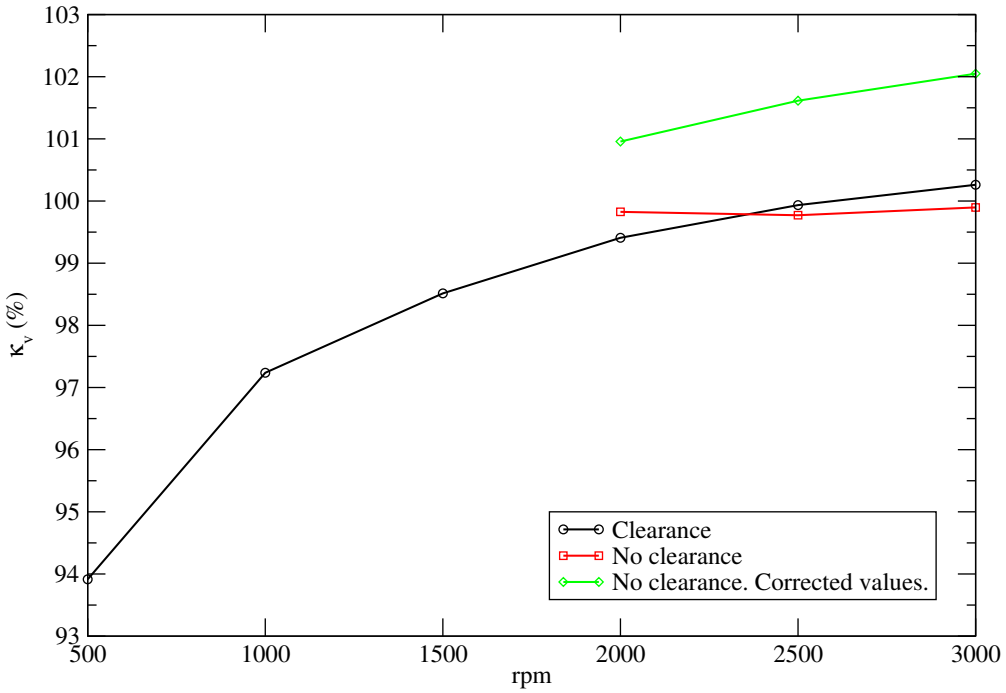

Figure 6.40: Volumetric ratio against operating velocity with and without gear's tip clearances, and corrected volumetric ratio (according to equation 6.3) subtracting the effect of the volume of air trapped in the inter-teeth volumes.

on the volumetric ratio.

In conclusion, the following points regarding the cavitation and suction characteristics of the reference pump when the tip leakage is largely reduced, should be noticed:

- The evolution of the volume of air in the pump along the gearing cycle and the morphology of the cavitation clouds are almost identical to the ones that were found in the simulations with gear tip leakage, except for a shift in the total volume of air. This shift was found to be caused by a numerical issue.
- By defining a corrected volumetric ratio which treats the volume found in the inter-teeth volumes as oil, in order to discount the effect of this numerical issue, it is seen that the new volumetric ratios become considerable higher (in more than 1.5%) than the ones previously obtained with tip clearances, and values higher than 100% are found in all cases.

6.7 Conclusions

In this chapter, the results of the numerical simulations are presented. A variety of cases have been analyzed and some important contributions have been extracted, especially regarding the understanding of the effect of cavitation on the volumetric ratio on external gear pumps. The numerical models employed have been presented in chapter 4. The main conclusions are the following:

- The jump in the contact point position between two gearing cycles is responsible for a water hammer at the inlet when no cavitation is simulated.

- The air content present in the suction chamber very effectively damps the inlet flow pulsations associated to the water hammer at all rotational speeds. Nevertheless, other flow rate peaks appear due to the mass transfer rate phenomena.

- Flow and pressure oscillations due to cavitation are noticed at the outlet.

- The main cavitation mechanism is the low pressure that appears in the volumes opening towards the suction side in the meshing region, in order to fill them. At relatively high rotational speeds, flow separation at the gear's tips that advance towards the inlet becomes another source of cavitation.

- The average volume of air in a cycle rapidly increases with the rotational speed, as flow velocity also increases. The higher the pump speed, the shorter the time for cavitation clouds to dissipate before a new cavitation mechanism takes place, and therefore the more stable the air volume content becomes.

- The inlet flow increases with positive net mass transfer rate from vapor to liquid and vice versa. Therefore, the more stable the air content, the lower the inlet flow irregularity.

- Before the end of a gearing cycle, some amount of gas appears at the backlash clearance between the gears due to the oil jet that takes place in order to fill the increasing volume that is found next to the contact point. This cloud acts as a virtual second contact point, blocking the backward oil flow and therefore increasing the outlet flow rate.

- The effect of this virtual contact point is that of increasing the volumetric efficiency, which may even become larger than unity, as the cavitation mechanisms are not taken into account when defining the theoretical volumetric capacity of the pump (for this reason we have renamed the volumetric efficiency as "volumetric ratio").

- When allowing cavitation, the volumetric ratio increases with the rotational speed in a similar way as it does without cavitation effects.

- The volumetric ratio with cavitation is considerably higher than without it (with differences ranging from 0.65% at 500 rpm to 2.53% at 3000 rpm). These differences are mainly caused by the effect of the air generated at the backlash clearance.

- The strong effect of cavitation on outlet flow and pressure ripples seen at low operating pressure disappears when a higher outlet pressure is imposed.

- Inlet flow and pressure ripples, volume of air evolution, and the morphology and air content of the cavitation clouds, are not significantly affected by the mean outlet pressure, with the exception of the cavitating jet that was found in the backlash clearance, which may not be present at high working pressure.

- Volumetric ratio is highly reduced at high operating pressure because of the gear tip leakage, especially in our case in which the tip clearance width is relatively high. This fact is independent from cavitation.

- The volumetric ratios at high operating pressure are very similar with or without cavitation, as the virtual contact point created by the cavitating jet at the backlash clearance at low operating pressure, which acted as a virtual contact point, is no longer present at high operating pressure.
- When preventing cavitation, it is observed that bigger chambers have an effect in reducing the inlet water hammer frequency.
- No significant difference is seen in the outlet when using one or another inlet chamber, both when allowing or preventing cavitation.
- The flow patterns in the central region of the inlet chamber, through which the meshing region is filled, remains very similar for all the geometries.
- The evolution of the absolute volume of air and the cavitation clouds morphology and air content are not significantly affected by the inlet chamber geometry.
- The volumetric ratio is very similar for all inlet chambers except for number 4 (the bigger one). The volumetric ratio reduction obtained with this chamber is very similar with and without, and is related to the lower area adjacent to its casing, which increases the pressure jump between teeth and therefore the gear's tip leakage.
- For the smaller chambers, up to the reference one, as the inlet chamber grows in size and opens towards the gearing zone, the acceleration of the fluid reaching the meshing region increases. For the bigger ones, more open chambers have the opposite effect. This acceleration is unrelated to the volumetric ratio.
- Decreasing the main inlet pressure has a small damping effect on the inlet water hammer pulsation when no cavitation is allowed. With cavitation, this damping effect is bigger, and grows with the volume of air generated by cavitation. In this case, at high rotational speeds, the inlet flow may become almost uniform.
- When decreasing the mean inlet pressure, cavitation extends towards the suction chamber. This is especially noticed in the generation of new or bigger cavitation clouds attached to the gear's tips.
- Decreasing the mean inlet pressure through an inlet loss factor, at 1500 rpm, has a negligible effect on the volumetric ratio despite the increase of 20% in the volume of air. Therefore it remains higher than when not allowing cavitation.
- At 3000 rpm and using an inlet pressure loss factor such that the mean inlet pressure drops to 0.2 bar, cavitation clouds are also formed at the corner between the inlet chamber and the casing and the volume of air increases in over 3 times its original value. These clouds get trapped in the inter-teeth volume and are transported towards the impulsion chamber. In this case the volumetric ratio drops far below the value that was found when cavitation is not allowed.
- With the gear tip leakage nearly prevented, the evolution of the volume of air in the pump along the gearing cycle and the morphology of the cavitation clouds are almost identical to

the ones previously found, except for a shift in the total volume of air, which was found to caused by a numerical issue.

- Cavitation is unaffected by gear tip leakage, while the volumetric ratio drops in more than 1.5% in all the cases studied. Therefore, despite our simplified model is not appropriate to study the volumetric ratio of real pumps, it is useful to study the effect of cavitation on it.

Chapter 7

Final conclusions and future work

7.1 Introduction

In this chapter, the main topics covered in this thesis will be summarized, as well as the numerical and experimental procedures followed along the work. The final conclusions will be divided into two sections: the first one is dedicated to the knowledge gained in the field of numerical simulation of external gear pumps with cavitation effects, and the second one to the results obtained from the simulations. Finally, suggestions on how this research can be continued will be given.

7.2 Topics covered and procedures followed

In chapter 1, the main aim of this thesis, which is to advance the understanding of the influence of cavitation on the volumetric efficiency of external gear pumps, was presented.

Firstly, in chapter 2, general concepts about cavitation and aeration phenomena were presented, with special attention to the cavitation behavior of hydraulic oils.

Secondly, in chapter 3, the working principles of hydraulically-balanced external gear pumps was described. Although the use of these type of pumps is widely extended, the simulated pump is two-dimensional and non balanced, because of the necessary simplifications introduced in the numerical modeling of the problem. Therefore a good knowledge of the leakages related to three-dimensional effects is essential to understand the limitations of the numerical simulations, in order to be able to decide, taking into account the scope of this thesis, if we can cope with them.

In chapter 4, after presenting the pump geometry and the properties of the hydraulic oil, the numerical modeling of the problem was detailed and justified. The problem was simulated with the commercial finite-volumes based code ANSYS Fluent 12.0. The spatial discretization uses an upwind second order scheme for the density and a QUICK scheme for the momentum equations, while the time derivatives are calculated with a first order implicit scheme. The gradients are approximated with the Green-Gauss node-based method. A body-force-weighted pressure interpolation is used to model the pressure in the boundaries. A pressure-based coupled scheme was selected to solve the equations. Turbulence was modeled using the standard $k-\varepsilon$ RANS model. Modified wall functions were employed to characterize the boundary layers. The mixture model with no slip velocity was

used to take into account multiphase flow associated to cavitation. The phase-transfer mechanisms (cavitation) are simulated using the model developed by Zwart et al. [101]. This model was chosen after making some tests and comparing with experimental data regarding cavitation in hydraulic oil published by Yamaguchi [98], as the validation made by Zwart et al. employed water instead of hydraulic oil. The convergence criteria used in the simulations was presented. An Arbitrary Lagrangian-Eulerian (ALE) formulation with mesh deformation and local remeshing was employed to adapt the mesh to the unsteady geometry of the pump. The deformation algorithm is based on the improved Laplacian smoothing method. A mesh quality analysis, based on the number of cells and its average equivolume skewness is presented. A method for simulating the contact between gears itself and between gears and casing, without the need for geometrical contact, has been developed. This method is based on changing the viscosity at the contact region. The boundary conditions are constant atmospheric inlet pressure and a 10 bar average pressure jump, which has been imposed through a loss factor (a relation between the pressure jump and the outlet dynamic pressure). Hydraulic diameters and turbulent intensities have been used to set the boundary conditions for turbulence. Finally, the following limitations of the simulations are exposed:

- The two-dimensionality of the simulated pipes implies that the flow cannot be properly simulated in the regions where the pipes join with the chambers.
- The axial leakage through the clearance between the gears and the compensation plates cannot be simulated in our two-dimensional model.
- The effect of the pressure relief groove cannot be predicted with a two-dimensional simulation. This forced us to use unity contact ratio between gears.
- The effect of the circumferential grooves that connect several inter-teeth volumes cannot be simulated with our two-dimensional model.
- The pressure jump of 10 bar employed is far from the typical operational conditions of these pumps. This value was selected in order to avoid excessive leakage through the clearances between teeth and casing and also to be able to compare with experimental results (because of the limitations of the experimental method).
- The clearances between teeth and casing in the model are considerable higher than the typical real values. This was necessary in order to avoid excessively small grid cells that would lead to a very high simulation time. This has the effect of increasing the leakages through the gear's tip clearances.

These limitations prevent us accurately predicting the volumetric efficiency of the pump, but allow us to study the effect of cavitation by comparing simulations performed with and without enabling the cavitation model. Therefore our method is useful from the point of view of understanding the complex phenomenology involved in the flow that takes place inside the pump.

In chapter 5 the methodology for measuring the velocity field in the inlet chamber of the pump by means of Time-Resolved Particle Image Velocimetry (TRPIV) is explained. The experiments were performed as a validation of the numerical methods, at 500 rpm, where cavitation is negligible (as the experimental method is not suitable for cavitating flows). The pump casing was built in

methacrylate. The pump was moved by an electric motor. The flow was seeded with $5 - 10\,\mu$m tracing particles and the middle plane was illuminated with a 800 nm thin laser sheet. Pictures were taken at 3000 frames per second with 1024 x 1024 pixels resolution. The working pressure was just 1.1 bar because of the limited strength of the methacrylate casing. Images were processed with the open-source code GPIV. For image processing, the common background of all the in-phase images was subtracted. The size of the interrogation areas was 32 x 32 pixels and the cross-correlation was combined with an image deformation iterative method. Gaussian estimators were employed to obtain sub-pixel accuracy and spurious vectors were detected using the normalized median within the considered vector and the eight nearest neighbors. The final velocity fields were calculated as the average from all the in-phase fields. The main conclusions extracted from comparing the numerical results against the experiments were the following:

- Matching between numerical and experimental streamlines is very poor at the entrance zone of the inlet chamber, as the real inlet pipe is circular while the numerical one is rectangular. The inlet velocity is lower in the case of the pipe with the bigger cross section (the rectangular one) and therefore the flow expands more towards the lateral boundaries of the chamber at the entrance, creating small vortices.

- In the half of the inlet chamber which is nearest to the meshing area, where flow is more two-dimensional, matching between experimental and numerical results gets much better: the position at which streamlines bend through one gear or the other is matched precisely. The position of the cores of the main vortices is approximately matched, although it is closer to the gears in the numerical simulations as the main vortices are pushed in that direction by the smaller ones.

- Finally, it is concluded that in the region in which cavitation should take place (near the meshing area), the three-dimensionality of the flow is small enough to consider the simulations appropriate for studying its effect on the volumetric efficiency of the pump.

The results of the numerical simulations are exposed in chapter 6 and the conclusions will be summarized in section 7.4.

7.3 Knowledge gained in the numerical field

Beyond the conclusions thrown out by the results of the numerical simulations, some contributions to the numerical modeling of two-dimensional gear pumps with cavitation effects have been made:

- An Arbitrary Lagrangian-Eulerian (ALE) formulation with mesh deformation and local remeshing is able to adapt the mesh to the complex deformations associated to the rotation of the gears, along many cycles, keeping stable the number of cells and the quality of the mesh. Nevertheless, an improved Laplacian smoothing method, which adjusts the location of each mesh vertex to the geometric center of the neighboring ones, should be used, and the parameters involved in the algorithm should be carefully adjusted.

- A method was developed for simulating the contact point between gears. The geometry is such that a very small clearance is left where the contact between gears should take place. In each time step, the cell in the center of this clearance is identified and a very high value of the dynamic viscosity is imposed in it as well as in the ones that belong to a small region around it. A similar method was developed for simulating the contact between the tips of the gears and the casing, which is useful when it is desired to get rid of the radial leakage in our simulation.

- Two different models were considered when deciding between the existing cavitation models: the one proposed by Schnerr and Sauer [75], and the one proposed by Zwart et al. [101]. Both have been tested by the authors for transient cavitation cases using water as fluid. In hydraulic oil, as far as the author knows, these models had not been tested before. Therefore, it was needed to make some tests in order to decide between both models, and also to adjust the model constants and decide the convergence criteria. Firstly, the test case employed by Zwart et al. [101], a venturi nozzle, was reproduced with oil using both cavitation models and different cavitation criteria. It was seen that, despite the model from Schnerr and Sauer yields lower mass flow imbalance for a certain convergence criteria, the cloud shedding frequency was highly dependent on the selected model. As the model from Zwart et al. provides model constants which can be changed in order to tune this frequency (as the author did for matching his simulations with experimental results from Stutz and Reboud [81]), it was decided to select this model and tune its constants employing the results from Yamaguchi [98], who tested cavitation in a circular orifice using hydraulic oil. Furthermore, the venturi nozzle was also simulated with water in order to compare with the simulations performed by Zwart et al. [101] and to identify which constants were to be modified in order to control the cloud shedding frequency. Yamaguchi [98] identified the cavitation numbers at which cavitation started in the orifice and at which choking conditions appeared, at different Reynolds numbers. When simulating these experiments, three different combinations of the model constants were tested, at different cavitation numbers and at two different Reynolds numbers. Finally, the optimum parameters for the model from Zwart et al. with unsteady cavitation in oil were identified and applied to our simulations.

7.4 Conclusions from the numerical simulations

In chapter 6 the results of the numerical simulations that have been performed are presented. These cases are the following:

- Reference pump at six different rotational speeds, ranging from 500 rpm to 3000 rpm in 500 rpm intervals, both with and without simulating cavitation. In these cases an average pressure jump of 10 bar is imposed by a constant atmospheric pressure in the inlet and an outlet loss factor (given by equation 4.48).

- Reference pump at 1000 rpm, both with and without simulating cavitation. In these cases an average pressure jump of 100 bar is imposed by a constant atmospheric pressure in the inlet and an outlet loss factor.

- Four alternative pumps with different inlet chamber geometries at the same six rotational speeds as the reference pump, with cavitation. Cases at 1500 rpm were also simulated without cavitation. An average pressure jump of 10 bar was imposed in the same way as in the previous simulations.

- Reference pump at 3000 rpm with and without cavitation and at 1500 rpm with cavitation. In these cases the same outlet loss factor as in the previous simulations is used, but also an inlet loss factor is employed (given by equation 6.2). This coefficient is the same for all cases and is such that at 3000 rpm an average pressure drop of 0.8 bar is obtained at the inlet.

- Reference pump at 2000, 2500 and 3000 rpm with cavitation and an average pressure jump of 10 bar imposed by a constant atmospheric pressure in the inlet and an outlet loss factor. In these simulations, leakage through the gear's tip clearances are greatly reduced by imposing a very high value of the dynamic viscosity in the clearance region, in the way explained in section 4.11.

The main conclusions extracted from the numerical simulations are the following:

- **The jump in the contact point position between two gearing cycles is responsible for a water hammer at the inlet** when no cavitation is simulated.

- **The air content present in the suction chamber very effectively damps the inlet flow pulsations associated to the water hammer** at all rotational speeds. Nevertheless, other flow rate peaks appear due to the mass transfer rate phenomena.

- Flow and pressure oscillations due to cavitation are noticed at the outlet.

- **The main cavitation mechanism is the low pressure that appears in the volumes opening towards the suction side** in the meshing region, in order to fill them. At relatively high rotational speeds, flow separation at the gear's tips that advance towards the inlet becomes another source of cavitation.

- **The average volume of air in a cycle rapidly increases with the rotational speed**, as flow velocity also increases. The higher the pump speed, the shorter the time for cavitation clouds to dissipate before a new cavitation mechanism takes place, and therefore the more stable the air volume content becomes.

- The inlet flow increases with positive net mass transfer rate from vapor to liquid and vice versa. Therefore, **the more stable the air content, the lower the inlet flow irregularity.**

- Before the end of a gearing cycle, **some amount of gas appears at the backlash clearance between the gears due to the oil jet that takes place in order to fill the increasing volume that is found next to the contact point. This cloud acts as a virtual second contact point, blocking the backward oil flow and therefore increasing the outlet flow rate.**

- **The effect of this virtual contact point is that of increasing the volumetric efficiency**, which may even become larger than unity, as the cavitation mechanisms are not taken

into account when defining the theoretical volumetric capacity of the pump (for this reason we have renamed the volumetric efficiency as "volumetric ratio").

- When allowing cavitation, **the volumetric ratio increases with the rotational speed** in a similar way as it does without cavitation effects.
- **The volumetric ratio with cavitation is considerably higher than without it** (with differences ranging from 0.65% at 500 rpm to 2.53% at 3000 rpm). These differences are mainly caused by the effect of the air generated at the backlash clearance.
- **The strong effect of cavitation** on outlet flow and pressure ripples seen at low operating pressure **disappears when a higher outlet pressure is imposed.**
- Inlet flow and pressure ripples, volume of air evolution, and the **morphology and air content of the cavitation clouds, are not significantly affected by the mean outlet pressure, with the exception of the cavitating jet that was found in the backlash clearance, which may not be present at high working pressure.**
- **Volumetric ratio is highly reduced at high operating pressure** because of the gear tip leakage, especially in our case in which the tip clearance width is relatively high. This fact is independent from cavitation.
- **The volumetric ratios at high operating pressure are very similar with or without cavitation**, as the virtual contact point created by the cavitating jet at the backlash clearance at low operating pressure, which acted as a virtual contact point, is no longer present at high operating pressure.
- When preventing cavitation, it is observed that **bigger chambers have an effect in reducing the inlet water hammer frequency.**
- **No significant difference is seen in the outlet when using one or another inlet chamber**, both when allowing or preventing cavitation.
- **The flow patterns in the central region of the inlet chamber**, through which the meshing region is filled, **remains very similar for all the geometries.**
- The evolution of the absolute volume of air and the cavitation clouds morphology and air content are not significantly affected by the inlet chamber geometry.
- **The volumetric ratio is very similar for all inlet chambers** except for number 4 (the bigger one). The volumetric ratio reduction obtained with this chamber is very similar with and without, and is related to the lower area adjacent to its casing, which increases the pressure jump between teeth and therefore the gear's tip leakage.
- For the smaller chambers, up to the reference one, as the inlet chamber grows in size and opens towards the gearing zone, the acceleration of the fluid reaching the meshing region increases. For the bigger ones, more open chambers have the opposite effect. This acceleration is unrelated to the volumetric ratio.

- **Decreasing the main inlet pressure has a small damping effect on the inlet water hammer pulsation** when no cavitation is allowed. **With cavitation, this damping effect is bigger**, and grows with the volume of air generated by cavitation. In this case, at high rotational speeds, **the inlet flow may become almost uniform**.

- **When decreasing the mean inlet pressure, cavitation extends towards the suction chamber.** This is especially noticed in the generation of new or bigger cavitation clouds attached to the gear's tips.

- Decreasing the mean inlet pressure through **an inlet loss factor, at 1500 rpm, has a negligible effect on the volumetric ratio despite the increase of 20% in the volume of air.** Therefore it remains higher than when not allowing cavitation.

- **At 3000 rpm and using an inlet pressure loss factor** such that the mean inlet pressure drops to 0.2 bar, **cavitation clouds are also formed at the corner between the inlet chamber and the casing** and the volume of air increases in over 3 times its original value. **These clouds get trapped in the inter-teeth volume and are transported towards the impulsion chamber. In this case the volumetric ratio drops far below the value that was found when cavitation is not allowed.**

- **With the gear tip leakage nearly prevented, the evolution of the volume of air in the pump along the gearing cycle and the morphology of the cavitation clouds are almost identical to the ones previously found**, except for a shift in the total volume of air, which was found to caused by a numerical issue.

- **Cavitation is unaffected by gear tip leakage**, while the volumetric ratio drops in more than 1.5% in all the cases studied. Therefore, despite our simplified model is not appropriate to study the volumetric ratio of real pumps, it is useful to study the effect of cavitation on it.

7.5 Future work

The results obtained from this thesis suggest us several future lines of research.

From the point of view of the numerical models developed, we can think of continuing our research in the following topics:

- The study made in order to decide which model of cavitation to employ and with which parameters was based on experiments and simulations performed by other authors, either with water or with hydraulic oil. Nevertheless, very few experiments of cavitation in hydraulic oil can be found. By **performing our own experiments on cavitation, and the equivalent numerical simulations**, we would be able to better understand the appropriateness of different cavitation models and their parameters in several types of steady and transient cavitating flows with hydraulic oil. **The influence of assuming an incompressible vapor phase** in the cavitation model should also be studied.

- The technique developed for simulating the contact point between rigid boundaries that move while keeping in contact with each other can be applied to other types of pumps (e.g. internal

gear pumps) or oleohydraulic machinery in general (e.g. valves). Therefore it would be useful to **adapt the user-defined function to make it easily applicable to generic geometries**. Nevertheless, the code should be enhanced in order to avoid the numerical instabilities that were found when simulating contact between teeth and casing.

- Studying the possibility of **simulating the flow through very narrow clearances by adjusting the value of the viscosity** imposed in the method employed to simulate contact between rigid parts. This way we would avoid grids with excessively small cells and, moreover, we would be able to simulate different clearances heights without the need to modify the grid.

Regarding the possibilities that are now open to deepen into the aim of this thesis, several research lines can be followed:

- It has been seen that the effect of cavitation on volumetric efficiency is small when a constant pressure is imposed at the inlet, but it is noticeable when flow fluctuations are allowed through an impedance. Therefore it would be desirable to **make more simulations with inlet loss factors**, and to test the influence of the inlet chamber geometries in the volumetric ratios in these cases.

- As a first step for performing three-dimensional simulations, the priority would be being able to **simulate the circular pipes**, as it has been seen how simulating rectangular pipes derives in a wrong velocity field at the regions where the pipes join with the chambers. This is not difficult from the point of view of setting up the case, as the two-dimensional grid used at the gearing zone and the chambers can be extruded, and only the pipes would need to be remeshed. Nevertheless, the number of cells would be multiplied, and cases would require parallel processing. This is not possible right now as we only have one license of the code employed. A solution would be to switch to an open-source code, as OpenFOAM[1], but in this case, several functionalities would need to be programmed in order to be able to continue using the same numerical models. Some of them have already been implemented in OpenFOAM by Parra Viol[2].

- As a second step in getting closer to the real pump, we can think of **simulating other three-dimensional effects related to the gearing zones as axial clearances, circumferential grooves, and relief grooves.** The dependence of the axial clearance on the working pressure makes it difficult to model the three-dimensional geometry. Furthermore, the small height of the clearance would lead to similar problems of mesh resolution as the ones we had at the gear's tip clearances. A first approach that we suggest to avoid these problems is to keep within a two-dimensional simulation, and mathematically model, through user-defined-functions, some of these three-dimensional effects (for example, modeling mass and momentum source terms)[3].

- User-defined functions can also be employed to model the flow through the gear's tip clearances, in a such a way that they provide a leakage equivalent to the one that would appear

[1] http://www.openfoam.com

[2] Parra Viol, J.P. Estudio e implementación de nuevas funcionalidades de deformación de malla en un software de mecánica de fluidos computacional. Final Degree Project. Universitat Politècnica de Catalunya. Directed by Roberto Castilla López and David del Campo Sud.

[3] The two-dimensional simulation of relief grooves through the use of mass source and sink terms is currently being developed as part of a Final Degree Project under my supervision.

with smaller clearances. Furthermore, the existing models that describe the orbits followed by the axes of the gears can be used to **model the clearance height at each gear tip and at each instant**, an therefore impose the corresponding flow.

Appendix A

Mechanical properties of involute gear pumps

In involute gears, the profiles of the teeth are involutes of a circle, which is called the base circle. The involute of a circle is the spiraling curve traced by the end of an imaginary taut string unwinding itself from that stationary circle. The gears are normally joined to the root circle through a fillet, which has generally a trochoidal geometry.

Contact between a pair of gear teeth occurs at a single instantaneous point which, due to the rotation of the gears, moves across the respective tooth surfaces. In order to better understand the interesting properties of gears with involute profile, some geometrical definitions should be made:

- Line of action: The path traced by the contact point.
- Pitch point: Point where the line of action crosses a line joining the axes of the two gears.
- Pitch circle: A circle with its center in the gear axis that passes through the pitch point. The pitch circle of both gears are tangent to each other.
- Addendum: The radial height of a tooth above the pitch circle.
- Dedendum: The radial depth of a tooth below the pitch circle.
- Clearance: The difference between the addendum and the dedendum.
- Whole depth: The sum of the addendum and the dedendum.
- Working depth: The maximum depth that the tooth extends into the tooth space of a mating gear.
- Addendum circle: The circle which contains the tops of the teeth. Its diameter is the outside or blank diameter.
- Dedendum or root circle: The circle which contains the bottoms of the tooth spaces. Its diameter is the root diameter.
- Circular pitch: The distance from a point on one tooth to the corresponding point on the next tooth, measured along the pitch circle.

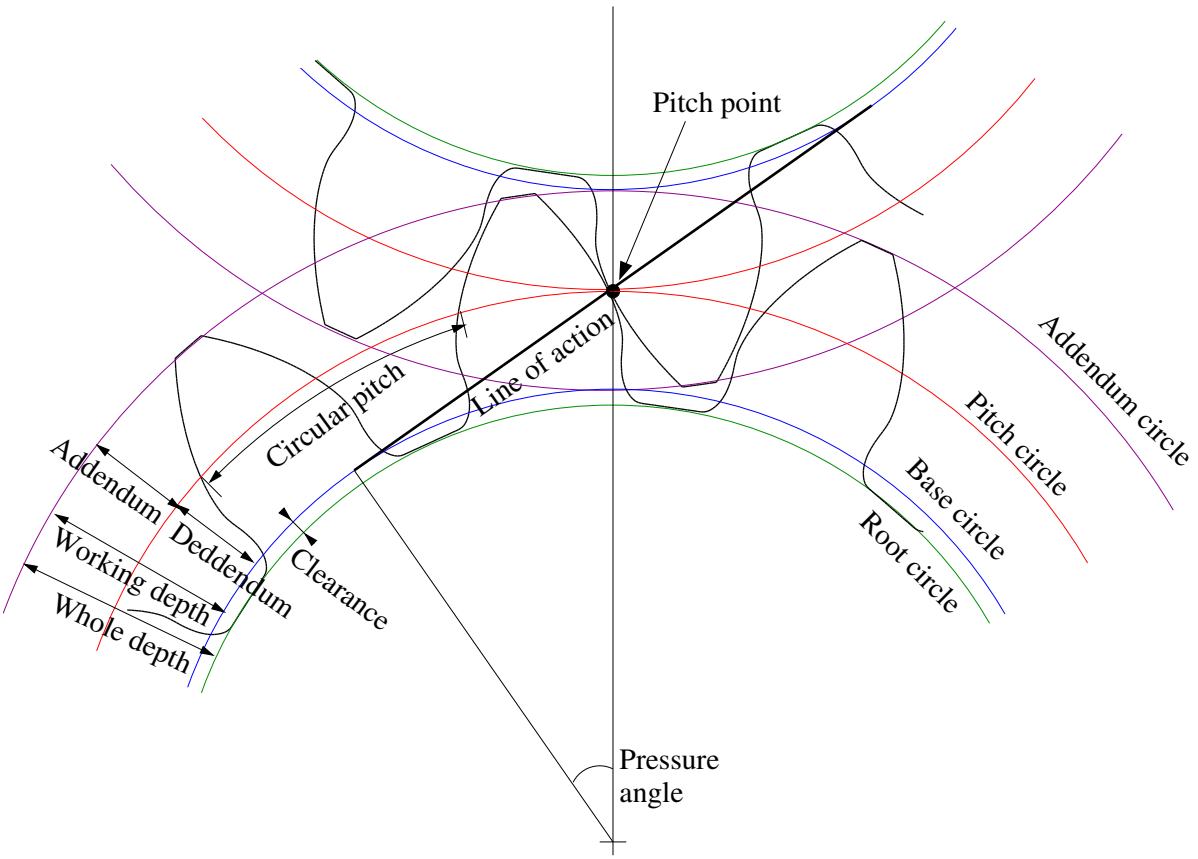

Figure A.1: Main geometrical elements of spur involute gears.

- Modulus: The pitch circle diameter divided by the number of teeth.
- Pressure angle: The angle between the line of action and the common tangent to the pitch circles at the pitch point.
- Tooth face: The surface of a tooth above the pitch circle, parallel to the axis of the gear.
- Tooth flank: The tooth surface below the pitch circle, parallel to the axis of the gear. If any part of the flank extends inside the base circle it cannot have involute form. It may have another form, which does not interfere with mating teeth.

Figure A.1 shows the main geometrical elements of spur involute gears. It represents the instant in which the contact point passes over the pitch point.

The most interesting advantages of using involute teeth profiles are the following:

- The line of action is straight and tangent to the base circles, passing through the pitch point of the gears. The contact point moves, along a gearing cycle, from the point of tangency with the upper gear to the point of tangency with the lower one. The length of the line of action is the length of action.
- The relative rates of rotation of both gears are constant while the teeth are engaged, and also, the force between gears remains constant and aligned with the line of action. In teeth of other shapes, the relative speeds and forces rise and fall as successive teeth engage, resulting

in vibration, noise, and excessive wear. For this reason, nearly all modern gear teeth bear the involute shape.

- Small variations in the center distance do not affect the correct working of the gears. This is important since the pressure forces acting on the gears produce an oscillating displacement of the axes of rotation.

The pressure angle of the gear is a function of the involute tooth shape and pairs of gears must have the same pressure angle in order for the teeth to mesh properly. While any pressure angle can be manufactured, the most common stock gears have a 20° pressure angle. Increasing the pressure angle increases the width of the base of the gear tooth, leading to greater strength and load carrying capacity. Decreasing the pressure angle provides lower backlash, smoother operation, and less sensitivity to manufacturing errors.

Appendix B

Data tables

In the following tables, a summary of the simulations performed and the main results obtained are presented: volumetric ratio (which is defined in section 6.2) and mean relative air volume.

Simulations with constant inlet pressure and no sealing in tip clearance

Chamber	Δp (bar)	rpm	Cavitation?	κ_v (%)	$\langle V_{air}/V_T \rangle$ (%)
Ref	10	500	No	93.263	-
Ref	10	1000	No	95.742	-
Ref	10	1500	No	96.674	-
Ref	10	2000	No	97.164	-
Ref	10	2500	No	97.487	-
Ref	10	3000	No	97.730	-
Ref	10	500	Yes	93.915	0.019
Ref	10	1000	Yes	97.237	0.140
Ref	10	1500	Yes	98.514	0.255
Ref	10	2000	Yes	99.408	0.412
Ref	10	2500	Yes	99.934	0.647
Ref	10	3000	Yes	100.261	0.960
Ref	100	1000	No	83.908	-
Ref	100	1000	Yes	83.939	0.132
1	10	1500	No	96.634	-
2	10	1500	No	96.669	-
3	10	1500	No	96.604	-
4	10	1500	No	96.211	-
1	10	500	Yes	93.799	0.020
1	10	1000	Yes	97.171	0.142
1	10	1500	Yes	98.505	0.260
1	10	2000	Yes	99.419	0.422
1	10	2500	Yes	99.937	0.659

Chamber	Δp (bar)	rpm	Cavitation?	κ_v (%)	$\langle V_{air}/V_T \rangle$ (%)
1	10	3000	Yes	100.481	0.991
2	10	500	Yes	93.899	0.019
2	10	1000	Yes	97.226	0.143
2	10	1500	Yes	98.603	0.260
2	10	2000	Yes	99.364	0.420
2	10	2500	Yes	99.927	0.664
2	10	3000	Yes	100.301	0.993
3	10	500	Yes	93.715	0.019
3	10	1000	Yes	97.193	0.136
3	10	1500	Yes	98.652	0.249
3	10	2000	Yes	99.440	0.401
3	10	2500	Yes	100.150	0.632
3	10	3000	Yes	100.322	0.899
4	10	500	Yes	92.672	0.018
4	10	1000	Yes	96.573	0.130
4	10	1500	Yes	98.171	0.238
4	10	2000	Yes	98.927	0.380
4	10	2500	Yes	99.815	0.607
4	10	3000	Yes	100.105	0.907

Simulations with inlet loss factor and no sealing in tip clearance

Chamber	Δp (bar)	rpm	Cavitation?	κ_v (%)	$\langle V_{air}/V_T \rangle$ (%)
Ref	10	1500	Yes	98.550	0.296
Ref	10	3000	No	97.659	-
Ref	10	3000	Yes	96.259	2.992

Simulations with constant inlet pressure and sealing in tip clearance

Chamber	Δp (bar)	rpm	Cavitation?	κ_v (%)	$\langle V_{air}/V_T \rangle$ (%)
Ref	10	2000	Yes	99.826	0.572
Ref	10	2500	Yes	99.772	0.836
Ref	10	3000	Yes	99.897	1.228

Appendix C

Used-defined functions

The file `gears.c` is used to include some custom functionalities to the numerical simulations through the following user-defined functions:

- DEFINE_CG_MOTION: Gears rotation at the angular velocity given by `ang_vel`.
- DEFINE_GEOM: Turns gear cases into deformable surfaces so that nodes move along them at constant velocity in order to keep constant its relative position to the gears, thus preventing cell distortion between gear's tips and casings.
- DEFINE_ADJUST: Searches for the contact point position between gears and imposes a very high viscosity in a region around it, in order to simulate the effect of the contact point.
- DEFINE_PROPERTY: These functions define a variable density and sound speed for the oil.

```
#include "udf.h"

/************************************************************************
* Angular velocities of gears                                           *
************************************************************************/

/* Angular velocity (rad/s) */
#define ang_vel 157.0796325
/* Housing radius */
#define R  0.02683
/* Distance between gears centres */
#define D 0.04512279

/* Some constants for contact point search */
static int last_ts = -1;
static int count = 0;
static int marked[1000] = {0};
```

```
static real dist[1000] = {0.0};

/* Gear 1 motion */
DEFINE_CG_MOTION(vel_ang_negativa,dt,vel,omega,time,dtime)
{
  vel[0] = 0.0;
  vel[1] = 0.0;
  vel[2] = 0.0;
  omega[0] = 0.0;
  omega[1] = 0.0;
  omega[2] = -ang_vel;
}

/* Gear 2 motion */
DEFINE_CG_MOTION(vel_ang_positiva,dt,vel,omega,time,dtime)
{
  vel[0] = 0.0;
  vel[1] = 0.0;
  vel[2] = 0.0;
  omega[0] = 0.0;
  omega[1] = 0.0;
  omega[2] = ang_vel;
}

/************************************************************************
*  Definition of geometries for case in gear1 (up) and gear2 (low)    *
*                                                                      *
*  The nodes are projected on a circle of radius R, centered in (0,D) *
*  for gear1 and (0,0) for gear2 and move with the angular velocity   *
*  of the gears                                                        *
************************************************************************/

DEFINE_GEOM(case_gear1,domain,dt,pos)
{
  double R1;
  R1=sqrt(pos[0]*pos[0]+((pos[1]-D)*(pos[1]-D)));
  pos[0]=pos[0]*R/R1;
  pos[1]=D+(pos[1]-D)*R/R1;
}

DEFINE_GEOM(case_gear2,domain,dt,pos)
{
  double R1;
```

```
  R1=sqrt(pos[0]*pos[0]+pos[1]*pos[1]);
  pos[0]=pos[0]*R/R1;
  pos[1]=pos[1]*R/R1;
}

/************************************************************************
* Contact point search and viscosity adjustment                         *
************************************************************************/

DEFINE_ADJUST(buscar_contacto,domain)
{
  int gear1_ID=10;
  int gear2_ID=9;
  int gears_ID=4;
  int i,n1,n2,curr_ts;
  cell_t cell_ind,cells;
  real x_pos1,y_pos1,x_pos2,y_pos2,x_pos,y_pos,dx,dy,ts_norm;
  real x[ND_ND],xcell[ND_ND];
  real dist2=100;
  real dist2min=100;
  real distmax=6.325e-4;
  real dist2max;
  real mumax=100;
  face_t f1,f2;
  Node *node1,*node2;
  Thread *thread1,*thread2,*thread_gears,*thread_cells;
  domain = Get_Domain(2);   /* Domain 2 = liquid */
  thread1 = Lookup_Thread(domain,gear1_ID);
  thread2 = Lookup_Thread(domain,gear2_ID);
  thread_cells = Lookup_Thread(domain,gears_ID);
  curr_ts = N_TIME;
  dist2max=distmax*distmax;

  /* Find normalized time step for contact point zone identification */
  ts_norm = curr_ts;
  ts_norm = ts_norm/1000.0;
  ts_norm=1000*(ts_norm-floor(ts_norm));

  /* Search for contact point position only after the first iteration */
  if (last_ts != curr_ts)
  {
    last_ts = curr_ts;
    count=0;
```

```
begin_f_loop(f1,thread1) /* Face loop in gear 1 */
{
  f_node_loop(f1,thread1,n1) /* Node loop in gear 1 */
  {
    if (n1 != 0)
    {
      /* Get node position */
      node1 = F_NODE(f1,thread1,n1);
      x_pos1 = NODE_X(node1);
      y_pos1 = NODE_Y(node1);
      /* If node is within the correct region */
      if ( (ts_norm<300.5 && x_pos1>0.0) || (ts_norm>300.5 && x_pos1<0.0) )
      {
        begin_f_loop(f2,thread2) /* Face loop in gear 2 */
        {
          f_node_loop(f2,thread2,n2) /* Node loop in gear 2 */
          {
            if (n2 != 0)
            {
              /* Get node position */
              node2 = F_NODE(f2,thread2,n2);
              x_pos2 = NODE_X(node2);
              y_pos2 = NODE_Y(node2);
              /* Check distance between nodes */
              dx=x_pos2-x_pos1;
              dy=y_pos2-y_pos1;
              dist2=(dx*dx+dy*dy);
              /* If distance is minimum */
              if (dist2<dist2min)
              {
                dist2min=dist2;
                /* Get cell index of contact point */
                cell_ind=F_C0(f1,thread1);
                thread_gears=THREAD_T0(thread1);
                x_pos=x_pos1;
                y_pos=y_pos1;
              }
            }
          }
        }
        end_f_loop(f2,thread2)
      }
    }
```

```
      }
    }
    end_f_loop(f1,thread1)

    /* Get position of contact point */
    C_CENTROID(x,cell_ind,thread_gears);

    /* Loop around all cells */
    begin_c_loop(cells,thread_cells)
    {
      /* Mark the ones within a maximum distance from contact point */
      C_CENTROID(xcell,cells,thread_cells);
      dx=x[0]-xcell[0];
      dy=x[1]-xcell[1];
      dist2=(dx*dx+dy*dy);
      if (dist2 < dist2max)
      {
        marked[count]=cells;
        dist[count]=sqrt(dist2);
        count++;
      }
      /* Reset viscosity changes from previous time step*/
      C_MU_L(cells,thread_cells)=0.028;
    }
    end_c_loop(cells,thread_cells)
  } /* endif first iteration */

  /* Loop around the marked cells */
  for ( i=0 ; i<count ; i++ )
  {
    /* Set a linear variation of viscosity with distance to contact point*/
    C_MU_L(marked[i],thread_cells)=mumax-((mumax-0.028)/distmax)*dist[i];
  }
}

/************************************************************************
* Density and speed of sound UDFs for compressible liquid flows.      *
* For use with pressure-based solver, for single phase, multiphase    *
* mixture or cavitation models only.                                   *
* Note that for density function, dp is the difference between a cell *
* absolute pressure and reference pressure.                            *
************************************************************************/
```

```
#define BMODULUS 1.5e9
#define rho_ref 885.0
#define p_ref 101325

DEFINE_PROPERTY(density, c, t)
{
  real rho;
  real p, dp;
  real p_operating;

  p_operating = RP_Get_Real ("operating-pressure");
  p = C_P(c,t) + p_operating;
  dp = p-p_ref;
  rho = rho_ref/(1.0-dp/BMODULUS);
  return rho;
}

DEFINE_PROPERTY(sound_speed, c,t)
{
  real a;
  real p, dp,p_operating;

  p_operating = RP_Get_Real ("operating-pressure");
  p = C_P(c,t) + p_operating;
  dp = p-p_ref;
  a = (1.-dp/BMODULUS)*sqrt(BMODULUS/rho_ref);
  return a;
}
```

In case contact between gears and casings is simulated through viscosity, the DEFINE_ADJUST function has to be modified, and some static-type constants should be included. The `gears.c` file for these cases is:

```
#include "udf.h"

/************************************************************************
* Angular velocities of gears                                           *
************************************************************************/

/* Angular velocity (rad/s) */
#define ang_vel 157.0796325
/* Housing radius */
#define R  0.02683
```

```
/* Distance between gears centres */
#define D 0.04512279

/* Some constants for contact point search */
static int last_ts = -1;
static int count = 0;
static int counttips1 = 0;
static int counttips2 = 0;
static int marked[100] = {0};
static real dist[100] = {0.0};
static int facesgear1[11] = {169,343,517,691,865,1039,1213,1387,1561,1735,1909};
static int facesgear2[11] = {169,343,517,691,865,1039,1213,1387,1560,1734,1908};
static int cellspertip1[11] = {0};
static int cellspertip2[11] = {0};
static int markedtips1[8][100]={{0}};
static real disttips1[8][100]={{0.0}};
static int markedtips2[8][100]={{0}};
static real disttips2[8][100]={{0.0}};

/* Gear 1 motion */
DEFINE_CG_MOTION(vel_ang_negativa,dt,vel,omega,time,dtime)
{
  vel[0] = 0.0;
  vel[1] = 0.0;
  vel[2] = 0.0;
  omega[0] = 0.0;
  omega[1] = 0.0;
  omega[2] = -ang_vel;
}

/* Gear 2 motion */
DEFINE_CG_MOTION(vel_ang_positiva,dt,vel,omega,time,dtime)
{
  vel[0] = 0.0;
  vel[1] = 0.0;
  vel[2] = 0.0;
  omega[0] = 0.0;
  omega[1] = 0.0;
  omega[2] = ang_vel;
}

/*********************************************************************
*  Definition of geometries for case in gear1 (up) and gear2 (low)    *
```

```
*                                                                    *
*  The nodes are projected on a circle of radius R, centered in (0,D) *
*  for gear1 and (0,0) for gear2 and move with the angular velocity   *
*  of the gears                                                      *
*********************************************************************/

DEFINE_GEOM(case_gear1,domain,dt,pos)
{
  double R1;
  R1=sqrt(pos[0]*pos[0]+((pos[1]-D)*(pos[1]-D)));
  pos[0]=pos[0]*R/R1;
  pos[1]=D+(pos[1]-D)*R/R1;
}

DEFINE_GEOM(case_gear2,domain,dt,pos)
{
  double R1;
  R1=sqrt(pos[0]*pos[0]+pos[1]*pos[1]);
  pos[0]=pos[0]*R/R1;
  pos[1]=pos[1]*R/R1;
}

/*********************************************************************
* Contact points search and viscosity adjustment                     *
*********************************************************************/

DEFINE_ADJUST(buscar_contacto,domain)
{
  int gear1_ID=10;
  int gear2_ID=9;
  int gears_ID=4;
  int i,j,n1,n2,curr_ts,celltip,cpt;
  cell_t cell_ind,cells;
  real x_pos1,y_pos1,x_pos2,y_pos2,x_pos,y_pos,dx,dy,ts_norm;
  real x[ND_ND],xcell[ND_ND],xtip[ND_ND];
  real dist2=100;
  real dist2min=100;
  real distmax=6.325e-4;
  real distmaxt=1.3e-3;
  real dist2max,dist2maxt,dlimit;
  real mumax=100;
  face_t f1,f2;
  Node *node1,*node2;
```

```
Thread *thread1,*thread2,*thread_gears,*thread_cells;
domain = Get_Domain(2);   /* Domain 2 = liquid */
thread1 = Lookup_Thread(domain,gear1_ID);
thread2 = Lookup_Thread(domain,gear2_ID);
thread_cells = Lookup_Thread(domain,gears_ID);
curr_ts = N_TIME;
dist2max=distmax*distmax;
dist2maxt=distmaxt*distmaxt;
dlimit=0;

/* Find normalized time step for contact point zone identification */
ts_norm = curr_ts;
ts_norm = ts_norm/1000.0;
ts_norm=1000*(ts_norm-floor(ts_norm));

/* Search for contact point position only after the first iteration */
if (last_ts != curr_ts)
{
  last_ts = curr_ts;
  count=0;
  counttips1=0;
  counttips2=0;
  begin_f_loop(f1,thread1) /* Face loop in gear 1 */
  {
    f_node_loop(f1,thread1,n1) /* Node loop in gear 1 */
    {
      if (n1 != 0)
      {
        /* Get node position */
        node1 = F_NODE(f1,thread1,n1);
        x_pos1 = NODE_X(node1);
        y_pos1 = NODE_Y(node1);
        /* If node is within the correct region */
        if ( (ts_norm<300.5 && x_pos1>0.0) || (ts_norm>300.5 && x_pos1<0.0) )
        {
          begin_f_loop(f2,thread2)) /* Face loop in gear 2 */
          {
            f_node_loop(f2,thread2,n2)) /* Node loop in gear 2 */
            {
              if (n2 != 0)
              {
                /* Get node position */
                node2 = F_NODE(f2,thread2,n2);
```

```
                x_pos2 = NODE_X(node2);
                y_pos2 = NODE_Y(node2);
                /* Check distance between nodes */
                dx=x_pos2-x_pos1;
                dy=y_pos2-y_pos1;
                dist2=(dx*dx+dy*dy);
                /* If distance is minimum */
                if (dist2<dist2min)
                {
                  dist2min=dist2;
                  /* Get cell index of contact point */
                  cell_ind=F_C0(f1,thread1);
                  thread_gears=THREAD_T0(thread1);
                  x_pos=x_pos1;
                  y_pos=y_pos1;
                }
              }
            }
          }
          end_f_loop(f2,thread2)
        }
      }
    }
  }
  end_f_loop(f1,thread1)

  /* Get position of contact point */
  C_CENTROID(x,cell_ind,thread_gears);

  /* Loop around all cells */
  begin_c_loop(cells,thread_cells)
  {
    /* Mark the ones within a maximum distance from contact point */
    C_CENTROID(xcell,cells,thread_cells);
    dx=x[0]-xcell[0];
    dy=x[1]-xcell[1];
    dist2=(dx*dx+dy*dy);
    if (dist2 < dist2max)
    {
      marked[count]=cells;
      dist[count]=sqrt(dist2);
      count++;
    }
```

```
  /* Reset viscosity changes from previous time step */
  C_MU_L(cells,thread_cells)=0.028;
}
end_c_loop(cells,thread_cells)

/* Mark tips of gear 1 and distances */
for (i=0 ; i<11 ; i++)
{
  /* Get index of cell adjoining the gear tip face center */
  celltip=F_C0(facesgear1[i],thread1);
  /* Get its centroid position */
  C_CENTROID(xtip,celltip,thread_cells);
  /* Check that gear tip is at the caseing region */
  if (xtip[1] > .03834131)
  {
    j=0;
    /* Loop around all cells */
    begin_c_loop(cells,thread_cells)
    {
      /* Mark the ones within a maximum distance from tip center */
      C_CENTROID(xcell,cells,thread_cells);
      dx=xtip[0]-xcell[0];
      dy=xtip[1]-xcell[1];
      dist2=(dx*dx+dy*dy);
      if (dist2 < dist2maxt)
      {
        markedtips1[counttips1][j]=cells;
        disttips1[counttips1][j]=sqrt(dist2);
        j++;
      }
    }
    end_c_loop(cells,thread_cells)
    cellspertip1[counttips1]=j;
    counttips1++;
  }
}

/* Mark tips of gear 2 and distances */
for (i=0 ; i<11 ; i++)
{
  /* Get index of cell adjoining the gear tip face center */
  celltip=F_C0(facesgear2[i],thread2);
  /* Get its centroid position */
```

```
    C_CENTROID(xtip,celltip,thread_cells);
    /* Check that gear tip is at the caseing region */
    if (xtip[1] < .00623758)
    {
      j=0;
      /* Loop around all cells */
      begin_c_loop(cells,thread_cells)
      {
        /* Mark the ones within a maximum distance from tip center */
        C_CENTROID(xcell,cells,thread_cells);
        dx=xtip[0]-xcell[0];
        dy=xtip[1]-xcell[1];
        dist2=(dx*dx+dy*dy);
        if (dist2 < dist2maxt)
        {
          markedtips2[counttips2][j]=cells;
          disttips2[counttips2][j]=sqrt(dist2);
          j++;
        }
      }
      end_c_loop(cells,thread_cells)
      cellspertip2[counttips2]=j;
      counttips2++;
    }
  }
} /* endif first iteration */

/* Loop around the marked cells near contact point */
for ( i=0 ; i<count ; i++ )
{
  /* Set a linear variation of viscosity with distance to contact point */
  C_MU_L(marked[i],thread_cells)=mumax-((mumax-0.028)/distmax)*dist[i];
}

/* Loop around the marked cells near tips of gear 1 */
for ( i=0 ; i<counttips1 ; i++ )
{
  cpt=cellspertip1[i];
  for (j=0 ; j < cpt ; j++)
  {
    /* Set a trapezoidal variation of viscosity with distance to contact point */
    dlimit=distmaxt/2;
    if (disttips1[i][j] < dlimit)
```

```
      {
        C_MU_L(markedtips1[i][j],thread_cells)=mumax;
      } else {
        C_MU_L(markedtips1[i][j],thread_cells)=2*(mumax-0.028)-
        (2*(mumax-0.028)/distmaxt)*disttips1[i][j];
      }
    }
  }

  /* Loop around the marked cells near tips of gear 2 */
  for ( i=0 ; i<counttips2 ; i++ )
  {
    cpt=cellspertip2[i];
    for (j=0 ; j<cpt ; j++)
    {
      /* Set a trapezoidal variation of viscosity with distance to contact point */
      dlimit=distmaxt/2;
      if (disttips2[i][j] < dlimit)
      {
        C_MU_L(markedtips2[i][j],thread_cells)=mumax;
      } else {
        C_MU_L(markedtips2[i][j],thread_cells)=2*(mumax-0.028)-
        (2*(mumax-0.028)/distmaxt)*disttips2[i][j];
      }
    }
  }

}


/************************************************************************
* Density and speed of sound UDFs for compressible liquid flows.       *
* For use with pressure-based solver, for single phase, multiphase     *
* mixture or cavitation models only.                                   *
* Note that for density function, dp is the difference between a cell  *
* absolute pressure and reference pressure.                            *
************************************************************************/

#define BMODULUS 1.5e9
#define rho_ref 885.0
#define p_ref 101325

DEFINE_PROPERTY(density, c, t)
```

```
{
  real rho;
  real p, dp;
  real p_operating;

  p_operating = RP_Get_Real ("operating-pressure");
  p = C_P(c,t) + p_operating;
  dp = p-p_ref;
  rho = rho_ref/(1.0-dp/BMODULUS);
  return rho;
}

DEFINE_PROPERTY(sound_speed, c,t)
{
  real a;
  real p, dp,p_operating;

  p_operating = RP_Get_Real ("operating-pressure");
  p = C_P(c,t) + p_operating;
  dp = p-p_ref;
  a = (1.-dp/BMODULUS)*sqrt(BMODULUS/rho_ref);
  return a;
}
```

Bibliography

[1] *ANSYS Fluent 12.0 Theory guide*, 2009.

[2] A.J. Acosta and B.R. Parkin. Cavitation inception – a selective review. *Journal of ship research*, 19(4):193–205, 1975.

[3] V.H. Arakeri. Cavitation inception. *Proc. Indian Acad. Sci.*, C2:149–147, 1979.

[4] ASME. *An effect of air content on the occurrence of cavitation.* Trans ASME, 82, Ser. D. Jr. Basic Engineering, 1960.

[5] ASME. *Limited Cavitation.* The ASME Fluids Engineering and Applied Mechanics Conference, June 1969.

[6] M.L. Billet. Cavitation nuclei measurement—a review. In *Proc. 1985 ASME Cavitation and Multiphase Flow Forum*, pages 31–38, 1985.

[7] M. Borghi, B. Zardin, and E. Specchia. External gear pump volumetric eficienciency: numerical and experimental analysis. *SAE*, 2009.

[8] C. Brahic. Dolphins swim so fast it hurts. *New Scientist*, 2008.

[9] C.E. Brennen. *Cavitation and Bubble Dynamics.* Oxford University Press, 1995.

[10] D. Bruce, M. Wilson, and S. Generalis. Flow field analysis of both the trilobal element and mixing disc zones within a closely intermeshing, co-rotating twin-screw extruder. *Intern. Polymer Processing*, 4:323–330, 1997.

[11] J. Cadalfach, A. Oliva, G. van der Graaf, and X. Albets. Convection in a large, inclined, channel with assymetric heating and surface radiation. *Journal of Heat Transfer*, 125, 2003.

[12] R. Castilla, P.J. Gamez-Montero, N. Ertürk, A. Vernet, M. Coussirat, and E. Codina. Numerical simulation of the turbulent flow in the suction chamber of a gear pump using deforming mesh and mesh replacement. *Elsevier*, 2009.

[13] Roberto Castilla, Jan Wojciechowski, Pedro Javier Gamez-Montero, Anton Vernet, and Esteve Codina. Analysis of the turbulence in the suction chamber of an external gear pump using Time Resolved Particle Image Velocimetry. *Journal of Flow Measurement and Instrumentation*, 19(6):377–384, 2008.

[14] Y.S. Cha. On the equilibrium of cavitation nuclei in liquid-gas solutions. *ASME Journal of Fluids Engineering*, 103:425–431, September 1981.

[15] H. C. Chen and V. C. Patel. Near-wall turbulence models for complex flows including separation. *AIAA Journal*, (26):641–648, June 1988.

[16] O. Coutier-Delgosha, R. Fortes-Patella, and J. L. Reboud. Evaluation of the turbulence model influence on the numerical simulations of unsteady cavitation. *Journal of Fluids Engineering*, 2003.

[17] R. E. Dorey. Modelling of losses in pumps and motors. In *1st Bath International Fluid Power Workshop*, 1988.

[18] M. Eaton, P. S. Keogh, and K. A. Edge. The modelling, prediction, and experimental evaluation of gear pump meshing pressures with particular reference to aero-engine fuel pumps. *Journal os Systems and Control Engineering*, 220, 2006.

[19] D.N. Edge, K.A. Johnston. The 'secondary source' method for the measurement of pump pressure ripple characteristics. part 1: Description of method. *Proc Institution of Mechanical Engineers Journal of Power and Energy*, 204:8, 1990.

[20] N. Ertürk, A. Vernet, R. Castilla, P.J. Gamez-Montero, and J. A. Ferré. Experimental analysis of the flow dynamics in the suction chamber of an external gear pump. *International Journal of Mechanical Sciences*, 53:135–144, 2011.

[21] N. Ertürk, A. Vernet, J. A. Ferré, R. Castilla, and E. Codina. Analysis of the turbulent flow of an external gear pump by Time Resolved Particle Image Velocimetry. In *14th Int Symp on Applications of Laser Techniques to Fluid Mechanics*, July 2008.

[22] H.M. Fitzpatrick and M. Strasberg. Hydrodynamic sources of sound. In *First ONR Symp. on Naval Hydrodynamics*, pages 241–280, 1956.

[23] F. J. Freitas. *The generation and transmission of pressure fluctuations in pump suction lines.* PhD thesis, Bath University, 1982.

[24] S. Fujikawa and T. Akamatsu. Some recent aspects of bubble dynamics. In *2nd International Conference on Cavitation.* ImechE, 1983.

[25] A. G. Gerber. A cfd model for devices operating under extensive cavitation conditions. *International Mechanical Engineering Congress and Exhibit*, 2002.

[26] M. Guiseppe, J. Cadalfach, G. van der Graaf, and A. Oliva. Air cavities with parallel slats inside. In *EuroSun2004*, 2004.

[27] W. Gutbrod. Druckpulsation von aussen-und innenzahnradpumpen und deren auswirkungenauf das pumpengeräusch. *Ölhydraulik und Pneumatik*, 19(4):250–257, 1975.

[28] W. Gutbrod. Förderstrom von aussen-und innenzahnradpumpen und seine ungleichförmigkeit. *Ölhydraulik und Pneumatik*, 19(2):97–104, 1975.

[29] M. Gutés. *Estudio de un cojinete hidrodinámico en una bomba de engranajes externos.* PhD thesis, Polytechnic University of Catalonia, December 2007.

[30] Rainer Hain, Christian J. Kähler, and Cam Tropea. Comparison of ccd, cmos and intensified cameras. *Experiments in Fluids*, 2007.

[31] E.N. Harvey, D.K. Barnes, W.D. McElroy, A.H. Whiteley, D.C. Pease, and K.W. Cooper. Bubble formation in animals: physical factors. *Journal of Cell. and Comp. Physiology*, 24(1):1–22, 1944.

[32] A.T.J. Hayward. Aeration in hydraulic systems - its assessment and control. In *Oil Hydrulics Conf.* Instn. Mech. Engineers, 1961.

[33] J.W. Holl and A.L. Treaster. Cavitation hysteresis. In *Conf. Cavitation in Fluid Machinery.* Applied Mech. Fluid Engineering G., 1965.

[34] D. G. Holmes and S. D. Connell. Solution of the 2d navier-stokes equations on unstructured adaptive grids. *AIAA 9th Computational Fluid Dynamics Conference*, June, 1989.

[35] Guillaume Houzeaux and Ramon Codina. A finite element method for the solution of rotary pumps. *Computers & Fluids*, 36:667–679, 2007.

[36] K. J. Huang and W. C. Lian. Kinematic flowrate characteristics of external spur gear pumps using an exact closed solution. *Mechanism and Machine Theory*, 44:1121–1131, 2009.

[37] IMechE, editor. *Damage due to cavitation and subcooled boiling bubble collapse*, 1968.

[38] M. Ishii. *Thermo-fluid Dynamics Theory of Two-Phase Flow.* Eyrolles, 1975.

[39] J. Ivantysyn and M. Ivantysynova. *Hydrostatic pumps and motors.* Tech Books International, 2003.

[40] Adrian R. J. Twenty years of particle image velocimetry. *Experiments in Fluids*, 2005.

[41] C.A. Johnsson. Cavitation inception on headforms, further tests. In *Proc. 12th Towing Tank Conf.*, pages 381–392, 1969.

[42] B. Jones. *The suction characteristics of power steering pumps.* PhD thesis, Bath University, 1999.

[43] T. Jongen. *Simulation and Modeling of Turbulent Incompressible Flows.* PhD thesis, EPF Lausanne, Lausane, Switzerland, 1992.

[44] Riemslagh K., Vierendeels J., and Dick E. An arbitrary lagrangian–eulerian finite-volume method for the simulation of rotary displacement pump flow. *Applied Numerical Mathematics*, 32:419–433, 2000.

[45] H. Katakura, S. Tsuji, R. Yamane, and H. Fujita. A research on air in oils. *JSME*, 27(231), September 1984.

[46] Hinsch K.D. Particle image velocimetry. In Sirohi R.S., editor, *Speckle Metrology*, pages 235–342. Marcel Dekker Inc., 1993.

[47] R. D. Keane and Adrian R. J. Theory of cross-correlation analysis of piv images. *Appl. Sci. Res.*, (49):191 215, 1992.

[48] A. P. Keller and H. K. Rott. The effect of flow turbulence on cavitation inception. *ASME FED*, 194, 1997.

[49] A. H. Khalaf. *The design and performance of gear pumps with particular reference to marginal suction condition*. PhD thesis, Cranfield Institute of Technology, 1989.

[50] H. Kimoto, Y. Tsuda, and T. Hirose. A modelling study of the cavitation microjet. In *2nd International Conference on Cavitation*. ImechE, 1983.

[51] R.T. Knapp. Cavitation and nuclei. *Transactions of ASME*, 80:1315–1324, 1958.

[52] R.T. Knapp, J.W. Daily, and F.G. Hammitt. *Cavitation*. McGraw-Hill, New York, 1970.

[53] R.T. Knapp and A. Hollander. Laboratory investigations of the mechanism of cavitation. *Transactions of ASME*, 70:419–435, 1948.

[54] W.S. Lamb. *Cavitation and aeration in hydraulic systems*. PhD thesis, BHR Group, Bedfordshire, UK, 1983.

[55] B. E. Launder and D. B. Spalding. *Mathematical Models of turbulence*. Academic Press, London, 1972.

[56] H. Lindgren and C.A. Johnsson. Cavitation inception on headforms, ittc comparative experiments. In *Proc. 11th Towing Tank Conf.*, pages 219–323, 1966.

[57] D. Lohse, B. Schmitz, and M. Versluis. Snapping shrimp make flashing bubbles. *Nature*, (413), 2001.

[58] P.A. Lush and B. Angell. Correlation of cavitation erosion and sound pressure level. *ASME. J. Fluids Eng.*, 106:347–351, 1984.

[59] Raffel M., Willert C., and Kompenhans J. *Particle image velocimetry. A practical guide*. Springer, 1998.

[60] N. D. Manring and S. B. Kasaragadda. The theoretical flow ripple of an external gear pump. *Journal of Dynamic Systems, Measurement, and Control*, 125, September 2003.

[61] R.H. Mellen. Ultrasonic spectrum of cavitation noise in water. *Journal of the Acoustical Society of America*, 1954.

[62] H. Molly. Die zahnradpumpe mit evolventischen zähnen. *Ölhydraulik und Pneumatik*, 1:24–26, 1958.

[63] Y. Mori, K. Hijikata, and T. Nagatani. Fundamental study of bubble dissolution in liquid. *Int. J. Heat Mass Transfer*, 20:41–50, 1977.

[64] J. Myllykylä. *Semi-empirical model for the suction capability of an external gear pump*. PhD thesis, Tampere University of Technology, 1999.

[65] K Nagamura, K Ikejo, and F G Tutulan. Design and performance of gear pumps with a non-involute tooth profile. *Journal of Engineering Manufacture*, 218:699–711, 2004.

[66] Proceedings of the 12th international symposium on applications of laser techniques to fluid mechanics, editor. *Consideration and improvements of the analysis algorithms used for Time Resolved PIV of wall bounded flows.* Proceedings of the 12th international symposium on applications of laser techniques to fluid mechanics, 2004.

[67] Mario Panizza. *Environmental Geomorphology.* Elsevier, Amsterdam, 1996.

[68] B. Persson. *Theoretical investigation on the dynamics of cavitation bubble growth.* PhD thesis, Chalmers TH, 1974.

[69] M.S. Plesset. The dynamics of cavitation bubbles. *ASME J. Appl. Mech.*, 16:218–231, 1948.

[70] R. D. Rauch, J. T. Batira, and T. Y. Yang. Spatial adaption procedures on unstructured meshes for accurate unsteady aerodynamic flow computations. Technical Report 91-1106, AIAA, 1991.

[71] Lord Rayleigh. On the pressure developed in a liquid during the collapse of spherical cavity. *Phil. Mag.*, 34:94–98, 1917.

[72] K. Sato and K. Kakutani. Measurements of cavitation inception. *JSME International Journal*, 37(2), 1994.

[73] F. Scarano. Iterative image deformation methods in piv. *Measurement Science & Technology*, 13, 2002.

[74] W. Schlösser. Mathematical model for displacement pump and motors. *Hydraulic Power Transmission*, 1961.

[75] G.H. Schnerr and J. Sauer. Physical and numerical modeling of unsteady cavitation dynamics. In *Fourth International Conference on Multiphase Flow*, 2001.

[76] P. H. Schweitzer and V. G. Szebehely. Gas evolution in liquids and cavitation. *Journal of Applied Physics*, 1950.

[77] I. Senocak and W. Shyy. Evaluation of cavitation models for navier-stokes computations. *ASME Fluids Engineering Division Summer Meeting*, 2002.

[78] A. K. Singhal, M. M. Athavale, H. Li, and Y. Jiang. Mathematical basis and validation of the full cavitation model. *Journal of Fluids Engineering*, 124, September 2002.

[79] G.W. Stachowiak and A.W. Batchelor. *Engineering tribology.* Butterworth-Heinemann, Boston, 2001.

[80] Wayne Strasser. Cfd investigation of gear pump mixing using deforming/agglomerating mesh. *Journal of Fluids Engineering*, 129(4):476–484, 2007.

[81] B. Stutz and J.L. Reboud. Experiments on unsteady cavitation. *Experiments in Fluids*, 1997.

[82] G. C. Svedberg. The viscosity influence on cavitation in hydraulic pumps. In *9th Aachener Fluidtechnische Kolloquium*, 1990.

[83] Second Fluid Power Symposium, editor. *Discharge performance of long orifices with cavitating flow*, January 1971.

[84] J. Thoma. Mathematical models and effective performance of hydrostatic machines and transmissions. *Hydraulic and Pneumatic Power*, pages 642–651, 1969.

[85] Y. Tomita and A. Shima. High-speed photographic observations of laser-induced cavitation bubbles in water. *Acustica*, 71(3):161–171, 1990.

[86] J. Tsai and Y. Chen. A generalised approach on equilibrium theory of cavitation nuclei in liquid-gas solutions. *Journal of Fluids Engineering*, 112, December 1990.

[87] H. C. van de Hulst. *Light scattering by small particles*. John Wiley & Sons, Inc., 1957.

[88] G. van der Graaf. Gpiv: An open source project for piv. In *Presentation at PIVNET/ERCOFTAC workshop*, July 2004.

[89] T.J. Viersma. *Analysis, Synthesis and Design of Hydraulic Servosystems and Pipelines*. Elsevier, 1980.

[90] J. Vande Voorde, J. Vierendeels, and E. Dick. Development of a Laplacian-based mesh generator for ALE calculations in rotary volumetric pumps and compressors. *Comput. Methods Appl. Mech. Engrg.*, 193:4401–4415, 2004.

[91] M. P. Wernet. Temporally resolved piv for space-time correlations in both cold and hot jet flows. *Measurement Science and Technology*, 2007.

[92] J. Westerweel and F. Scarano. Universal outlier detection for piv data. *Experiments in Fluids*, 39:1096–1100, 2005.

[93] D.C. Wiggert and M.J. Sundquist. The effect of gaseous cavitation on fluid transients. *Journal of Fluids Engineering*, 101:79–86, March 1979.

[94] P. Wiklund and G. C. Svedberg. Cavitation properties of an axial piston pump using a vegetable and mineral oil. In *9th Bath International Fluid Power Workshop*, 1996.

[95] W. E. Wilson. Performance criteria for positive displacement pumps and fluid motors. In *ASME Semi-annual Meeting (48-SA-14)*, 1948.

[96] M. Wolfshtein. The velocity and temperature distribution of one-dimensional flow with turbulence augmentation and pressure gradient. *Int. J. Heat Mass Transfer*, 12:301–318, 1969.

[97] Z. Xiaodong, F. Yong, L. Zhiyi, and Z. Zongchang. The numerical simulation of collapse pressure and boundary of the cavity cloud in venturi. *Chinese Journal of Chemical Engineering*, 17:896–903, December 2009.

[98] A. Yamaguchi. Cavitation characteristics of long orifices in hydraulic systems. In *5th International Fluid Power Symposium*, 1978.

[99] G. L. Zarotti and N. Nervegna. Pump efficiencies approximation and modelling. In *6th International Fluid Power Symposium*, pages 145–164, 1981.

[100] L. Zhou and Z. Wang. Numerical simulation of cavitation around a hydrofoil and evaluation of a rng k-e model. *Journal of Fluids Engineering*, 130, January 2008.

[101] Philip J. Zwart, Andrew G. Gerber, and Thabet Belamri. A two-phase flow model for predicting cavitation dynamics. *ICMF International Conference on Multiphase Flow*, 2004.

[102] P.J. Zwart. Personal communication, 2010.